

AN ABSTRACT OF THE THESIS OF

Yissu Wu for the degree of Doctor of Philosophy

in Mechanical Engineering presented on March 10, 1995

Title: LAMINAR NATURAL CONVECTION IN VERTICAL TUBES WITH
ONE END OPEN TO A LARGE RESERVOIR

Redacted for Privacy

Abstract approved: _____

James R. Welty

The problem of laminar natural convection in vertical tubes with one end open to a large reservoir, designated open thermosyphons, is numerically and experimentally examined to predict flow behavior and the heat transfer rates. In the numerical study, a semi-implicit, time-marching, finite-volume solution procedure was adopted to solve the three governing equations - mass, momentum, and energy - sequentially. Experimental work involved the use of a Mach-Zehnder interferometer to examine the temperature field for a modified rectangular open thermosyphon through the interpretation of fringe patterns. These experimental fringe patterns were used for the qualitative comparison with those obtained from the numerical analyses. Nusselt numbers were determined from the interferometer results and compared with numerical results.

Heat transfer rates through the tube wall were found to be strong functions of the tube radius, and approached an asymptotic limit as the tube radius was increased. Both experimental and numerical results exhibited an oscillatory nature for large height-to-width (aspect ratio) open cavities. Comparisons between experimental and numerically-generated fringe patterns indicated good agreement. Based on experimental results, a correlation between Nusselt number, Nu , and Rayleigh number, Ra_w , for different aspect ratios, L/W , was determined to be

$$Nu = 0.036 \cdot Ra_w^{2/5} \cdot (L/W)^{-1/5}.$$

Copyright by Yissu Wu

March 10, 1995

All Rights Reserved

Laminar Natural Convection in Vertical Tubes
with One End Open to A Large Reservoir

by

Yissu Wu

A THESIS

submitted to

Oregon State University

in partial fulfillment of
the requirements for the
degree of

Doctor of Philosophy

Completed March 1995

Commencement June 1995

Doctor of Philosophy thesis of Yissu Wu presented on
March 10, 1995

APPROVED:

Redacted for Privacy

Major Professor, representing Mechanical Engineering

Redacted for Privacy

Head of Department of Mechanical Engineering

Redacted for Privacy

Dean of Graduate School

I understand that my thesis will become part of the permanent collection of Oregon State University libraries. My signature below authorizes release of my thesis to any reader upon request.

Redacted for Privacy

U

Yissu Wu, Author

ACKNOWLEDGMENTS

I would like to thank my major professor Dr. James R. Welty for his long time advice of my thesis work. Thanks to my minor professor, Dr. D. S. Trent, for his valuable assistance of the development of the computer program of this work. Thanks to Dr. Gordon M. Reistad, the department head, for the financial support, and thanks to my graduate committee members, Dr. Lorin R. Davis, Dr. Blake Peterson, and Dr. R. E. Wilson, for their help.

I also like to thank to Dr. E. G. Wollf let me use his optical table for my experimental work. Thanks to Dr. Milton B. Larson, Dr. A. Murty Kanury, Dr. Richard B. Peterson, and Dr. Heidi Pattee for the working experience as a teaching assistant for them. Special thanks to Dr. Joseph Zaworski for his information concerning everything in Corvallis.

Without the help of my colleagues and friends, completion of this thesis would have been almost impossible. Thanks to Boon Chua for his advices on computer programming day and night while he was a graduate student in this department. Thanks to R. J. Murphy, who works in the University Computer Center, for his quick responses and help whenever there was a computer problem. Thanks to Dr. Chang-Yuan Ju for his advice on the setup of the interferometer. And thanks to Mr. Orrie Page and Ken

McCracken for their willingness to consult on any trifling question in the machine shop.

Finally, I would like to thank my family, especially my parents, for their encouragement of my study.

TABLE OF CONTENTS

I.	INTRODUCTION.....	1
1.1	PROBLEM STATEMENT.....	3
1.2	A REVIEW OF PAST WORK.....	4
1.3	SCOPE OF THE STUDY.....	7
II.	NUMERICAL SOLUTION.....	10
2.1	GOVERNING EQUATIONS AND ANALYSIS.....	11
2.2	STAGGERED GRID SYSTEM AND CELL GEOMETRY...	16
2.3	POISSON-TYPE EQUATION AND CONNECTOR LOGIC.....	18
2.4	EVALUATION OF CONNECTORS IN 2-D CYLINDRICAL COORDINATES.....	20
2.5	TREATMENT OF BOUNDARY CONDITIONS.....	25
2.6	NUMERICAL ITERATION METHOD.....	27
2.7	TEMPEST SOLUTION PROCEDURE.....	32
2.8	NUMERICAL DISCRETIZATION AND STABILITY...	38
2.9	MEASUREMENT PARAMETERS.....	39
III.	RESULTS OF NUMERICAL SOLUTION.....	41
3.1	VERIFICATION OF COMPUTER PROGRAM AND CASES SELECTED.....	42
3.2	SUMMARY OF RESULTS OF ALL 80 SELECTED CASES.....	45
3.3	TYPE A OPEN THERMOSYPHONS WITH FIXED TUBE LENGTH.....	48
3.4	TYPE B OPEN THERMOSYPHONS WITH FIXED TUBE RADIUS.....	60
3.5	RESULTS FOR RECTANGULAR OPEN THERMOSYPHONS.....	66
IV.	EXPERIMENTAL SETUP AND INTERFERENCE FRINGES.....	72
4.1	THEORY OF PLANE WAVES INTERFERENCE.....	75
4.2	OPTICAL PATH DIFFERENCE AND FRINGE PATTERNS.....	78

TABLE OF CONTENTS (Continued)

4.3	RELATION BETWEEN TEMPERATURE AND REFRACTIVE INDEX.....	82
4.4	IMAGE PROCESSING.....	86
4.5	NUMERICAL SIMULATION OF INTERFERENCE PATTERN.....	89
4.6	SETUP OF THE MACH-ZEHNDER INTERFEROMETER..	99
4.7	POST DATA PROCESSING OF THE NUMERICAL RESULTS.....	102
V.	EXPERIMENTATION AND RESULTS.....	114
5.1	CONSTRUCTION OF THE TEST SECTION.....	116
5.2	EXPERIMENTAL PROCEDURES AND MISCELLANEOUS.....	120
5.3	EXPERIMENTAL FRINGES INTERPRETATION.....	122
5.4	EXPERIMENTAL VERIFICATIONS AND VERTICAL CHANNEL FLOW.....	128
5.5	COMPARISON OF FRINGE PATTERNS BETWEEN EXPERIMENTAL AND NUMERICAL RESULTS....	142
5.6	COMPARISON OF HEAT TRANSFER RATES BETWEEN EXPERIMENTAL AND NUMERICAL RESULTS.....	155
5.7	HEAT TRANSFER CORRELATIONS.....	165
5.8	FRINGE COMPARISONS BETWEEN EXPERIMENTS AND NUMERICAL RESULTS AT THE TUBE OPENING.....	168
VI.	CONCLUSIONS AND RECOMMENDATIONS.....	175
6.1	CONCLUSIONS.....	175
6.2	RECOMMENDATIONS.....	177
	REFERENCES.....	180
	APPENDICES.....	185
	APPENDIX A. NUMERICAL DISCRETIZATION OF THE GOVERNING EQUATIONS.....	186
	APPENDIX B. SETUP OF THE MACH-ZEHNDER INTERFEROMETER.....	200

LIST OF FIGURES

<u>Figures</u>	<u>Page</u>
1.1 Schematic of a vertical tube above a large reservoir.....	4
1.2 Experiment setup of a Mach-Zehnder interferometer.....	8
2.1 Axisymmetrical vertical tube and reservoir.....	12
2.2 Computational cell arrangement.....	15
2.3 Staggered grid system of continuity and momentum cells.....	16
2.4 Cell geometry in cylindrical coordinates.....	17
2.5 Connectors in 2-D cylindrical coordinates.....	19
2.6 Heat transfer resistances of two computational cells in the r- and z-directions in cylindrical coordinates.....	21
2.7 Treatment of boundary conditions in cylindrical coordinates.....	26
2.8 Solution algorithm based on the TEMPEST solution procedure.....	37
3.1 Streamlines and isotherms of air in a square cavity.....	42
3.2 Plots of time-average heat-transfer coefficient (h_t) and time-average Nusselt number Nu_t).....	46
3.3 Plots of time-average heat-transfer coefficient (h_t) and time-average Nusselt number (Nu_t).....	47
3.4 Streamlines and isotherms for cases of open thermosyphons, A1-A4, with AR = 1, 2, 3, and 6 at 1000 s.....	49
3.5 Streamlines and isotherms for cases of open thermosyphons, A5 and A6, with AR = 10 and 20 at 1000 s.....	50
3.6 Streamlines and isotherms for cases of open thermosyphons, A7 and A8, with AR = 100 and 200 at 1000 s.....	51
3.7 Streamlines and isotherms at selected times for the case A2 with AR = 2.....	52
3.8 Vertical velocity and temperature profiles near the tube wall for the case with AR = 2.....	54

LIST OF FIGURES (Continued)

<u>Figures</u>	<u>Page</u>
3.9 Streamlines and isotherms at selected times for the case A7 with AR = 100.....	55
3.10 Vertical velocity and temperature profiles for the case with AR = 100.....	56
3.11 Heat transfer coefficient histories and Nusselt number histories for cases A1-A8.....	57
3.12 Heat transfer coefficient histories for cases of open thermosyphons with R = 0.5 cm and their neighboring cases with R = 2.5 cm and R = 0.05 cm.....	59
3.13 Streamlines and isotherms for cases of open thermosyphons with R = 5 cm at 1000 s for AR = 2, 4, 6, 8, and 10.....	61
3.14 Plots of vertical velocity and temperature profiles for selected cases of open thermosyphons with fixed radius, R = 5 cm....	62
3.15 Streamlines and isotherms for selected cases of open thermosyphons at 1000 s.	64
3.16 Heat transfer coefficient histories and Nusselt number histories for selected cases with type B thermal boundaries.....	65
3.17 Modified rectangular open thermosyphons	67
3.18 Plots of streamlines for the modified rectangular open cavity with L = 7.62 cm and W = 3.81 cm at different times	68
3.19 Plots of isotherms for the modified rectangular open cavity with L = 7.62 cm and W = 3.81 cm at different times	69
3.20 Plots of streamlines for the case of open cavity with L = 2.54 cm and W = 2.54 cm at different times	71
4.1 Schematic of Mach-Zehnder interferometer for the experiment.....	73
4.2 Interference of two light rays.....	77
4.3 Relation between the order of loci of constant phase difference, S, and the fringe pattern..	80
4.4 Graphic representation of a CCD array.....	87
4.5 Fringe pattern of a flame using the wedged fringe field interference.....	88

LIST OF FIGURES (Continued)

<u>Figures</u>	<u>Page</u>
4.6	Undesirable fringes for the infinite fringe field alignment..... 89
4.7	Schematic of a plane wave passing through a wedged beamsplitter..... 90
4.8	Geometry of a wedged beamsplitter with a rotation angle θ_r91
4.9	Geometry of a wedged beamsplitter with a rotation angle, θ_r , and an incident angle, θ_i 93
4.10	Coordinates of two-point-source interference.... 94
4.11	Fringe patterns of plane-wave interference..... 95
4.12	Fringe patterns of two-point-source interference..... 96
4.13	Fringe pattern results from numerical simulations..... 97
4.14	Comparison between theoretical plane wave and other possible wave forms from a diverging beam passing through a spatial filter and a collimating lens..... 98
4.15	Arrangement of beamsplitters and mirrors for the interferometer.....100
4.16	Fringes for a vertical heating plate using the infinite fringe field..... 101
4.17	Mapping for the temperature field with 40 x 40 data points into 496 x 375 data points..... 104
4.18	Numerically-generated images of natural convection in a square cavity..... 106
4.19	Numerically-generated fringes of natural convection in a square cavity at selected times..... 110
4.20	Optical path length of a light ray travelling through an axisymmetric temperature field... 111
4.21	Plot of isotherms and streamlines for case of an open thermosyphon with $D = 2.5$ cm and $L = 5$ cm..... 112
5.1	Schematics of the constant temperature control device..... 116

LIST OF FIGURES (Continued)

<u>Figures</u>	<u>Page</u>
5.2 Construction of the modified open thermosyphon.....	117
5.3 Test section with windows on both ends.....	119
5.4 Fringe interpretation.....	122
5.5 Curve fitting for the temperature profile near the wall at selected positions.....	124
5.6 Contribution of errors for the counting of fringes due to the imperfect alignment of the interferometer.....	127
5.7 Natural convection over a vertical flat plate..	129
5.8 Fringe pattern of a 1/4" vertical channel at different times.....	132
5.9 Fringe patterns for different width vertical channels with one wall heated and the other wall maintained at room temperature...	133
5.10 Temperature profiles at different elevations for vertical channels with $W = 0.175"$, $1/4"$, $1/2"$ and $1"$	134
5.11 Local and average Nusselt number for different cases of vertical channel flow with one wall heated.....	135
5.12 Fringe patterns for vertical channels with both walls heated.....	137
5.13 Temperature profiles at different elevations for vertical channels; both walls maintained at the same constant temperature.....	138
5.14 Temperature profiles at 5-mm and 65-mm for selected cases of vertical channels with both walls heated.....	139
5.15 Local Nusselt number and Average Nusselt for vertical channels with both walls held at the steam temperature.....	140
5.16 Experimental and numerically-generated fringe patterns at different times for the case of an open cavity with $L = 5.08$ cm and $W = 1.588$ cm.....	144
5.17 Experimental and numerically-generated fringes patterns for the case of an open cavity with $L = 5.08$ cm and $W = 3.81$ cm.....	145

LIST OF FIGURES (Continued)

<u>Figures</u>	<u>Page</u>
5.18	Experimental and numerically-generated fringe patterns for the 16 selected case of open cavities..... 147
5.19	Fringe patterns at different times for the case of an open cavity with $W = 0.635$ cm and $L = 5.08$ cm..... 154
5.20	Comparison between the numerical and experimental results of Nusselt number for selected cases of open cavities..... 157
5.21	Comparison between the numerical and experimental results of Nusselt number for selected cases of open cavities..... 159
5.22	Nusselt number from experimental results evaluated using all 5 points data and using only the mid-point in figure 5.3 160
5.23	Temperature profiles at the mid-section of the open cavities with a fixed width at $W = 3.81$ cm..... 162
5.24	Temperature profiles at the mid-section of the open cavities with a fixed width at $W = 0.635$ cm..... 163
5.25	Correlation between Nusselt numbers and Rayleigh numbers..... 165
5.26	Relationship between Nu and Ra_W for different aspect ratio open cavities based on experimental results with windows on both ends of the test section..... 167
5.27	Schematic of the apparatus for observing fringes at the tube opening..... 169
5.28	Comparison of experimental and numerical fringes at the tube opening for case A..... 171
5.29	Comparison of experimental and numerical fringes at the tube opening for case B..... 172
5.30	Comparison of experimental and numerical fringes at the tube opening for case C..... 173
5.31	Comparison of experimental and numerical fringes at the tube opening for case D..... 174

LIST OF TABLES

<u>Table</u>		<u>Page</u>
3.1	Dimensions and numerical results of all selected open thermosyphons	44
4.1	Temperatures corresponding to orders of fringes in air	85
5.1	Experiments and numerical results of Nusselt number for the selected cases of open cavities	156

LIST OF APPENDICES FIGURES

<u>Figures</u>	<u>Page</u>
A.1	Advective fluxes across the computational cell surfaces for the three governing equations..... 187
A.2	Non-uniform "u" and "v" momentum cells for advective term discretization in the momentum equation..... 190
A.3	Non-uniform cell for the advective term discretization in the energy equation..... 193
B.1	Schematic of a beamsplitter..... 200
B.2	Geometrical depict of rays traveling through a wedged beamsplitter..... 202
B.3.	Plot of θ_d , δ_p , $D_i - D_o$ as functions of θ_i for a beamsplitter..... 203
B.4	Light spots reflected from the semi-reflection surface of a beamsplitter..... 204
B.5	Light spots reflected from the anti-reflection surface of a beamsplitter..... 205
B.6	Arrangement of the Mach-Zehnder interferometer..... 206
B.7	Alignment procedures of the Mach-Zehnder interferometer..... 208

NOMENCLATURE

Normal style

A	temperature gradient
A1	computational cell surface area in r direction
A2	computational cell surface area in z direction
AR	aspect ratio
C1	connector in r direction
C2	connector in z direction
CV	computational cell volume
D	divergence
D _p	sum of all connectors of a computational cell
D _{Res}	reservoir depth
e _p ⁿ	error residue
g	gravitational acceleration
h	heat-transfer coefficient
h _c	contact film coefficient
h _t	time average heat-transfer coefficient
J1	transport flux across cell surface in r direction
J2	transport flux across cell surface in z direction
L	tube length, cavity height
Nu	Nusselt number
Nu _t	time average Nusselt number
p	pressure
p'	pressure correction
Pr	Prandtl number
q _c	heat transfer rate by conduction
q _v	heat transfer rate by convection
R	tube radius
R ₁₋₃	heat-transfer resistances between two cells
R _{A-B}	heat-transfer resistances between two cells
R _{aw}	Rayleigh number
RC _i	i th computational cell radius at the center
R _i	i th computational cell radius at the outward surface
R _{res}	reservoir radius

\mathbf{r} position vector
 r radial coordinates
 S source term
 T temperature
 T_b temperature at the bottom of the tube wall
 T_m mean temperature of T_o and T_b
 T_o temperature at the top of the tube wall
 T_{res} reservoir temperature
 t time
 \mathbf{u} velocity vector
 $\tilde{\mathbf{u}}$ provisional velocity vector of \mathbf{u}
 \mathbf{u}' velocity vector correction
 u velocity component in r direction
 \tilde{u} provisional velocity of u
 u' velocity correction of u
 v velocity component in z direction
 \tilde{v} provisional velocity of v
 v' velocity correction of v
 W cavity width
 z axial coordinates

Greek symbols

α thermal diffusivity
 β coefficient of volumetric thermal expansion
 Δr cell spacing in radial direction
 ΔT temperature difference ($T_m - T_{res}$)
 Δt advanced time interval
 Δz cell spacing in axial direction
 δ_T thermal boundary layer thickness
 δ_v momentum boundary layer thickness
 ϵ converge criterion
 Φ transport variables such as temperature or scalar potential
 $\delta\Phi$ difference of Φ between two iteration levels

Γ transport properties such as thermal conductivity or permeability
 κ thermal conductivity
 ν kinematic viscosity
 ρ density
 ω relaxation factor of numerical iteration

Superscripts

n current iteration step
 $n+1$ advanced iteration step

Subscripts

B boundary cells
 i i^{th} cell number in radial direction
 i_{max} maximum cell number in r direction
 j j^{th} cell number in axial direction
 j_{max} maximum cell number in z direction
 m mean value
 w wall cell number
 p short hand notation for the index of i, j
 Φ irrotational part of flow field
 ω rotational part of flow field

Italic style

A amplitude of the electric field
 E electrical field
 I irradiance
 i unit vector in x direction
 j unit vector in y direction
 K Gladstone-Dale constant
 k unit vector in z direction
 k wave number
 L length of the apparatus test section

M molecular weight
 n refractive index
 \mathbf{n} direction normal
 P pressure
 R universal gas constant
 \mathbf{r} position vector
 r distance from origin
 r_s specific refractivity
 T temperature of the test medium
 TZ function of thickness of a beamsplitter
 t time
 x x axis
 y y axis
 z z axis, direction of electric wave propagation

Greek symbol

λ wavelength
 θ angle
 θ_i angle of incidence
 θ_r angle of rotation of a beamsplitter
 θ_w wedged angle of a beamsplitter
 ρ density
 ω angular frequency

Superscript

i complex number

Subscript

i pixel number in the x axis
 j pixel number in the y axis
 k order of fringe
 p front surface of the beamsplitter
 w wedged surface of the beamsplitter

LAMINAR NATURAL CONVECTION IN VERTICAL TUBES WITH ONE END OPEN TO A LARGE RESERVOIR

I. INTRODUCTION

Laminar natural convection in vertical tubes with one end open to a large reservoir was examined in this study. Such devices are called "tubular open thermosyphons." They are used to transfer heat across the tube wall by fluid circulation in the tube. Unlike closed thermosyphons, one end of an open thermosyphon is open to its surroundings allowing fluids to flow to and from a reservoir.

Thermosyphons are useful in a variety of applications. Turbine blade cooling is one of the best-known engineering applications for thermosyphons. Schmidt [1] suggested applying open thermosyphons to cool turbine blades using the high centrifugal acceleration resulting from turbine rotation. His idea was first to drill small holes in the blades with their axes parallel to the direction of the centrifugal acceleration, then to fill them with liquid coolant free to circulate to and from the hollowed rotor to cool the blades.

Another application of open thermosyphons is the freezing of soil in northern regions where the ground is frozen most of the year. Long [2,3] designed a device

named the Long thermopile, an open thermosyphon, to withdraw heat from the foundation of a building area by inserting a pipe into the ground. The result was that the soil near the pipe would uphold its structural integrity by maintaining its temperature below the melting point. Another important application of the open thermosyphon similar to a Long thermopile is the extraction of geothermal energy for commercial use. In such an application, vertical tubes are inserted into the ground at geothermal sites to extract thermal energy, which is then converted into electric power. The first commercial use of geothermal-generated electric power took place in Italy in 1904 [4]. In a survey by the U.S. department of energy in 1980, the total worldwide installed geothermal electric power capacity in operation at that time was about 1750 MW, with an additional 1827 MW under construction or in planning [5].

There are many other applications of thermosyphons. Lock [6] suggested the use of an array of thermosyphons, called cryosphons, strung across a river in northern regions to block, or partially block the flow of water by forming an ice barrier. Japikse and Winter [7] proposed the use of open thermosyphons to expel large amounts of energy quickly in case of an emergency in a nuclear reactor. They also suggested cooling a reactor by connecting an open thermosyphon to a water supply located on the building roof. The water supply would serve as a

natural reservoir for an open thermosyphon and would allow the discharge of large amounts of energy. Other applications include thermosyphon solar heaters; cooling of electronic packages, electric motors and machine bearings; and waste heat recovery. Detailed descriptions of several applications of thermosyphons are described by Lock [6] and Dunn and Reay [8].

Studies of this subject have been conducted analytically, numerically, and/or experimentally. In this work, the performance of open thermosyphons has involved numerical analysis and experiments.

1.1 PROBLEM STATEMENT

The open thermosyphon is shown schematically in figure 1.1. A tube with its axis arranged parallel to the direction of an acceleration field - such as gravity or centrifugal force - with one end closed and the other open, is shown. Such a device involves the transfer of heat through the influence of buoyancy forces resulting from temperature variations between the fluid and the tube wall. During operation, fluid flows in and out of the tube to and from a connecting reservoir. Information of interest in this study includes a description of the fluid flow field in the tube and the heat transfer rate along the tube wall.

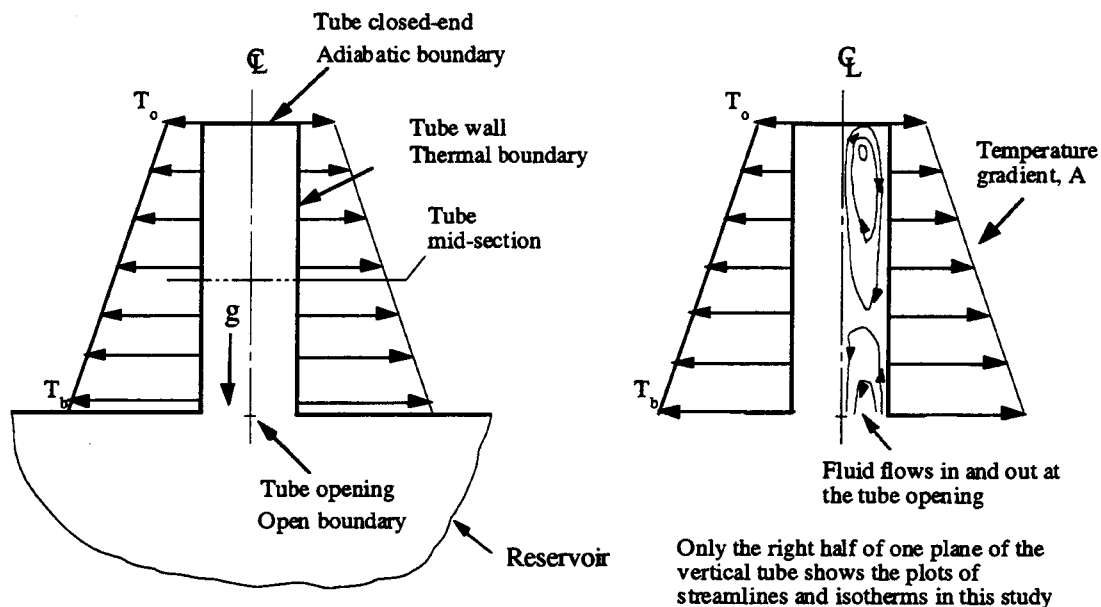


Figure 1.1 Schematic of a vertical tube above a large reservoir

Boundary conditions considered included the following features: (1) the vertical cylindrical wall condition was one of linearly-varying temperature with gradient, A , (for uniform temperature $A = 0$); (2) the top of the cylinder was insulated; (3) the initial fluid temperature throughout the modeled system was T_{res} , the walls of the reservoir were maintained at T_{res} ; and (4) the fluid was confined within the system, which consisted of the vertical tube and the reservoir.

1.2 A REVIEW OF PAST WORK

The open thermosyphon was first studied analytically by Eckert and Jackson [9] in 1950. They were most

interested in preventing flow circulation in a vertical tube by optimizing the length-to-radius (aspect) ratio. Assuming a similar shape for the momentum and temperature boundary-layers, an integral technique based on the one-seventh power law was used to find the turbulent momentum boundary layer thickness. For the open thermosyphon with a linear temperature distribution along the wall, Ostrach and Thornton [10] employed an integral method to obtain a solution satisfying the integrated forms of the differential equations assuming polynomial functions for both the velocity and temperature profiles. They concluded that flow circulation near the closed end of a vertical tube with a sufficiently large aspect ratio does not provide effective cooling.

A significant analytical investigation of the open thermosyphon was conducted by Lighthill [11] based on Schmidt's [1] suggestion for turbine-blade cooling. In his analytical model for laminar flow, he simplified the equations of conservation of mass, momentum, and energy in steady axisymmetric flow using the boundary layer approximation, i.e. neglecting the gradient of a quantity in the axial direction compared with its gradient along a radius. Three flow regimes were characterized by the length-to-radius aspect ratio, a modified Raleigh number, and the Prandtl number. The first flow regime, flow with the laminar boundary layer not filling the tube, was considered by Lighthill to be similar to boundary layer

flow along a vertical flat plate. Thus, a solution was obtained using an approximate procedure assuming a cubic polynomial velocity profile and a quadratic temperature profile. For the second flow regime, similarity flow, and the third flow region, laminar flow filling the tube without similarity, polynomials of higher orders for both velocity and temperature profiles were used to obtain solutions.

Analytical results of flow regimes reported by Lighthill have been confirmed by many studies. These included Martin's [12] experimental study using thermocouple probes to measure the tube wall temperature and the fluid temperature at the tube opening of an open thermosyphon; and Hasegawa's [13] experimental study to detect the flow pattern using Schlieren methods in a modified rectangular open thermosyphon.

In a numerical study of an open thermosyphon, Japikse [14] first reduced the three integral forms of the governing equations, suggested by Lighthill, into a set of coupled, first order, non-linear, ordinary differential equations by introducing approximate velocity and temperature profiles. This set of equations was further reduced to a set of non-linear algebraic equations which were solved numerically by an iterative stepping procedure for both momentum and thermal boundary layer thicknesses and the centerline velocity. Later, Fukuda [15] solved the open thermosyphon problem numerically using a

vorticity/stream-function method for a vertical tube and the associated reservoir, achieving a steady-state solution.

With rapid improvements in computer speed and solution procedures for the governing equations, transient solutions for an open thermosyphon are now possible. For example, the program, TEMPEST, developed by Trent and Eyler [16] can be used to achieve transient solutions for various hydrothermal problems.

1.3 SCOPE OF THE STUDY

To describe laminar flow behavior in the tube and the heat transfer along the tube wall, a numerical solution based on TEMPEST [16] solution procedures was used to obtain transient numerical results for the flow and temperature fields in the open thermosyphon. A FORTRAN computer program was developed for this numerical solution. Streamlines and isotherms in the vertical tube, based on these numerical results, were plotted to help in understanding the nature of open thermosyphon behavior. Other heat-transfer parameters, such as the Nusselt number and the heat-transfer coefficient, were obtained for various length-to-radius aspect ratios (AR) of the vertical tube.

To corroborate the numerical results, a Mach-Zehnder interferometer was set up to depict the temperature field

of the open thermosyphon. This interferometer employed an argon laser emitting at 514.5 nm. Interference fringes on the observation screen at the output of the interferometer were pictured using a CCD digital camera. The interferometer is shown in figure 1.2.

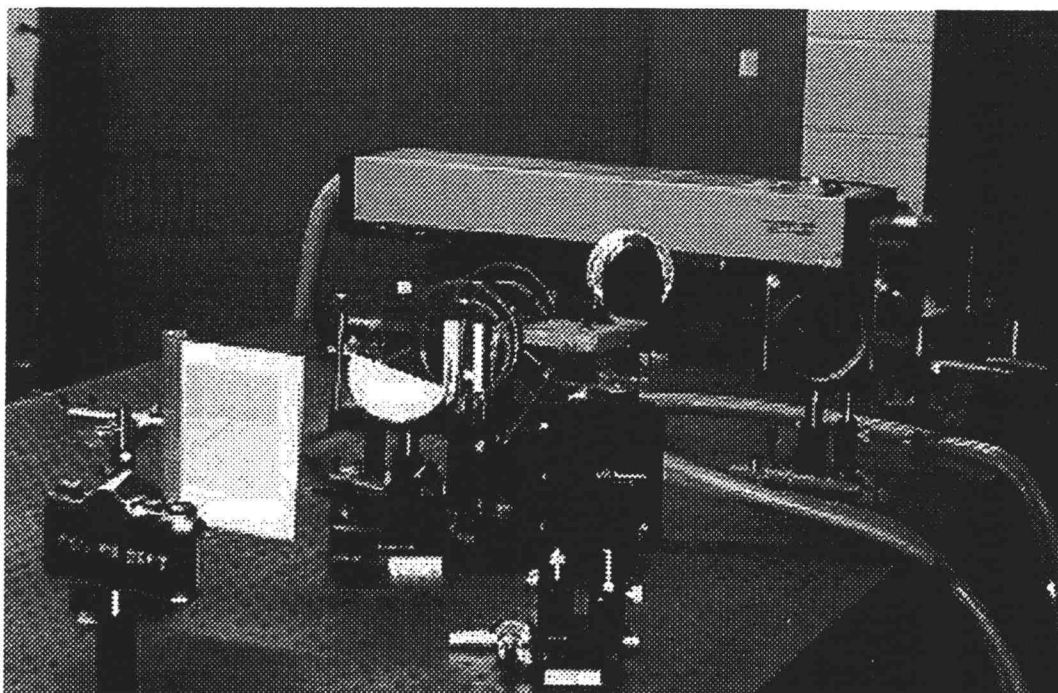


Figure 1.2 Experiment setup of a Mach-Zehnder interferometer

To help in aligning the interferometer, a computer program, written in C language, was developed to simulate two-wave interference. Numerical results were plotted for comparison with the actual interference fringes on the observation screen of the interferometer. This comparison was used in adjusting the two beamsplitters and the two

mirrors of the interferometer to obtain a maximum area of infinite fringe field on the observation screen.

Interference fringes result from the change in optical path length of a collimated light beam passing through a disturbed temperature field in a medium such as air. The relation between the temperature and the refractive index is described by the Lorentz-Lorenz [17] equation and the equation of state of the medium. Using the temperature field from the numerical result coupled with these relations, fringes can be generated numerically. Another computer program was also developed to obtain these fringes in both rectangular and cylindrical coordinates. This enabled an easier comparison of fringes between the numerical and experimental results.

Results of heat transfer rate from the tube wall of a modified open thermosyphon were calculated by examining the fringes on the observation screen of the interferometer. The heat transfer rates were also obtained from numerical simulations for this same modified open thermosyphon configuration. These results together with the temperature contour lines were used for verification of the numerical and experimental solutions. Based on these results, correlations between Nusselt number and Rayleigh number were determined for different aspect ratios open cavities.

II. NUMERICAL SOLUTION

The numerical solution for the open thermosyphon, as described in this chapter, was done to predict the flow behavior in the vertical tube and the heat transfer through the tube wall. The numerical solution was based on the discretization of the three conservation equations describing fluid flow in a two-dimensional cylindrical coordinate system. A staggered grid system was used for marking and tracking locations of scalar and vector variables in the computational region. Non-uniform grids were used for the consideration of boundary layer flow near the tube wall.

A semi-implicit, time marching, finite-volume solution procedure - which solved all governing equations sequentially - was used. The solution procedure included solving for the scalar potential of the irrotational part of the flow field which is mathematically described by a Poisson-type equation. In this study, a Line Successive Over Relaxation (LSOR) iteration method, together with a balancing technique to speed up the iteration process, was used to solve the finite-volume form of the Poisson-type equation. Connectors relating a transport flux across computational cell surfaces in terms of cell geometries and

transport properties were used as coefficients in the finite-volume form of the Poisson-type equation. Boundary conditions can easily be described using connectors by specifying the transport property of the boundary cells.

Governing equations were used in the conservative forms in this study and finite-volume methods were employed in the numerical discretization. All discretization schemes for the three governing equations are described in Appendix A. An explicit upwind method was used for discretizing the advective terms in the momentum and energy equations. Stability criteria were set based on the cell spacings and velocity fields in the computational region.

2.1 GOVERNING EQUATIONS AND ANALYSIS

The open thermosyphon was modeled using the two-dimensional coordinate system shown in figure 2.1. The open end of the tube was connected to a large cylindrical reservoir to provide accurate inflow information. The vertical tube and the reservoir were axisymmetric. The computational region consisted of the right-half of one plane as shown by the dashed lines. Water was selected as the working fluid.

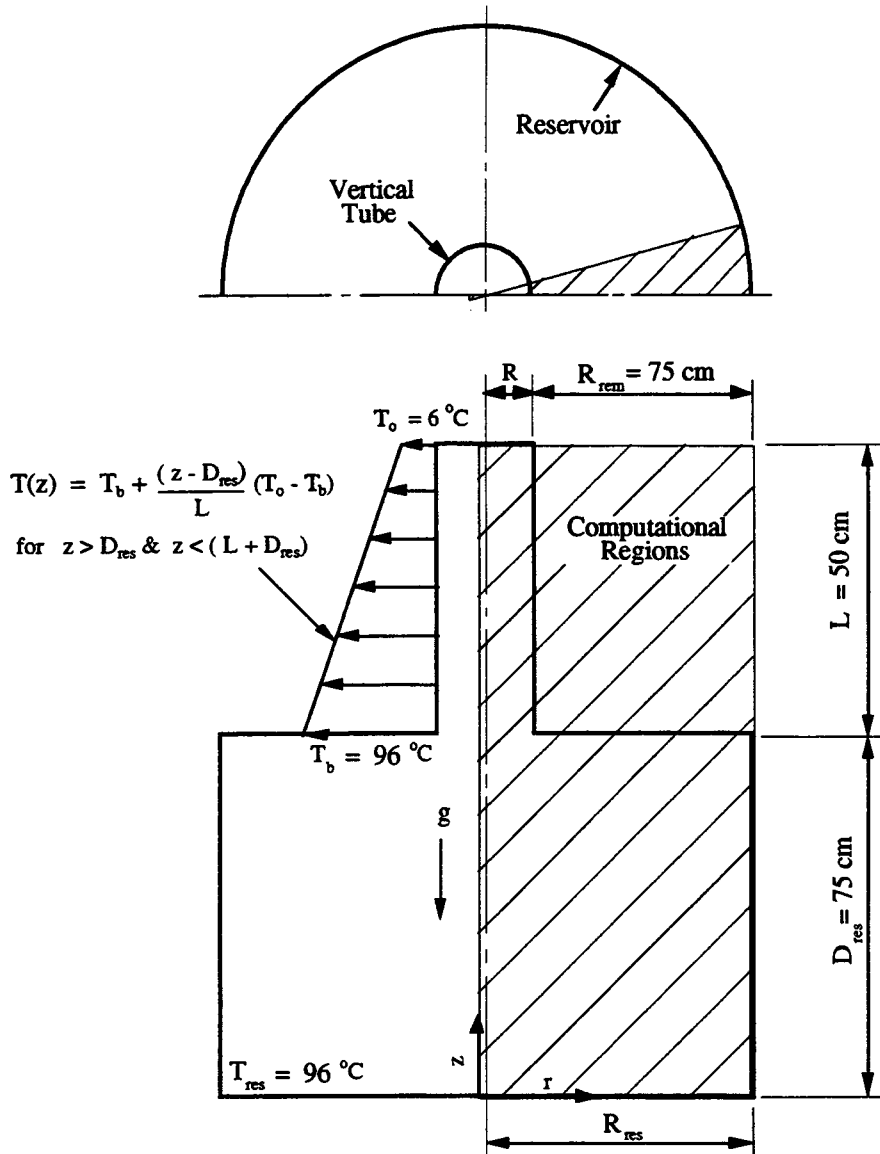


Figure 2.1 Axisymmetrical vertical tube and reservoir

Governing equations for laminar flow in the two-dimensional cylindrical coordinate system are:

Continuity:

$$\frac{\partial \rho}{\partial t} + \frac{1}{r} (\rho u) + \frac{\partial}{\partial r} (\rho u) + \frac{\partial}{\partial z} (\rho v) = 0 \quad (2.1)$$

Momentum:

$$\begin{aligned} \frac{\partial u}{\partial t} + \frac{1}{r}(\underline{uu}) + \frac{\partial}{\partial r}(\underline{uu}) + \frac{\partial}{\partial z}(\underline{vu}) \\ = -\frac{1}{\rho_o} \frac{\partial p}{\partial r} + \frac{\mu}{\rho_o} \left[\frac{1}{r} \frac{\partial}{\partial r} \left(r \frac{\partial u}{\partial r} \right) - \frac{u}{r^2} + \frac{\partial}{\partial z} \left(\frac{\partial u}{\partial z} \right) \right] \end{aligned} \quad (2.2)$$

$$\begin{aligned} \frac{\partial v}{\partial t} + \frac{1}{r}(\underline{uv}) + \frac{\partial}{\partial r}(\underline{uv}) + \frac{\partial}{\partial z}(\underline{vv}) \\ = -\frac{1}{\rho_o} \frac{\partial p}{\partial z} + \frac{\mu}{\rho_o} \left[\frac{\partial}{\partial r} \left(r \frac{\partial v}{\partial r} \right) + \frac{\partial}{\partial z} \left(\frac{\partial v}{\partial z} \right) \right] + \frac{\rho g}{\rho_o} \end{aligned} \quad (2.3)$$

Energy:

$$\frac{\partial T}{\partial t} + \frac{1}{r}(\underline{uT}) + \frac{\partial}{\partial r}(\underline{uT}) + \frac{\partial}{\partial z}(\underline{vT}) = \frac{\kappa}{\rho_o c_p} \left[\frac{1}{r} \frac{\partial}{\partial r} \left(r \frac{\partial T}{\partial r} \right) + \frac{\partial}{\partial z} \left(\frac{\partial T}{\partial z} \right) \right] \quad (2.4)$$

The Boussinesq approximation was applied, as was the assumption of negligible dissipation. To use a non-uniform, staggered grid system for the numerical discretization, it was necessary to retain the first derivative in the governing equations. Details for such a grid system and numerical discretization will be described later.

Due to dramatic changes in both velocity and temperature near the wall, it was necessary to adjust computational-cell sizes in this region to provide the necessary resolution for both the momentum and thermal boundary layers. Clearly, if computational-cell sizes near

the wall were larger than the boundary-layer thickness, information would be lost.

Predictions for both boundary-layer thicknesses from scale analysis suggest the following orders of magnitude:

$$\delta_T \sim L \cdot Ra_L^{-\frac{1}{4}} \quad (2.5)$$

$$\delta_v \sim Pr^{\frac{1}{2}} \delta_T \quad (2.6)$$

where,

$$Ra_L = \frac{g\beta\Delta TL^3}{\alpha\nu} \quad (2.7)$$

Both boundary-layer thicknesses were based on the height, L , of a rectangular enclosure. For a 50-cm-long tube, and an average temperature difference, $\Delta T = T_{res} - T_m$, of 45°C, the predicted thermal and momentum boundary-layer thicknesses from Eqs. (2.5) and (2.6), for water at 50°C, are $\delta_T \sim 0.068\text{cm}$, and $\delta_v \sim 0.129\text{cm}$. Numerical results for these thicknesses should be of this same order.

To retain accurate velocity and temperature information, two cells were specified within the predicted momentum-boundary layer region as shown in figure 2.2. Since the numerical results (discussed in chapter 3) show the thickness of the thermal boundary layer to be about 0.3 cm and the corresponding value for the momentum boundary layer to be 0.5 cm at the tube mid-section (where the wall temperature is T_m), four cells near the tube wall

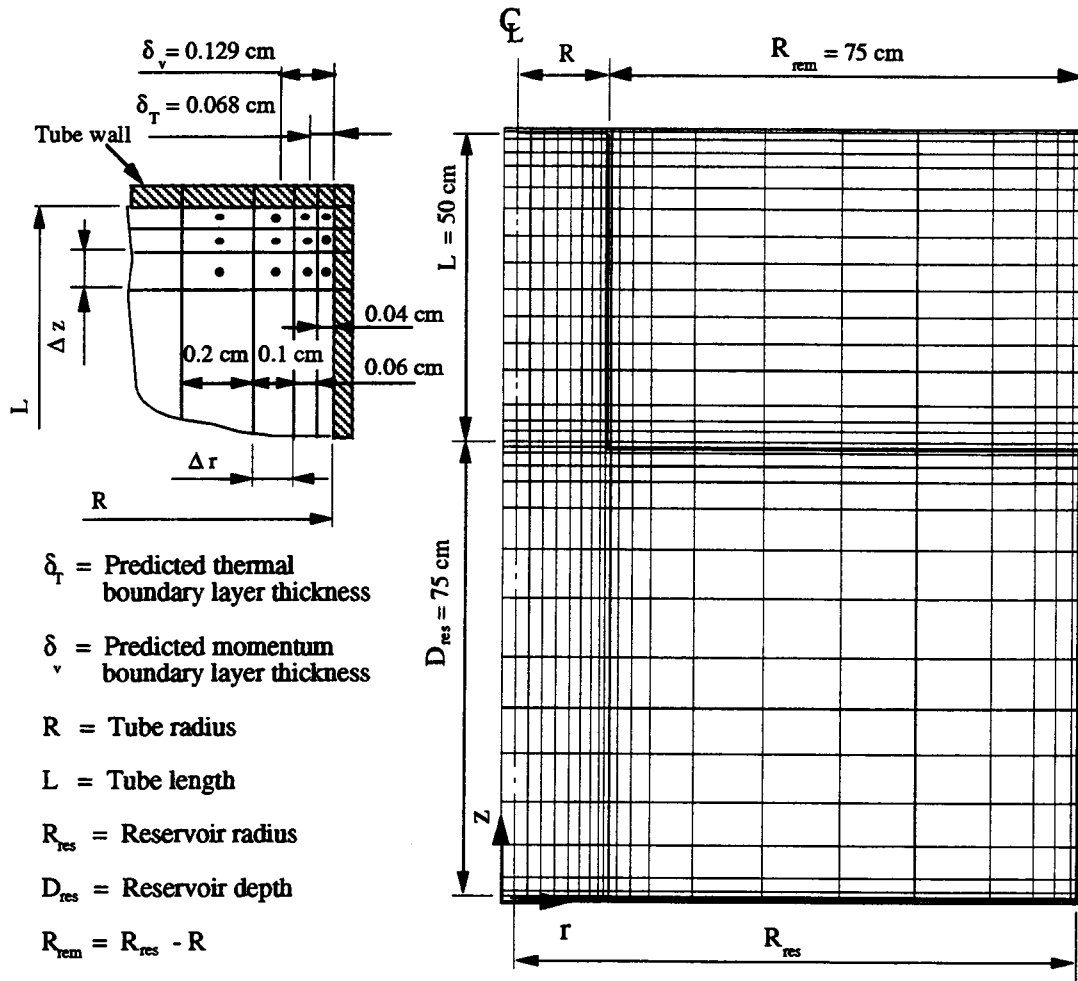


Figure 2.2 Computational cell arrangement

provided sufficiently detailed velocity and temperature information.

For a tube radius of 20 cm, with 20 uniform cells in the radial direction, a normal cell dimension would be 1 cm which is much too large to yield adequate information in the boundary layers.

2.2 STAGGERED GRID SYSTEM AND CELL GEOMETRY

The staggered grid system used for the numerical scheme is shown in figure 2.3. Three cell types were specified. For continuity cells, all scalar variables, such as temperature, pressure, and scalar potential, were determined at the cell centers, and all vector variables, such as velocities and heat fluxes, were evaluated at the cell boundaries. Unless specified otherwise, the term "cell" refers to a continuity cell.

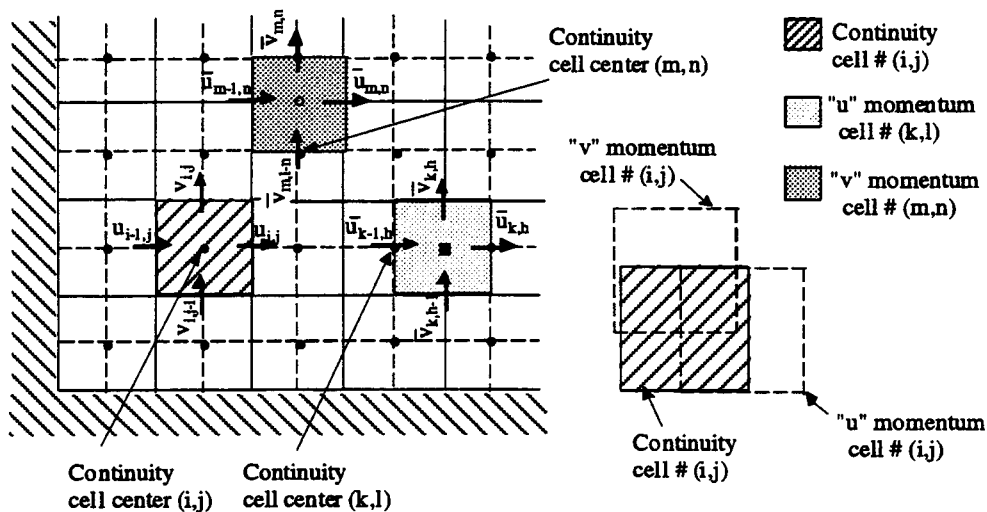


Figure 2.3 Staggered grid system of continuity and momentum cells

The u momentum and v momentum-cell types were used to specify the average velocities, \bar{u} 's and \bar{v} 's (Figure 2.3), interpolated from the velocities located at the continuity cell boundaries. These average velocities were required for discretizing the advective terms in the governing equations. The use of these u momentum and v momentum-cell

types helps the tracking and marking the location of all variables while discretizing the advective terms.

Figure 2.4 shows the geometry of cell (i,j) in a two-dimensional cylindrical coordinate system. The indices i and j locate the cell in the r - and z -directions, respectively. Geometric cell quantities include: cell width, Δr ; cell height, Δz ; cell surface areas, $A_{1,i,j}$, $A_{1,i-1,j}$, $A_{2,i,j}$, $A_{2,i,j-1}$; cell volume $CV_{i,j}$; and radii of curvatures, R_{i-1} , RC_i , and R_i .

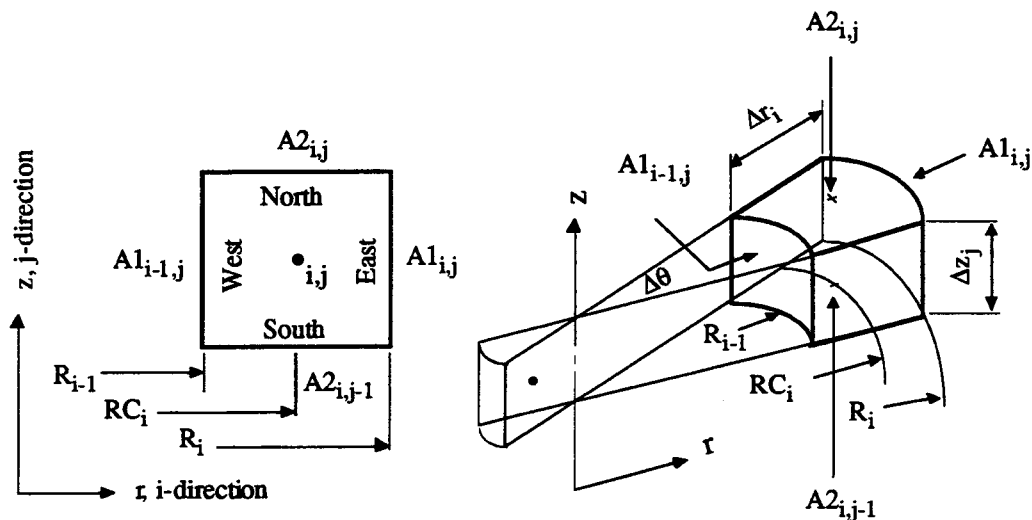


Figure 2.4 Cell geometry in cylindrical coordinates

Some rules were applied to specify these geometrical variables. For example, the number, 1, applied to the surface area, A_1 , indicates the surface area normal to the r -direction. Similarly, the number, 2, applied to the surface area, A_2 , indicates the surface area normal to the z -direction. In the r -direction, the index for the "east" cell surface area, i , is the same as the cell number

specified at the cell center, i . However, the index for the "west" cell surface area, $i-1$, is always less the number at the cell center by one. The same scheme was applied in the z -direction for the areas and the radii of the cell curvatures. The subscript, p , is often used as short-hand notation for the subscripts i and j . A dropout of the cell index representing the missing subscript is either i in the r -direction or j in the z -direction. For example, the cell surface areas A_{1i} is equivalent to $A_{1i,j}$, and A_{2j-1} is equivalent to $A_{2i,j-1}$.

Tracking of the cell indices is essential for computer programming. A computational cell map similar to figure 2.2 was used for marking and tracking the indices for the open thermosyphon.

2.3 POISSON-TYPE EQUATION AND CONNECTOR LOGIC

General diffusion transport phenomena are described by the Poisson-type equation. In this study, the phenomena are the diffusion of temperature in the case of heat conduction and the diffusion of scalar potential for irrotational flow. The form of the Poisson-type equation is

$$\nabla \cdot (\Gamma \nabla \Phi) = S \quad (2.8)$$

where, Φ is the transport variable, i.e. temperature or scalar potential; Γ is the transport property, i.e. thermal

conductivity for the heat flow or permeability for fluid flow.

To express the Poisson-type equation in finite-volume form, a connector logic was used describing the coefficients of the finite-volume equation. The connector logic is shown in figure 2.5.

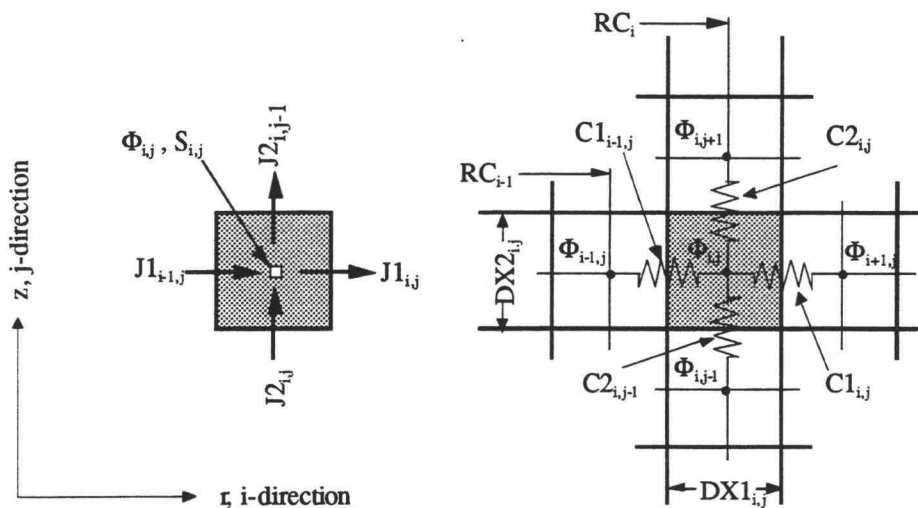


Figure 2.5 Connectors in 2-D cylindrical coordinates

Consider a computational cell (i,j) with its transport fluxes, such as energy flux due to heat conduction, in a 2-D cylindrical coordinate system. The steady state expression for the balance of these fluxes, J 's, and the internal source, S , in a the control volume, CV , is

$$(J1_{i,j} - J1_{i-1,j}) + (J2_{i,j} - J2_{i,j-1}) = CV_{i,j} \cdot S_{i,j} \quad (2.9)$$

Each flux is related to the difference of the transport variable between two adjacent cells multiplying a connector as shown in figure 2.5. For example, the flux, $J_{i,j}$, between the cell (i,j) and $(i+1,j)$ is $C_{1,i,j}(\Phi_{i+1,j} - \Phi_{i,j})$. Replacing the fluxes by the connectors and the transport variable, Eq.(2.9) becomes

$$C_{1,i,j} \Phi_{i+1,j} + C_{1,i-1,j} \Phi_{i-1,j} + C_{2,i,j} \Phi_{i,j+1} + C_{2,i,j-1} \Phi_{i,j-1} - D_p \Phi_{i,j} = CV_{i,j} \cdot S_{i,j} \quad (2.10)$$

where,

$$D_p = C_{1,i,j} + C_{1,i-1,j} + C_{2,i,j} + C_{2,i,j-1} \quad (2.11)$$

This is the finite-volume form of the Poisson-type equation expressed using connector logic.

2.4 EVALUATION OF CONNECTORS IN 2-D CYLINDRICAL COORDINATES

Connectors appear in different forms depending on the coordinate frame. For discussion purposes, the transport equation will be the heat conduction equation with temperature as the transport variable and the thermal conductivity as the transport property. The energy flux for heat conduction is governed by Fourier's law, i.e. $J = -\Gamma \nabla \Phi$.

Consider the heat flux, $J_{2,i,j-1}$, between two cells $(i,j-1)$ and (i,j) in the z-direction, shown in figure 2.6. Three thermal resistances, R_1 , R_2 , and R_3 , are involved between

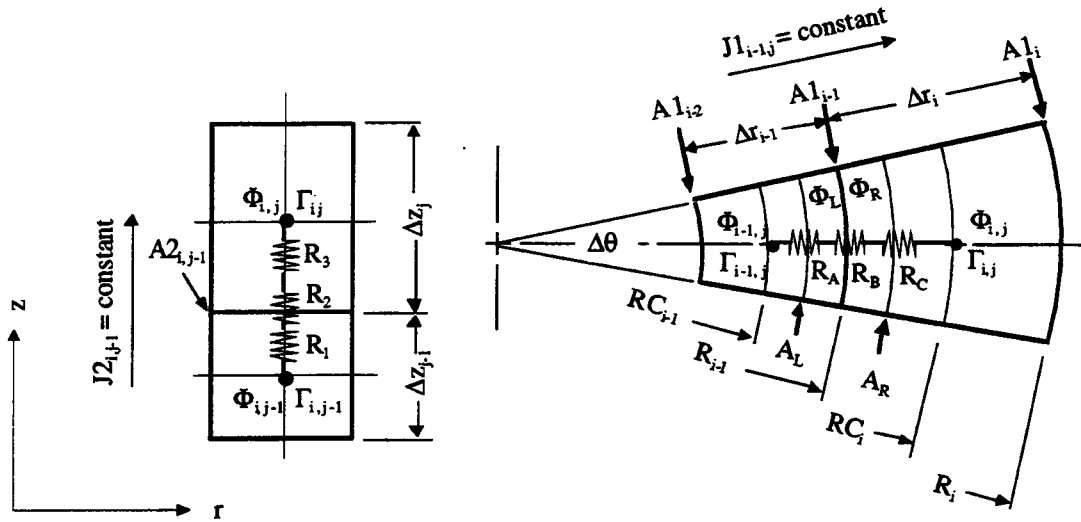


Figure 2.6 Heat transfer resistances of two computational cells in the r - and z -directions in cylindrical coordinates

the two cell centers. R_1 and R_3 are the resistances due to the thermal conductivities of the two cells, and R_2 is the contact resistance. The temperatures at the cell centers are $\Phi_{i,j-1}$ and $\Phi_{i,j}$, and the thermal conductivities of the cells are $\Gamma_{i,j-1}$ and $\Gamma_{i,j}$ respectively. By Fourier's law, the heat flux across these two cells with the constant area $A_{2,i,j-1}$ is

$$J_{2,i,j-1} = \frac{(\Phi_{i,j} - \Phi_{i,j-1})}{R_1 + R_2 + R_3} = \frac{(\Phi_{i,j} - \Phi_{i,j-1})}{\frac{(\Delta z_{j-1} / 2)}{\Gamma_{i,j-1} \cdot A_{2,i,j-1}} + \frac{1}{h_{C_{j-1}} \cdot A_{2,i,j-1}} + \frac{(\Delta z_j / 2)}{\Gamma_{i,j} \cdot A_{2,i,j-1}}} \quad (2.12)$$

where, h_c is the contact film coefficient. Rearrangement of Eq. (2.12), yields

$$J2_{i,j-1} = \frac{2 \cdot A2_{i,j-1}}{\left(\frac{\Delta z_{j-1}}{\Gamma_{i,j-1}} + \frac{\Delta z_j}{\Gamma_{i,j}} + \frac{2}{h_{C_{j-1}}} \right)} (\Phi_{i,j} - \Phi_{i,j-1}) \quad (2.13)$$

The coefficient in Eq.(2.13) is the connector, $C2_{i,j-1}$, between cells (i,j-1) and (i,j). Using this same scheme, the connectors between cells (i,j) and (i,j+1) can be described in the same fashion. Thus, the two connectors in the z-direction are

$$C2_{i,j-1} = \frac{2 \cdot A2_{i,j-1}}{\left(\frac{\Delta z_{j-1}}{\Gamma_{i,j-1}} + \frac{\Delta z_j}{\Gamma_{i,j}} + \frac{2}{h_{C_{j-1}}} \right)}$$

$$C2_{i,j} = \frac{2 \cdot A2_{i,j}}{\left(\frac{\Delta z_j}{\Gamma_{i,j}} + \frac{\Delta z_{j+1}}{\Gamma_{i,j+1}} + \frac{2}{h_{C_j}} \right)} \quad (2.14)$$

In the r-direction, the connectors will take on a more complex form due to the curvatures of the cell surfaces. Consider the heat flux, $J1_{i-1,j}$, between cell numbers (i-1,j) and (i,j) in the r-direction shown in figure 2.6. The area normal to the direction of the heat flux changes. As shown in [18], expressions for the constant heat flux across each resistance according to Fourier's law are

$$@R_A: \quad J1_{i-1,j} = \left[\Gamma_{i-1,j} (r \Delta \theta \Delta z) \frac{d\Phi}{dr} \right]_{r=R_{C_{i-1}}, \Phi=\Phi_{i-1,j}}^{r=R_{i-1}, \Phi=\Phi_L} \quad (2.15)$$

$$@R_B: \quad J_{l_{i-1,j}} = h_{C_{i-1}} A_{l_{i-1}} (\Phi_R - \Phi_L) \quad (2.16)$$

$$@R_C: \quad J_{l_{i-1,j}} = \left[\Gamma_{i,j} (r \Delta \theta \Delta z) \frac{d\Phi}{dr} \right]_{r=R_{i-1}, \Phi=\Phi_R}^{r=RC_i, \Phi=\Phi_{i,j}} \quad (2.17)$$

Performing the integration over the limits for Eq.(2.15) and Eq.(2.17), we obtain

$$@R_A: \quad J_{l_{i-1,j}} \ln \left(\frac{R_{i-1}}{RC_{i-1}} \right) = \Gamma_{i-1,j} \Delta \theta \Delta z (\Phi_L - \Phi_{i-1,j}) \quad (2.18)$$

$$@R_C: \quad J_{l_{i-1,j}} \ln \left(\frac{RC_i}{R_{i-1}} \right) = \Gamma_{i,j} \Delta \theta \Delta z (\Phi_{i,j} - \Phi_R) \quad (2.19)$$

Note that the surface area, $A_{l_{i-1,j}}$, is $R_{i-1} \Delta \theta \Delta z$. Multiplying Eqs.(2.18) and (2.19) by R_{i-1} , and moving the temperature difference to the left-hand side of Eq.(2.16), Eqs.(2.18)-(2.19) and Eq.(2.16) are rewritten as

$$@R_A: \quad (\Phi_L - \Phi_{i-1,j}) = \frac{J_{l_{i-1,j}}}{A_{l_{i-1,j}}} \left[\frac{R_{i-1} \ln(R_{i-1} / RC_{i-1})}{\Gamma_{i-1,j}} \right] \quad (2.20)$$

$$@R_B: \quad (\Phi_R - \Phi_L) = \frac{J_{l_{i-1,j}}}{A_{l_{i-1,j}}} \left(\frac{1}{h_{C_{i-1}}} \right) \quad (2.21)$$

$$@R_C: \quad (\Phi_{i,j} - \Phi_R) = \frac{J_{l_{i-1,j}}}{A_{l_{i-1,j}}} \left[\frac{R_{i-1} \ln(RC_i / R_{i-1})}{\Gamma_{i,j}} \right] \quad (2.22)$$

Adding these equations, we obtain

$$J_{i-1,j} = \frac{A_{i-1,j} \cdot (\Phi_{i,j} - \Phi_{i-1,j})}{\left[\frac{R_{i-1} \ln(R_{i-1}/RC_{i-1})}{\Gamma_{i-1,j}} + \frac{1}{h_{C_{i-1}}} + \frac{R_{i-1} \ln(RC_i/R_{i-1})}{\Gamma_{i,j}} \right]} \quad (2.23)$$

Thus, the connector, $Cl_{i-1,j}$ is

$$Cl_{i-1,j} = \frac{A_{i-1,j}}{\left[\frac{R_{i-1} \ln(R_{i-1}/RC_{i-1})}{\Gamma_{i-1,j}} + \frac{1}{h_{C_{i-1}}} + \frac{R_{i-1} \ln(RC_i/R_{i-1})}{\Gamma_{i,j}} \right]} \quad (2.25)$$

Similarly, the connector $Cl_{i,j}$ is

$$Cl_{i,j} = \frac{A_{i,j}}{\left[\frac{R_i \ln(R_i/RC_i)}{\Gamma_{i,j}} + \frac{1}{h_{C_i}} + \frac{R_i \ln(RC_{i+1}/R_i)}{\Gamma_{i+1,j}} \right]} \quad (2.26)$$

Eq. (2.14) and Eqs. (2.25)-(2.26) are the four connectors for the finite-volume form of the Poisson-type equation, Eq. (2.9). These connectors completely characterize the heat flux across each cell boundary in terms of the cell geometry and transport properties. For fluid flow problems with the scalar potential as the transport variable, the connectors are in the same form except the transport property is the permeability and there are no contact film coefficients. Also, note that the heat transfer contact film coefficient is zero for this study since the open thermosyphon is filled with fluid.

2.5 TREATMENT OF BOUNDARY CONDITIONS

For the open thermosyphon problem, there are two types of boundary conditions; designated as Dirichlet and Neumann boundary conditions. The mathematical forms of these are

- Dirichlet type: $\Phi = f_1(\mathbf{r})$ on the boundary surface
- Neumann type: $\nabla\Phi = f_2(\mathbf{r})$ on the boundary surface

In words, the Dirichlet boundary condition specifies a prescribed transport variable, Φ , on the boundary surface as a function of the position vector, \mathbf{r} , and the Neumann boundary condition specifies the flux, $\nabla\Phi$, normal to the boundary as a function of the position vector, \mathbf{r} .

For heat transfer on the surface of the open thermosyphon, two types of boundary surfaces were specified. For a prescribed temperature distribution on the wall, $f_1(\mathbf{r})$ described a linear temperature profile, i.e. $f_1(\mathbf{r}) = T(z)$ as in figure 2.1. For an adiabatic boundary, $f_2(\mathbf{r})$ was set equal to zero. With fluid flowing at an impermeable boundary, the case is equivalent to a Neumann boundary condition with $f_2(\mathbf{r})$ equal to zero.

In a staggered grid system, all transport variables and transport properties are located at the cell centers including boundary cells with a finite width as shown in figure 2.7. For Dirichlet type boundary conditions, the transport variables were prescribed on the boundary.

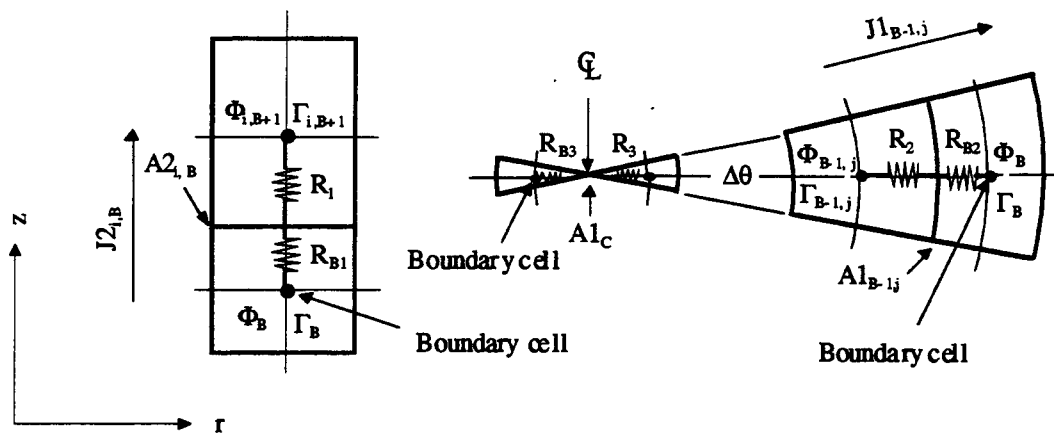


Figure 2.7 Treatment of boundary conditions in cylindrical coordinates

Consider the boundary cells in both r and z -directions shown in figure 2.7. There are two ways to specify the Dirichlet boundary condition at the wall surface - (i) to specify the finite width of all boundary cells to be zero, or (ii) to specify the resistances, R_{B1} , R_{B2} , and R_{B3} , to be zero. For this study, the resistances of the boundary cells were set equal to zero by prescribing the boundary transport properties, Γ_B , to approach infinite.

To set a zero flux across the surface of a Neumann type boundary, there are also two ways - (i) to specify the width of the boundary cells to approach infinite, or (ii) to specify large value resistances for R_{B1} , R_{B2} , R_{B3} . In this study, the resistances of the boundary cells were made infinitely large by specifying the boundary transport properties, Γ_B , to approach zero.

For programming purposes, a large number, 10^{+30} , and a small number, 10^{-30} , were used. Thus, the treatment of the two types of boundary conditions was

- Dirichlet type: $\Gamma_B = 10^{+30}$
- Neumann type with zero flux: $\Gamma_B = 10^{-30}$

Across a line of symmetry, for example the centerline, a boundary cell is the mirror image of the computation cell next to it. Fluid flow will be zero and no heat transfer will occur across the center line. This is like a Neumann type boundary with zero flux. In the transient case, for the open thermosyphon, the temperature at the centerline needed to be updating at each new time step.

2.6 NUMERICAL ITERATION METHOD

Many well-documented numerical iteration methods exist which solve the finite volume form of Poisson-type equations. In this study, a Line Successive Over-Relaxation (LSOR) method was used. Eq.(2.10) is written as

$$C1_{i,j} \Phi_{i+1,j}^n + C1_{i-1,j} \Phi_{i-1,j}^n + C2_{i,j} \Phi_{i,j+1}^n + C2_{i,j-1} \Phi_{i,j-1}^n - D_p \Phi_{i,j}^n = -S_p + e_p^n \quad (2.27)$$

where n is the iteration level, $S_p = -CV_{i,j} S_{i,j}$, and e_p^n is the error residue at the n^{th} iteration, the error residue will be zero if the current level of iteration satisfies the

finite-volume form of the Poisson equation. This error residue was used as the criterion for stopping the iteration process.

For a simple Jacobi iteration procedure, values of the transport variable at the new iteration level, $\Phi_{i,j}^{n+1}$, are obtained by the following equation

$$\Phi_{i,j}^{n+1} = \left(C1_{i,j} \Phi_{i+1,j}^n + C1_{i-1,j} \Phi_{i-1,j}^n + C2_{i,j} \Phi_{i,j+1}^n + C2_{i,j-1} \Phi_{i,j-1}^n + S_p \right) / D_p \quad (2.28)$$

For the next iteration level of Eq.(2.27) satisfying the Poisson-type equation, the expression becomes,

$$C1_{i,j} \Phi_{i+1,j}^{n+1} + C1_{i-1,j} \Phi_{i-1,j}^{n+1} + C2_{i,j} \Phi_{i,j+1}^{n+1} + C2_{i,j-1} \Phi_{i,j-1}^{n+1} - D_p \Phi_{i,j}^{n+1} = -S_p \quad (2.29)$$

Note that the source term remains unchanged during the iteration process. Subtracting Eq.(2.28) from Eq.(2.29), we have

$$C1_{i,j} \delta\Phi_{i+1,j}^n + C1_{i-1,j} \delta\Phi_{i-1,j}^n + C2_{i,j} \delta\Phi_{i,j+1}^n + C2_{i,j-1} \delta\Phi_{i,j-1}^n - D_p \delta\Phi_{i,j}^n = -e_p^n \quad (2.30)$$

where,

$$\delta\Phi_{i,j}^n = \Phi_{i,j}^{n+1} - \Phi_{i,j}^n \quad (2.31)$$

To obtain a convergence criterion, substitution of Eq.(2.28) into Eq.(2.31), yields

$$\Phi_{i,j}^{n+1} - \Phi_{i,j}^n = \frac{\left(C1_{i,j} \Phi_{i+1,j}^n + C1_{i-1,j} \Phi_{i-1,j}^n + C2_{i,j} \Phi_{i,j+1}^n + C2_{i,j-1} \Phi_{i,j-1}^n - D_p \Phi_{i,j}^n + S_p \right)}{D_p} \quad (2.32)$$

We note that the numerator of Eq.(2.32) is the error residue, e_p^n , at the current iteration level of Eq.(2.27), thus Eq.(2.31) becomes

$$\delta\Phi_{i,j}^n = \frac{e_p^n}{D_p} \quad (2.33)$$

This expression was used as the convergence criterion to stop the iteration process. The value used in this study was

$$\text{Max} \left| \delta\Phi_{i,j}^n \right| \leq 10^{-6} \quad (2.34)$$

To use the LSOR iteration method, it was necessary to write Eq.(2.30) in the i- and j-directions and then add an over-relaxation factor, ω , giving

$$\text{i-direction: } C1_{i,j} \delta\Phi_{i+1,j}^n + D_p \delta\Phi_{i,j}^n + C1_{i-1,j} \delta\Phi_{i-1,j}^n = -\omega \cdot e_p^n \quad (2.35)$$

$$\text{j-direction: } C2_{i,j} \delta\Phi_{i,j+1}^n + D_p \delta\Phi_{i,j}^n + C2_{i,j-1} \delta\Phi_{i,j-1}^n = -\omega \cdot e_p^n \quad (2.36)$$

To speed up the iteration process, a balancing technique, as used in TEMPEST was applied. If we consider the cell structure shown in figure 2.2, for each cell, an expression of the form given by Eq.(2.30) can be written.

Summing the equations for all cells along a column in the computational region, we obtain

$$\sum_{j=2}^{j_{\max}-1} C1_{i,j} \delta\Phi_{i+1,j}^n + \sum_{j=2}^{j_{\max}-1} C1_{i-1,j} \delta\Phi_{i-1,j}^n - \sum_{j=2}^{j_{\max}-1} (C1_{i,j} + C1_{i-1,j}) \delta\Phi_{i,j}^n +$$

$$\sum_{j=2}^{j_{\max}-1} C2_{i,j} \delta\Phi_{i,j+1}^n + \sum_{j=2}^{j_{\max}-1} C2_{i,j-1} \delta\Phi_{i,j-1}^n - \sum_{j=2}^{j_{\max}-1} (C2_{i,j} + C2_{i,j-1}) \delta\Phi_{i,j}^n = - \sum_{j=2}^{j_{\max}-1} e_p^n$$

(2.37)

An expansion of the last three terms on the left-hand side of Eq. (2.37) and then adding them together yields the following;

	$C2_{i,j} \delta\Phi_{i,j+1}$	$C2_{i,j-1} \delta\Phi_{i,j-1}$	$-C2_{i,j} \delta\Phi_{i,j}$	$-C2_{i,j-1} \delta\Phi_{i,j}$
$j=2$	$C2_{i,2} \delta\Phi_{i,3}$	$+ C2_{i,1} \delta\Phi_{i,1}$	$- C2_{i,2} \delta\Phi_{i,2}$	$- C2_{i,1} \delta\Phi_{i,2}$
$j=3$	$C2_{i,3} \delta\Phi_{i,4}$	$+ C2_{i,2} \delta\Phi_{i,2}$	$- C2_{i,3} \delta\Phi_{i,3}$	$- C2_{i,2} \delta\Phi_{i,3}$
$j=4$	$C2_{i,4} \delta\Phi_{i,5}$	$+ C2_{i,3} \delta\Phi_{i,3}$	$- C2_{i,4} \delta\Phi_{i,4}$	$- C2_{i,3} \delta\Phi_{i,4}$
⋮				
$j=j_{\max}-2$	$C2_{i,j_{\max}-2} \delta\Phi_{i,j_{\max}}$	$+ C2_{i,j_{\max}-3} \delta\Phi_{i,j_{\max}-3}$	$- C2_{i,j_{\max}-2} \delta\Phi_{i,j_{\max}-2}$	$- C2_{i,j_{\max}-3} \delta\Phi_{i,j_{\max}-2}$
$j=j_{\max}-1$	$C2_{i,j_{\max}-1} \delta\Phi_{i,j_{\max}}$	$+ C2_{i,j_{\max}-2} \delta\Phi_{i,j_{\max}-2}$	$- C2_{i,j_{\max}-1} \delta\Phi_{i,j_{\max}-1}$	$- C2_{i,j_{\max}-2} \delta\Phi_{i,j_{\max}-1}$
Sum	$C2_{i,1} \delta\Phi_{i,1}$	$- C2_{i,1} \delta\Phi_{i,2}$	$+ C2_{i,j_{\max}-1} \delta\Phi_{i,j_{\max}}$	$- C2_{i,j_{\max}-1} \delta\Phi_{i,j_{\max}-1}$

If the boundary cells at $j=1$ and $j=j_{\max}$ are Neumann type boundary conditions with zero flux, the connector, $C2_{i,1}$ and $C2_{i,j_{\max}-1}$, are zero. Thus, the last three terms of Eq. (2.37) are zero, and Eq. (2.37) becomes

$$\sum_{j=2}^{j_{\max}-1} C1_{i,j} \delta\Phi_{i+1,j}^n + \sum_{j=2}^{j_{\max}-1} C1_{i-1,j} \delta\Phi_{i-1,j}^n - \sum_{j=2}^{j_{\max}-1} (C1_{i,j} + C1_{i-1,j}) \delta\Phi_{i,j}^n = - \sum_{j=2}^{j_{\max}-1} e_p^n \quad (2.38)$$

Similarly, summing along a row in the computational region, yields

$$\sum_{i=2}^{i_{\max}-1} C2_{i,j} \delta\Phi_{i,j+1}^n + \sum_{i=2}^{i_{\max}-1} C2_{i,j-1} \delta\Phi_{i,j-1}^n - \sum_{i=2}^{i_{\max}-1} (C2_{i,j} + C2_{i,j-1}) \delta\Phi_{i,j}^n = - \sum_{i=2}^{i_{\max}-1} e_p^n \quad (2.39)$$

Eqs.(2.38) and (2.39) are restricted for use in a computational region with Neumann type boundary conditions of zero flux. The forms of Eqs.(2.38) and (2.39) are similar to those of Eqs.(2.35) and (2.36). An LSOR iteration scheme can be applied to these equations. An over-relaxation factor, ω , was used on the right-hand terms of Eqs.(2.38) and (2.39). The computer program for accomplishing the LSOR iteration procedure and the balancing technique have the features described below:

I-direction(intermediate step):

- Step 1: Compute the summation of error residue along the J-direction in Eq.(2.38) according to Eq.(2.30)
- Step 2: Apply the Thomas tri-diagonal matrix algorithm to solve Eq.(2.38) for $\delta\Phi$
- Step 3: Update $\Phi_{i,j}^{n+1}$ according to Eq.(2.31)

J-direction(Final step):

Step 4: Compute the summation of error residues along the J-direction in Eq.(2.39) according to Eq.(2.30)

Step 5: Apply the Thomas tri-diagonal matrix algorithm to solve Eq.(2.39) for $\delta\Phi$

Step 6: Update $\Phi_{i,j}^{n+1}$ according to Eq.(2.31)

Step 7: Stop the iteration if the maximum error residue satisfies the convergence criterion, Eq.(2.34)

Note that the LSOR iteration process must converge since the tri-diagonal matrices of Eqs.(2.38) and (2.39) are diagonally dominant [19].

2.7 TEMPEST SOLUTION PROCEDURE

The TEMPEST solution procedure described by Trent and Eyler [16] was used for the numerical solution in this study. This solution procedure is a semi-implicit, time-marching finite-volume procedure with all governing equations solved sequentially. A descriptions of the solution procedure stated in the TEMPEST manual is repeated here for the convenience of the reader.

There are three phases involved in this procedure.

Phase I - Tilde Phase The three momentum equations are advanced in time $(t + \Delta t)$ to obtain approximate (Tilde) velocities, \tilde{u} , \tilde{v} , and \tilde{w} , based on the previous time values of pressure and density, p and ρ . Although these

velocity component values satisfy the momentum equations based on current values of p and ρ , continuity will usually not be satisfied.

Phase II - Implicit Phase The velocity and pressure corrections (u', v', w' , and p') are obtained such that the quantities $u^{n+1} = \tilde{u} + u'$, $v^{n+1} = \tilde{v} + v'$, $w^{n+1} = \tilde{w} + w'$, and $p^{n+1} = p^n + p'$ satisfy continuity.

Phase III - Scalar Phase Using the previously-computed values of u^{n+1} , v^{n+1} , and w^{n+1} , updated values of temperature T^{n+1} and other scalar quantities are computed as required.

The solution is advanced, step by step in time, by continued application of the above three solution phases.

One important aspect of this solution procedure is to force updated values of the velocity field to satisfy continuity by adding velocity corrections. These values happen to be the gradient of the scalar potential, $\nabla\Phi$, of the irrotational flow field as discussed in the next paragraph. Together with the divergence of the irrotational flow field, a Poisson-type equation with the scalar potential, Φ , as the transport variable is generated. Thus, this Poisson-type equation can be solved by the LSOR numerical iteration method.

Consider the divergence of the approximate velocity vector field at the current time level in the tilde phase, $\nabla \cdot \tilde{\mathbf{u}}$. Since the approximate velocity field was obtained from the momentum equations, there is a divergence, D ,

associated with its divergence, i.e. $\nabla \cdot \tilde{\mathbf{u}} = D$. Our objective is to force this velocity vector field at the advanced time satisfying the continuity, i.e. $\nabla \cdot \mathbf{u}^{n+1} = 0$ by adding a velocity correction field, \mathbf{u}' . We wish \mathbf{u}' to be related to D .

The advanced-time velocity vector field, \mathbf{u}^{n+1} , and the approximate provisional velocity vector field, $\tilde{\mathbf{u}}$, are decomposed into rotational flow vector fields, \mathbf{u}_ω^{n+1} and $\tilde{\mathbf{u}}_\omega$ respectively, and irrotational flow vector fields, \mathbf{u}_ϕ^{n+1} and $\tilde{\mathbf{u}}_\phi$ respectively, as

$$\mathbf{u}^{n+1} = \mathbf{u}_\omega^{n+1} + \mathbf{u}_\phi^{n+1} \quad (2.40)$$

$$\tilde{\mathbf{u}} = \tilde{\mathbf{u}}_\omega + \tilde{\mathbf{u}}_\phi \quad (2.41)$$

The difference between $\tilde{\mathbf{u}}$ and \mathbf{u}^{n+1} is made up by the velocity-correction vector field, \mathbf{u}' , as

$$\mathbf{u}^{n+1} = \tilde{\mathbf{u}} + \mathbf{u}' \quad (2.42)$$

Also, we purposely add this velocity-correction vector field to the irrotational part of the flow. In other words, this velocity-correction vector field is irrotational. Thus, Eq.(2.42) becomes

$$\mathbf{u}_\omega^{n+1} + \mathbf{u}_\phi^{n+1} = \tilde{\mathbf{u}}_\omega + (\tilde{\mathbf{u}}_\phi + \mathbf{u}') \quad (2.43)$$

The divergence theorem states that the divergence, D , of the rotational part of the flow field is zero. Taking the divergence of Eqs.(2.40), (2.41), and (2.43) and noting

that $\nabla \cdot \tilde{\mathbf{u}} = D$ and $\nabla \cdot \mathbf{u}^{n+1} = 0$, we obtain an expression for the divergence of velocity-correction vector field as

$$\nabla \cdot \mathbf{u}' = -\nabla \cdot \tilde{\mathbf{u}}_{\phi} = -\nabla \cdot \tilde{\mathbf{u}} = -D \quad (2.44)$$

Since the flow is irrotational, we can define a scalar potential, Φ , such that

$$\mathbf{u}' = \nabla \Phi, \quad (2.45)$$

Substituting Eq.(2.45) into Eq.(2.44), we obtain a Poisson-type equation with the divergence as the source term for irrotational flow

$$\nabla \cdot (\nabla \Phi) = D \quad (2.46)$$

Eq.(2.46) was solved using the LSOR numerical iteration method as discussed in section 2.5.

These velocity corrections ensure that the advanced-time velocity fields satisfy the continuity equation but they do not satisfy the momentum equation. To satisfy the momentum equation with these advanced-time velocity fields, a pressure field correction related to the scalar potential, is used. This pressure correction is obtained as described below.

Consider the momentum equation in the r-direction, Eq.(2.2). For simplicity, Eq.(2.2) is rearranged as

$$\frac{\partial u}{\partial t} = -\frac{1}{\rho_0} \frac{\partial p}{\partial r} + S_{\text{Rem}} \quad (2.47)$$

$$\text{where, } S_{\text{Rem}} = \frac{\mu}{\rho_0} \left[\frac{1}{r} \frac{\partial}{\partial r} \left(r \frac{\partial u}{\partial r} \right) - \frac{u}{r^2} + \frac{\partial}{\partial z} \left(\frac{\partial u}{\partial z} \right) \right] - \left[\frac{1}{r} (uu) + \frac{\partial}{\partial r} (uu) + \frac{\partial}{\partial z} (vu) \right]$$

Using a semi-implicit finite-difference discretization, Eq.(2.47) at the advanced time level becomes

$$(\bar{u}_i + u_i') - u_i^n = \frac{\Delta t}{\rho_0 \Delta r_i} \left[(p^n + p')_{i+1} - (p^n + p')_i \right] + \Delta t S_{\text{Rem}}^n \quad (2.48)$$

Similarly, the finite-difference form of Eq.(2.47) at the previous time step is

$$\bar{u}_i - u_i^n = \frac{\Delta t}{\rho_0 \Delta r_i} (p_{i+1}^n - p_i^n) + \Delta t S_{\text{Rem}}^n \quad (2.49)$$

Subtracting Eq.(2.48) from Eq.(2.49), yields

$$u_i' = \frac{\Delta t}{\rho_0 \Delta r_i} (p_{i+1}' - p_i') \quad (2.50)$$

Expressing the velocity correction by Eq.(2.45), and integrating Eq.(2.50) with respect to r , the pressure correction is seen to be related to the scalar potential according to

$$p' = \frac{\rho_0}{\Delta t} \Phi \quad (2.51)$$

The solution algorithm based on this solution procedure is shown in figure 2.8.

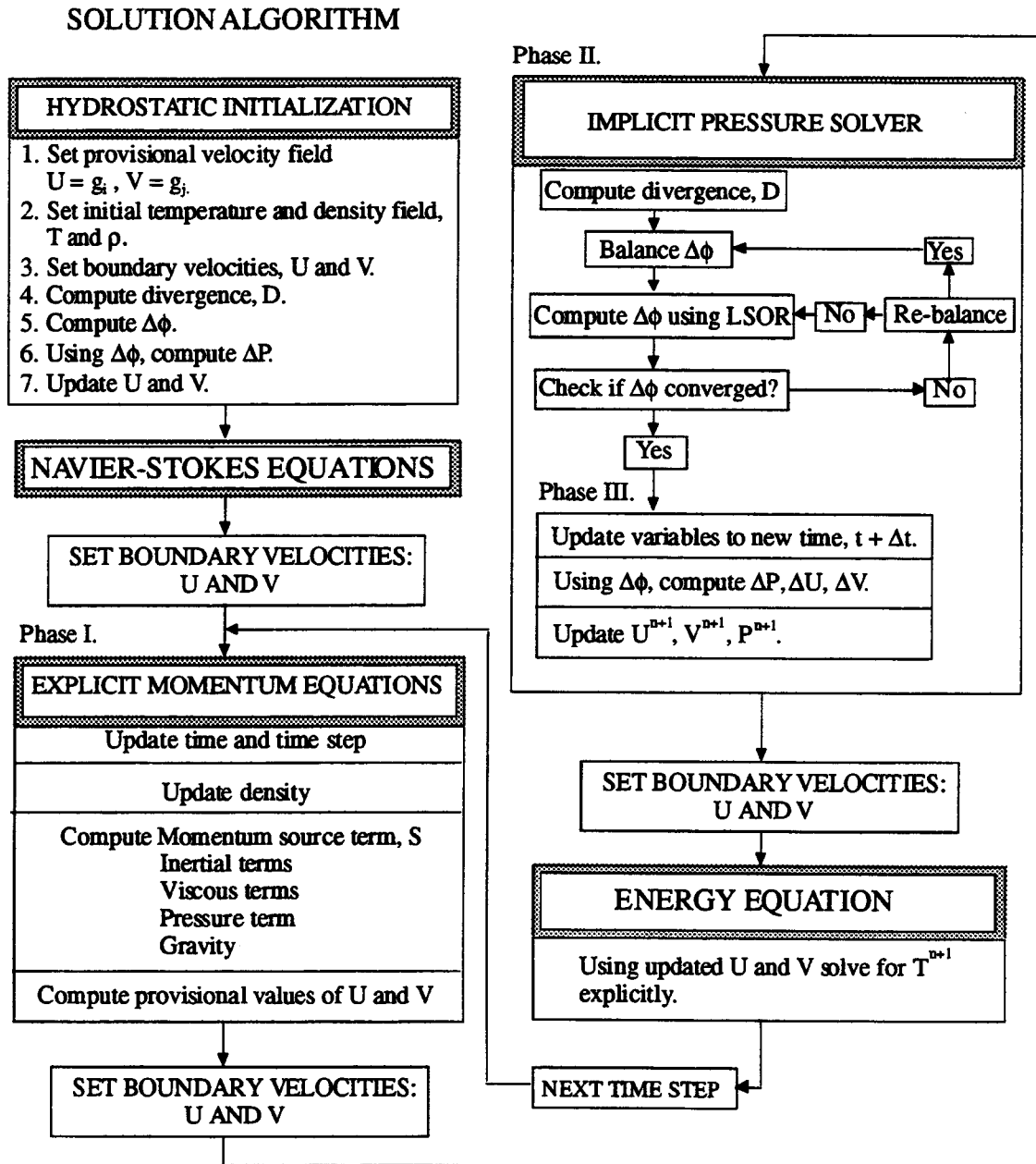


Figure 2.8 Solution algorithm based on the TEMPEST solution procedure

2.8 NUMERICAL DISCRETIZATION AND STABILITY

Numerical discretization for the three governing equations was based on the non-uniform staggered grid system shown in figure 2.3. Discretization of the advective terms was based on the u-momentum cell for the momentum equation in the r-direction, and on the v-momentum cell for the momentum equation in the z-direction. Discretization of the advective terms in the energy equation was based on the continuity cell. An explicit upwind scheme was used for all advective terms.

The governing equations were retained in a conservative form as shown in Eqs.(2.1)-(2.4). A first-order, backward, finite-difference formulation was used for the viscous and gravity terms in the momentum equations, and for the diffusion terms in the energy equation. Details of these finite-difference discretizations are provided in Appendix A.

The provisional velocity fields, \tilde{u} and \tilde{v} , were calculated based on the sum of the inertial, pressure, viscous, and gravity terms in the momentum equations as shown in the solution algorithm, figure 2.8. Divergence from the continuity equation was calculated for each cell based on these provisional velocity fields. The discretization scheme for the divergence is described in Appendix A. Using the LSOR iteration method, velocity and pressure corrections were evaluated to update the velocity and pressure fields. New temperature fields were updated

using the energy equation. After all four fields; u , v , p , and T ; were determined, the solution proceeded to the next time step. A criterion based on the velocity fields and cell sizes was used to determine the time step which would assure numerical stability. The stability criterion, as described by Roache [20], for a uniform grid system is

$$\Delta t \leq \text{Min} \left\{ \left(\frac{|u_{i,j}|}{\Delta r_i} + \frac{|v_{i,j}|}{\Delta z_j} + 2 \text{Min} \left\{ \frac{\alpha}{\nu} \right\} \left[\frac{1}{(\Delta r_i)^2} + \frac{1}{(\Delta z_j)^2} \right] \right)^{-1} \right\} \quad (2.52)$$

where, ν is kinematic viscosity, and α is the thermal diffusivity of the fluid. The smaller Δt was used. The stability criterion for the non-uniform grid system for this study is described in appendix A.

2.9 MEASUREMENT PARAMETERS

Several heat transfer parameters were evaluated to describe the open thermosyphon characteristics. They were based on heat conduction and heat convection near the vertical tube wall.

The net heat transfer from the fluid near the wall to the wall by convection was evaluated as

$$q_v = \sum_j \left(-\kappa \cdot 2\pi R \cdot \Delta z_{w,j} \right) \frac{T_{w,j} - T_{w-1,j}}{\frac{1}{2} \Delta r_{w-1,j}} \quad (2.53)$$

where the subscripts represent the cell number at the wall in the radial direction. The index for cell numbers runs from the tube opening to the closed end.

The net heat transfer from the fluid to the wall based on the tube radius, R , was evaluated as

$$q_c = -\kappa \cdot 2\pi R \cdot L \left(\frac{T_m - T_{res}}{R} \right) \quad (2.54)$$

The Nusselt number based on the tube radius, Nu_R , is the ratio of Eq.(2.53) to Eq.(2.54).

The net heat transfer from the fluid to the wall based on the tube length, L , was evaluated as

$$q_c = -\kappa \cdot 2\pi R \cdot L \left(\frac{T_m - T_{res}}{L} \right) \quad (2.55)$$

The Nusselt number based on tube length, Nu_L , was evaluated as the ratio of Eq.(2.53) to Eq.(2.55).

The heat transfer coefficient referred to the tube radius is therefore

$$h = \frac{Nu_R \kappa}{R} \quad (2.56)$$

III. RESULTS OF NUMERICAL SOLUTION

Results of the numerical solution of the open thermosyphon are presented in this chapter. A FORTRAN computer program was developed based on the solution procedures described in the previous chapter. This computer program was developed particularly for the open thermosyphon in two-dimensional cylindrical coordinates. However, if necessary for experimental verification, a solution in Cartesian coordinates can be accomplished by changing the input parameters appropriately.

Cases of open thermosyphons with two different types of thermal boundaries were studied. In addition to the thermal boundary conditions, another parameter significantly influencing the numerical results is the length-to-radius (aspect) ratio of the vertical tubes. The classification of flow regimes defined by Lighthill [11] was based on the aspect ratio of the tubes. The computer program also provided a transient solution for the problem. Plots of streamlines and isotherms indicates that some steady-state cases involve oscillating fluid motion.

The heat transfer rates were found to increase as the tube radius increased for the open thermosyphon and to approach an asymptotic limit. It is likely that the longer

the vertical tubes, the smaller the heat transfer rates. For open thermosyphons with very high aspect ratios, flow circulates weakly at the closed-end of the vertical tube, and thus doesn't transfer a significant amount of heat to and from reservoir.

3.1 VERIFICATION OF COMPUTER PROGRAM, AND CASES SELECTED

The computer program was first tested by solving the problem of laminar natural convection in a square cavity. Plots of streamlines and isotherms are shown in figure 3.1. Contour plots of this configuration are abundant in the

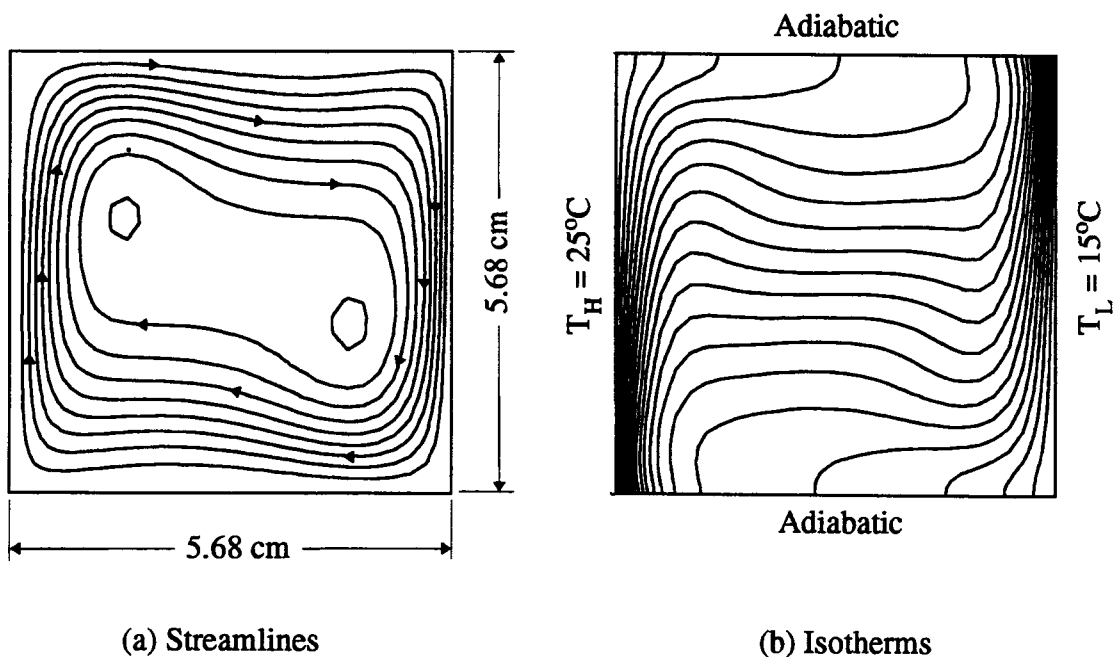


Figure 3.1 Streamlines and isotherms of air in a square cavity

literature. This configuration was considered a benchmark problem as proposed by De Vahl Davis and Jones [21]. This problem will also be used to illustrate the procedures for numerically-generated fringe patterns in section 4.7.

Dimensions of the square cavity used in this study were 5.68cm x 5.68cm. The upper and lower boundaries were insulated; the right boundary was maintained at 25 °C and the left boundary at 15 °C as shown.

Numerical results were achieved for eighty cases of open thermosyphons in this study. Table 3.1 summarizes the dimensions and the numerical results for the selected 80 cases. Two types of thermal boundaries, each with 40 geometric variations, were examined. Cases with type A thermal boundaries had a linearly varying temperature distributed along the vertical tubes. The upper limit of this linear temperature profile was set at 6 °C and the bottom at 96 °C as shown in figure 2.1. Cases with type B thermal boundaries had a constant temperature of 51 °C along the vertical wall. The reservoir wall temperature was specified at 96 °C for all 80 cases. Lengths and radii of the vertical tubes were varied as shown in the table.

Values of two calculated heat-transfer parameters are also listed in table 3.1. The time-averaged heat transfer coefficients, h_t , and the time-averaged Nusselt numbers, Nu_t , are presented for elapsed times between 200 and 1000 seconds. Data points were determined each 10 seconds.

Table 3.1 Dimensions and numerical results of all selected open thermosyphons

Type A thermal boundary						Type B thermal boundary					
Linearly varying wall temperature						Constant wall temperature					
#	L(cm)	R(cm)	AR	h_t (w/cm ² K)	Nu_t	#	L(cm)	R(cm)	AR	h_t (w/cm ² K)	Nu_t
A1	50	50	1	0.0369	319.13	B1	50	50	1	0.0612	478.63
A2	50	25	2	0.0360	155.67	B2	50	25	2	0.0578	226.01
A3	50	16.7	3	0.0319	92.013	B3	50	16.7	3	0.0538	140.14
A4	50	8.33	6	0.0303	43.680	B4	50	8.33	6	0.0430	55.983
A5	50	5.00	10	0.0295	25.475	B5	50	5.00	10	0.0402	31.420
A6	50	2.50	20	0.0247	10.659	B6	50	2.50	20	0.0342	13.366
A7	50	0.50	100	0.0138	1.1886	B7	50	0.50	100	0.0046	0.3580
A8	50	0.25	200	7.0E-5	0.0032	B8	50	0.25	200	0.0013	0.0503
A9	40	50	0.8	0.0419	316.62	B9	40	50	0.8	0.0652	510.07
A10	40	25	1.6	0.0406	175.53	B10	40	25	1.6	0.0620	242.36
A11	40	16.7	2.4	0.0376	108.28	B11	40	16.7	2.4	0.0580	151.22
A12	40	8.33	4.8	0.0330	47.467	B12	40	8.33	4.8	0.0473	61.593
A13	40	5.00	8	0.0311	26.828	B13	40	5.00	8	0.0430	33.627
A14	40	2.50	16	0.0288	12.432	B14	40	2.50	16	0.0359	14.038
A15	40	0.50	80	0.0147	1.2726	B15	40	0.50	80	0.0057	0.4452
A16	40	0.25	160	9.0E-5	0.0039	B16	40	0.25	160	0.0016	0.0630
A17	30	50	0.6	0.0452	390.84	B17	30	50	0.6	0.0715	559.20
A18	30	25	1.2	0.0437	188.87	B18	30	25	1.2	0.0681	266.13
A19	30	16.7	1.8	0.0408	117.48	B19	30	16.7	1.8	0.0642	167.32
A20	30	8.33	3.6	0.0359	51.700	B20	30	8.33	3.6	0.0534	69.555
A21	30	5.00	6	0.0346	27.411	B21	30	5.00	6	0.0471	36.795
A22	30	2.50	12	0.0334	14.448	B22	30	2.50	12	0.0413	16.133
A23	30	0.50	60	0.0231	1.9920	B23	30	0.50	60	0.0076	0.5916
A24	30	0.25	120	1.2E-4	0.0053	B24	30	0.25	120	0.0021	0.0836
A25	20	50	0.4	0.0565	488.29	B25	20	50	0.4	0.0807	631.21
A26	20	25	0.8	0.0543	234.48	B26	20	25	0.8	0.0781	305.20
A27	20	16.7	1.2	0.0517	148.90	B27	20	16.7	1.2	0.0741	193.28
A28	20	8.33	2.4	0.0449	64.676	B28	20	8.33	2.4	0.0634	82.558
A29	20	5.00	4	0.0423	36.565	B29	20	5.00	4	0.0559	43.700
A30	20	2.50	8	0.0403	17.411	B30	20	2.50	8	0.0461	18.007
A31	20	0.50	40	0.0120	1.0360	B31	20	0.50	40	0.0098	0.7662
A32	20	0.25	80	6.6E-4	0.0284	B32	20	0.25	80	0.0027	0.1068
A33	10	50	0.2	0.0684	591.09	B33	10	50	0.2	0.0984	769.68
A34	10	25	0.4	0.0667	288.32	B34	10	25	0.4	0.0969	378.89
A35	10	16.7	0.6	0.0647	186.27	B35	10	16.7	0.6	0.0935	243.70
A36	10	8.33	1.2	0.0586	84.283	B36	10	8.33	1.2	0.0844	109.98
A37	10	5.00	2	0.0537	46.411	B37	10	5.00	2	0.0756	59.077
A38	10	2.50	4	0.0511	22.103	B38	10	2.50	4	0.0600	23.451
A39	10	0.50	20	0.0215	1.8580	B39	10	0.50	20	0.0186	1.4517
A40	10	0.25	40	6.2E-3	0.2699	B40	10	0.25	40	0.0054	0.2119

3.2 SUMMARY OF RESULTS OF ALL 80 SELECTED CASES

Plots of two heat-transfer parameters, h_t and Nu_t , for all cases listed in table 3.1 are shown in figure 3.2 and figure 3.3.

From figure 3.2, h_t is seen to increase as the tube radius increases and to approach an asymptotic limit for both type A and type B thermal boundaries. Beyond this limit, a further increase in tube radius did not increase the rate of heat transfer per unit area. Values of h_t for cases with type B boundaries are higher than their corresponding cases with type A boundaries at the same tube radius. The time-averaged Nusselt number, Nu_t , increases in a linear fashion as the tube radius increases for both types of thermal boundaries. Values of Nu_t for type B boundaries are higher than those for type A. Another observation from figure 3.2 is that open thermosyphons with smaller tube lengths display higher heat-transfer rates; this can also be seen from figure 3.3.

Figure 3.3 shows both h_t and Nu_t as functions of the tube length for large tube radius cases. For both h_t and Nu_t , an increase in tube length is associated with decreases in the values of both h_t and Nu_t . The larger the tube radius, the higher are the values of h_t and Nu_t .

To provide more information for the characteristics of open thermosyphons, two cases were chosen for more detailed

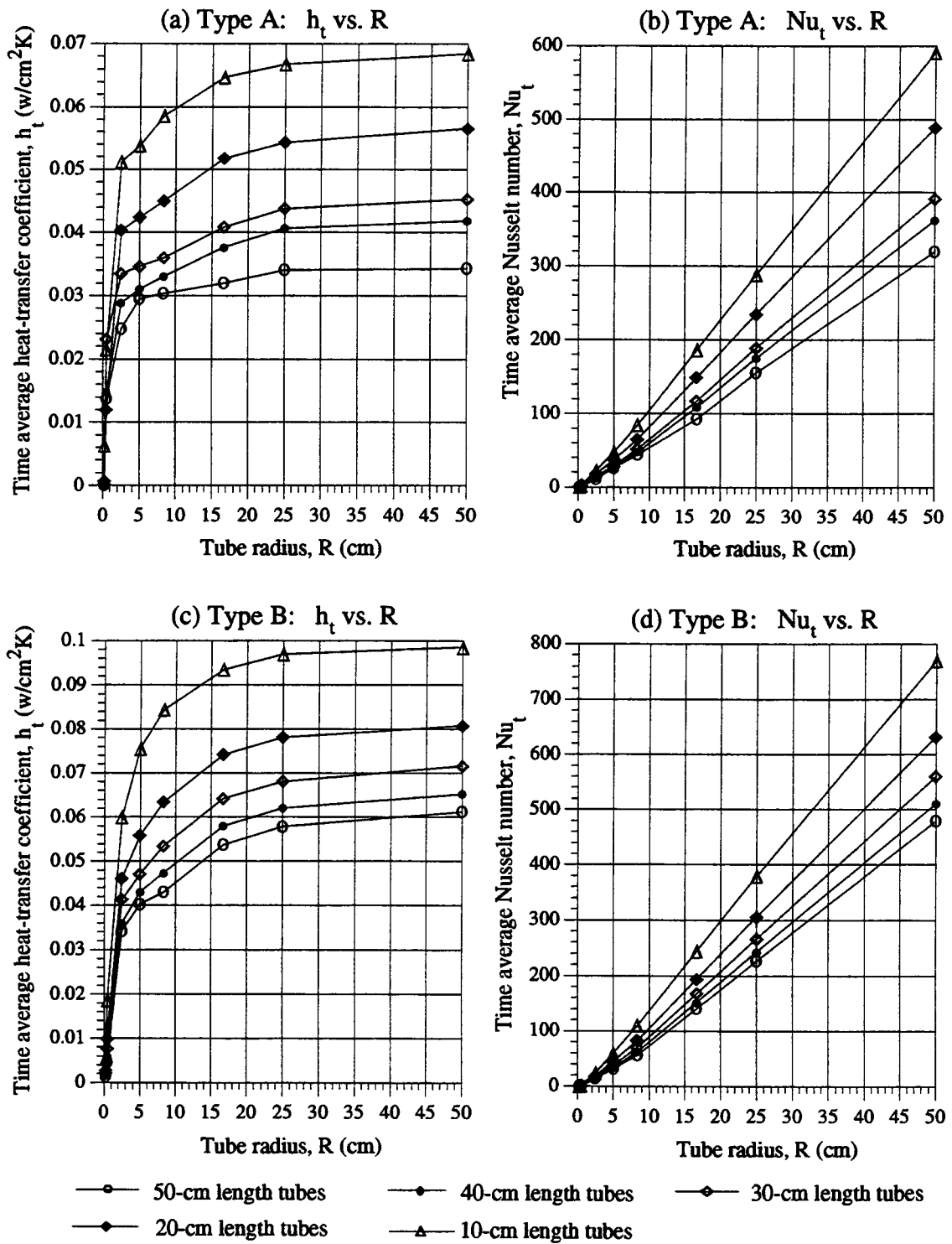


Figure 3.2 Plots of time-average heat-transfer coefficient (h_t) and time-average Nusselt number (Nu_t); (a) h_t versus radius for type A thermal boundary (b) Nu_t versus radius for type A thermal boundary (c) h_t versus radius for type B thermal boundary (d) Nu_t versus radius for type B thermal boundary

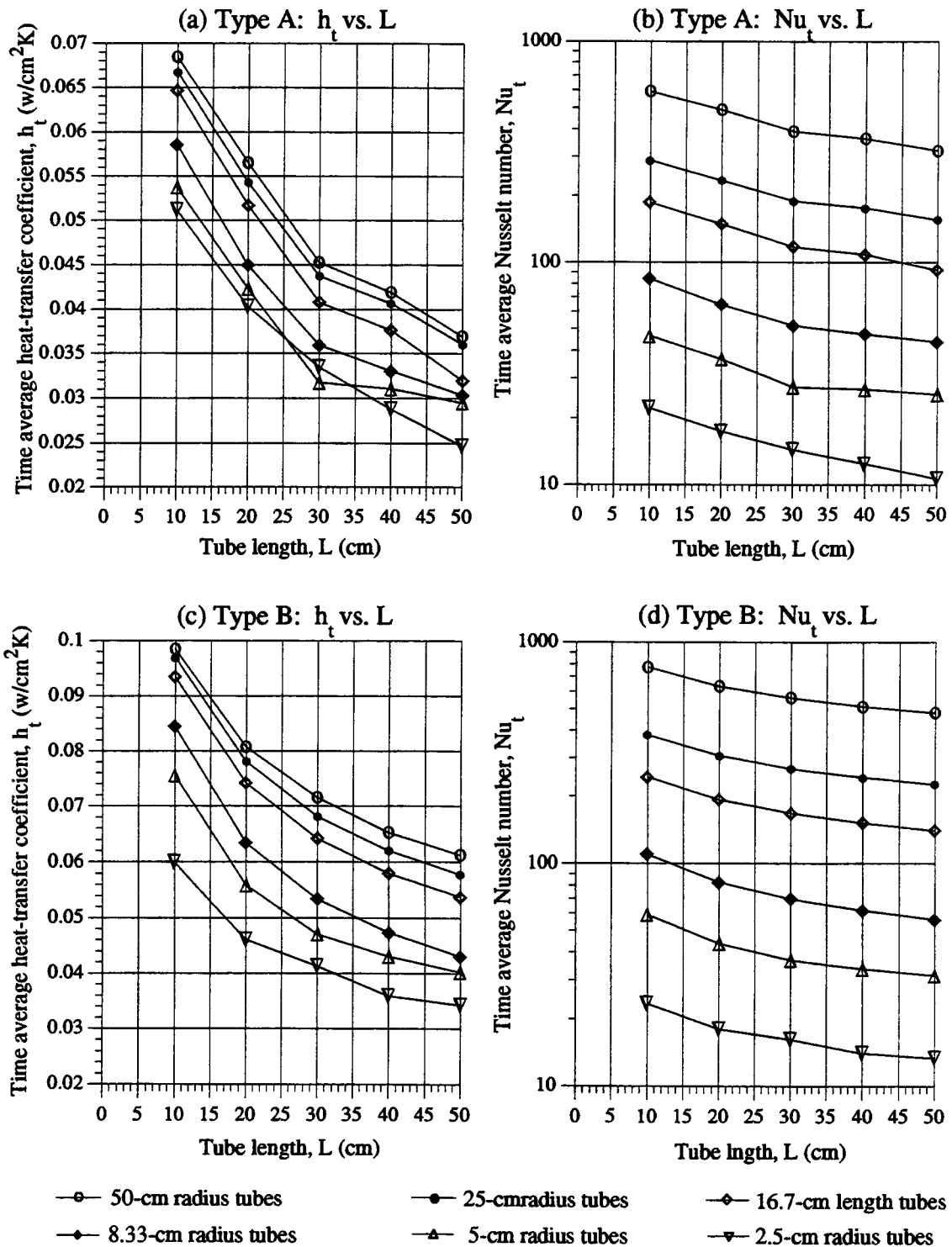


Figure 3.3 Plots of time-average heat-transfer coefficient (h_t) and time-average Nusselt number (Nu_t); (a) h_t versus length for type A thermal boundary (b) Nu_t versus length for type A thermal boundary (c) h_t versus length for type B thermal boundary (d) Nu_t versus length for type B thermal boundary

examination. These cases are described in sections 3.3 and 3.4. The first of these sets consisted of 8 cases, A1 to A8 in table 3.1, with a fixed tube length of 50 cm and with type A thermal boundaries. The second set consisted of 5 cases; B5, B13, B21, B29 and B37 in table 3.1; with a fixed radius of 5 cm and with type B thermal boundaries.

3.3 TYPE A OPEN THERMOSYPHONS WITH FIXED TUBE LENGTH

Eight cases, A1-A8, of type A open thermosyphons with a fixed tube length of 50 cm are discussed in this section. The aspect ratios of these eight cases are $AR = 1, 2, 3, 6, 10, 20, 100, \text{ and } 200$, and the corresponding tube radii are $R = 50, 25, 16.67, 8.33, 5, 2.5, 0.5, \text{ and } 0.25$ cm, respectively. All eight cases have a negative temperature gradient ($A < 0$) linearly distributed along the surface of the vertical tube.

Figures 3.4-3.6 show the streamlines and isotherms at 1000 seconds for the selected eight cases. These plots illustrate the three flow regimes for laminar flow defined by Lighthill [11]. They are: (i) Flow with the laminar boundary layer not filling the tube, where the boundary-layer thickness is relatively small compared to the tube radius. Tubes with $AR = 1, 2, 3, \text{ and } 6$ are in this regime as indicated by the relatively thin boundary-layer

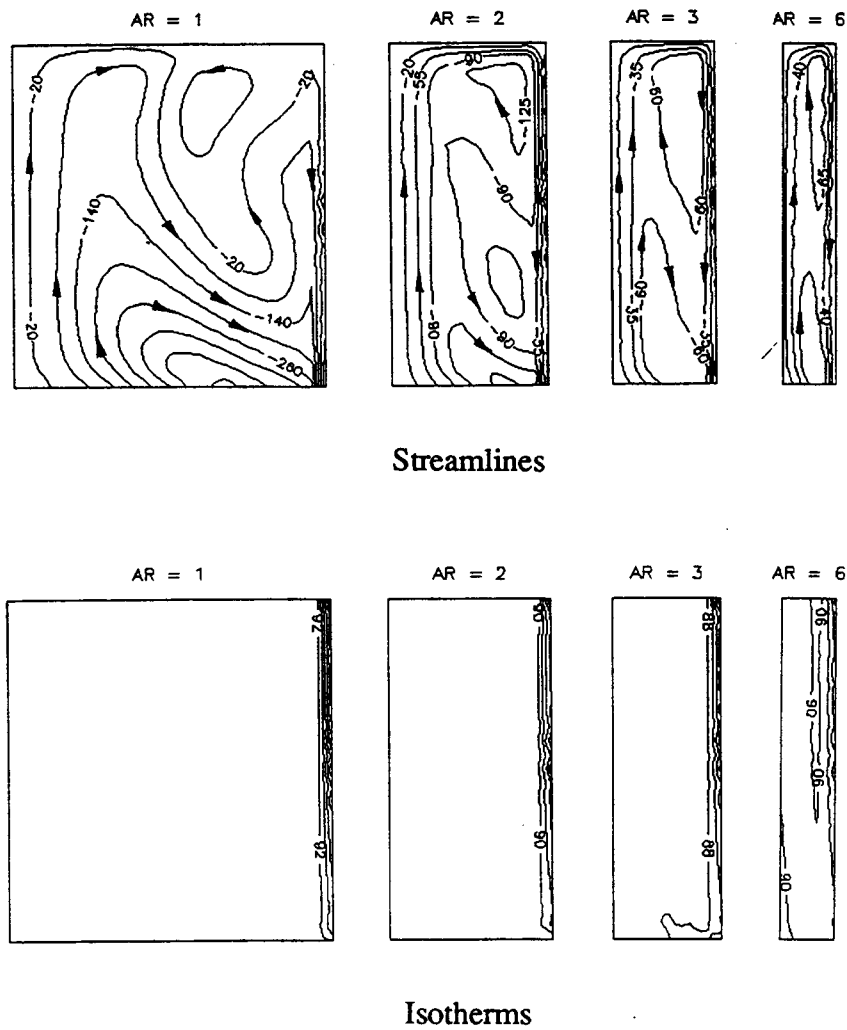


Figure 3.4 Streamlines and isotherms for cases of open thermosyphons, A1-A4, with $AR = 1, 2, 3,$ and 6 at 1000 s . Note that the scale of the plots for these cases is true.

thicknesses in each case shown in figure 3.4. (ii) The similarity region, where the boundary-layer flow, together with a central flow in the opposite direction, fills the entire tube. Tubes with $AR = 10$ and 20 , shown in

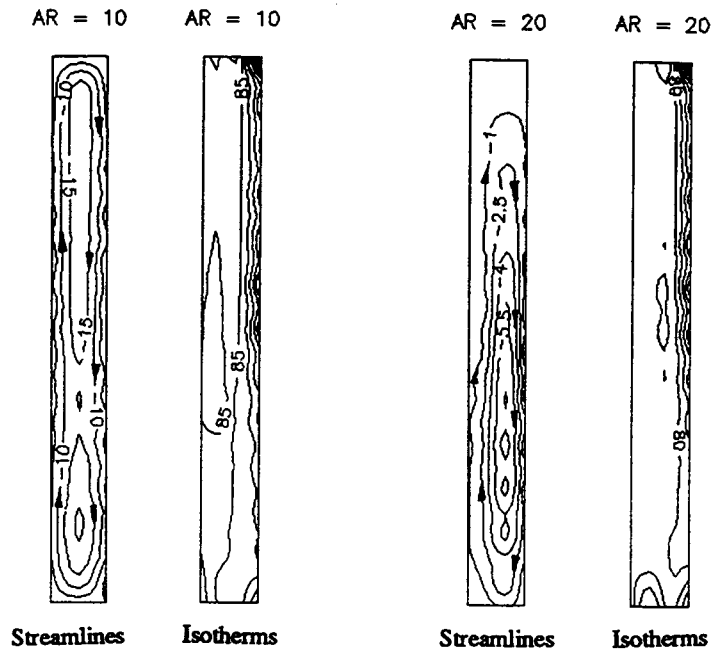


Figure 3.5 Streamlines and isotherms for cases of open thermosyphons, A5 and A6, with $AR = 10$ and 20 at 1000 s. Note that the scale of these plots has been adjusted for ease in viewing.

figure 3.5, display behavior typical of this regime. (iii) Laminar flow filling the tube without similarity, where fluid stagnation or a weak vortex ring is formed at the closed-end of the tube. Tubes with $AR = 100$ and 200 , with behavior shown in figure 3.6, are in this regime.

The formation of boundary layers is illustrated in greater detail in figure 3.7, which shows a series of streamlines and isotherms at selected times for $AR = 2$. Figure 3.8 shows the corresponding vertical velocity and temperature profiles near the tube wall for this case.

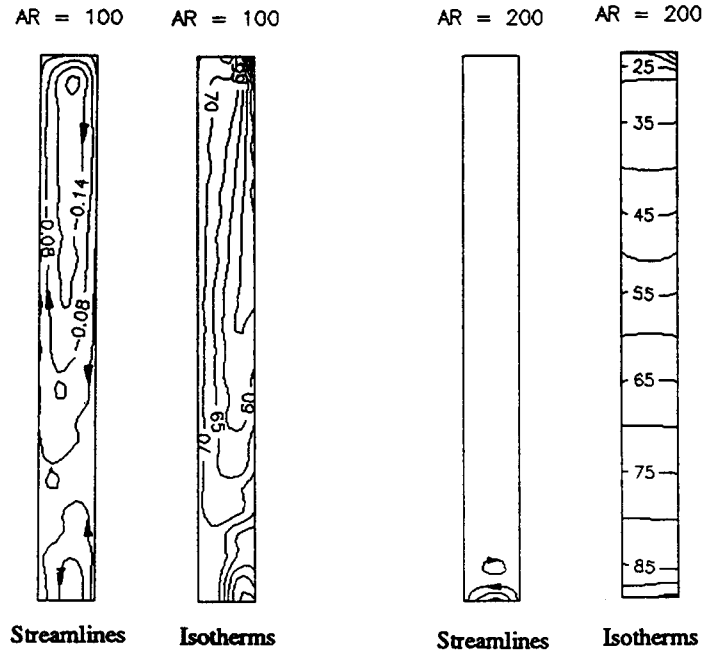
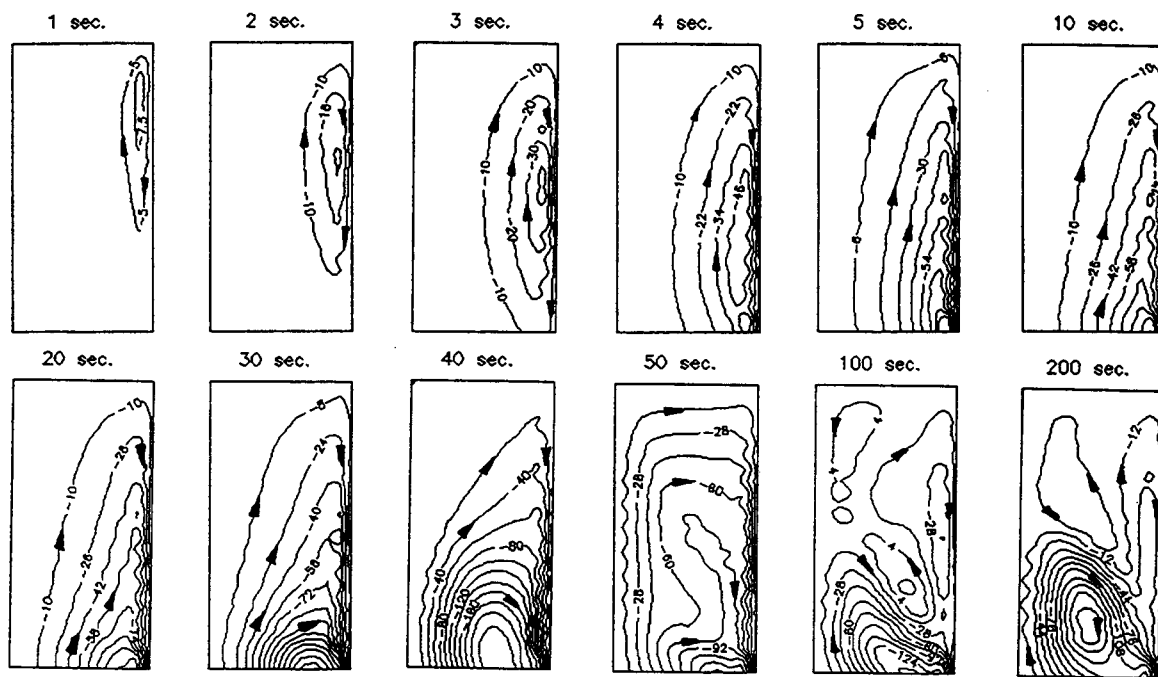
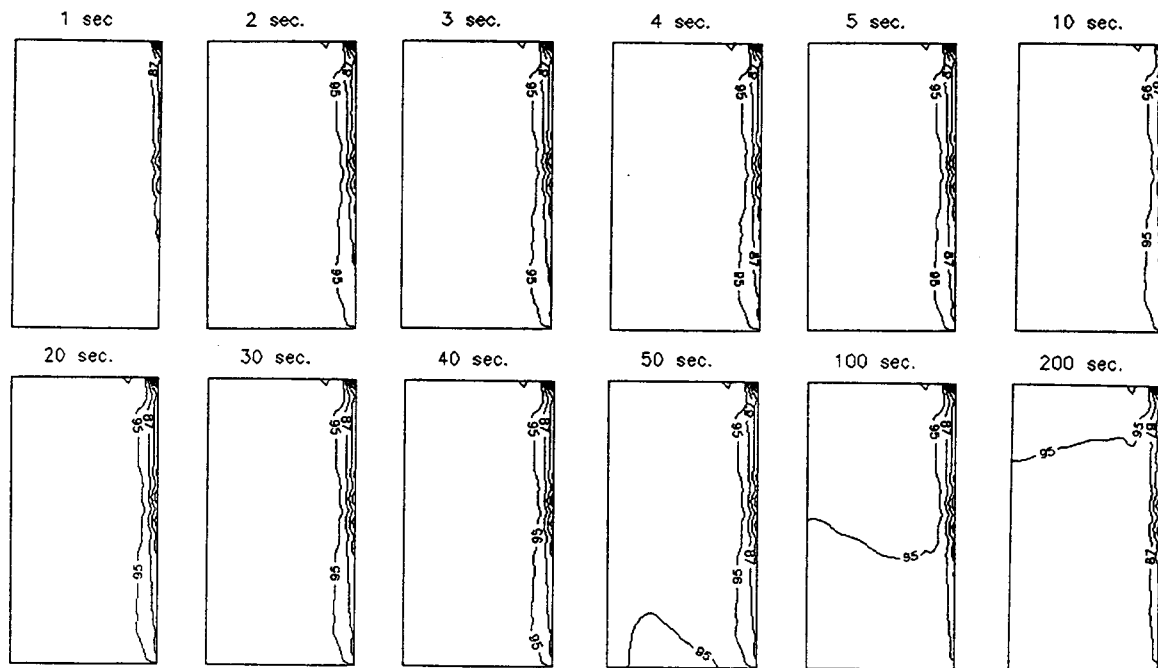


Figure 3.6 Streamlines and isotherms for cases of open thermosyphons, A7 and A8, with AR = 100 and 200 at 1000 s. Note that the scale of these plots has been adjusted for ease in viewing.

When the fluid, initially at 96 C, was suddenly exposed to a cooler boundary as depicted in figure 2.1, a ring-vortex is evident at the closed-end of the tube at the 1-second plot indicated in figure 3.7. The corresponding vertical velocity profile near the wall in figure 3.8 shows that the fluid midway between the top and bottom of the tube, which is cooler, is more sensitive than the fluid at the tube opening. As time proceeds, this ring-vortex continues to grow causing the fluid in the tube to interchange with fluid in the reservoir as shown from the streamline plots from 2 seconds to 40 seconds in figure 3.7. Although



Streamlines



Isotherms

Figure 3.7 Streamlines and isotherms at selected times for the case A2 with $AR = 2$

the streamline patterns continue to change, the representation at 1000 seconds, in figure 3.4, was selected to represent a steady-state solution for this case. A core region, where fluid is almost motionless, is formed between the center stream and the boundary-layer. Both the vertical velocity and temperature profiles, shown in figure 3.8, change little after 200 seconds.

Another result of interest is the oscillatory nature of streamlines and isotherms in the tube. Such behavior is shown in figure 3.9 for the case with $AR = 100$. Due to the high aspect ratio, a weak vortex-ring forms at the tube closed-end. At still smaller radii, the fluid becomes nearly stationary at the closed-end as shown in figure 3.6 for $AR = 200$. Streamlines and isotherms for $AR = 100$, in figure 3.9, at 10 seconds, 60 seconds and 110 seconds are almost identical with variable behavior during the intervening times. The fluid motion is thus seen to be oscillatory with a period of approximately 50 seconds. This oscillatory behavior can also be seen in figure 3.11 where the time sequences for Nu and h are plotted up to 1000 seconds. Unlike the cases with large AR , both the momentum and temperature boundary-layers are sufficiently large that they fill the small-radius tube. This case is shown in figure 3.10 where one cycle of oscillatory behavior is shown from 90 to 120 seconds. Additionally, no core region is apparent in the tube for high AR values.

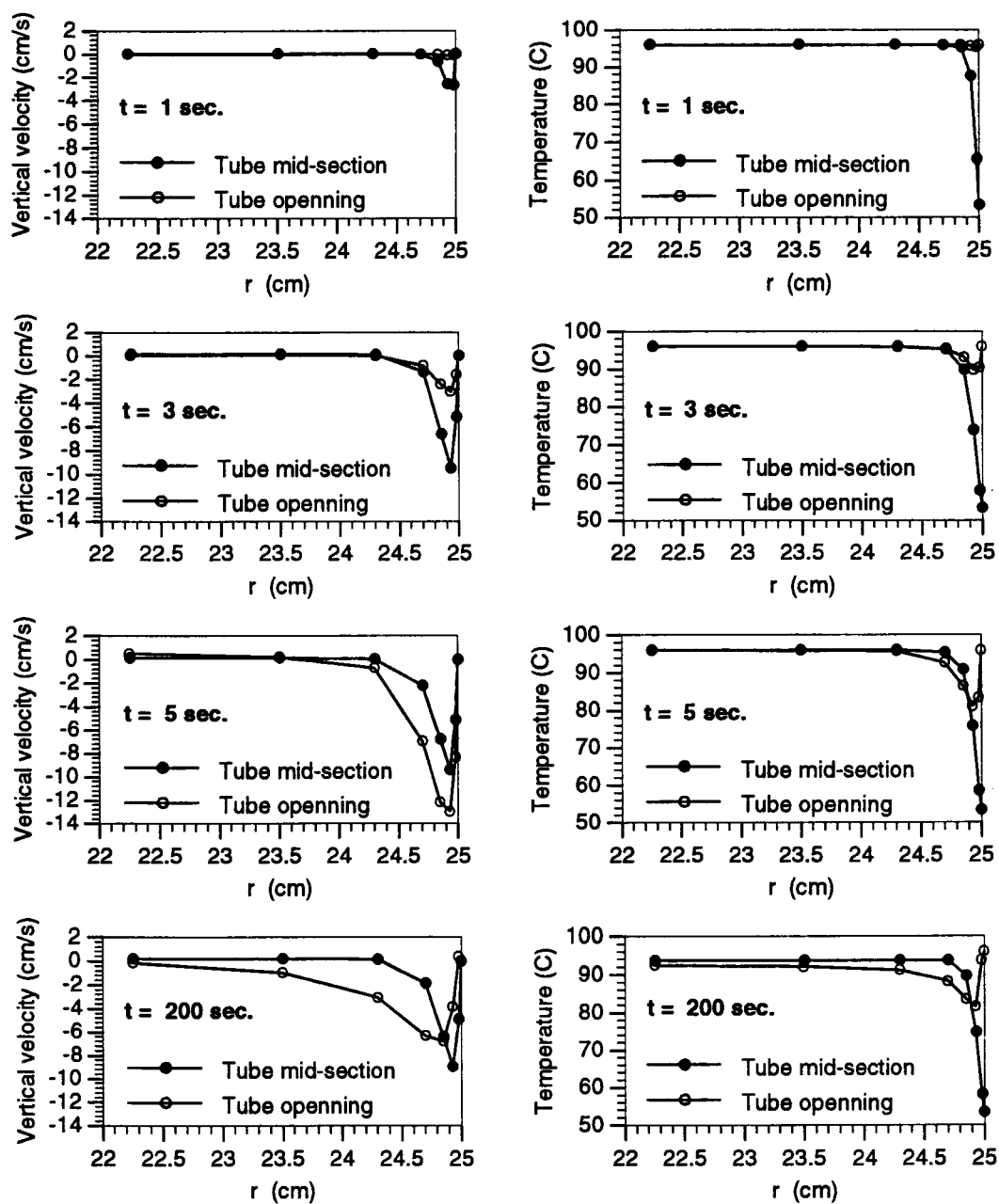


Figure 3.8 Vertical velocity and temperature profiles near the tube wall for the case with $AR = 2$

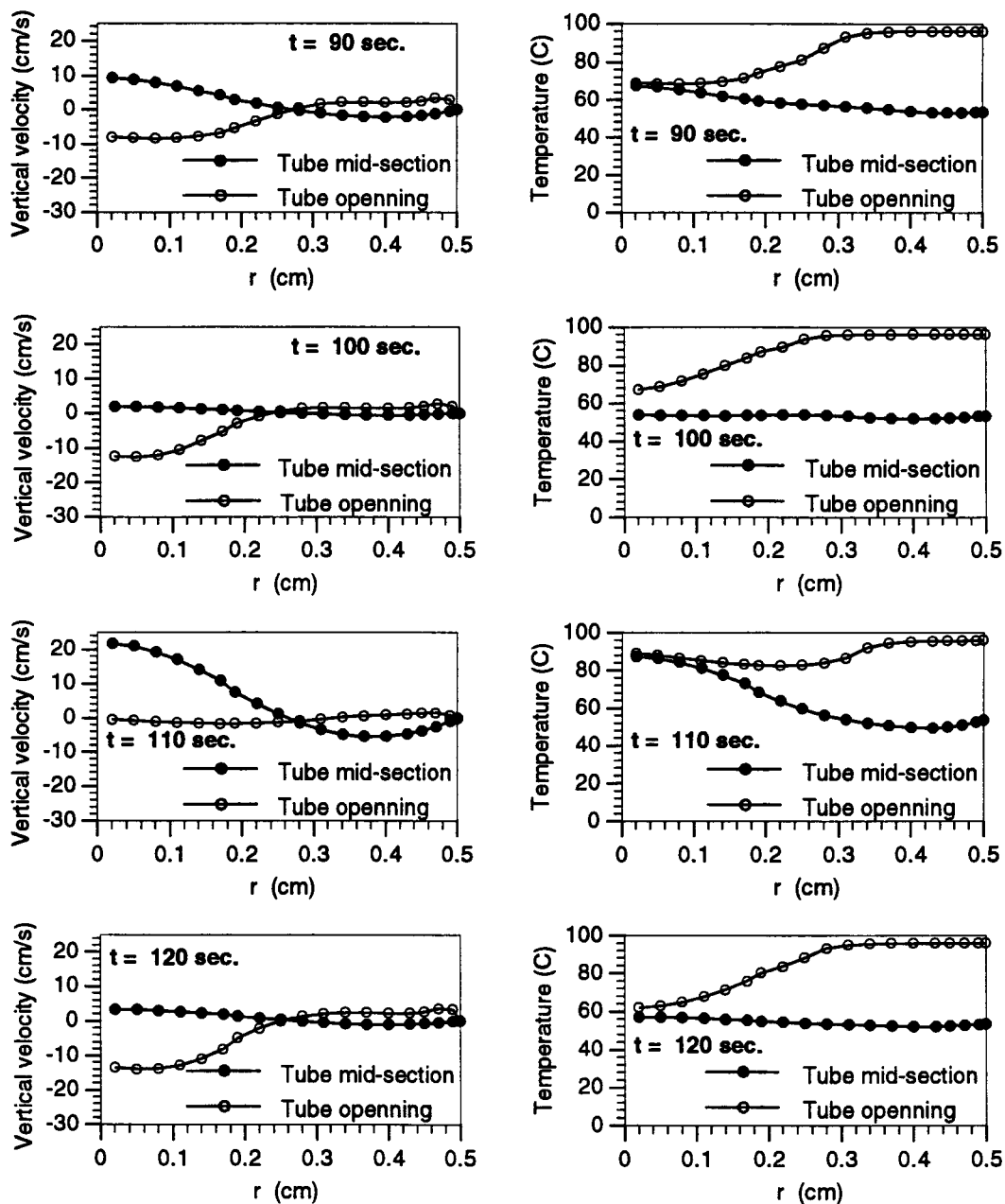


Figure 3.10 Vertical velocity and temperature profiles for the case with $AR = 100$

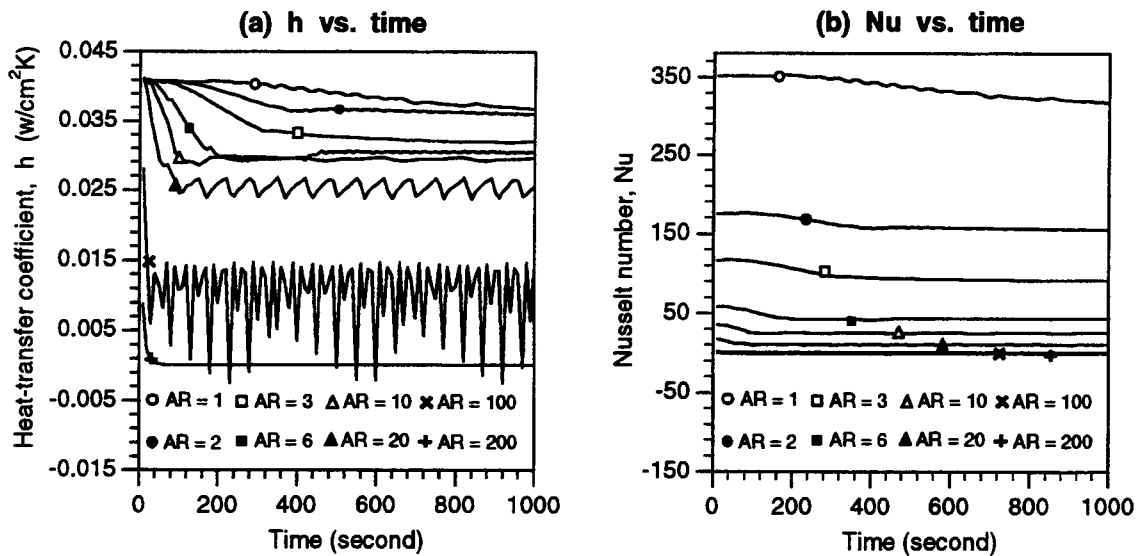


Figure 3.11 Heat transfer coefficient histories and Nusselt number histories for cases A1-A8

Oscillatory behavior of fluid motion for natural convection in enclosures is closely related to boundary-layer instability. The flow behavior shown in figure 3.11 is analogous to the results reported by Paolucci and Chenoweth [22], related to a square cavity. Their numerical and experimental studies indicated that the time-dependent instability was due to the boundary-layer along the vertical walls, or the internal waves caused by a hydraulic jump near the corners [22-23].

Figure 3.11(a) shows a large fluctuating amplitude for case A7, $AR = 100$. As a matter of fact, this large

fluctuating amplitude is particularly evident for the cases of open thermosyphons with $R = 0.5$ cm. Figure 3.12 shows the relatively large fluctuating behavior of the time history of h_t for all cases of type A open thermosyphons with $R = 0.5$ cm and their neighboring cases with $R = 2.5$ cm and $R = 0.05$ cm.

Results for these selected 8 cases show that, for a cooled tube with one end open to a reservoir, the rate of heat-transfer through the wall varies significantly with the tube radius for high AR tubes, where boundary-layer thicknesses are of similar magnitudes to the tube radii. For low AR tubes, boundary-layer thicknesses are relatively small compared with the tube radii and a core region appears between the tube center and the boundary layers. The heat-transfer rate is nearly constant for these cases.

Flow behavior in the tube was observed to be well characterized by the three flow regimes defined by Lighthill [11], these being determined by the tube aspect ratio. In certain cases, fluid motion appears to reach an oscillatory condition at long times. As predicted by Ostrach [10], fluid near the closed-end of the tube becomes stagnant and no longer transfers heat at large values of AR. The similarity regime is associated with the highest heat transfer rates between the tube and reservoir.

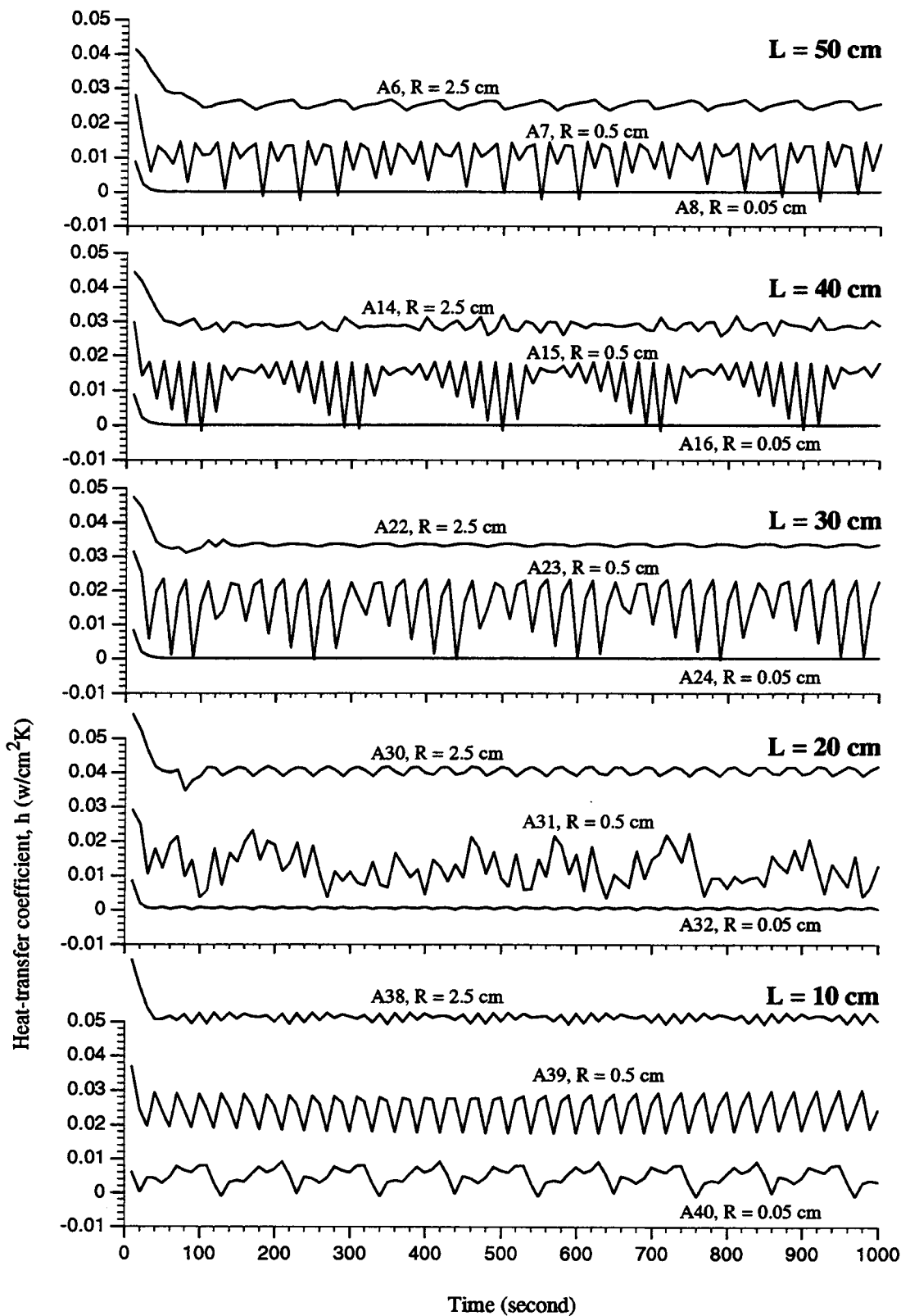


Figure 3.12 Heat transfer coefficient histories for cases of open thermosyphons with $R = 0.5$ cm and their neighboring cases with $R = 2.5$ cm and $R = 0.05$ cm

3.4 TYPE B OPEN THERMOSYPHONS WITH FIXED TUBE RADIUS

This section includes a detailed examination of open thermosyphons with type B thermal boundary conditions and a fixed radius of $R = 5$ cm. From table 3.1, these cases are designated B5, B13, B21, B29, and B37. The corresponding tube lengths are 50 cm, 40 cm, 30 cm, 20 cm, and 10 cm, and the aspect ratios are 10, 8, 6, 4, and 2 respectively. To show the flow regimes, 7 cases, B2, B7, B8, B33, B34, B39 and B40 were also selected to provide additional information for this type of thermal boundary condition.

Figure 3.13 shows the streamlines and isotherms at 1000 seconds for the selected cases with $R = 5$ cm. Due to the relatively large radius, all 5 cases fall into the first flow regime category defined by Lighthill [11]: Flow with the laminar boundary layer not filling the tube. It is relatively easy to locate the momentum and thermal boundary layers in this figure. Another observation that can be made from this figure is that the momentum boundary layer thickness and the strength of the boundary-layer flow both increase as the tube length increases. This observation is confirmed by figure 3.14(a). At the tube opening, due to interaction with the reservoir, both the velocity and the boundary layer thickness decreased. No direct comparisons can be made regarding the flow for these selected cases due to significant inflow and outflow at the tube opening. The temperature profiles shown in figure 3.14(b) provide distinguishable thermal boundary-layer

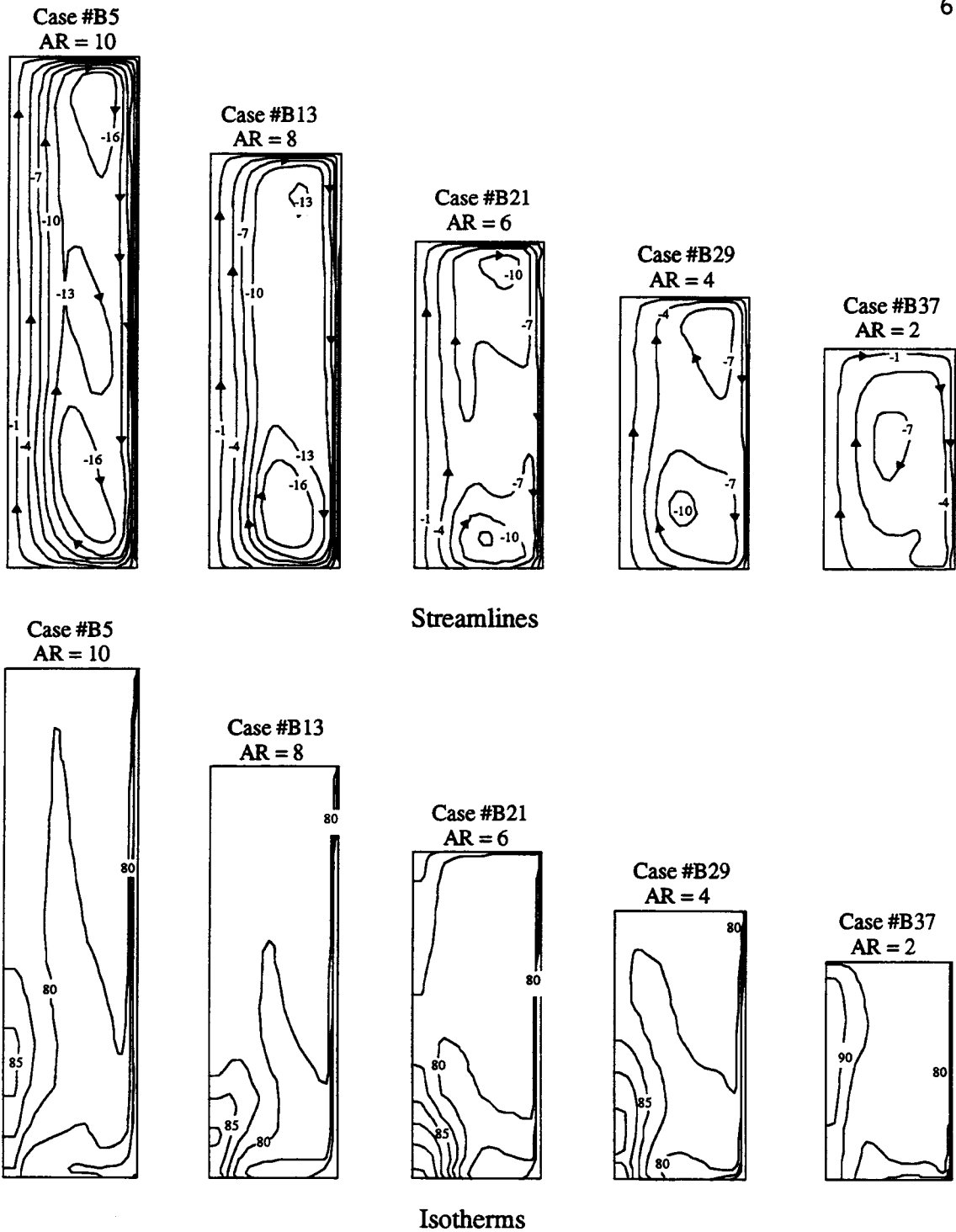
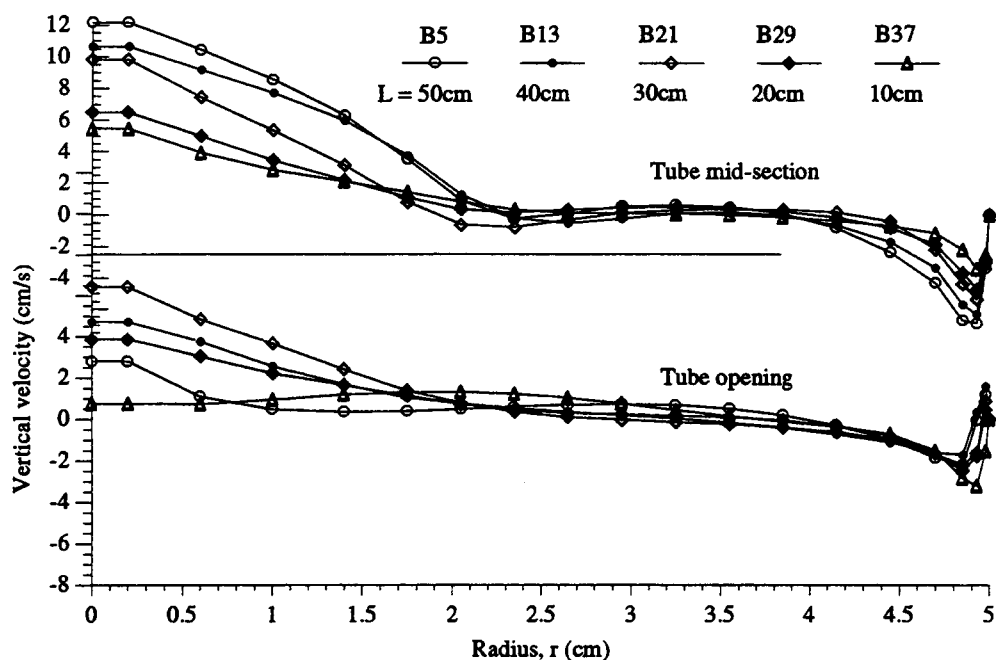
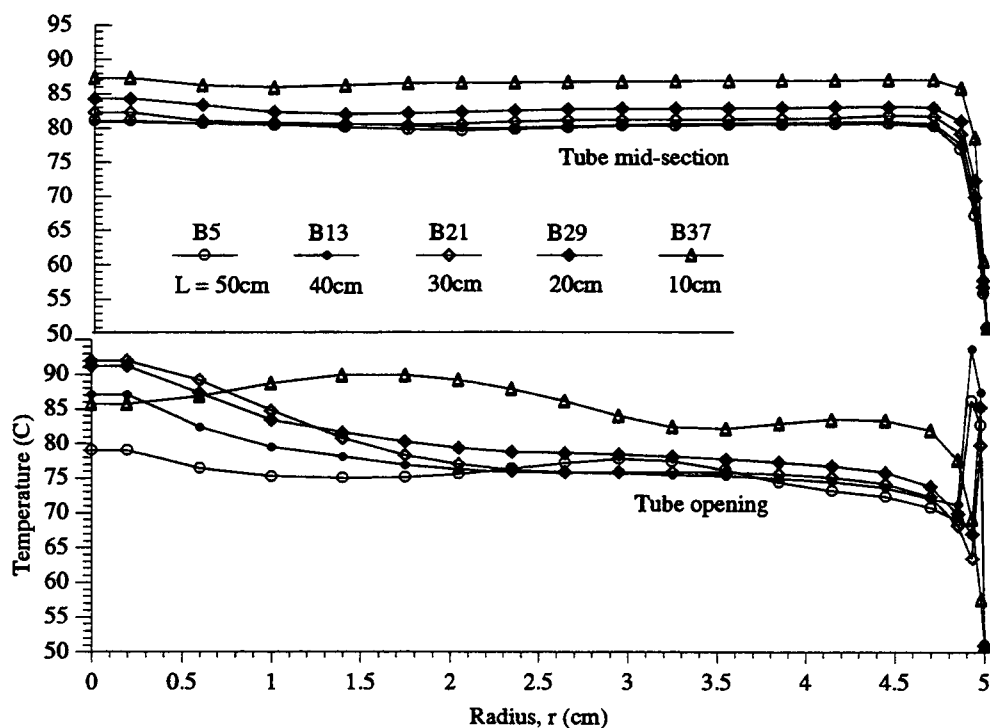


Figure 3.13 Streamlines and isotherms for cases of open thermosyphons with $R = 5$ cm at 1000 s for $AR = 2, 4, 6, 8,$ and 10 . Note that the scale of the plots for the case with $AR = 2$ is accurate. Scale of the plots for other cases has been adjusted for ease in viewing.



(a) Vertical velocity profiles at the tube mid-section and at the tube opening



(b) Temperature profiles at the tube mid section and at the tube opening

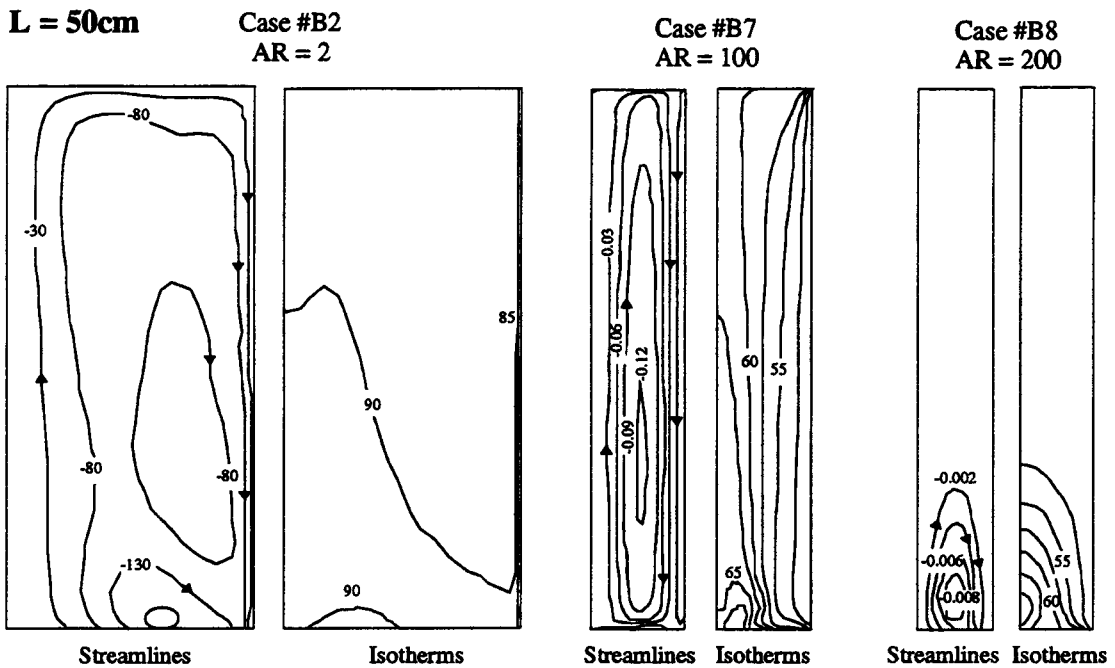
Figure 3.14 Plots of vertical velocity and temperature profiles for selected cases of open thermosyphons with fixed radius, $R = 5\text{cm}$

thicknesses for these 5 cases. At the tube mid-section, cases with shorter tube lengths demonstrate generally higher temperatures than do those with longer tube lengths. At the tube opening, the same argument applies, but the temperature profiles are much more irregular due to flow interchange between the tube and the reservoir.

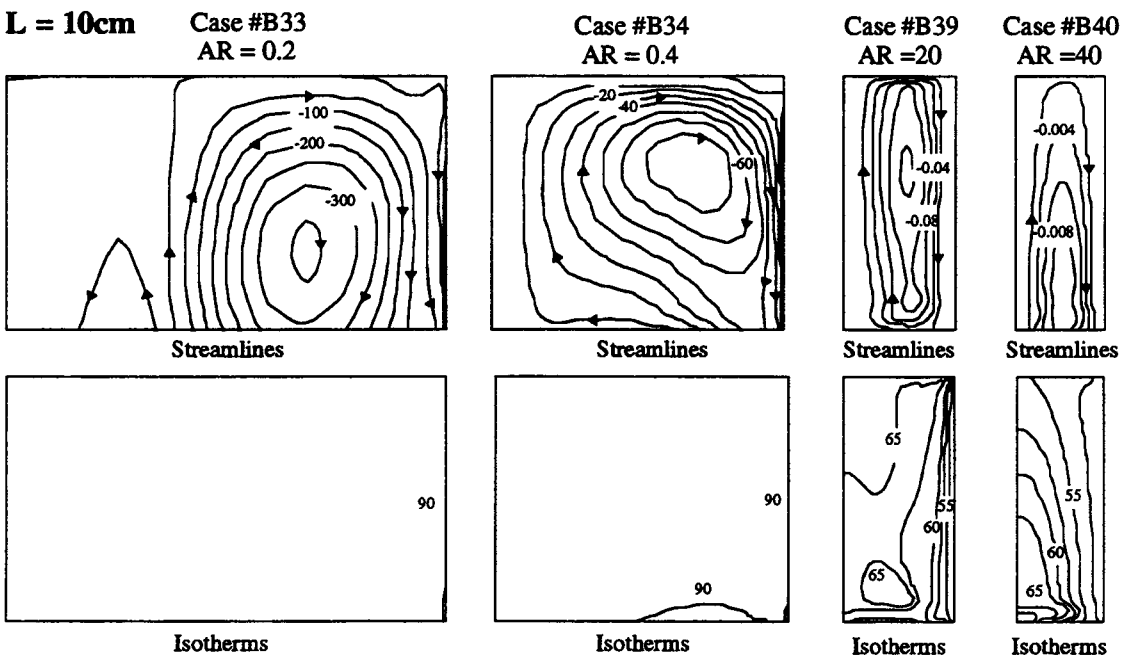
Other flow regimes, defined by Lighthill [11], were examined in cases B2, B7, B8, B33, B34, B39 and B40. Figure 3.15 shows plots of streamlines and isotherms at 1000 seconds for these cases. Even with different thermal boundary conditions, the three cases designated B2, B7 and B8, show the three flow regimes as discussed in section 3.3. One distinguishing difference between the behavior for type A and type B thermal boundaries is the appearance of isotherms at very high aspect-ratios, cases A8 and B8, where the fluid was linearly stratified for case A8, and the fluid was at a constant temperature except at the tube opening for case B8.

For cases with short tube lengths, $L = 10$ cm, shown in figure 3.15, only two types of flow regimes are indicated. The third flow regime, which generally requires a very high aspect ratio, was not present in these cases. These cases demonstrate the greatest heat transfer rates as shown in figure 3.2.

The histories of h and Nu of these selected cases with type B thermal boundary are plotted in figure 3.16. Similar to the cases with type A thermal boundaries, the



(a)



(b)

Figure 3.15 Streamlines and isotherms for selected cases of open thermosyphons at 1000 s; (a) Cases with $L = 50$ cm and $AR = 2, 100$ and 200 (b) Cases with $L = 10$ cm and $AR = 0.2, 0.4, 20,$ and 40

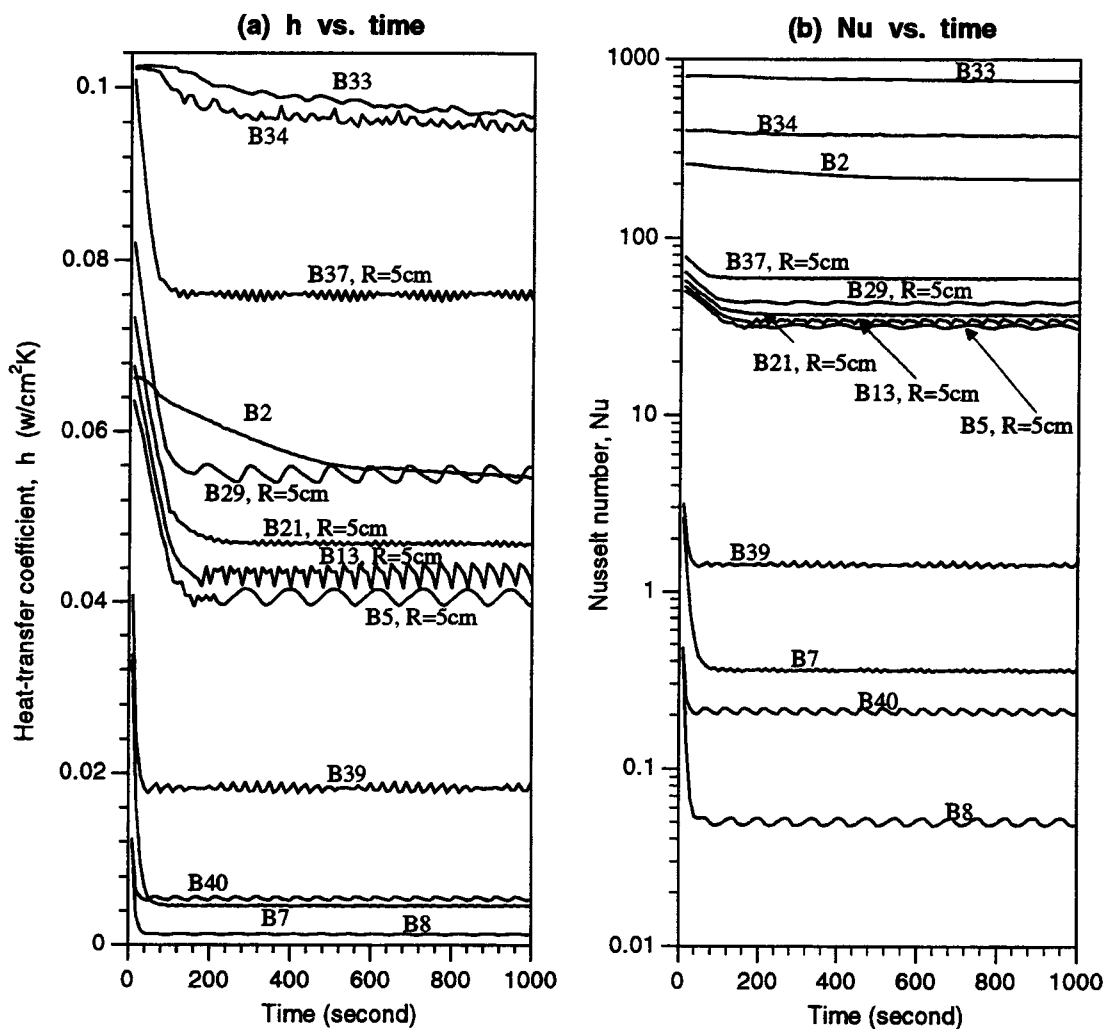


Figure 3.16 Heat transfer coefficient histories and Nusselt number histories for selected cases with type B thermal boundaries

plots of h and Nu for type B cases also show oscillating behavior.

Flow behavior and heat transfer rates of open thermosyphons with type B thermal boundaries are similar to the those with type A thermal boundaries. Both types show three flow regimes which are related to the radius and the

aspect ratio of the vertical tube. Oscillating flow behavior has been found to occur for both cases. One difference between these two situations is that the heat transfer rates for type B conditions are somewhat higher since the tube-wall temperature near the tube opening is much lower.

For the 5 cases examined with fixed tube radii and with type B thermal boundaries, shorter tubes were associated with higher heat transfer rates. Boundary-layer flow increased as the tube length increased. This is the same general trend as boundary flow over a two-dimensional flat plate.

3.5 RESULTS FOR RECTANGULAR OPEN THERMOSYPHONS

A modified open thermosyphon with rectangular geometry was selected for verifying the experimental results presented in chapter 5. This section provides a brief description of the numerical results for this case.

The rectangular open thermosyphon, examined in this study, was considered to be two-dimensional. Variations in the third dimension was neglected. Figure 3.17 shows the schematic of the open cavity.

Unlike the open thermosyphon cases described in previous sections, the open cavity in this study was situated below the reservoir to agree with the setup of the

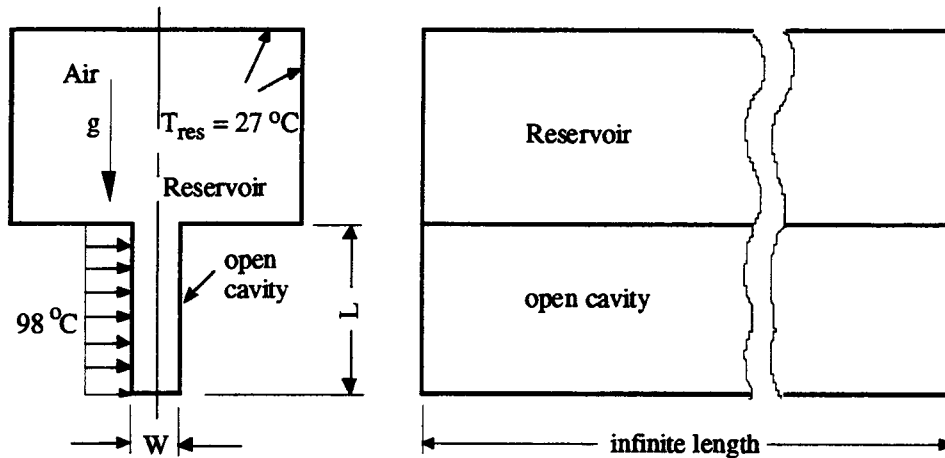


Figure 3.17 Modified rectangular open thermosyphons

experimental setup. Air was used as the working fluid in this case. The cavity wall was set at 98 °C, and the reservoir wall at 27 °C. The third dimension was assumed to be infinitely long so that a two-dimensional numerical model applied.

Plots of streamlines and isotherms for several cases of this geometry were developed. Figure 3.18 and 3.19 show streamlines and isotherms for the case of an open cavity, with $W = 1.5''$ and $L = 3''$, at various times from the start of the process.

The streamline plots in figure 3.18 show two symmetric vortices in the cavity. Air enters the cavity at the center and flow out to the reservoir from both sides of the cavity. Oscillating flow behavior inside the cavity can be observed. The strength of the flow as well as the

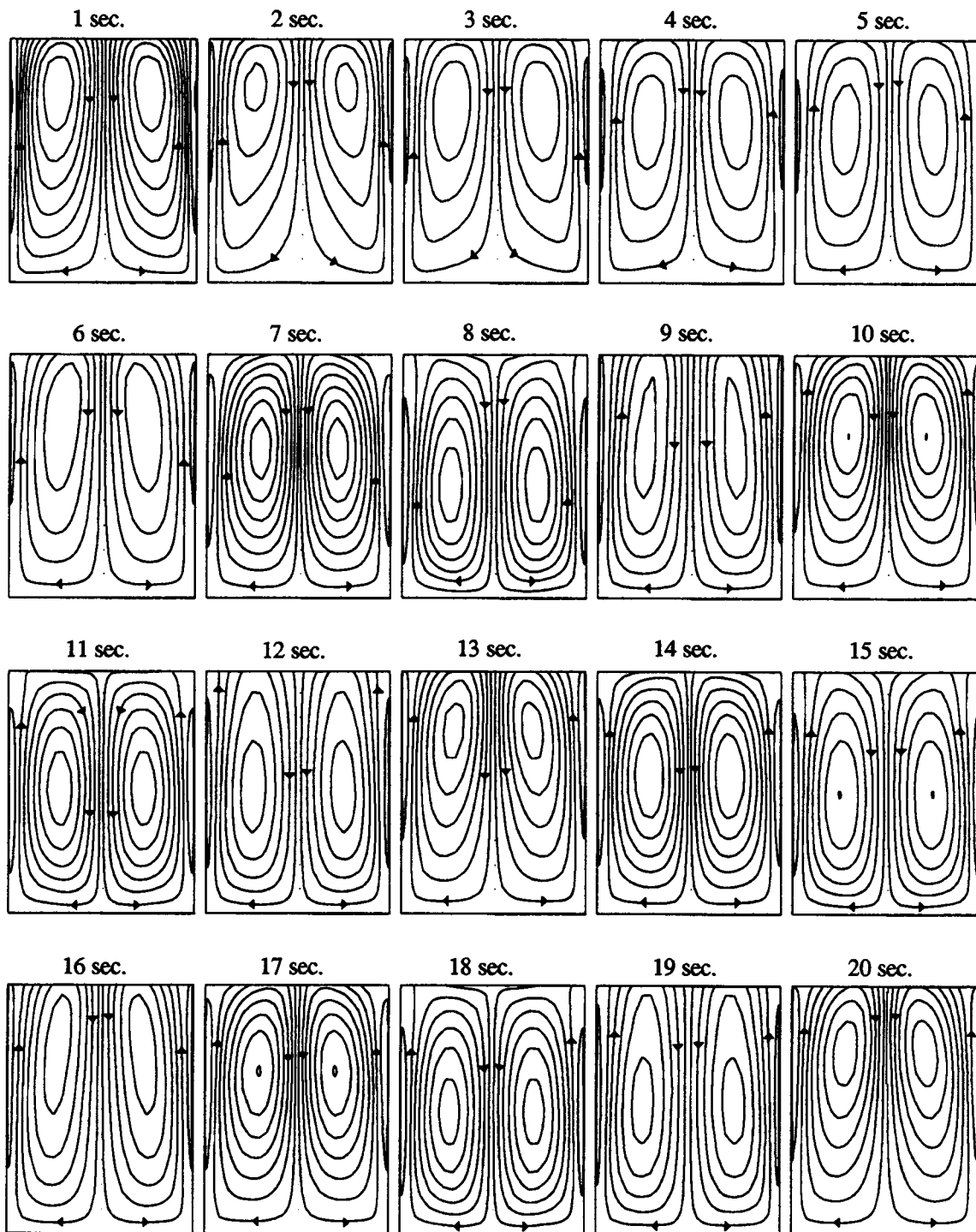


Figure 3.18 Plots of streamlines for the modified rectangular open cavity with $L = 7.62$ cm and $W = 3.81$ cm at different times

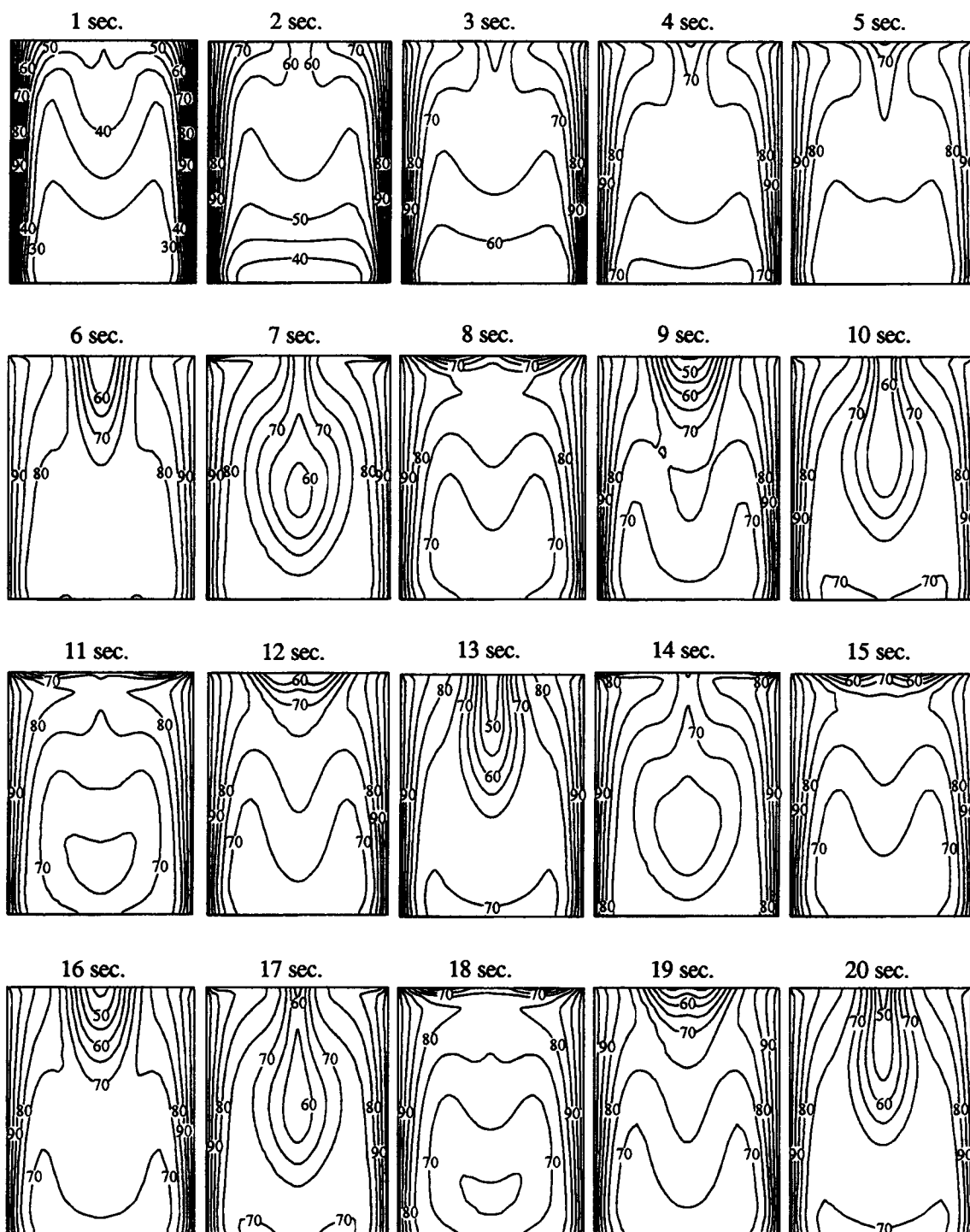


Figure 3.19 Plots of isotherms for the modified rectangular open cavity with $L = 7.62$ cm and $W = 3.81$ cm at different times

locations of the two vortices also oscillate as the plots show. The flow behavior reached what appears to be an oscillatory steady state at 7 seconds with a period of about 3 seconds. Streamlines patterns at 7, 10, 13, 17, and 20 second appear to be identical. Oscillating behavior is also observable from the plots of isotherms in figure 3.19. Initially, the rate of heat transfer through the vertical wall of the open cavity was large as shown for 1 second. As the time progressed, cold air was introduced down the center of the cavity, and was subsequently heated. As the cavity filled with hotter air as shown at 5 and 6 seconds, the strength of the flow increased resulting in more rapid expulsion of the hot air out of the cavity into the reservoir. As a result, colder air was drawn in more vigorously along the center, and the cycle of oscillation was repeated.

Figure 3.20 shows the plots of streamlines and isotherms for the case of an open cavity with $W = 2.54$ cm and $L = 2.54$ cm. The same scenario was ensued as for the case of the open cavity previously described. Plots of streamlines show two symmetric vortices in the cavity, and the flow behavior was oscillatory. The amplitude of oscillation was much smaller in this case. Plots of streamlines and isotherms are shown only up to 5 seconds. At this time, the flow had reached an oscillating steady-state behavior.

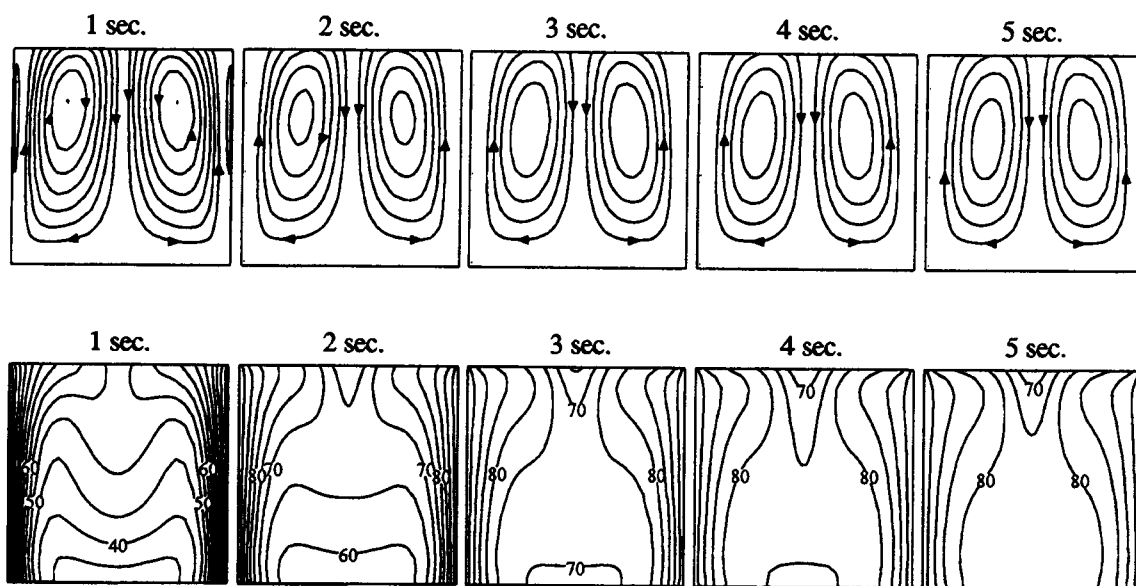


Figure 3.20 Plots of streamlines for the case of open cavity with $L = 2.54$ cm and $W = 2.54$ cm at different times

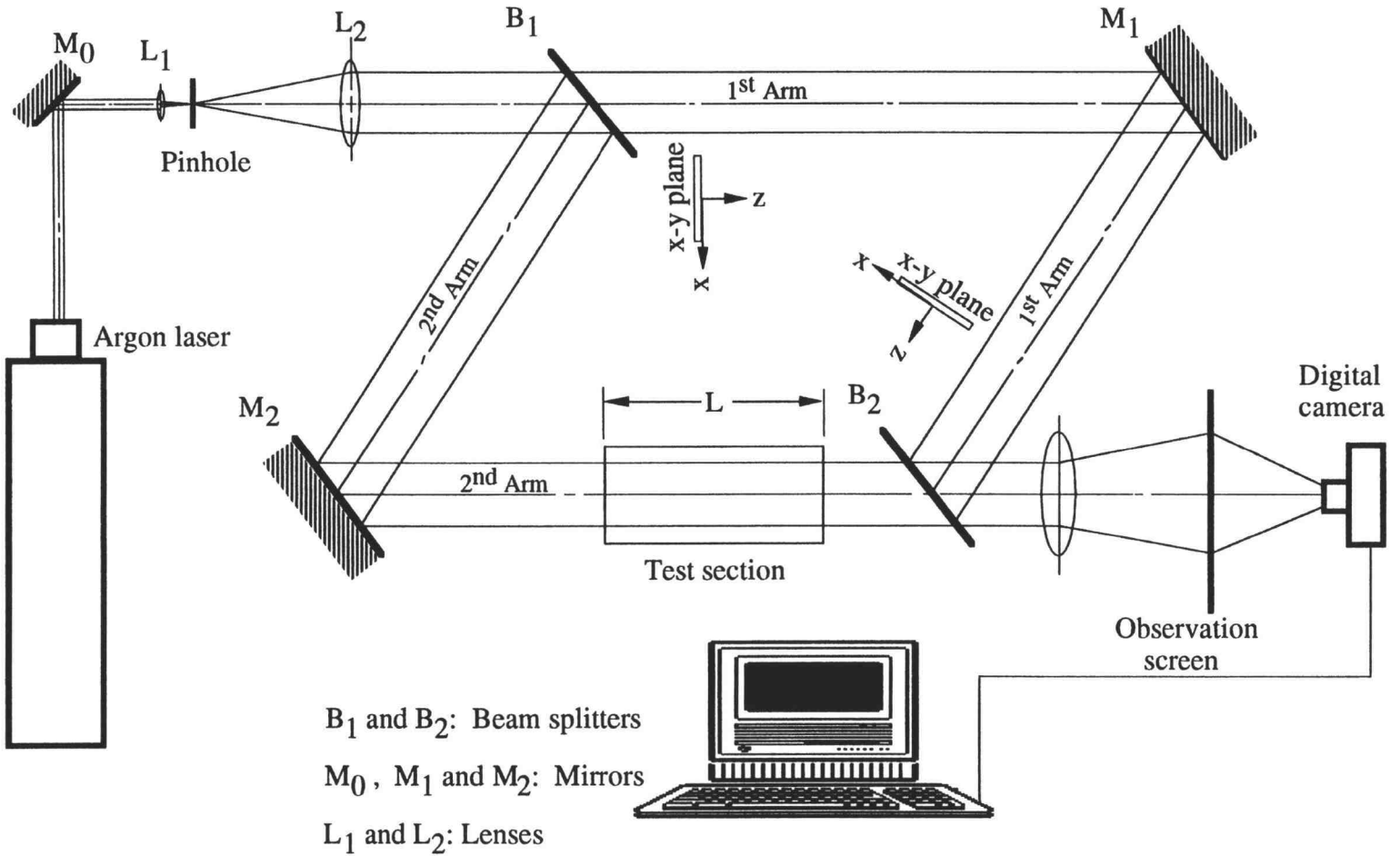
Other cases of an open cavity were also selected for numerical computation. These selected cases were used for the comparison with the experimental results to be discussed in chapter 5. More discussions of the rate of heat transfer and the fringe patterns of the temperature field will be presented in the next section.

IV. EXPERIMENTAL SETUP AND INTERFERENCE FRINGES

An experimental program was undertaken to examine the temperature field for the open thermosyphon problem. The instrument used in this experiment was an amplitude-division Mach-Zehnder (MZ) interferometer.

Figure 4.1 shows the schematic of the MZ interferometer used in this study. An argon laser was used to provide a coherent light source with a wavelength of 514.5 nm. This light source was guided by a mirror, M_0 , passing through a spatial filter, consisting of a lens and a pinhole, and then was collimated by lens L_2 . The collimated light is essential for the interferometer to provide a plane wave for the experiment. This plane wave light source was then divided into two beams by the first beam splitter, B_1 , of the interferometer. One beam served as a reference which was reflected by the first mirror, M_1 , and by the second beam splitter, B_2 , to form the first arm of the interferometer. The other beam was reflected by the second mirror, M_2 , and passed through the second beam splitter, B_2 , to form the second arm of the interferometer where the test section was placed. Fringes of interference between these two beams could be seen by placing an observation screen at the end of the two arms. The observation screen used in this study consisted two glass pieces with a semi-transparent paper placed in between. A

Figure 4.1 Schematic of Mach-Zehnder interferometer for the experiment



picture of the interference pattern, formed at the observation screen, was taken using a CCD digital camera with 496 x 375 pixels. The picture was digitized and then stored in a computer.

Coordinates used for the interferometer must be shifted according to the propagation direction of the light wave as shown in figure 4.1. The axis parallel to the direction of propagation is the z -axis. Any plane on the path normal to the direction of propagation is the x - y plane where the y -axis is normal to the paper.

A computer program in C language was developed to help in aligning the MZ interferometer. This program generated fringe patterns of two-plane-wave and two-point-source interference which were used as references for adjusting the two beamsplitters and two mirrors of the interferometer.

Fringe patterns were numerically generated by incorporating the numerical solution from chapter 3 with the Lorentz-Lorenz equation, which relates the temperature of a medium to the refractive index. An interpolating technique was used to improve the image quality of the numerically-generated fringes. These fringe patterns were then used for comparisons with the experimental results in chapter 5.

4.1 THEORY OF PLANE WAVE INTERFERENCE

An electric field of a simple plane wave linearly polarized in one direction can be mathematically described as

$$E = A \cos(\omega t - \mathbf{k} \cdot \mathbf{r}) \quad (4.1)$$

where A is the constant amplitude of the plane wave, \mathbf{k} is the propagation vector, and \mathbf{r} is the position vector.

Considering the wavefront of the plane wave to be perpendicular to the direction of propagation, the two plane waves divided by the first beam splitter, B_1 , can be described as follows:

$$E_1 = A_1 \cos(\omega t - k_z z_1) \quad (4.2)$$

$$E_2 = A_2 \cos(\omega t - k_z z_2) \quad (4.3)$$

where, k_z is the wave number in the direction of propagation, and z_1 and z_2 are the distances measured in the propagation direction from the light source to the point of observation through each arm.

These two plane waves, separated by B_1 , traveled along different paths, and were then recombined at the output of the interferometer. The electric field at the output of the interferometer was obtained using the superposition of E_1 and E_2 . Hecht [24] and Meyer-Arendt [25] listed several methods to derive the resultant wave for the superposition of E_1 and E_2 . Among them, the easiest method is to use

complex numbers. Expressing E_1 and E_2 in the complex plane, Eqs.(4.2) and (4.3) can be written as

$$E_1 = A_1 e^{i(\omega t - k_z z_1)} \quad (4.4)$$

$$E_2 = A_2 e^{i(\omega t - k_z z_2)} \quad (4.5)$$

Superposition of the two plane waves, E_1 and E_2 , gives

$$E_T = E_1 + E_2 = e^{i\omega t} (A_1 e^{-ik_z z_1} + A_2 e^{-ik_z z_2}) \quad (4.6)$$

The time-averaged value of E_T is the quantity which is observed on the screen; it is known as the irradiance, or intensity, I . Mathematically, in the complex plane, irradiance is proportional to the electric field, E_T , multiplied by its complex conjugate

$$\begin{aligned} I \propto \langle E_T E_T^* \rangle &= e^{i\omega t} (A_1 e^{-ik_z z_1} + A_2 e^{-ik_z z_2}) \cdot e^{-i\omega t} (A_1 e^{ik_z z_1} + A_2 e^{ik_z z_2}) \\ &= A_1^2 + A_2^2 + A_1 A_2 \left[e^{ik_z(z_1 - z_2)} + e^{-ik_z(z_1 - z_2)} \right] \\ &= A_1^2 + A_2^2 + 2A_1 A_2 \cos(k_z(z_1 - z_2)) \\ &= A_1^2 + A_2^2 + 2A_1 A_2 \cos\left(\frac{2\pi}{\lambda}(z_1 - z_2)\right) \end{aligned} \quad (4.7)$$

where the wave number, k_z , is expressed in terms of the wavelength, $2\pi/\lambda$, of the plane wave. If the two beamsplitters shown in figure 4.1 both reflect and transmit half of the incident light, the amplitudes A_1 and A_2 will

be the same. Thus, the maximum irradiance will be four times the square of the amplitude A_1 , or A_2 , if the two waves are in phase. The irradiance will be at its minimum value of zero if the waves are out of phase by 180 degrees. In other words, the formation of the fringe pattern depends on the optical path difference z_1 and z_2 in Eq.(4.7).

Figure 4.2 shows the interference of two light rays, A and B. The electric fields of ray A from both arms are in phase. The superposition of these two electric fields, $A_{\text{arm}1}$ and $A_{\text{arm}2}$, forms constructive interference. Thus, the cosine term in Eq.(4.7) is 1, i.e. a bright spot on the observation screen. In contrast, the superposition of $B_{\text{arm}1}$ and $B_{\text{arm}2}$ is destructive. The cosine term in Eq.(4.7) is 0. Thus, the irradiance caused by ray B is zero on the screen.

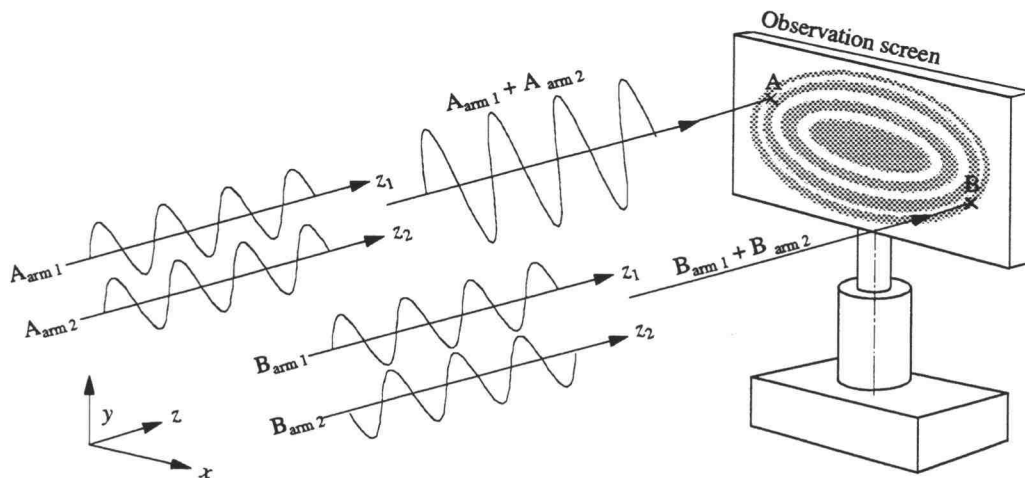


Figure 4.2 Interference of two light rays

4.2 OPTICAL PATH DIFFERENCE AND FRINGE PATTERNS

The refractive index, n , is used to indicate the speed of light in a given medium. The optical path length is determined by the refractive index, n , of the medium multiplied by the distance traveled by the light ray.

In figure 4.1, the distance measured from the source to the point of observation through the first arm in the direction of propagation along the centerline is z_1 ; and the distance through the second arm is z_2 . The optical path lengths of these two light rays are therefore $n_r z_1$ and $n_r z_2$. The refractive index, n_r , is that of undisturbed air without the presence of the test section. Assuming the refractive index of the undisturbed air to be unity, the optical path difference, *OPD*, of the two rays is then $(z_1 - z_2)$.

For other light rays in the x - y plane parallel to the z -axis in the absence of the test section, two fields, of optical path lengths z_1 and z_2 , through each arm can be expressed as $z_1(x_i, y_j)$ and $z_2(x_i, y_j)$. If the interferometer is perfectly aligned, $z_1(x_i, y_j) - z_2(x_i, y_j)$ will equal a constant, i.e. the interference pattern will be evenly distributed on the screen. If one optical element is slightly tilted in the x - and/or y -direction, $z_1(x_i, y_j) - z_2(x_i, y_j)$ will be a function of x and/or y , i.e. lines of bright and dark fringes will be formed on the screen. An infinite fringe field is the term used for $z_1(x_i, y_j) - z_2(x_i, y_j)$ equal to a

constant, and a wedge fringe field is the designation when $z_1(x_i, y_j) - z_2(x_i, y_j)$ is a function of x , y , or both.

To detect the temperature contour lines for a certain medium, a test section with a length, L , was placed on one arm of the interferometer. In this case, it was placed in the path of the second arm. Light will also travel at different speeds in a medium with variable density. Assuming the refractive index, $n(x_i, y_j)$, of the medium in the test section to vary in the x - and y -directions only, the field of the optical path lengths of light rays traveling through the test section can be expressed as $n(x_i, y_j)$ times L . With the test section present, the optical path difference, $OPD(x_i, y_j)$, for the field of the two beams can be expressed as

$$OPD(x_i, y_j) = z_1(x_i, y_j) - z_2(x_i, y_j) - L \cdot n_r(x_i, y_j) + L \cdot n(x_i, y_j) \quad (4.8)$$

where, $n_r(x_i, y_j)$ is the refractive index field of the medium replaced by the test section, which is undisturbed air for this case. The value of $n_r(x_i, y_j)$ was thus assumed to be 1.

If an infinite fringe field were used, the optical path difference would equal a constant plus $L \cdot n(x_i, y_j)$. Since the constant would not affect the fringe pattern, the quantity, $L \cdot n(x_i, y_j)$, would determine the fringe pattern on the observation screen.

If a wedge fringe field is used to detect temperature contours, two frames of fringe patterns need be recorded at

two different times. This is usually referred to as a double-exposure technique. The optical path difference of the two beams at these two times can be expressed as

$$OPD(x_i, y_j) = \left\{ z_1(x_i, y_j) - z_2(x_i, y_j) - L + L \cdot n(x_i, y_j) \right\}_t - \left\{ z_1(x_i, y_j) - z_2(x_i, y_j) - L + L \cdot n(x_i, y_j) \right\}_{t+\Delta t} \quad (4.9)$$

The refractive index field at t is usually uniform, i.e. $L \cdot n(x_i, y_j)$ is constant at t . Thus, the optical path difference of a wedge fringe is also determined by $L \cdot n(x_i, y_j)$ at $t+\Delta t$.

Often, $OPD(x_i, y_j)$ is expressed in terms of the wavelength multiplied by a value which represents the fringe pattern on the observation screen. Hauf and Grigull [26] used such a term, the loci of constant phase difference - $S_k(x_i, y_j)$, to represent the fringe pattern on

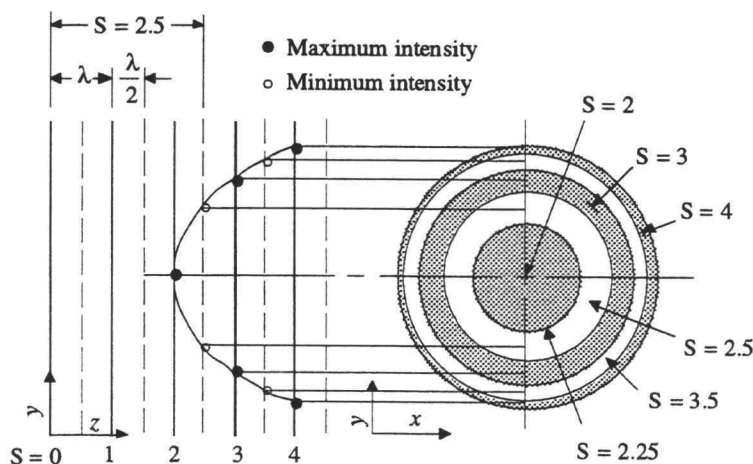


Figure 4.3 Relation between the order of the loci of constant phase difference, S , and the fringe pattern

the screen as shown in figure 4.3. Thus, the optical path difference can be described as:

$$OPD(x_i, y_j) = S_k(x_i, y_j) \cdot \lambda \quad (4.10)$$

The order of the loci of phase differences determines the contour lines of the fringe patterns on the observation screen. Figure 4.3 shows the order of the loci of phase differences, S , of a "bull's eye" fringe pattern. Bull's eye fringes can easily be obtained from a Mach-Zehnder interferometer without the collimating lens, L_2 , and the test section. The maximum intensity at the center of the bull's eye starts at a known temperature of order of $S = 0$. If there is a change in the surrounding air temperature, the center fringe will shift outward. Assuming that the maximum at the center of the bull's eye in figure 4.3 shifts twice, the order of the fringe pattern will be 2 as shown.

From Eqs. (4.8)-(4.10), fringe patterns on the screen related to the refractive index of the test medium can be expressed as:

$$S_k(x_i, y_j) \cdot \lambda = \text{constant} + L \cdot n(x_i, y_j) \quad (4.11)$$

Both S and n are functions of temperature in this expression. Taking derivatives with respect to temperature and integrating from a reference temperature, T_0 , the temperature of order k , T_k , is evaluated as follows

$$\left(\frac{dS}{dT}\right) = \left(\frac{L}{\lambda} \cdot \frac{dn}{dT}\right); \quad S_k(x_i, y_j) = \frac{L}{\lambda} \cdot \frac{dn}{dT} \int_{T_\infty}^{T_k} dT;$$

$$S_k(x_i, y_j) = \frac{L}{\lambda} \cdot \frac{dn}{dT} \cdot \Delta T_k \quad (4.12)$$

To interpret temperature differences from the orders of fringe patterns, $S_k(x_i, y_j)$, the relation between temperature and the refractive index of the test medium must be known.

4.3 RELATION BETWEEN TEMPERATURE AND REFRACTIVE INDEX

The equation relating the refractive index to the state of a substance is the Lorentz-Lorenz equation. The density is related to the refractive index of the substance according to

$$\frac{n^2 - 1}{\rho(n^2 + 2)} = r_s(\lambda) \quad (4.13)$$

where $r_s(\lambda)$ is the specific refractivity. It is a function of the substance and the wavelength of light.

Eq.(4.13) can be further simplified to yield a constant value for the refractive index gradient, dn/dT , for gases. For liquids, however, the relation between n and T is related by an empirical correlation. Vest [27] suggested the following relation for use with water subjected to a light source of 514.5 nm

$$n - 1.337253 = -(2.8767T + 0.14825T^2) \times 10^{-5} \quad (4.14)$$

where, T is in degrees Celsius. This equation is a quadratic fit to the Tilton-Taylor [28] data conducted by Dobbins and Peck [29].

For a gas with refractive index near unity, the Lorentz-Lorenz equation can be simplified to a first order approximation of the form

$$n-1 = \frac{3r_s(\lambda)}{2} \cdot \rho ; \quad n-1 = K\rho \quad (4.15)$$

Eq. (4.15) is the Gladstone-Dale equation. The constant, K , is the Gladstone-Dale constant and it is a property of the gas. Applying the ideal gas equation of state to Eq.(4.15), yields

$$n-1 = \frac{KMP}{RT} \quad (4.16)$$

The gradient of the refractive index for the gas with respect to temperature now becomes

$$\frac{dn}{dT} = \frac{-KMP}{RT^2} \quad (4.17)$$

If the temperature change is small, Eq.(4.17) suggests that the gradient of the refractive index can be treated as a constant. For greater precision in air, Vest [27] suggested using the following equation with a light source at 514.5 nm, based on Radulovic's [30] result

$$n-1 = \frac{0.294036 \times 10^{-3}}{1 + 0.369203 \times 10^{-2} T} \quad (4.18)$$

where, T is in degree Celsius.

Taking the derivative of n with respect to T in Eq.(4.14) and substituting it into Eq.(4.12), for water, the unknown ΔT_k can be expressed as function of the order of S as:

$$\{\Delta T_k\}_{water} = \frac{\lambda}{L} \left(\frac{-10^5}{2.8767 + 0.2965 \cdot T} \right) \cdot S_k(x_i, y_j) \quad (4.19)$$

Performing the same procedure for Eq.(4.18) and Eq.(4.12), for air, ΔT_k becomes

$$\{\Delta T_k\}_{air} = \frac{\lambda}{L} \left(\frac{(1 + 0.369203 \cdot 10^{-2} \cdot T)^2}{1.085590 \cdot 10^{-6}} \right) \cdot S_k(x_i, y_j) \quad (4.20)$$

For small temperature changes, Eqs.(4.19) and (4.20) are used to estimate temperature differences between fringes using a constant reference temperature T . For large temperature changes, the reference temperature must be changed for better accuracy. This can be done by numerically stepping the reference temperature, T , through a small increment, $\Delta T = T_i - T_{i-1}$, in Eq.(4.18) for air, or Eq.(4.14) for water, to obtain two discrete values of the refractive index, n_i , evaluated at T_i , and n_{i-1} at T_{i-1} . The procedure is now to subtract n_{i-1} from n_i to obtain a value for dn/dT , then to substitute this value into Eq.(4.12) to obtain the value of dS/dT . Summing these values for each small increment of ΔT , a relation for the temperature change and the order of fringes can be obtained.

Table 4.1 shows the relation between the temperature changes corresponding to fringe orders for air at $L = 7.62$ cm and 10 cm with a light source of 514.5 nm. A MathCad software application was used to perform the numerical stepping procedures. The increment used for the stepping reference temperature was 0.05 °C.

From table 4.1, it is clear that the temperature differences between sequential fringe orders are not the same. At higher temperatures, the temperature difference for one fringe order are relatively large, and at lower temperatures, the temperature differences are smaller for one fringe order according to Eq.(4.18). The length of the

TABLE 4.1 Temperatures corresponding to orders of fringes in air

L=0.0762m $\lambda=514.5\text{nm}$					L=0.10m $\lambda=514.5\text{nm}$		
k	$27+\Delta T_k$	ΔT_k	$98-\Delta T_k$	ΔT_k	k	$98-\Delta T_k$	ΔT_k
0.5	30.81		92.32		0.5	93.65	
1.0	34.72	7.72	86.81	11.19	1.0	89.48	8.52
1.5	38.73		81.47		1.5	85.28	
2.0	42.84	8.12	76.29	10.52	2.0	81.22	8.26
2.5	47.07		71.25		2.5	77.26	
3.0	51.42	8.58	66.36	9.93	3.0	73.40	7.82
3.5	55.87		61.61		3.5	69.61	
4.0	60.47	9.05	56.99	9.37	4.0	65.90	7.50
4.5	65.19		52.50		4.5	62.28	
5.0	70.04	9.57	48.13	8.86	5.0	58.73	7.17
5.5	75.04		43.87		5.5	55.26	
6.0	80.19	10.15	39.73	8.40	6.0	51.86	6.87
6.5	85.49		35.69		6.5	48.53	
7.0	90.95	10.76	31.76	7.97	7.0	45.28	6.58
7.5	96.56		27.93		7.5	42.07	
8.0	102.40	11.45	24.19	7.57	8.0	38.95	6.33
8.5	108.40		20.54		8.5	35.88	
9.0	114.60	12.20	16.99	7.20	9.0	32.86	6.09
9.5	121.00		13.52		9.5	29.92	
10	127.70	13.10	10.10	6.89	10	27.00	5.86

test section, L , is also a function of these temperature differences as shown in this table.

4.4 IMAGE PROCESSING

A CCD digital camera was used to capture fringe patterns from the observation screen. For use with an infinite fringe field, the fringe captured by the camera can be interpreted directly from Eq.(4.19) or Eq.(4.20). For use with a wedge-fringe field, i.e. the double-exposure technique, two image frames need be captured and then processed digitally to interpret the fringes.

The camera used in this experiment contained a chip consisting of a two-dimensional array of a charge-coupled device (CCD). This CCD array consisted of 496 x 375 pixels, which are equivalent to 186000 photo sensors. Each pixel captured a certain amount of electrons from the image. The amount of electrons was electronically shifted into a measurable DC voltage and was then converted into an 8-bit digital form. Thus, each pixel served as a 256-level gray scale sensor. Figure 4.4 shows a graphic representation of the CCD array.

From figure 4.4, it is seen that images captured by the digital camera can be mathematically represented by matrices consisting of 496 rows and 375 columns. Elements of the matrix have integer values from 0 to 255.

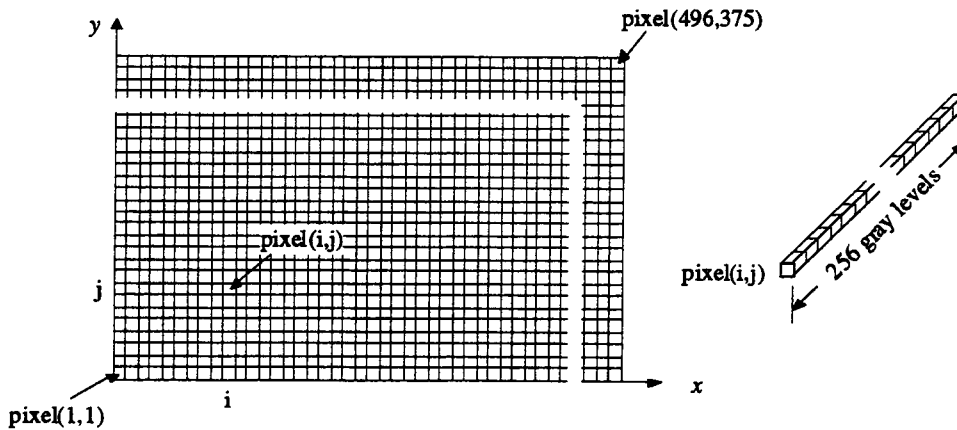


Figure 4.4 Graphic representation of a CCD array

To detect the temperature field using a wedge-fringe field, a reference frame of the image, matrix **A**, must be acquired for a uniform temperature field of the test section. The second frame of the image, matrix **B**, will be of the image with a temperature disturbance in the test section. The real fringe, matrix **C**, related to the temperature disturbance will be the absolute value of the arithmetic difference of the corresponding elements of **A** and **B** as follows.

$$\mathbf{C} = | \mathbf{B} - \mathbf{A} | \quad (4.21)$$

To do this calculation, a simple C-language program was written to deal with the image files of the CCD digital camera. Figure 4.5 shows the fringe pattern of a flame using the wedge-fringe field approach.

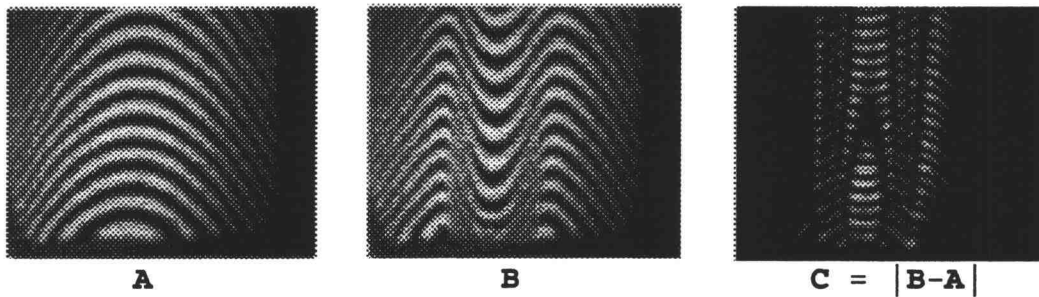


Figure 4.5 Fringe pattern of a flame using the wedge fringe field interference

In addition to the capability of digitizing the image, there are several other advantages using a CCD camera for an experiment. For example there is no need for printing the image and, similar to a Polaroid camera, images can be shown on a computer monitor instantly, without waiting for the film to be developed as with a regular camera. There are, however, also some disadvantages.

The CCD camera used in this experiment was the Logitect FotoMan Plus, which consisted of a non-interchangeable fixed-focus lens and a built-in auto flash. For this particular experiment, a drawback of this CCD camera was the inability to control the shutter speed and the aperture size. Thus, the contrast and, most importantly, the desired resolution of the image could not be achieved as desired.

Other laboratory and commercial digital cameras are available with the desired resolution for this experiment. For example, the Kodak DSC420 digital camera attached to a regular Nikon camera would be suitable for use in this experiment. A short description for this commercial

digital camera can be found [31]. Desirable resolution can be achieved through the control of the shutter speed and the aperture size in the regular Nikon camera. However, the current price of such a unit is very expensive. A detailed comparison among these cameras is described in [32]. To obtain high resolution images in this experiment, a regular camera, with shutter speed and aperture size control, and high sensitive film were used.

4.5 NUMERICALL SIMULATION OF INTERFERENCE PATTERN

To set up the interferometer for use with an infinite fringe field, alignment of the apparatus is critical. The alignment must be very precise and the necessary procedures often become trial-and-error processes. An ideal infinite fringe field will have a uniform intensity distribution on an observation screen. However, even with a slight misalignment of the interferometer, instead of an infinite fringe field pattern, undesirable fringes, such as those shown in figure 4.6 will occur.

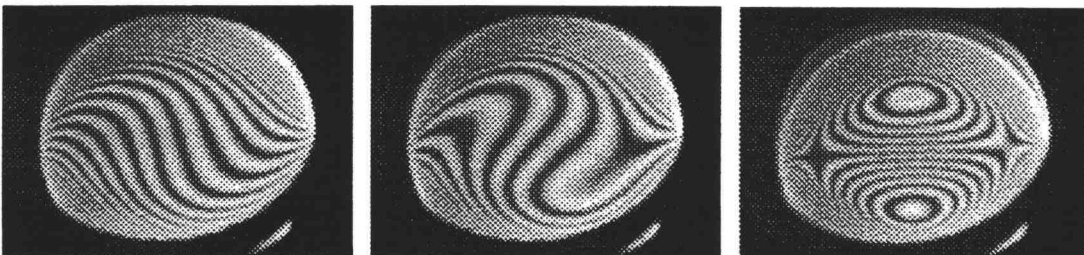


Figure 4.6 Undesirable fringes for the infinite fringe field alignment

To reduce the task of trial and error, a C-language computer program was developed to simulate the interference of two monochromatic light waves. In this code, numerical results are converted into picture-like interference fringes to aid in aligning the optical components. Two major concerns of the apparatus set up are: (1) how the presence of the wedged angles of the beamsplitters affect the plane wave interference fringes, and (2) why fringe patterns shown in figure 4.6 occur often during the alignment procedure.

Plane wave interference with wedged beamsplitters

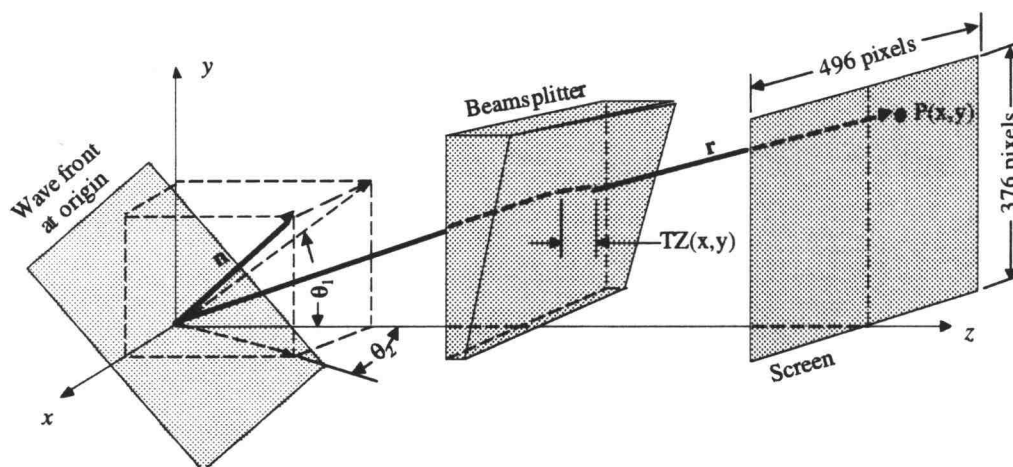


Figure 4.7 Schematic of a plane wave passing through a wedged beamsplitter

A collimated plane wave passing through a wedged beamsplitter is shown in figure 4.7. The electric field of a plane wave, described by Eq.(4.1), is rewritten as

$$E = A \cos(\omega t - \mathbf{k}\mathbf{r} \cdot \mathbf{n}) \quad (4.22)$$

where, k is the wave number, \mathbf{n} is the normal vector of the wavefront and \mathbf{r} is the position vector relative to the screen. Projecting the normal vector using components θ_1 and θ_2 as shown in figure 4.7 and introducing the function $TZ(x,y)$ to describe the thickness of the beamsplitter, the vector multiplication in Eq.(4.22) becomes,

$$\mathbf{r} \cdot \mathbf{n} = x \cdot \cos \theta_1 \sin \theta_2 + y \cdot \cos \theta_2 \sin \theta_1 + [z + (n-1) \cdot TZ(x,y)] \cos \theta_1 \cos \theta_2 \quad (4.23)$$

where, n is the refractive index of the beamsplitter. Note that only the third term of Eq.(4.23) includes $TZ(x,y)$ since the thickness of the beamsplitter varies only in the z -direction was concerned. Beamsplitter thickness as a function of x and y can be obtained using the equation of planes as follows.

Figure 4.8 shows the geometry of a beamsplitter with a wedge angle, θ_w , in rectangular coordinates. In addition

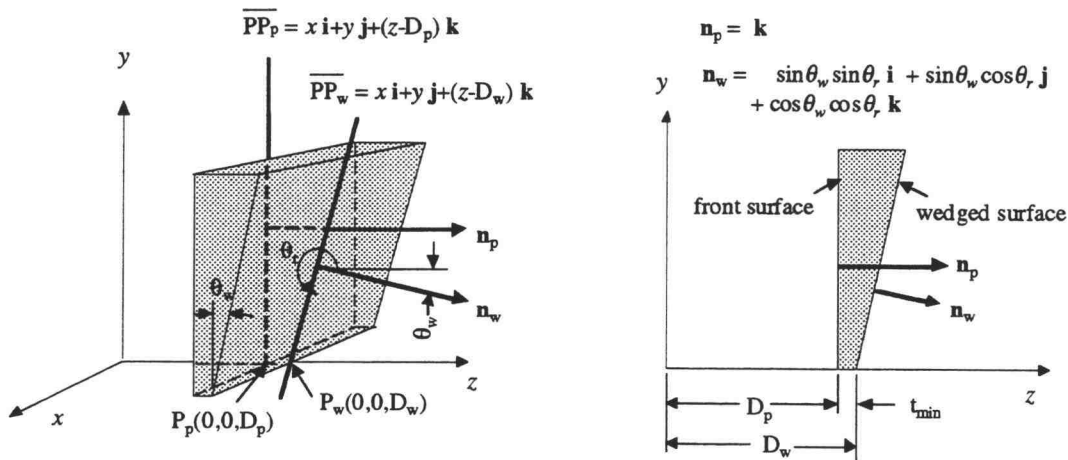


Figure 4.8 Geometry of a wedged beamsplitter with a rotation angle θ_r

to the wedge angle, the beamsplitter also undergoes a rotation along the z -axis. The rotation angle is θ_r . From analytic geometry, the following relationships apply; i.e. $\overline{PP_p} \cdot \mathbf{n}_p = 0$ for the front surface and, $\overline{PP_w} \cdot \mathbf{n}_w = 0$ for the wedged surface. The line $\overline{PP_p}$ passes through the point $P_p(0,0,D_p)$ and the line $\overline{PP_w}$ passes through the point $P_w(0,0,D_w)$.

Carrying out the vector multiplication, $\overline{PP_p} \cdot \mathbf{n}_p = 0$, the equation of the front surface becomes,

$$z = D_p \quad (4.24)$$

Similarly, the equation of the wedged surface is,

$$z = D_w - \frac{1}{(\cos \theta_w \cos \theta_r)} [(\sin \theta_w \sin \theta_r)x + (\sin \theta_w \cos \theta_r)y] \quad (4.25)$$

Subtracting Eq.(4.24) from Eq.(4.25), the thickness of the beamsplitter can now be expressed as

$$TZ(x,y) = t_{\min} - \frac{1}{(\cos \theta_w \cos \theta_r)} [(\sin \theta_w \sin \theta_r)x + (\sin \theta_w \cos \theta_r)y] \quad (4.26)$$

In similar fashion, the thickness of a beamsplitter in rectangular coordinates, with an angle of incidence, θ_i , shown in figure 4.9 is

$$TZ(x,y) = t_{\min} \sin \theta_i + \frac{y}{\tan \theta_i} - \frac{\cos(\theta_i + \theta_w) \sin \theta_r \cdot x + \cos(\theta_i + \theta_w) \cos \theta_r \cdot y}{\sin(\theta_i + \theta_w) \cos \theta_r} \quad (4.27)$$

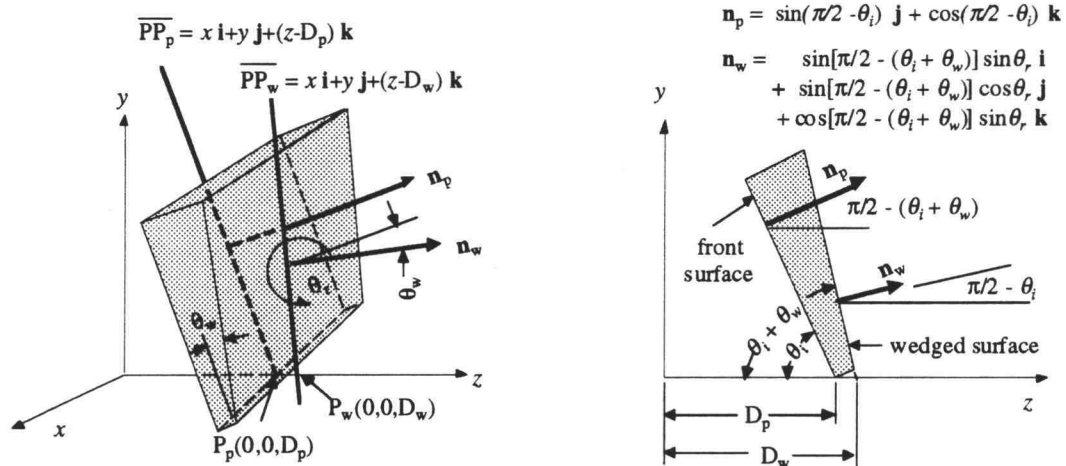


Figure 4.9 Geometry of a wedged beamsplitter with a rotation angle, θ_r , and an incident angle, θ_i

In the Mach-Zehnder interferometer, each beam of a plane wave passes one of the beamsplitters only once, and is then recombined. For two plane waves with angles of inclination, θ_1 and θ_2 , as shown in figure 4.7, passing through the beamsplitter with the same wedge angle, θ_w , but with different rotation and incident angles, θ_r and θ_i , the irradiance on the screen can be derived from the principle of superposition and the time average value of Eq.(4.22) as

$$I \propto \frac{1}{\Delta t} \int_t^{t+\Delta t} (E_1 + E_2) \cdot (E_1 + E_2) dt \quad (4.28)$$

Spherical waves interference

Since the amplitude of the electrical field of a spherical wave is inversely proportional to distance, and because the wavefront is always normal to the direction of

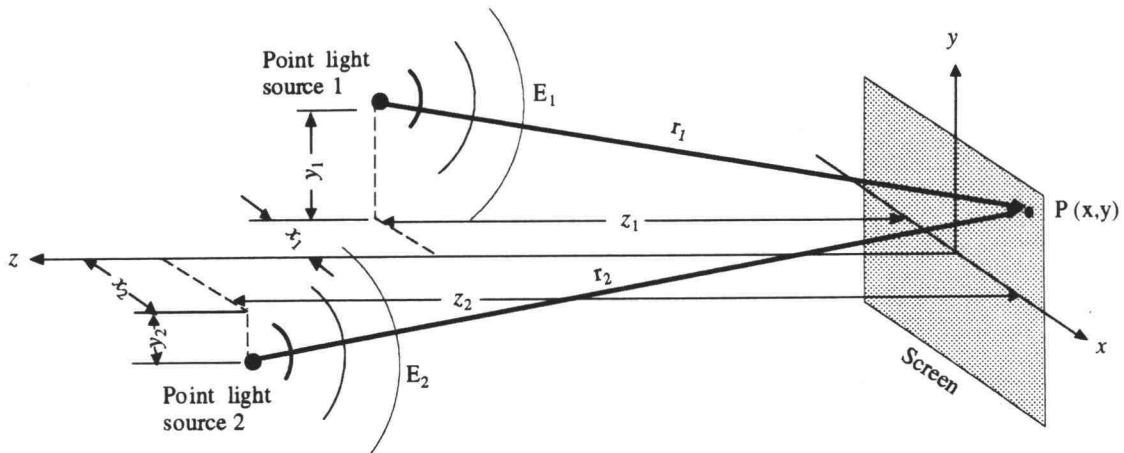


Figure 4.10 Coordinates of two-point-source interference

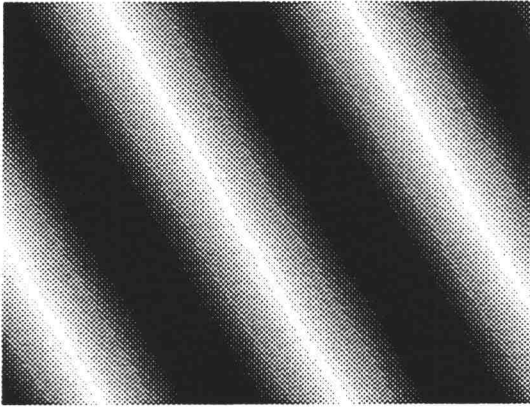
propagation as shown in figure 4.10, the electrical field becomes

$$E = \frac{A}{r} \cos(\omega t - kr) \quad (4.29)$$

where r is merely the distance from the point source to the screen in figure 4.10. The irradiance of the two-point-source interference case also can be obtained from Eq. (4.28).

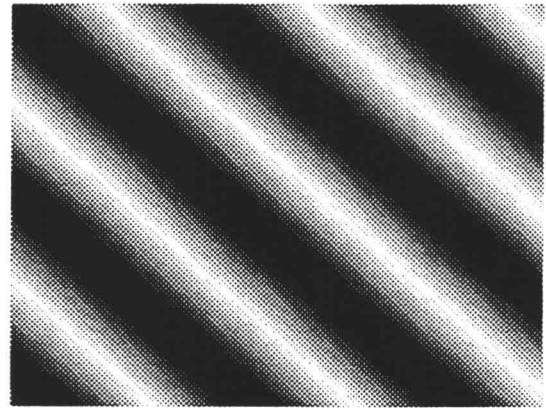
Results and conclusions of computer simulation

Many computer simulations for two-plane-wave interference have been done by varying the four angles, θ_1 , θ_2 , θ_r and θ_i , and the distance from the screen shown in figures (4.7)-(4.9). All results show only one type of fringe, the stripe-like fringe.



(a) 1st wave: $\theta_w = 0.5^\circ$, $\theta_r = \pi/100$, $\theta_i = \pi/3$,
 $\theta_1 = \pi/500$, $\theta_2 = \pi/500$, $z = 47000$.

2nd wave: $\theta_w = 0.5^\circ$, $\theta_r = \pi/3$, $\theta_i = \pi/2$,
 $\theta_1 = -\pi/700$, $\theta_2 = -\pi/800$, $z = 47000$.



(b) 1st wave: $\theta_w = 0.5^\circ$, $\theta_r = \pi/100$, $\theta_i = \pi/3$,
 $\theta_1 = \pi/100$, $\theta_2 = 0$, $z = 47000$.

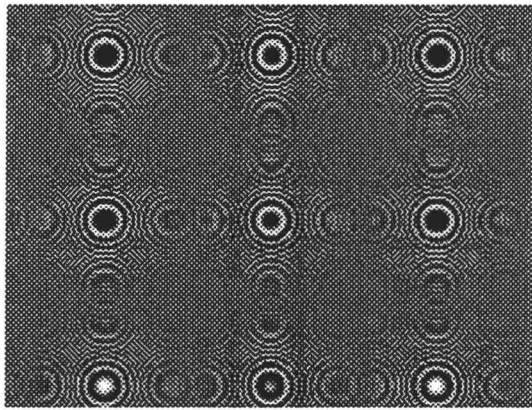
2nd wave: $\theta_w = 0.5^\circ$, $\theta_r = -\pi/200$, $\theta_i = \pi/3.1$,
 $\theta_1 = 0$, $\theta_2 = 0$, $z = 47000$.

Figure 4.11 Fringe pattern of plane-wave interference

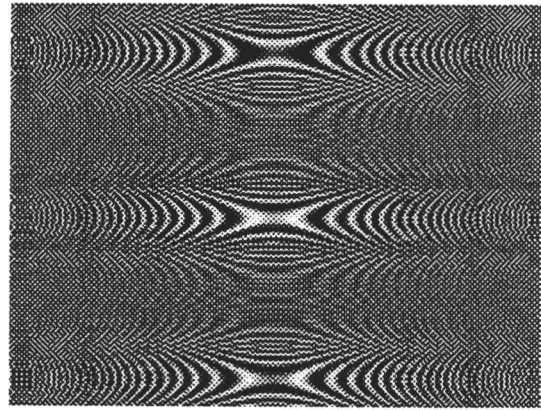
Two examples of plane-wave interference are shown in figure 4.11. The length unit used in the computer program is the pixel - 100 pixels is equivalent to 1 cm for the selected wavelength of 514.5 nm. From the numerical simulation, changes in the four angles, θ_1 , θ_2 , θ_r and θ_i , primarily change the direction and the width of the stripes. Changes in the fringe patterns are small.

In contrast to the similar fringe patterns obtained from two-plane-wave interference, fringe patterns from two-point-source interference show considerable variation as the positions of the two point sources are varied as shown in figure 4.10.

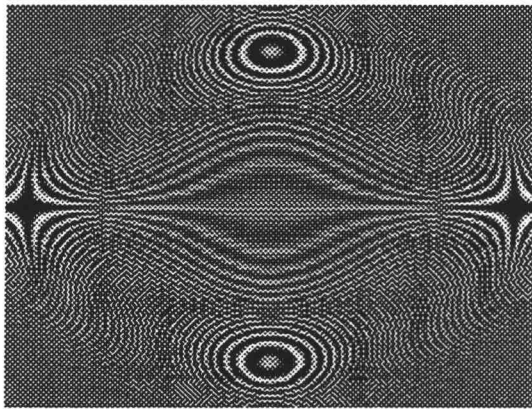
Four frames of fringe patterns from two-point-source interference are shown in figure 4.12. The length unit again is the pixel as used for plane wave interference.



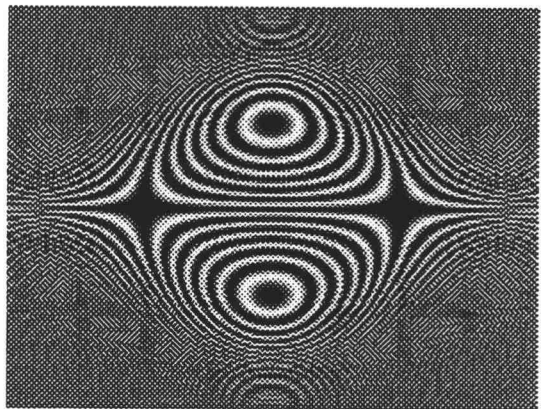
(a) $x_1 = 0$ $y_1 = 188$ $z_1 = 150000$
 $x_2 = 0$ $y_2 = -584$ $z_2 = 100000$



(b) $x_1 = 0$ $y_1 = 76812$ $z_1 = 30000$
 $x_2 = 0$ $y_2 = 77412$ $z_2 = 30000$



(c) $x_1 = 0$ $y_1 = 1400$ $z_1 = 3000$
 $x_2 = 0$ $y_2 = -1400$ $z_2 = 3000$



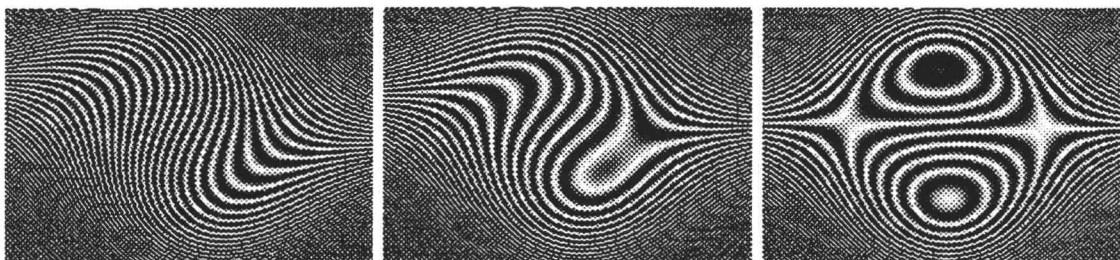
(d) $x_1 = 0$ $y_1 = 194$ $z_1 = 300$
 $x_2 = 0$ $y_2 = -194$ $z_2 = 300$

Figure 4.12 Fringe patterns of two-point-source interference

The ideal infinite fringe field will have uniform intensity distribution on the screen in the absence of a disturbance. Two important results are obtained through this numerical simulation. First, two-plane-wave interference will display ideal characteristics if all of the corresponding angles in figure 4.11, for the 1st and the 2nd waves, are identical. Secondly, two-point source

interference will also appear as an infinite fringe field if the two point sources overlap.

Three fringe patterns obtained from the numerical results for two-point-source interference are shown in figure 4.13. These three fringe patterns are identical to those shown in figure 4.6. This explains why undesired fringes occur - because the shape of the waves is not plane, instead, they are spherical.



(a) $x_1 = -18$ $x_2 = 0$ (b) $x_1 = -8$ $x_2 = 0$ (c) $x_1 = -1$ $x_2 = 0$
 $y_1 = -194$ $y_2 = 194$ $y_1 = -194$ $y_2 = 194$ $y_1 = -192$ $y_2 = 194$
 $z_1 = 330$ $z_2 = 300$ $z_1 = 330$ $z_2 = 300$ $z_1 = 312$ $z_2 = 300$

Figure 4.13 Fringe pattern results from numerical simulations

Two other conclusions can be drawn from these numerical simulations: (1) The presence of the wedge angle from the beamsplitter primarily affects the change in propagation direction of the plane wave. Changes in fringe patterns due to the wedge angle are small. This is shown in figure 4.11. (2) The collimated wavefront of the MZ interferometer setup for this study is not quite "plane". The shape of the wavefront is similar to a point source wavefront. Even with this type of wavefront, an infinite

fringe field with uniform intensity still can be obtained by aligning the two arms of the interferometer at equal distances, i.e. to overlap two point sources at the same position.

Comparisons between an ideal plane wave and possible wave form outputs are shown in figure 4.14. The curvatures shown in figure 4.14(b) are exaggerated. A perfect plane wave for a large cross section is quite difficult to obtain for the experimental apparatus used in this study, some

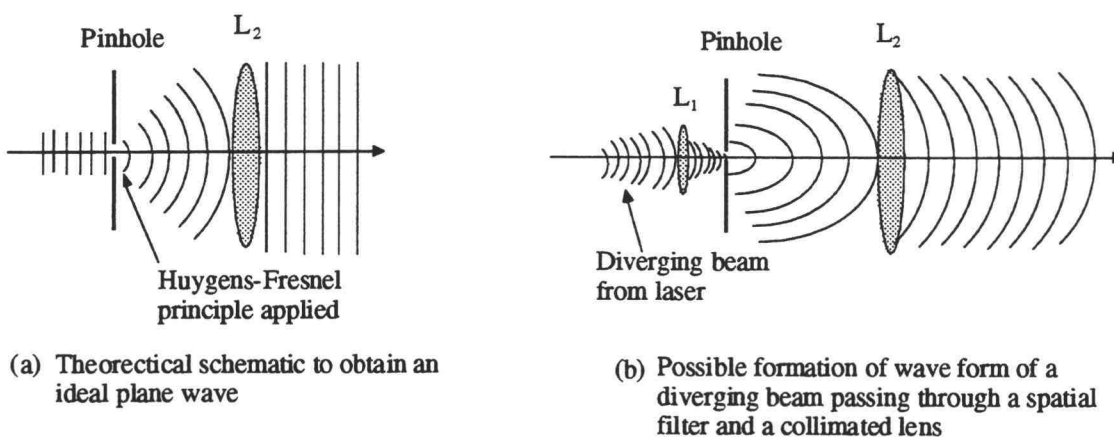


Figure 4.14 Comparison between theoretical plane wave and other possible wave forms from a diverging beam passing through a spatial filter and a collimating lens

reasons being: (1) The output beam from the argon laser used in this experiment diverges as it propagates. This is due to the two concave mirrors used for the laser cavity configuration specified by the manufacturer [33]. (2) The convex lens, L_1 , focuses the beam into a point where the

pinhole was placed. This differs from the Huygens-Fresnel principle where a spherical wave is obtained from a plane wave passing through a very small aperture. The convex lens can be removed from the spatial filter, however, the intensity will be dramatically reduced for such a removal. (3) Wavefront distortion due to the deviations of surface flatness for all optics and, more importantly, inhomogeneities in the refractive indexes of lenses and beamsplitters will all cause a deformation of the outgoing wavefront [34]. Also, the surface of the collimating lens, L_2 , must be very smooth. Variations in surface smoothness may cause distortion of the wavefront. (4) The design wavelength for L_2 specified by the manufacturer was at 546.1 nm. This differs from the wavelength of the light source used in this study which is 514.5 nm. Thus, plane wave may not be obtained due to a different dispersion rate by the glass material.

Since overlapping of the two point sources will produce the infinite fringe field, the interferometer used in this experiment employed this type of arrangement.

4.6 SETUP OF THE MACH-ZEHNDER INTERFEROMETER

The most tedious task in setting up a Mach-Zehnder interferometer to obtain an infinite fringe field involved aligning the four optics, B_1 , B_2 , M_1 , M_2 , of the two arms shown in figure 4.1. Since the two beamsplitters with

wedge angles and optical coatings on both surfaces, appropriate orientation of these two elements was critically important.

Figure 4.15 shows the arrangement of the four optical components of the interferometer. To obtain equal distances for the two arms, the two beamsplitters were arranged in the fashion shown.

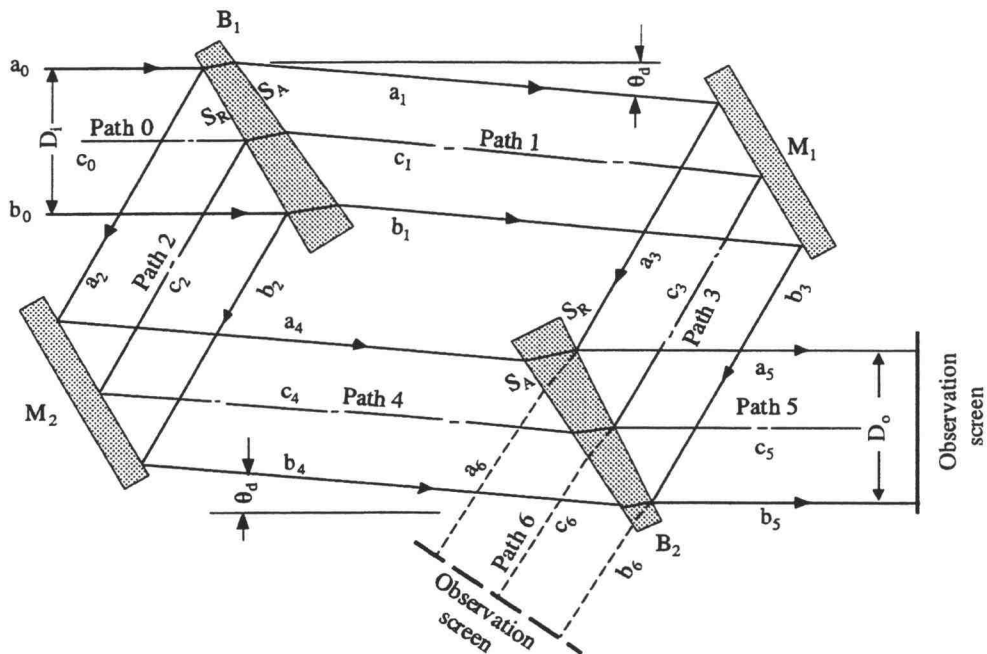


Figure 4.15 Arrangement of beamsplitters and mirrors for the interferometer

With fixed diameters of the four optical components, the 60° parallelogram configuration shown in figure 4.15 will yield a larger beam cross section suggested by Hauf and Grigull [26]. In this figure, S_R represents the front surface with a semi-reflecting coating, and S_A represents a

surface with an anti-reflecting coating. Details of the interferometer arrangement and the distribution of intensity due to the beamsplitters are described in Appendix B. The output of the interferometer can be located either on a screen in path 5 or in path 6. A test section can be placed in paths 1, 2, 3 or 4. However, to minimize far-field Fraunhofer diffraction, the test section should be placed either in path 3 or path 4. The test section and the observation screen should be arranged as close as possible to each other. The test section was placed in path 4 in this experiment.



Figure 4.16 Fringes for a vertical heating plate using the infinite fringe field

Referring to the fringes and the coordinates shown in figure 4.13, a nearly maximum (bright fringe) of approximately 2.5 inches in diameter can be obtained for the infinite-fringe-field alignment. Figure 4.16 shows the fringe pattern of a vertical heated plate using the infinite fringe field.

4.7 POST DATA PROCESSING OF THE NUMERICAL RESULTS

The objective of the experiments with the MZ interferometer were to detect the temperature field for the open thermosyphon and compare this information with the results of numerical solutions. The temperature field detected by the interferometer consisted of fringe patterns which look much like a plot of isotherms except that temperature differences between adjacent fringes are not constant. The formation of fringes is a result of the change in optical path length of a laser beam passing through the uneven temperature field in the test section. Since the order of fringes can be related to the temperature field by the Lorentz-Lorenz equation and the equation of state of the fluid, the temperature field obtained from the numerical solution can be transformed into a fringe-like image. This section describes the techniques used in this study to process the results from the numerical solution into a picture-like image.

To illustrate the procedures that produce an image, consider the temperature field for a square cavity in two dimensional rectangular coordinates as shown in figure 3.1. The number of data points for the temperature field obtained from the numerical solution are 40×40 . The plot of isotherms in figure 3.1 is the result of these 40×40 data points processed using existing commercial software programs such as Golden Surfer and DeltaGraph. For this plot, the temperature difference between isotherms is constant.

To obtain higher-resolution images for the temperature field, more data points are required. This can be achieved either by specifying larger arrays for the temperature field, and consequently larger arrays for the pressure and velocity fields, for the numerical computation, or to achieve new data points by interpolation using the computed temperature field. Using a larger array for the T, P, U and V fields for the numerical computation will not only cause a computer RAM memory problem but also significantly slow down the speed of computation. For these reasons, new data points were generated by interpolation. Figure 4.17 shows the mapping of these two sets of data points.

The expected new image will be a 256-level gray scale with 496×375 pixels of resolution as the picture taken by a CCD array camera described in section 4.4. To do this, the temperature field of 40×40 data points was mapped

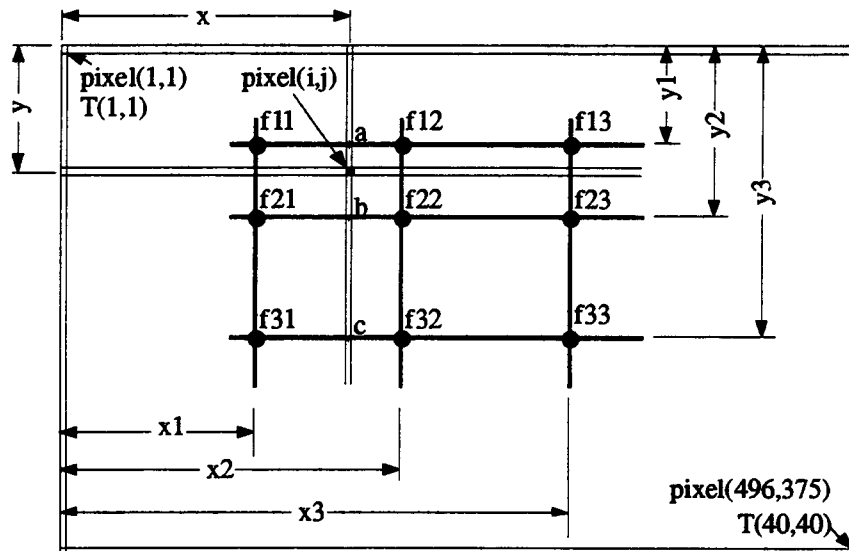


Figure 4.17 Mapping for the temperature field with 40 x 40 data points into 496 x 375 data points

into 496 x 375 equally spaced points as shown in figure 4.17. For discussion purposes, the new data points are called pixel data points and the old data points are called temperature data points.

Several techniques can be used for interpolation. For example, the point at (i,j) can be interpolated by knowing the temperatures at neighboring data points. Intuitively, we can imagine a plane existing in the space to include the four old data points of temperature, f11, f12, f21 and f22. The temperature at point (i,j) will be the result of linear interpolation using these temperature variables. A better method is to use a polynomial curve fit of the 9 data points, f11-f33. The procedure is first to interpolate the

temperature at point a from a polynomial curve using the three data points, f_{11} , f_{12} , and f_{13} . In similar fashion, temperatures at points b and c can be interpolated using polynomial curves passing through points f_{21} , f_{22} , f_{23} and f_{31} , f_{32} , f_{33} respectively. Then, the procedure is to evaluate the temperature at point (i,j) using the polynomial curve passing through data points a, b, and c.

Mathematically, the procedures can be described by the following equations.

$$a = \frac{(x-x_2)(x-x_3)}{(x_1-x_2)(x_1-x_3)} f_{11} + \frac{(x-x_1)(x-x_3)}{(x_2-x_1)(x_2-x_3)} f_{12} + \frac{(x-x_1)(x-x_2)}{(x_3-x_1)(x_3-x_2)} f_{13} \quad (4.30)$$

$$b = \frac{(x-x_2)(x-x_3)}{(x_1-x_2)(x_1-x_3)} f_{21} + \frac{(x-x_1)(x-x_3)}{(x_2-x_1)(x_2-x_3)} f_{22} + \frac{(x-x_1)(x-x_2)}{(x_3-x_1)(x_3-x_2)} f_{23} \quad (4.31)$$

$$c = \frac{(x-x_2)(x-x_3)}{(x_1-x_2)(x_1-x_3)} f_{31} + \frac{(x-x_1)(x-x_3)}{(x_2-x_1)(x_2-x_3)} f_{32} + \frac{(x-x_1)(x-x_2)}{(x_3-x_1)(x_3-x_2)} f_{33} \quad (4.32)$$

$$T(i,j) = \frac{(y-y_2)(y-y_3)}{(y_1-y_2)(y_1-y_3)} a + \frac{(y-y_1)(y-y_3)}{(y_2-y_1)(y_2-y_3)} b + \frac{(y-y_1)(y-y_2)}{(y_3-y_1)(y_3-y_2)} c \quad (4.33)$$

Higher-order polynomial curve fitting can be used. For example, one can use four data points for the interpolation. However, mis-interpolation can occur when the four data points are aligned such that they approximate a straight line. Thus four-data-point polynomial curve fitting is not recommended.

After a set of 496×375 new data values were obtained, they were converted into integer numbers from 0 to 255 to match the 256 gray levels for each pixel of the image. Equations used for these conversions as well as interpolating techniques will affect the final of the image. Figure 4.18 shows some numerically-generated images for the temperature field of the square cavity of figure 3.1.

Figure 4.18(a) shows the image of the temperature field for the square cavity using the original 40×40 data

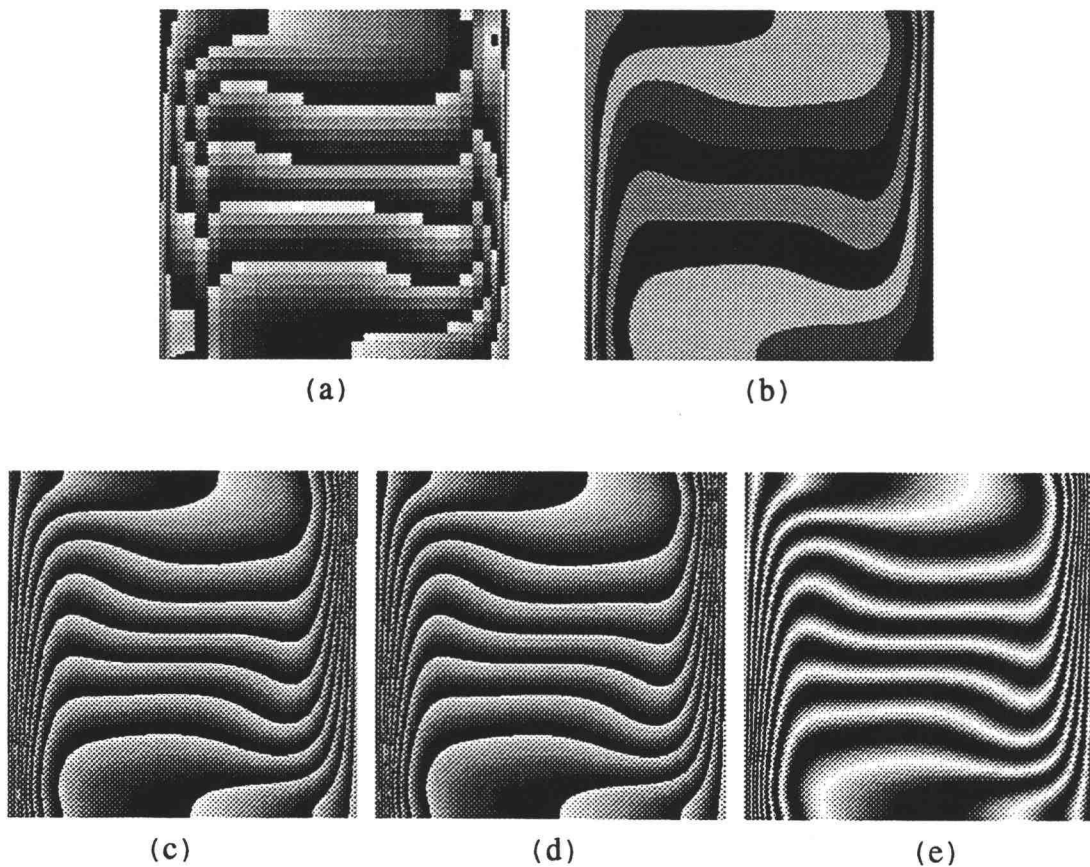


Figure 4.18 Numerically-generated images of natural convection in a square cavity

points from numerical computation. No interpolation was used for this image. Figure 4.18(b) is the image using linear interpolation for the new data points and the gray level was set at a constant integer value for each 1 °C temperature difference. Instead of a constant integer for 1 °C, figure 4.18(c) shows the image using linear interpolation with 256 gray levels applied for each degree of temperature.

The difference between image (c) and image (d) in figure 4.18 is the interpolating technique used. Figure 4.18(d) was obtained using the curve fitting equations from Eqs.(4.30)-(4.33). No obvious difference is apparent between these two images since the temperature difference between each cell is small and the cell spacing arrangement is relatively uniform for the square cavity problem. For cases of open thermosyphons with large temperature differences and large variations in cell spacing, the image quality from linear interpolation is not as smooth as for curve fitting interpolation.

Among the five images, figure 4.18(e) is the best for showing the temperature field. To obtain this fringe-like image, a sinusoidal function was used to smooth the sharp change from integer values 255 (black) to 0 (white). The electrical field of the laser light source used in this study is represented as a sinusoidal function, thus, the temperature field from the numerical calculation was coupled with Eq.(4.18) and Eq.(4.7) to obtain the image of

fringes as shown. Since the relation between the temperature and the refractive index was used to interpret the temperature field, the temperature difference between fringes is not constant. It is the real temperature difference as would be obtained using the MZ interferometer. As presented in table 4.1, temperature differences between fringes depend on the length of the test section and the wavelength of the light source.

There are two equations available to relate the air temperature to the refractive index. They are the experimental correlation, Eq.(4.18), and the Gladstone-Dale equation, Eq.(4.16). Numerical experiments were performed to examine the difference of fringe patterns between these two equations. The difference is small. Eq.(4.18) was used to generate picture-like fringes in this study because of its better accuracy as suggested by Vest [27].

Fringes result from the change of optical path length while light travels in space. Giving the length of the square cavity as L , the optical path length of the light ray traveling through the square cavity is $n \cdot L$, where n is the refractive index as a function of temperature obtained from Eq.(4.18). The light ray traveling through the other arm of the MZ interferometer obeys these same relationships. The intensity is, therefore, the optical path difference, OPD, between the two light rays. To obtain the 256 gray levels for each pixel, the following

equation, which is similar to Eq.(4.7), was used in the computer program,

$$\text{Gray level} = \text{Integer} \left\{ 127.5 + 127.5 \cdot \cos \left[\frac{2\pi}{\lambda} (n - n_{\text{ref}}) L \right] \right\} \quad (4.34)$$

where, λ is the wavelength, $(n - n_{\text{ref}}) \cdot L$ is the OPD of the two light rays. The reference refractive index, n_{ref} , was the room temperature value.

Figure 4.19 shows the numerically-generated fringes for the square cavity at selected times. Polynomial curve fitting was used for the temperature field and Eq.(4.18) was used to obtain the fringes.

The case of fringes with a light beam passing through an axisymmetrically distributed temperature field was also investigated in this study to compare results between the experiments and numerical results. Since it is not possible to detect fringes experimentally inside the vertical tube of the open thermosyphon, the comparison was made at the tube opening.

To obtain the fringe patterns for a light beam passing through an axisymmetric temperature field, consider the light ray propagating in the z -direction as shown in figure 4.20. The refractive index of the medium in the path of the beam varies with the temperature at different locations. Since the formation of fringes depends on optical path length, calculation of the OPL must be

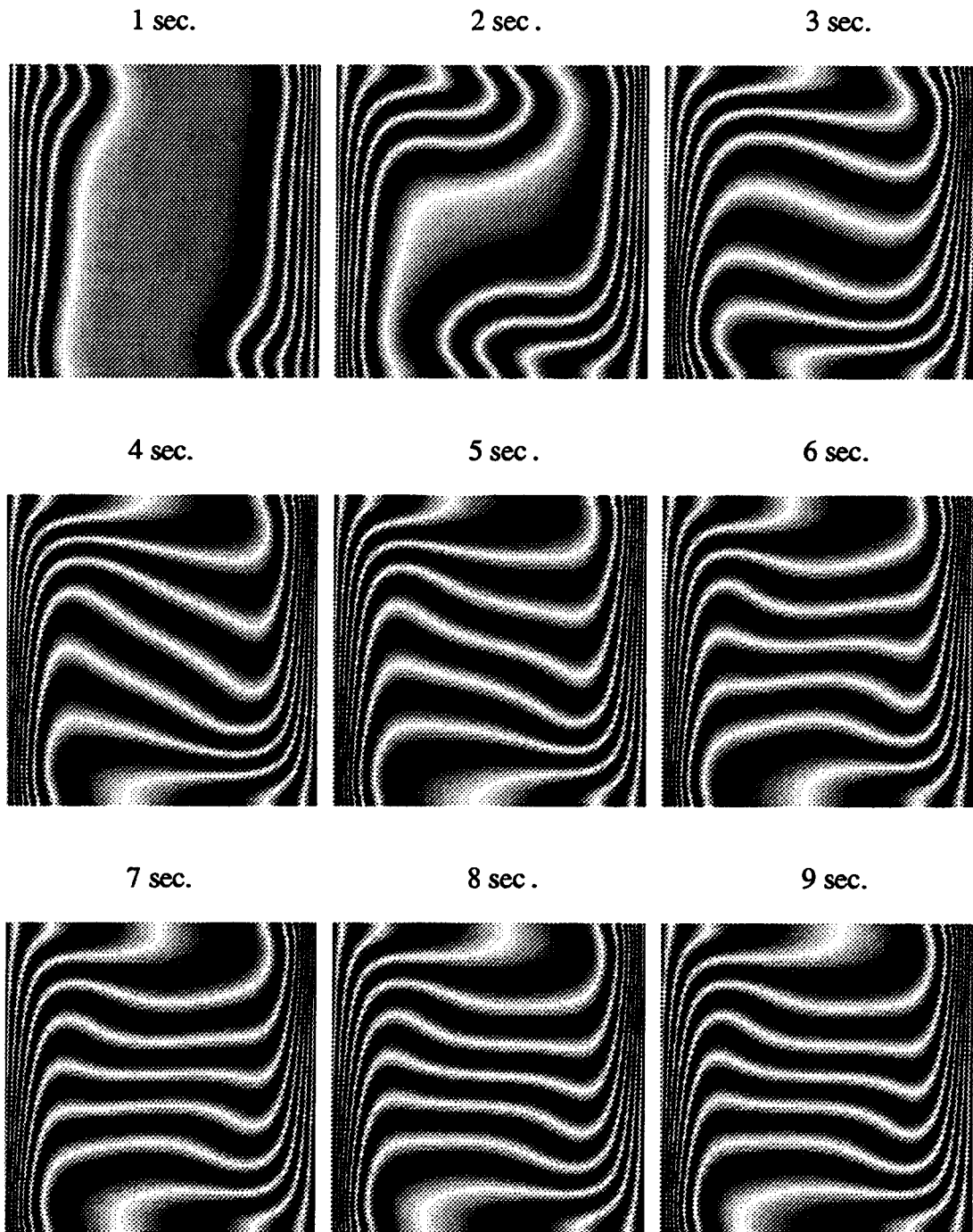
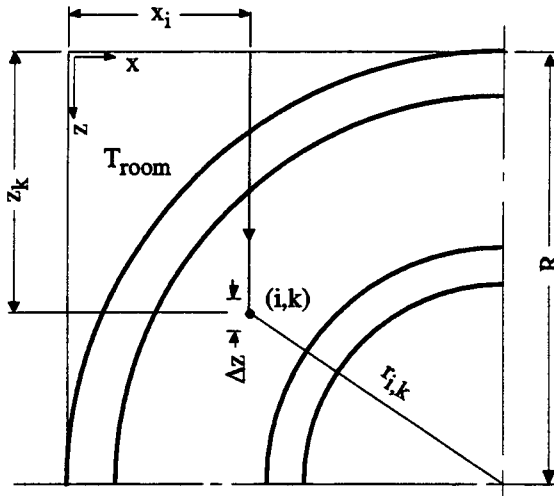


Figure 4.19 Numerically-generated fringe patterns of natural convection in a square cavity at selected times. The length of the test section is 60 cm, and the wavelength of the light source is 514.5 nm



$$r_{i,k} = [(R-x_i)^2 + (R-z_k)^2]^{1/2}$$

$$n_{i,k} = 1 + \frac{0.294036 \times 10^{-3}}{1 + 0.369203 \times 10^{-2} T_{i,k}}$$

$$n_{\text{ref}} = 1 + \frac{0.294036 \times 10^{-3}}{1 + 0.369203 \times 10^{-2} T_{\text{room}}}$$

$$\text{OPD} = (n_{\text{ref}} - n_{i,k}) \Delta z$$

Figure 4.20 Optical path length of a light ray travelling through an axisymmetric temperature field

accurate. This can be done by advancing the light ray by a small increment in space, Δz , in the z -direction. At the mid-point of Δz , interpolate the temperature at that location using polynomial curve fitting as pervious described. According to the interpolated temperature, the refractive index, and consequently the OPL, can be found. The total OPL is then the sum of each small increment.

Instead of finding out the OPL, the total optical path difference, OPD, between the light ray passing the disturbed temperature field and its counterpart of the light ray passing the other arm of the MZ interferometer was calculated. The OPD was then substituted into Eq.(4.34) to find the gray level, the intensity, for the image at that location.

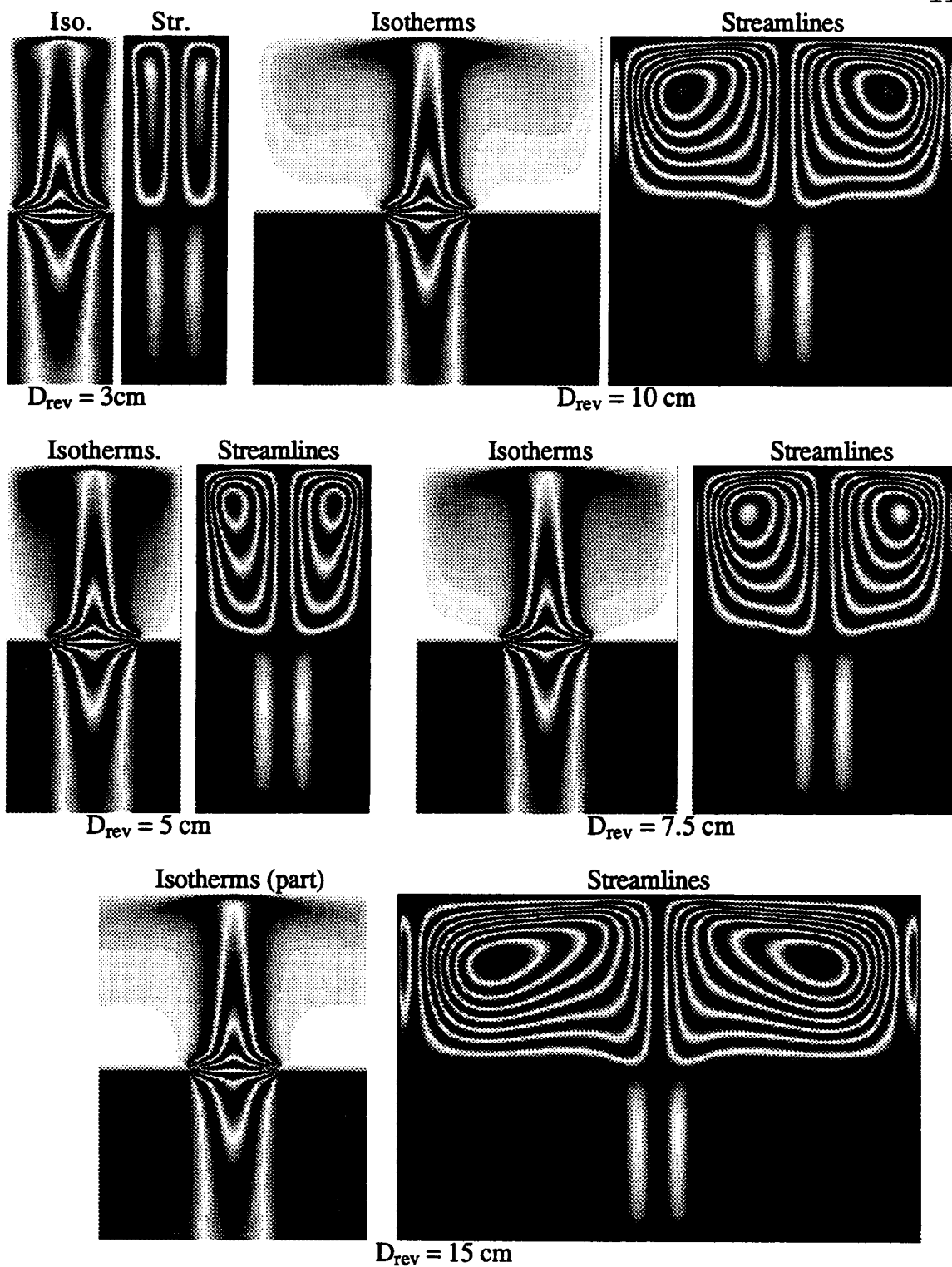


Figure 4.21 Plot of isotherms and streamlines for case of an open thermosyphon with $D = 2.5$ cm and $L = 5$ cm. The reservoir size is $L_{rev} = 5$ cm (fixed) and $D_{rev} = 3, 5, 7.5, 10,$ and 15 cm.

Fringes pattern for axisymmetrical flow using the techniques described above are presented in section 5.7 for a 1"-diameter and 2"-long vertical tube at a higher wall temperature open to the atmosphere at 27 °C. The numerically-generated fringe patterns are compared with the experimental results for the vertical tube with different wall temperatures.

These technique can also be applied to the streamlines plots. Figure 4.21 shows the isotherms and streamlines for case of an open thermosyphon with different reservoir sizes. In this figure, difference between each isotherm and streamline were artificially set at a constant value to show its contour lines. Unlike the numerically-generated fringe patterns, which were calculated according the dimension of the test section and the wavelength of a laser light source, the purpose of these plots is to show the temperature distribution and flow behavior in the tube and reservoir. Images of these plots, figure 4.21, are not related to the fringe patterns detected using a MZ interferometer.

V. EXPERIMENTATION AND RESULTS

Experiments to detect the temperature field of a test section using the MZ interferometer setup as discussed in chapter 4 was described here. The experimental results were then compared with the numerical results discussed in chapter 3. Nusselt number and interference fringes were used for these comparisons. Correlations between Nusselt numbers and Rayleigh numbers for different height-to-width (aspect ratio) open cavities were determined.

To control a constant wall temperature of the test section, steam was used. The test section was constructed in an adjustable fashion to vary the width and the height of the open cavity. Two models of the test section, one with two optical windows on both sides of the test section and the other without the two windows, were used to study the effect of the air flow in the z -direction.

Evaluations of the heat transfer rates were obtained by measuring the distances for each fringe from the wall. The temperature profiles at difference elevations can be determined using a parabolic regression curve fitting from these measured distances. The temperature gradient at the wall was then evaluated from the temperature profiles to determine the Nusselt numbers.

Fringe patterns for flow over a flat plate was examined to validate the use of the MZ interferometer. The situation with vertical channel flow were also studied.

Temperature profiles as well as the local and average Nusselt number were plotted and calculated for these cases.

Sixteen cases of open cavities were selected for both quantitative and qualitative comparisons between the numerical and experimental results. Experimental and numerically-generated fringe patterns were presented side-by-side for the qualitative comparisons. These comparisons illustrated a general agreement of the fringe patterns between the numerical model and the experimental model with two optical windows on both sides of the test section. Fringe patterns from the other experimental model were somewhat disagreed with the numerically-generated fringe patterns due to the z -directional air flow.

Nusselt number values from numerical calculations were found to be lower than that from the experimental results. This was due to several differences between the numerical and experimental modeling. Among them, the use of a laminar flow numerical model to predict a possible turbulent air flow could be the major reason for the disagreement.

In addition to these quantitative comparisons for the case of open cavities, a qualitative comparison of fringe patterns for the case of open thermosyphons between experiments and numerical results was also presented. These comparisons of fringe patterns were selected at the tube opening for four selected cases with different wall temperatures and tube diameters.

5.1 CONSTRUCTION OF THE TEST SECTION

The test section was constructed to use condensing steam as a mean to control the wall temperature. The apparatus is shown in figure 5.1. It was made with 3/8 inch thick acrylic. At the open-end of this device, a removable 0.01-inch thick aluminum sheet was attached allowing vapor condensation on its inner surface. The surface temperature of the aluminum sheet was thus maintained nearly constant. A schematic diagram of the device is also shown in figure 5.1.

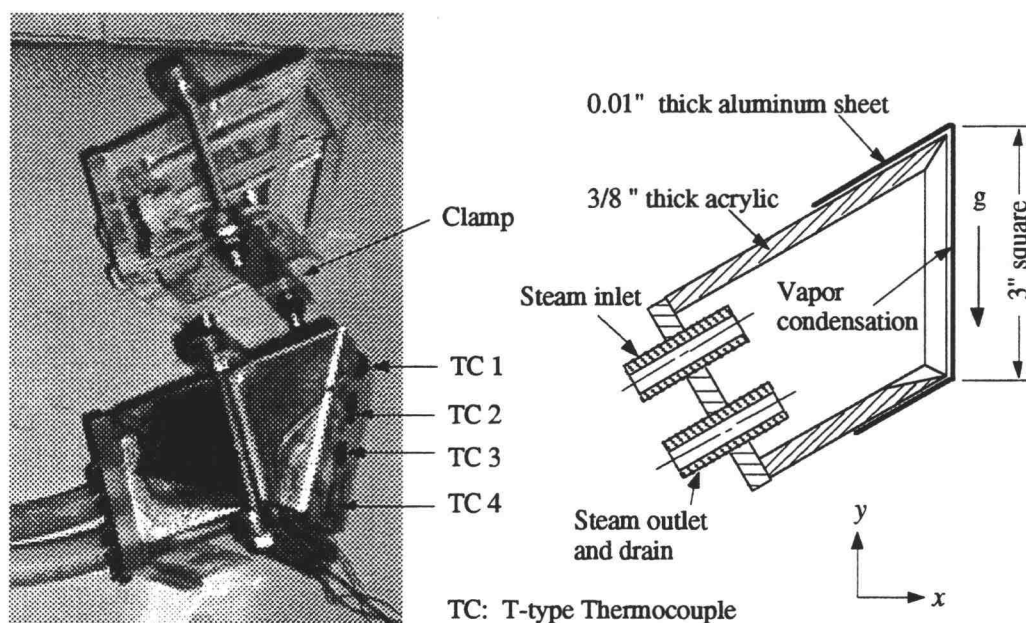


Figure 5.1 Schematics of the constant temperature control device

Four T-type thermocouples were used to measure the aluminum surface temperatures at different elevations as indicated. These thermocouples were bonded to the surface using a high

temperature conductive Omega-200 epoxy. Temperature values measured along the surface were 98.1°C , 98.1°C , 97.9°C , and 97.7°C , for TC 1 to TC 4 respectively, with the room temperature at 25°C . Variations from these values were within 0.1°C as indicated using a Fluke digital thermometer.

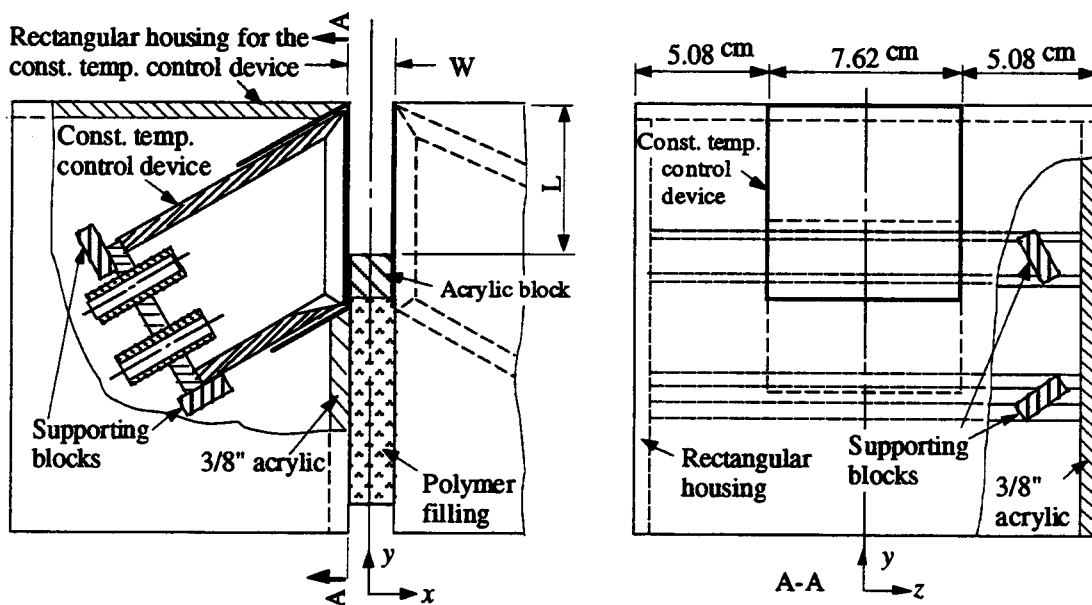


Figure 5.2 Construction of the modified open thermosyphon

A vertical open cavity in rectangular geometry was formed by two constant-temperature surfaces placed inside rectangular acrylic housings as shown in figure 5.2. The width, W , and the length, L , of the vertical open cavity was adjustable by replacing and moving the acrylic block between the two housings.

The length, L , and the width, W , of the vertical open cavity were limited by the maximum beam diameter of the Mach-Zehnder interferometer. In this study, L and W of the open cavity were limited to a maximum of 3 inches. The depth of the heating surface was determined by the desired readability of the fringes formed on the screen. A three-inch-long depth was chosen, which formed 8 fringes between the heating surface at 98 °C and the surrounding air temperature at approximately 27 °C (see table 4.1). As shown in table 4.1, a surface with greater depth will form more fringes for a vertical wall with a fixed temperature difference requiring a higher-resolution picture quality to distinguish each fringe. This is a major consideration when selecting a camera and the film sensitivity.

Steam was provided by a small boiler operating at a pressure of one atmosphere to the constant temperature control device.

Due to air flow in the z -direction from both sides of the test section, the Nusselt number obtained from the initial experimental results did not compare well with the predicted Nusselt number from numerical calculation. To minimize this effect, two flat windows, with anti-reflection coatings on both surfaces, were used. The test section with windows in place is shown in figure 5.3. Surface flatness of these two windows was $1/5 \lambda$ per inch which is the same as for the two mirrors and the two

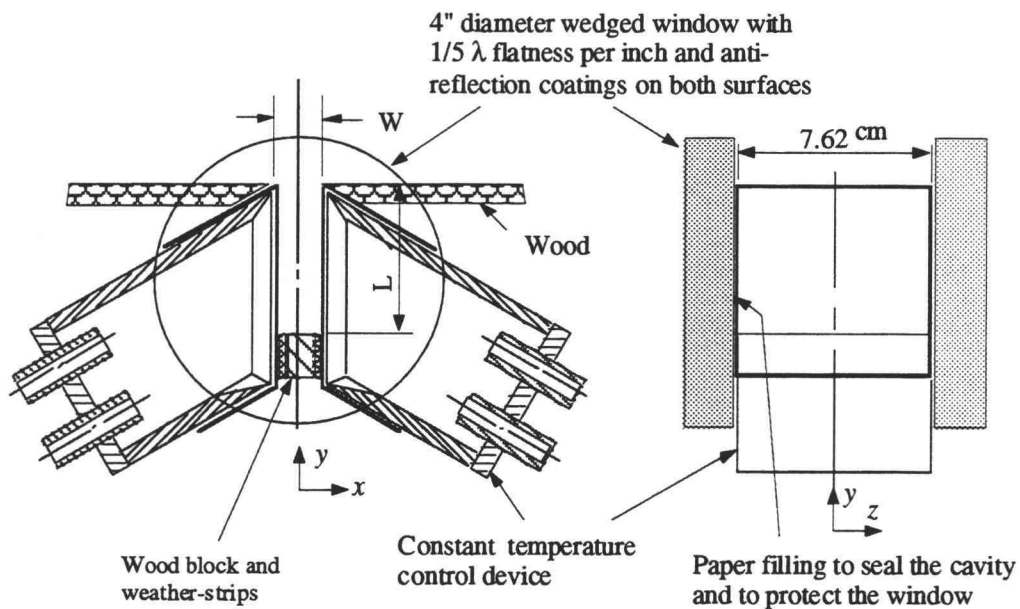


Figure 5.3 Test section with windows on both ends

beamsplitters used for the MZ interferometer. These high quality surfaces were necessary so that the fringe patterns would not be affected by the presence of the two windows. These two windows were also constructed with a 0.5° wedged angle to reduce the ghost image as with the two beamsplitters. As suggested by the two-plane-wave interference pattern discussed in chapter 4, presence of a wedge angle on the window will only change the direction of propagation of a light beam, and this change of direction can be easily corrected by tilting one of the two mirrors in the MZ interferometer.

5.2 EXPERIMENTAL PROCEDURES AND MISCELLANEOUS

The test section was placed in the second arm of the MZ interferometer as shown in figure 4.1. The distance between the test section and the screen was made as short as possible to avoid far-field diffraction on the edges of the open cavity.

A CCD camera and a regular camera were used to photographically record the fringes. Very high sensitive film rated at ISO 1600 rating was used for the regular camera. When using the CCD camera, a magnifying lens was placed in line with the observation screen. This allowed the CCD camera to capture higher-resolution images of the fringes when they were crowded together. When using the regular camera, a close-up lens and/or a extension tube were used. This allowed the size of the fringes to be measured by placing a ruler on the screen. Images from both the magnified lens and the close-up lens experiences pincushion or barrel distortion [35]. Distortion with the magnified lens was greater than for the close-up lens.

Mechanical vibration was of critical important when taking pictures of the images. The MZ interferometer is extremely sensitive to any source of vibration. To minimize these effects, the interferometer was placed on an optical table. The tabletop was supported by four air-filled legs. Other sources of vibration, such as operators' breathing and the building ventilation system may also affect the fringe shift during the experiment. A

transparent plastic sheet was used to cover the interferometer and thereby minimize effects of avoid any breeze. A black plastic sheet was also used to capture scatter from the laser light source. This reduced the possibility of the laser light directly contacting operators' eyes and skin.

Another important factor to consider was the fringe shift during the experiment. During a five-minute period of observation, without the test section in place, steam was introduced into the room at a small rate, similar to conditions when an experiment was in progress. The room temperature observed to increase due to a small amount of steam leakage. Fringes on the observation screen shifted rapidly during this 5 minute interval. The rate of fringe shifting then decreased. After approximately one hour, the fringe shift on the screen was negligibly small. All experiments to detect the temperature field for the test section were thus conducted one and one-half hours after steam was injected into the room at a small rate.

Many factors may contribute to the fringe shift as stated above. For this study, thermal expansion of the optical mounting parts, due to a change in room temperature, was thought to be a major source. Fringe shift was a significant problem when using the wedge fringe field interference technique described in chapter 4. When using the infinite fringe field interference, the shift was less critical as long as the interferometer was finely

adjusted to project a maximum or minimum intensity field on the screen.

5.3 EXPERIMENTAL FRINGES INTERPRETATION

To compare heat transfer rates between numerical and experiment results, the experimentally-obtained fringes need be interpreted to obtain the rate of heat transfer. Certain procedures involved for such an interpretation are given in Showole and Tarasuk [36].

Figure 5.4 shows an image for the case of an open cavity 1.5" wide and 2" high. Five locations near the wall were selected for evaluation. The fringe pattern was

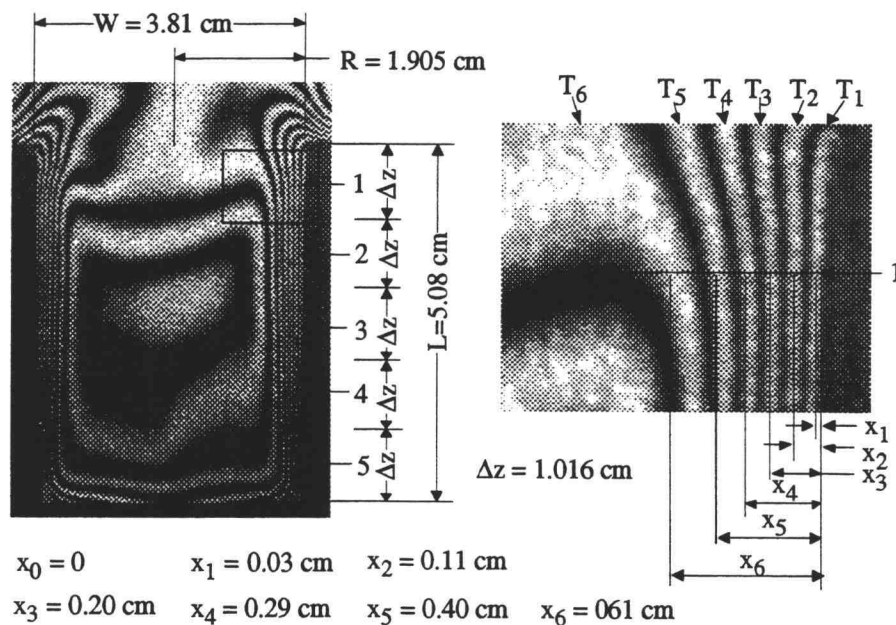


Figure 5.4 Fringe interpretation

magnified for enhanced accuracy. The magnified fringe pattern at position 1 is shown in the figure.

Interpretation of fringe temperature for an infinite fringe field depends on the room temperature and the fringe pattern obtained on the screen at that room temperature. This temperature interpretation was inferred using information from table 4.1 for case of an open cavity with $L = 0.0762$ m and the room temperature at 27 °C. For example, a maximum (bright) intensity field was adjusted to show on the screen in the room temperature, the temperature for the next maximum due to an increase of temperature will be 34.72 °C. Inside a boundary layer, information of fringes right next to the wall are more important for the calculation of heat transfer. For a wall temperature at 98 °C, the first fringe temperature, T_1 , at position x_1 was then considered to be the temperature on a maximum and this maximum will be at a temperature below the wall temperature. From table 4.1, this temperature is then 90.95 °C at the position x_1 . The temperature of the second fringe at position x_2 is 80.19 °C and so on. With values of temperature and location, a function of temperature with position as the dependent variable can be determined using statistical curve fitting methods.

The temperature profile within the boundary layer near the wall was assumed to vary parabolically in the form $T(x) = a_0 + a_1x + a_2x^2$. The coefficients, a_0 , a_1 , and a_2 were calculated according to a parabolic regression model from

the matrices A and C as

$$A = \begin{bmatrix} n & \sum_i x_i & \sum_i (x_i)^2 \\ \sum_i x_i & \sum_i (x_i)^2 & \sum_i (x_i)^3 \\ \sum_i (x_i)^2 & \sum_i (x_i)^3 & \sum_i (x_i)^4 \end{bmatrix} \quad C = \begin{bmatrix} \sum_i T_i \\ \sum_i (x_i T_i) \\ \sum_i (x_i)^2 T_i \end{bmatrix} \quad (5.1)$$

$$a = A^{-1}C \quad (5.2)$$

where n is the number of data points, and a is the coefficient matrix for a_0 , a_1 , and a_2 .

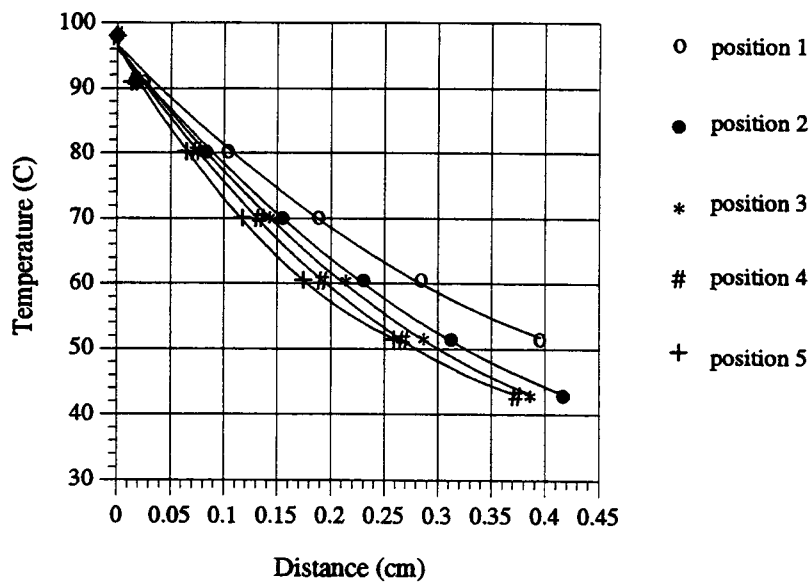


Figure 5.5 Curve fitting for the temperature profile near the wall at selected positions

MathCad and/or Deltagraph softwares were used to perform these calculations. After the function, $T(x)$, was determined using the parabolic regression model, the derivative of the function at $x = 0$, i.e. a_1 , which is directly related to the heat flux at the wall, was evaluated. Figure 5.5 shows the results of curve fitting for the 5 positions shown in figure 5.4. For this case, there were 7 measurable data points at positions 2, 3, and 4 in figure 5.4, and there were 6 data points at positions 1 and 5.

A Nusselt number based on Eq. (2.54) was used as the parameter for expressing the heat transfer rate in the open cavity. This parameter was determined according to

$$\text{Nu} = \frac{\sum_i \left(\Delta z \cdot \left. \frac{dT}{dx} \right|_{x=0} \right)}{\frac{L}{R} (T_w - T_{\text{res}})} \quad (5.3)$$

where i is the number of positions selected, T_w is the wall temperature of the open cavity and T_{res} is room temperature, which was 27 °C for this work. In the rectangular coordinates, R is one half of the width, W , of the cavity. Replacing the summation by the total length of the cavity, L , Eq. (5.3) becomes

$$\text{Nu} = \frac{W \cdot \left. \frac{dT}{dx} \right|_{\text{wall}}}{2(T_w - T_{\text{res}})} \quad (5.4)$$

Errors associated with fringe counting

There are some errors in the experiment associated with fringe counting. One very common type of error is the reading error of the distances - x 's in figure 5.4. However, the image can be magnified by a factor of 16 using existing computer graphic software such as Adobe Photoshop and Aldus Digital Darkroom. The reading error was much reduced using this large magnification. Another factor that affects the reading error is the fluctuation of the fringes while taking the picture. Pictures of fringes taken at different times show somewhat different patterns due to the fluctuation character of the flow. Statistical methods are required to cope with these fluctuation errors.

An encouraging feature of this experiment is that the fringes near the wall were relatively stable compared with those at the center of the cavity. This made a quantitative evaluation of the heat transfer rates through the wall possible since data points near the wall are more significant for calculating heat transfer rates. The fringes near the wall did, however, involve a certain amount of error due to the imperfect alignment of the interferometer. This error can be quantitatively described.

A uniform distributed intensity field, i.e. an infinite fringe field, was intended to be achieved on the observation screen in this study. A perfect infinite

fringe of uniform light intensity throughout the oval-shaped area of the light spot on the observation screen is technically impossible, because the flatness of the optics used for the experiment varied by $\lambda/5$ per inch of the light source. However, the error associated with this imperfect alignment can be quantitatively related to each fringe order on the screen.

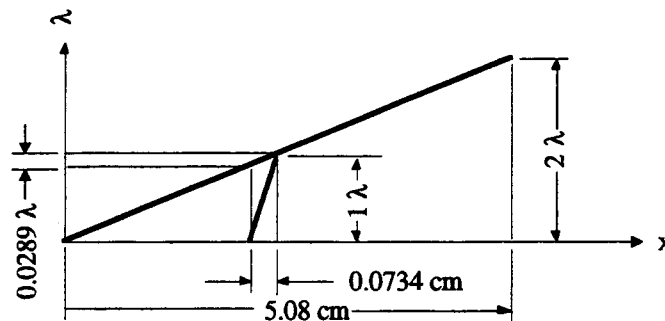


Figure 5.6 Contribution of errors for the counting of fringes due to the imperfect alignment of the interferometer

Figure 5.6 shows the wavelength variation with respect to the distance. The variation due to imperfect alignment of the interferometer in a 2.5" x 2" oval-shaped area is two fringe orders. The average spacing for the first 6 orders of fringes near the wall at position 3 in figure 5.4 is 0.0734 cm. Converting the average spacing for the first 6 order fringes in figure 5.4 into error associated with the variation of wavelength originated from the imperfect alignment, it is found that there is 0.0289 wavelength variation in a distance of 0.0734 cm. In other words, there is an average of 2.89% error associated with the

counting of fringes near the wall.

For graphic representation shown in figure 5.6, the error is associated with the size of spacing between fringes. The larger the spacing between fringes, the larger the error and vice versa. The fringes at the center of the open cavity in figure 5.4, for example, inherit more than 40% error. The fringe patterns at the centers of open cavities with greater width do not reflect the true temperature profiles.

5.4 EXPERIMENTAL VERIFICATIONS AND VERTICAL CHANNEL FLOW

To validate the use of the MZ interferometer, comparisons between experimental results and published analytical solutions of natural convection over a vertical flat plate were made. The situation with vertical channel flows were also studied.

LAMINAR NATURAL CONVECTION OVER A VERTICAL FLAT PLATE

Fringe patterns of natural convection over a flat plate are shown in figure 5.7(a). The same fringe pattern can be found in [37]. For figure 5.7(a), fringe patterns below 0 mm and above 70 mm associated much larger errors due to the imperfect alignment of the interferometer. The method described in section 5.3 was used to depict the temperature profiles and to evaluate the local Nusselt

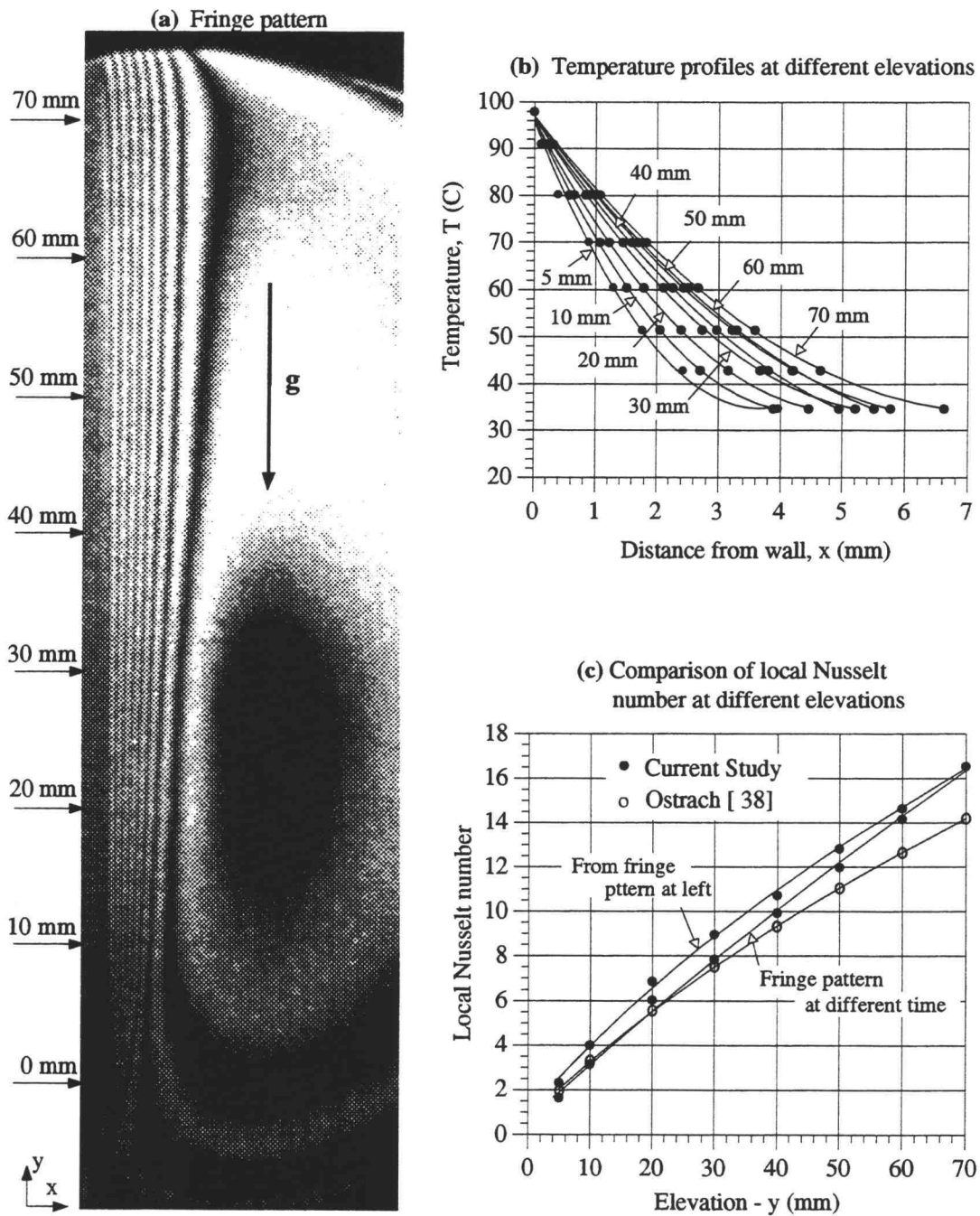


Figure 5.7 Natural convection over a vertical flat plate; (a) Interference fringe pattern for a constant wall temperature (b) Temperature profiles at different elevations interpreted from the fringe patterns (c) Comparison of local Nusselt numbers

numbers at different elevations. These temperature profiles and the local Nusselt numbers are shown in figure 5.7(b) and (c). The average Nusselt number, Nu_L , was then calculated from these local Nusselt numbers for a 70-mm-tall flat plate. The average Nusselt number evaluated from the fringe patterns in figure 5.7 was found to be 20.502

Heat transfer rates for natural convection over a constant temperature flat plate was analytically studied by Ostrach [38]. Procedures to evaluate the heat transfer rate can be found in Welty et al [18].

For air with a Prandtl number of 0.72 and a fluid film temperature of 90.95 °C, the first fringe temperature next to the wall, the resulting Local Nusselt numbers were evaluated and plotted in figure 5.7(c), and the average Nusselt number, Nu_L , for a 70-mm-tall flat plate with a 61 °C temperature difference was determined to be 18.925. A comparable result for the average Nusselt number for a 70 mm flat plate from Churchill and Chu [39] is 17.97 for laminar flow. The equation used to predict this average Nusselt can also be found in Welty et al [18]. The percentage difference of the average Nusselt number between figure 5.7(a) and Ostrach prediction, as well as figure 5.7(a) and Churchill's prediction, are 8.33% and 14.09% respectively. Small oscillations were observed near the wall for the case of flow over a flat plate. This produced a different value of the average Nusselt number at different times. Figure 5.7(c) shows results for the local

Nusselt number evaluated from the fringe pattern at a different time. The average Nusselt number for this case was calculated to be 18.373, which is 2.9% lower than the Ostrach value.

VERTICAL CHANNEL FLOW

Another case that was examined, using the apparatus of this study, was the vertical channel flow. The test section for vertical channel flow was configured removing the block on the bottom of the open cavity as shown in figure 5.3. The height of the vertical channel was fixed and the width of the channel was varied. Both walls of the channel were maintained at a constant temperature.

(a) Fringe patterns of a 1/4-in-wide vertical channel

Figure 5.8 shows a series of fringe patterns for a 1/4-in-wide vertical channel. The experimental procedure was first to introduce steam into the temperature control device to heat the left wall of the channel while the right side wall was maintain at room temperature. After a short time, the flow reached a steady state and a linear temperature profile was established in the upper portion of the channel. This behavior is evident in figure 5.8(a). Steam was next introduced to heat the right wall of the channel. Figure 5.8 (b)-(h) shows the sequential change in the fringe patterns at different times after the right wall

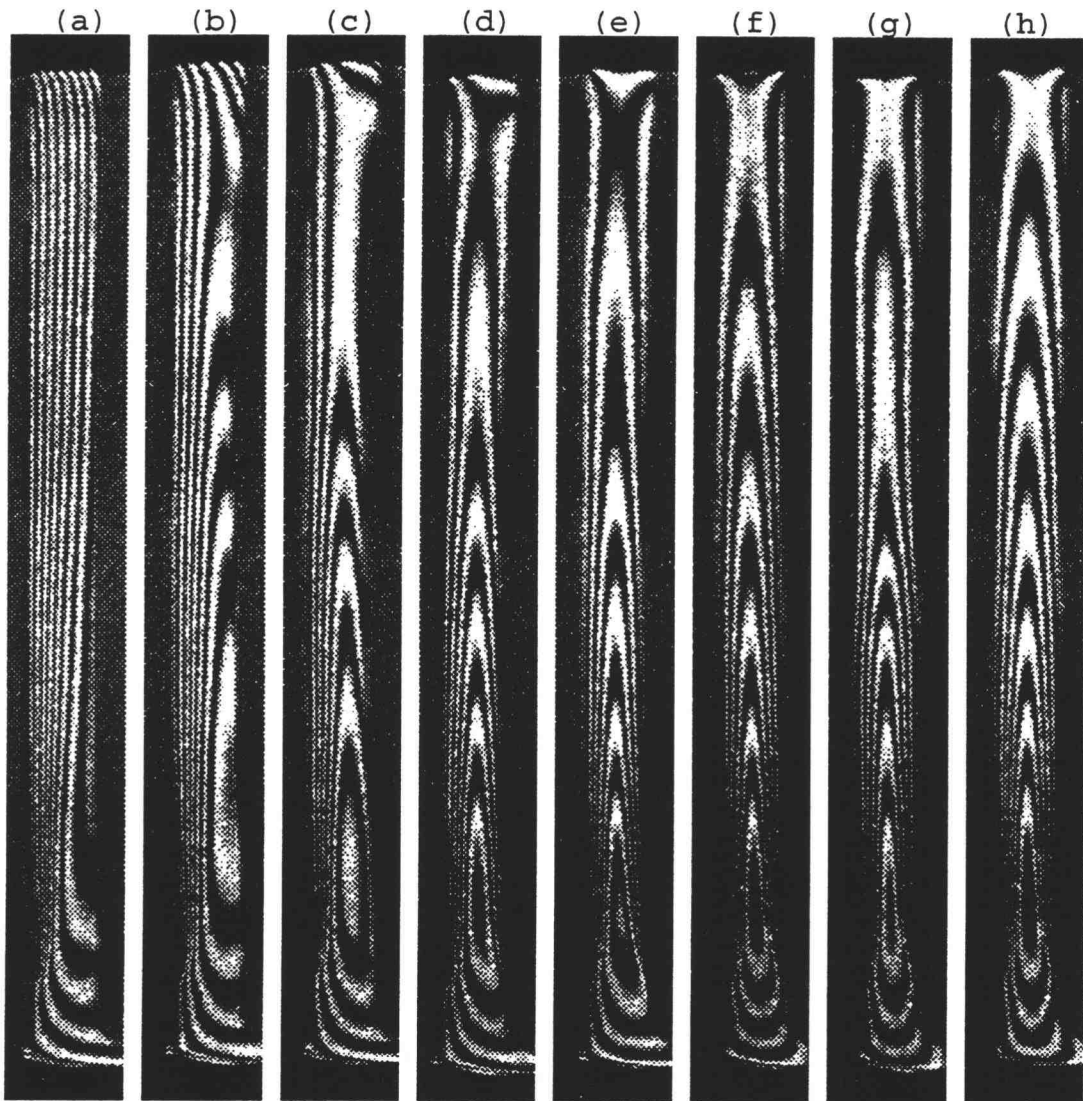


Figure 5.8 Fringe patterns of a 1/4" vertical channel at different times. The left wall of the channel was heated first, and then the right wall later.

of the channel was heated. The symmetrical fringe pattern of (f)-(h) appears to show the steady state case. It also shows oscillating flow behavior.

(b) Vertical channel flow with one wall heated

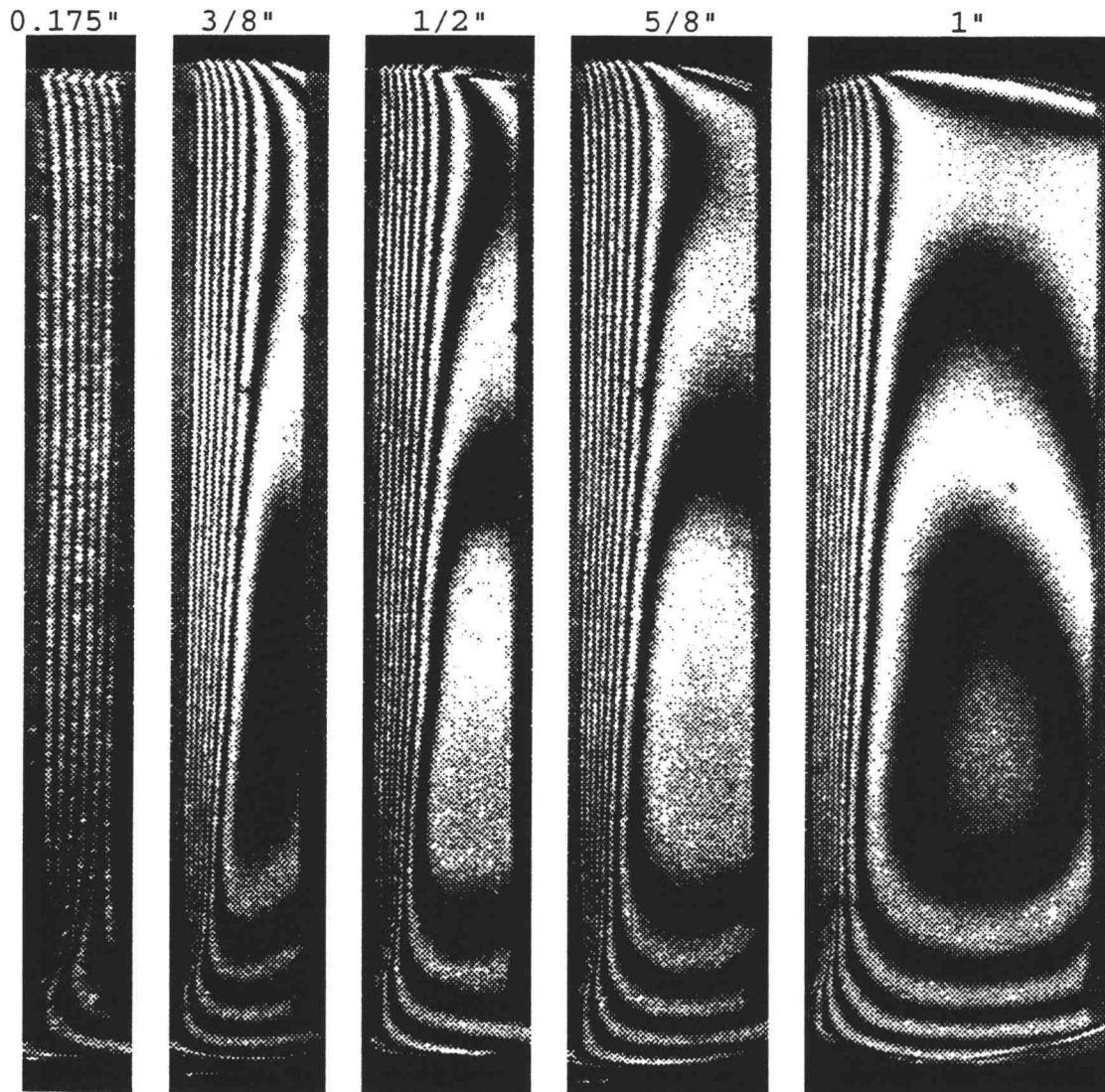


Figure 5.9 Fringe patterns for different width vertical channels with one wall heated and the other wall maintained at room temperature. The scale of these images is 1.5 times larger than the real dimensions. The width for the 0.175"-wide channel was doubled to distinguish the fringes.

The variation in boundary-layer thickness with the width of the vertical channel is illustrated in figure 5.9

for the case shown the left wall was heated. The fringe patterns shown are for steady state; i.e. when the temperature distribution across the top of the channel became linear. Note that the width has been increased by a factor of 2 of the 0.175"-wide channel to help in distinguishing the fringes.

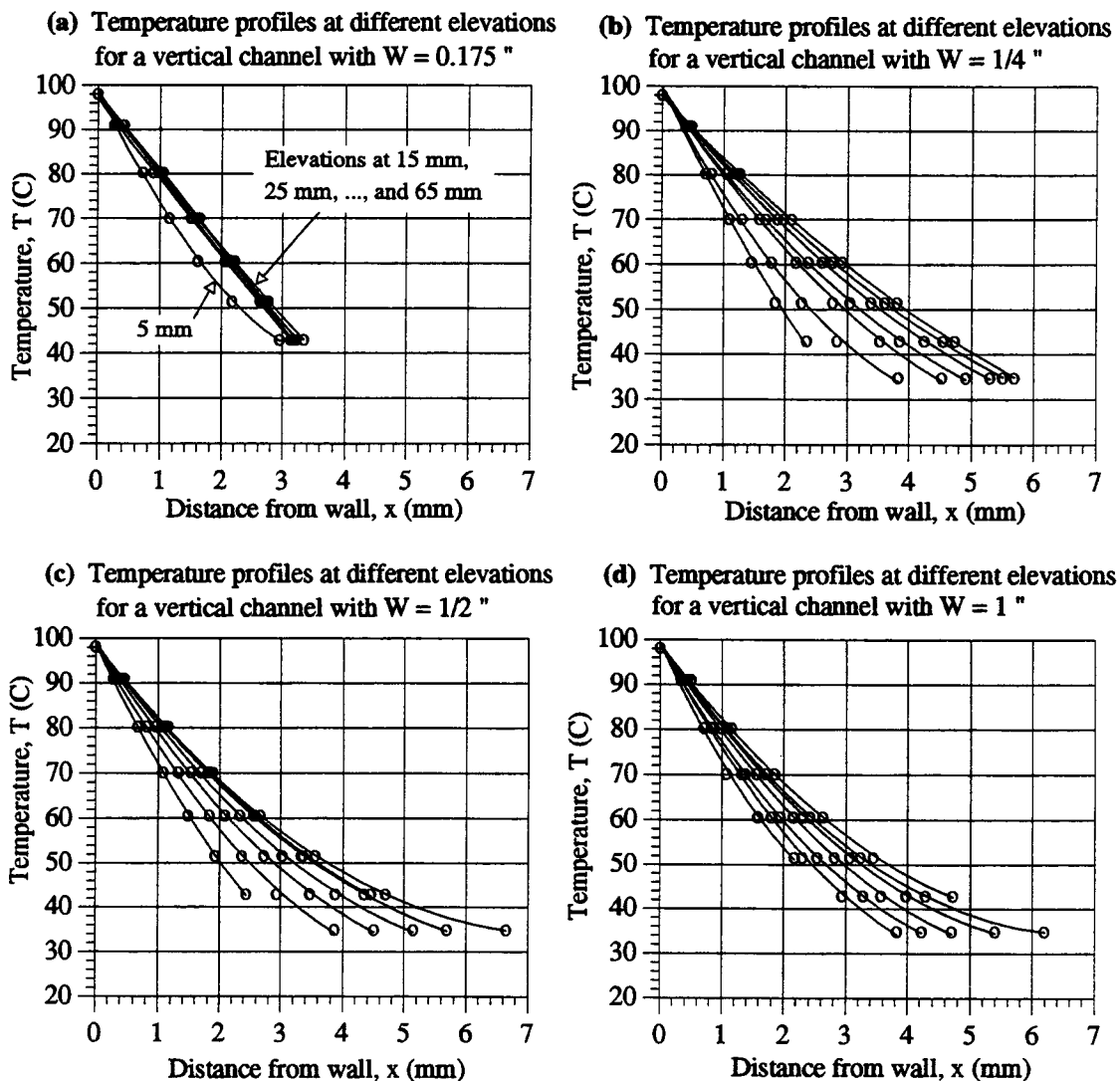


Figure 5.10 Temperature profiles at different elevations for vertical channels with $W = 0.175$ ", $1/4$ ", $1/2$ " and 1 "

Figure 5.10 shows temperature profiles at different elevations for several channel widths. For the 0.175"-wide channel, temperature profiles are linear at higher elevations. This is similar to the analytical solution predicted by Welty [40] for a vertical channel with one wall maintained at higher temperature and the other wall at a lower temperature.

Near the channel entrance, temperature profiles are clearly nonlinear since the cold wall and the ambient air temperatures were both at room temperature. As the width of the channel increased, the linearity of the temperature profiles decreased. As the width of the channel became very large, the fringe patterns and temperature profiles approached those for a flat plate.

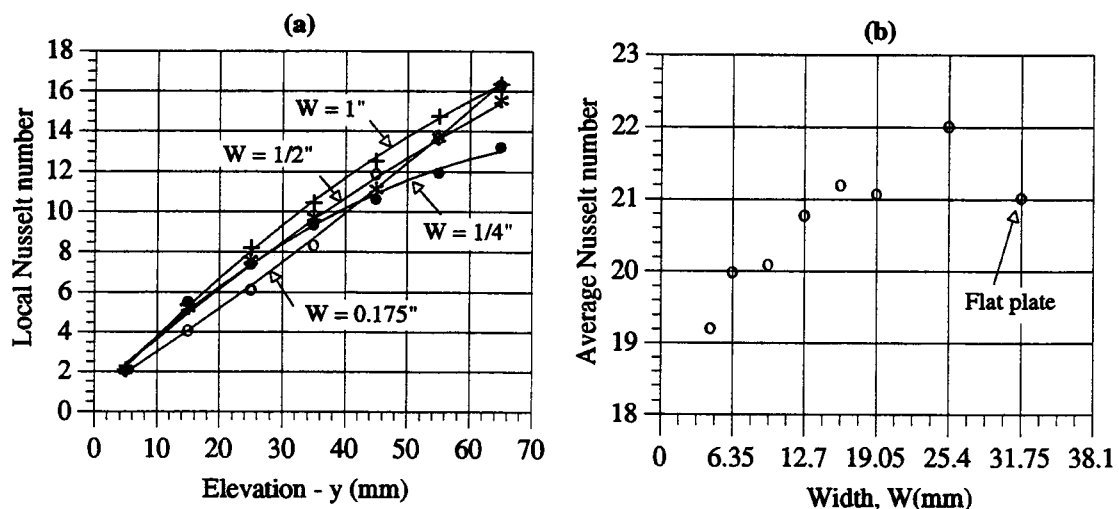


Figure 5.11 Local and average Nusselt number for different cases of vertical channel flow with one wall heated

The local Nusselt number varied linearly with elevation for the narrowest vertical channel as shown in figure 5.11(a). This is due to the presence of linear temperature profiles with equal gradients at every vertical position. The general trend of these results is that wider channels have higher heat transfer rates as figure 5.11(b) shown.

(c) Vertical channel flow with both walls heated

Fringe patterns for vertical channels with both walls maintained at the steam temperature are shown in figure 5.12. Similar to the case of 1/4" vertical channel in figure 5.8, symmetrical fringe patterns are shown after steady state were reached.

Referring to figures 5.8 and 5.12, the fringe patterns for the cases with $W = 1/4"$ and $0.175"$ shows a different behavior from other cases. For these two cases, the fluid at the top of the channel was stratified. A description of such a temperature profiles can be found in [40-41]. Counting the fringes for these two cases is difficult since all were crowded together at the channel entrance. The wall temperature near the entrance was impossible to determine due to the sudden change of temperature between fluid and the heated aluminum wall. For purposes of calculation, the wall temperature was assumed to be $98\text{ }^{\circ}\text{C}$. For the $0.175"$ case, a half fringe was counted at the elevation where the intensity was between bright and dark.

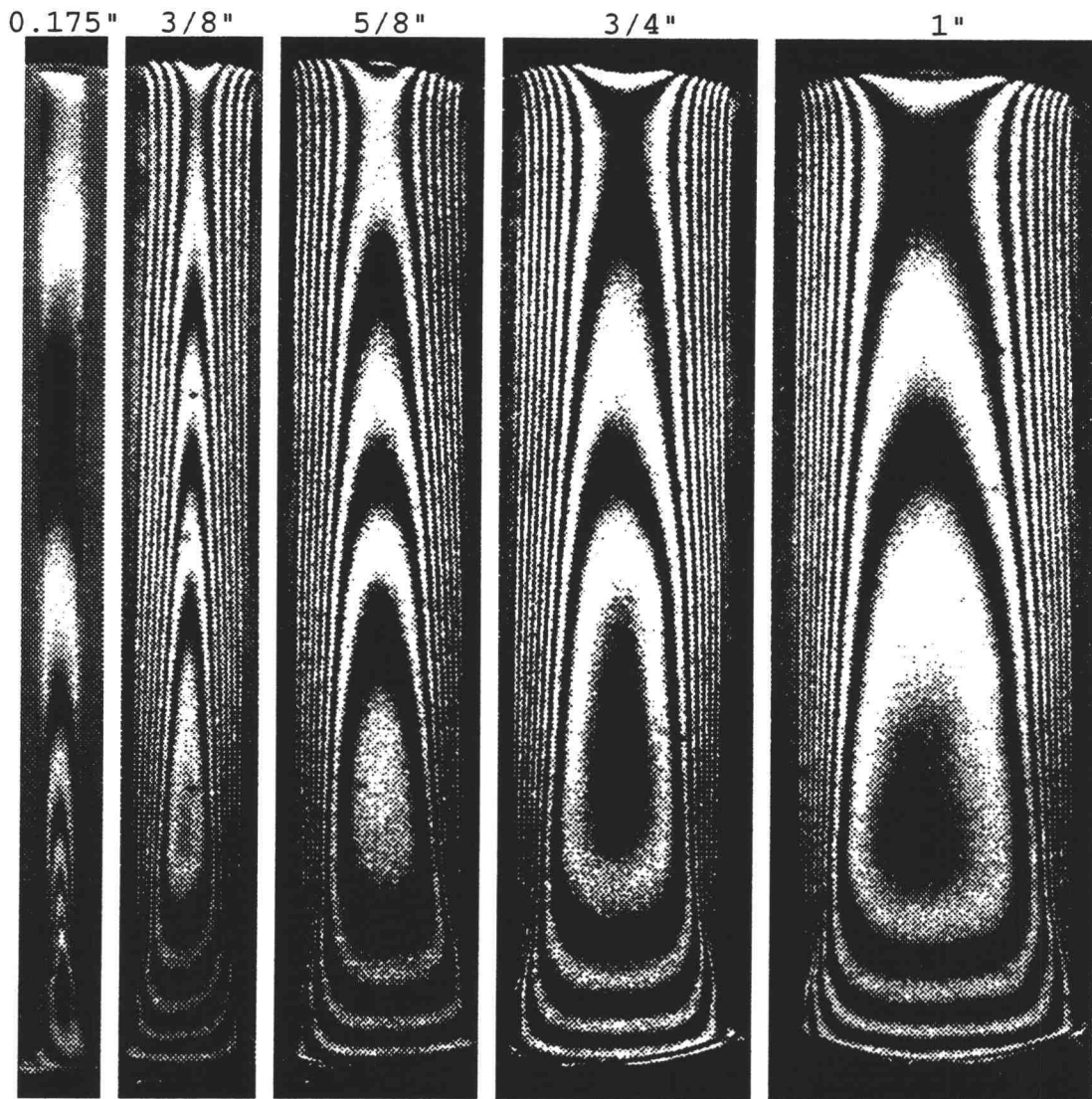


Figure 5.12 Fringe patterns for vertical channels with both walls heated. The scale of these images is 1.5 times larger than the actual dimensions.

Figure 5.13 shows temperature profiles at different elevations for selected cases. Differences in temperature gradients between the lowest and the highest elevations for narrower channels are larger than for the wider channel.

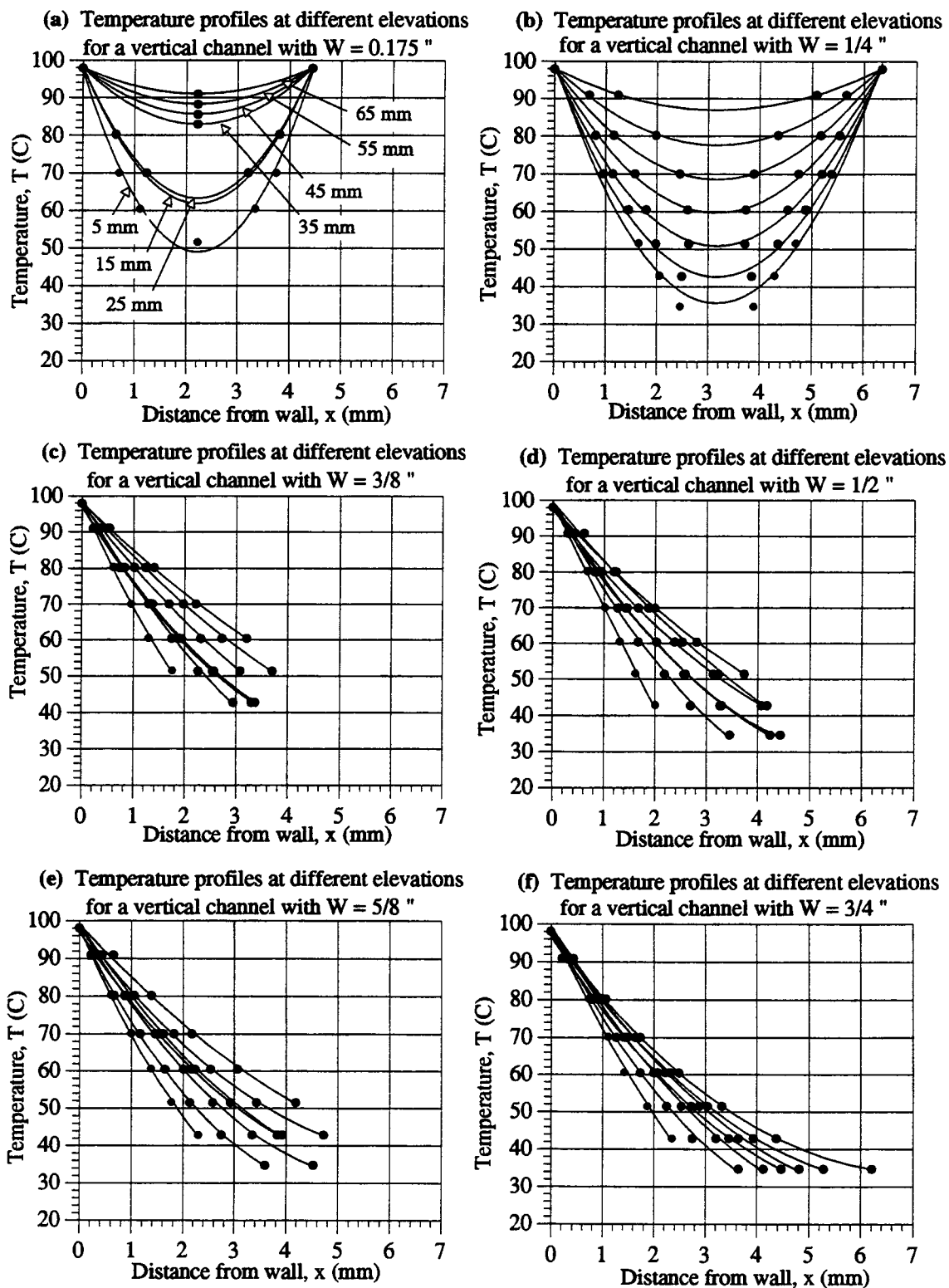


Figure 5.13 Temperature profiles at different elevations for vertical channels; both walls maintained at the same constant temperature.

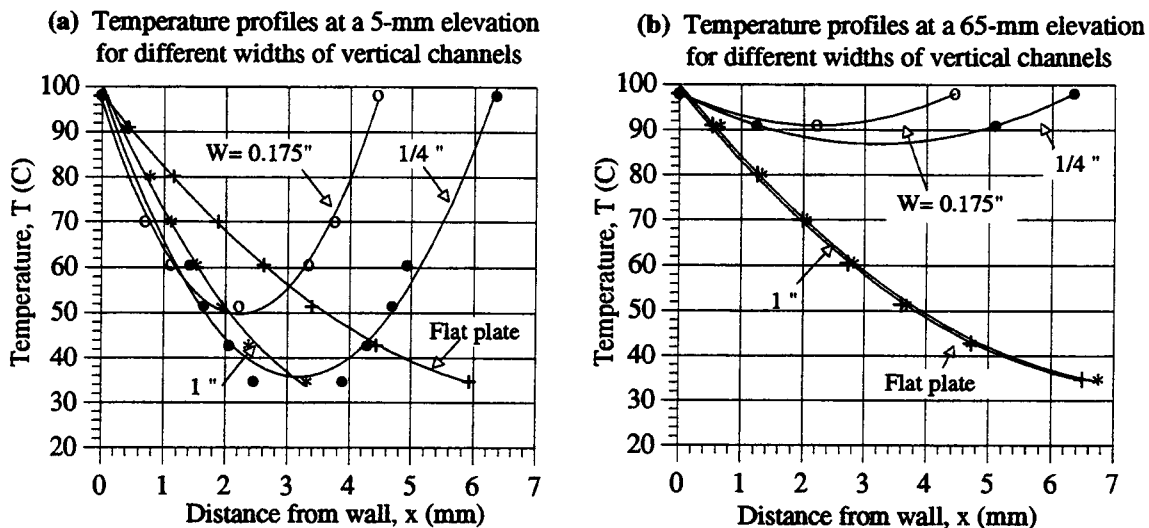


Figure 5.14 Temperature profiles at 5-mm and 65-mm for selected cases of vertical channels with both walls heated

Figure 5.14 shows the temperature profiles at the 5-mm and 65-mm elevations for selected cases. At the lower level, temperature gradients for the narrower channel are higher than for wider channels and the flat plate case, figure 5.14(a). In contrast, the temperature gradient at the higher position is lower for the narrower channels, as seen in figure 5.14(b).

Figure 5.15(a) shows the local Nusselt number for selected cases. The local Nusselt number for narrow channel first increases with elevation and then decreases. This can be understood since, for long channel, there will be no heat transfer at the top, because the fluid temperature will approach the wall temperature. The point where the local Nusselt number began to decrease varied with the length-to-width ratio of the channel. All cases

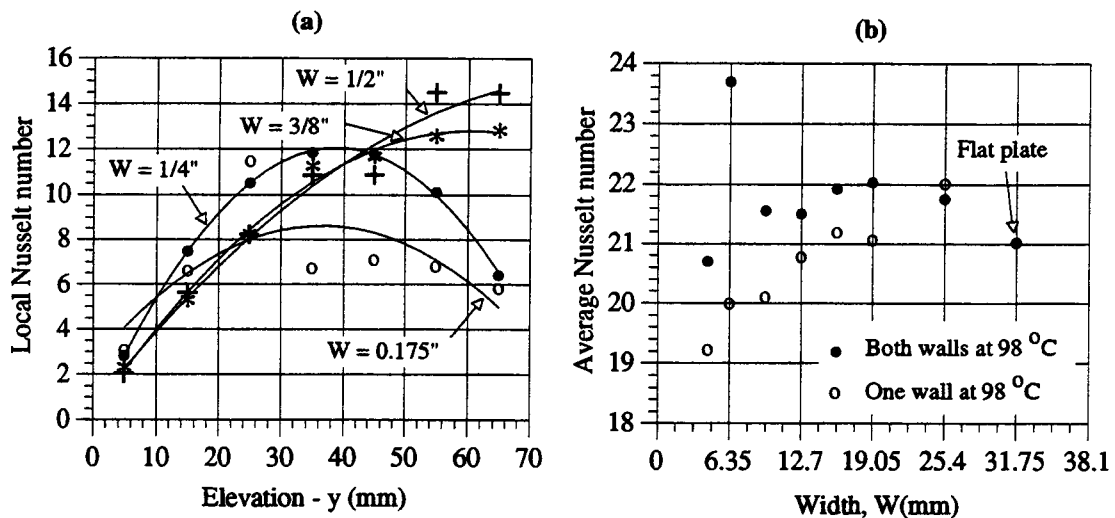


Figure 5.15 Local Nusselt number and Average Nusselt for vertical channels with both walls held at the steam temperature

of vertical channels used in this study had the same fixed length; only in the narrowest two cases, 0.175" and 1/4", did this decrease in the local Nusselt number occur.

The average Nusselt number for different channel widths with one wall and both walls heated is shown in figure 5.15(b). Channels with both walls heated experienced higher heat transfer rates than those with one wall heated.

Calculations of the Nusselt numbers for these channels were based on the assumption of a constant wall temperature at 98 °C measured at the aluminum surface in figure 5.1. This is true for most cases of vertical channels except for the very narrow cases, $W = 0.175"$ and $1/4"$. At the channel entrance, air at room temperature entered and thermal boundary layer grew as the elevation increased.

For a wide channel, there is enough space in the x -direction to allow the build-up of a thermal boundary starting at the channel entrance. For very narrow channels, there was insufficient room for development of the thermal boundary layer. Note that the thermal entrance length for the case with $W = 1/4"$ is much longer than for $W = 0.175"$.

With the test section used in this study, fully developed temperature profiles could be achieved only for the narrowest two cases, $W = 0.175$ and $W = 1/4"$. For these two cases, at steady state, oscillating fringe patterns with a relatively stable frequency were observed. Fringe patterns (f)-(h) as shown in figure 5.8 display this oscillating nature. Some cases without fully developed temperature profiles also exhibit this oscillating behavior. The frequency of oscillation was a function of the width of the channel.

One observation from oscillating behavior is that the narrower the channel, the higher the frequency rate and the magnitude of fluctuation. This is due to the stability of the fluid system in the vertical channel and the reservoir above the channel. For very narrow channels, the fluid at the upper portion of the vertical channel was very close to the wall temperature. Thus, it is much lighter the fluid at the top. For wider vertical channel, the fluid at the upper portion of the channel is colder than that for narrower channel. As a result, the fluid system for

narrower channel is more unstable and, consequently, causing a larger and faster oscillating motion.

5.5 COMPARISON OF FRINGE PATTERNS BETWEEN EXPERIMENTAL AND NUMERICAL RESULTS

For the comparing experimental and numerically-generated fringe patterns, cases of an open cavity, with different dimensions, in rectangular coordinates were used. Cavity dimensions were depicted and described in sections 3.5 and 5.1. For numerical purposes, boundary conditions can be easily altered by changing of the input parameters of the computer program. Boundary conditions at the bottom of the cavity were set as both adiabatic and at constant temperature for comparison with experimental results. For the experiments, two different test setups were used, as depicted in figure 5.2 and 5.3. Both were used in an attempt to model the open cavity as two-dimensional. The case depicted in figure 5.3 gave the better result when two optical flats were used on both ends of the cavity. An adiabatic boundary condition at the bottom of the cavity was approximated using the combination of weather-stripping and wood as shown in figure 5.3. Fringe patterns from both test section configurations are shown in figure 5.18.

A total of 16 cases were selected for both a qualitative comparison of fringe patterns, in this section, and a quantitative comparison of the heat transfer rates to

follow in the next section. Due to the limitation imposed by the light-beam diameter of the MZ interferometer, the maximum length and width of the open cavity were selected to be $L = 5.08$ cm (2 inches) and $W = 3.81$ cm (1.5 inch), respectively. Before discussing the 16 selected cases, two additional cases will be discussed first.

Figure 5.16 shows experimental and numerically-generated fringe patterns for an open cavity with $L = 5.08$ cm and $W = 1.588$ cm. The experimental setup in figure 5.2 was used to obtain these fringe patterns. Rather than an adiabatic boundary condition at the bottom of the cavity, a constant temperature of 98 °C was used in the numerical modeling for this case. This was done realizing that some heat was transferred to the acrylic block at the bottom of the cavity during the experiments.

Experimental results showed that the fringes oscillated. The experimental images in figure 5.16 do not capture these oscillating characteristics. Experimental fringe patterns in the cavity were stable except when hot fluid "burst" out into the reservoir. Numerical results at 1 second show features which are similar to the experimental results. After 1 second, the two sets of results were no longer similar. This difference was due to different physical characteristics of the experimental and numerical models. The open cavity was considered two-dimensional for calculation purposes. The experiment model was physically three-dimensional. Air streaming in from

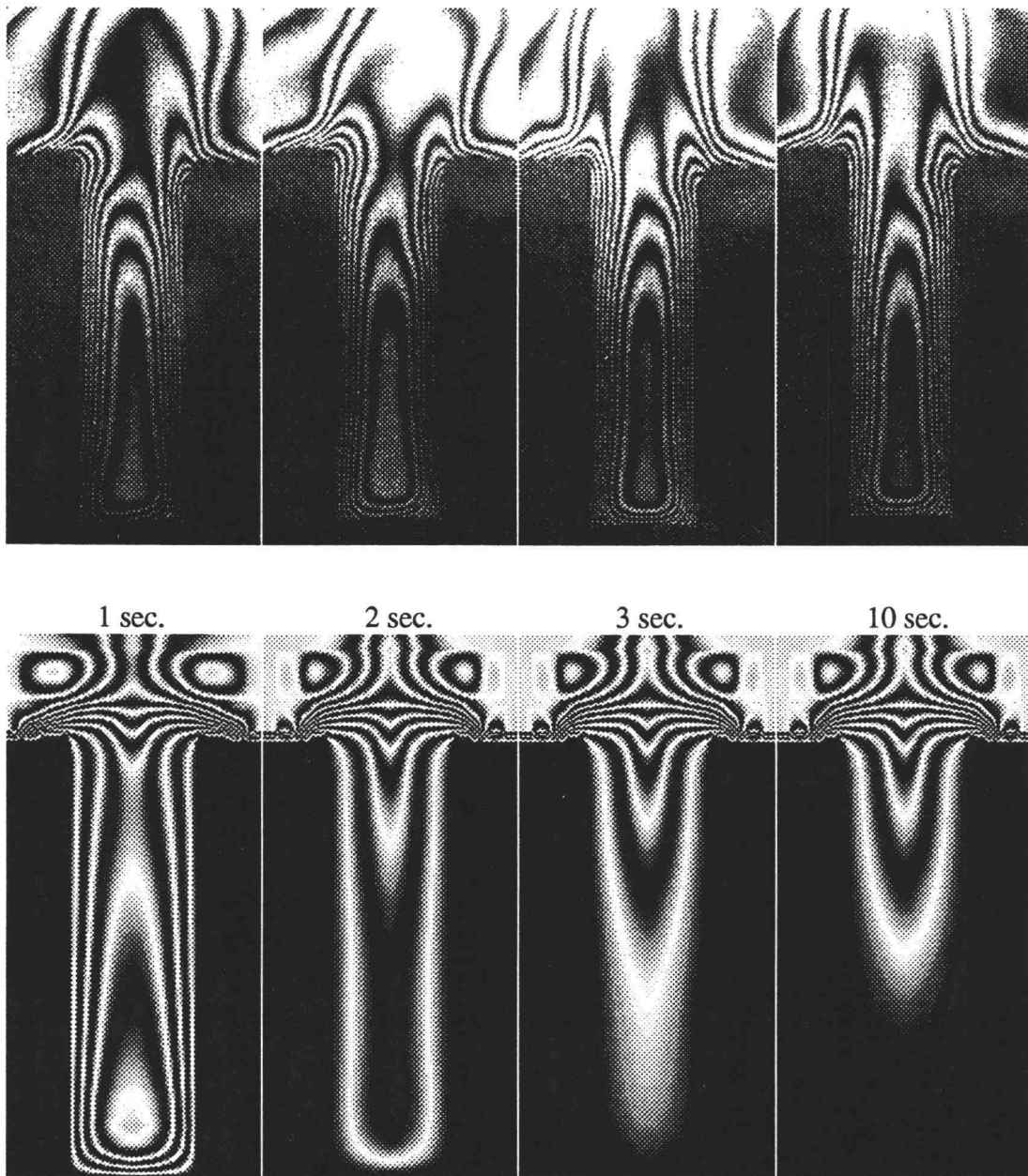


Figure 5.16 Experimental and numerically-generated fringe patterns at different times for the case of an open cavity with $L = 5.08$ cm and $W = 1.588$ cm. The top row depicts experimental results, and the bottom row shows the numerical results.

both ends of the cavity significantly affected the flow behavior in the cavity.

Experimental results showed that, for a wider cavity, the fringe pattern along one side was similar to a fringe pattern for free convection along a vertical flat plate as shown in section 5.4. Figure 5.17 shows another comparison for the case of an open cavity with $L = 5.08$ cm

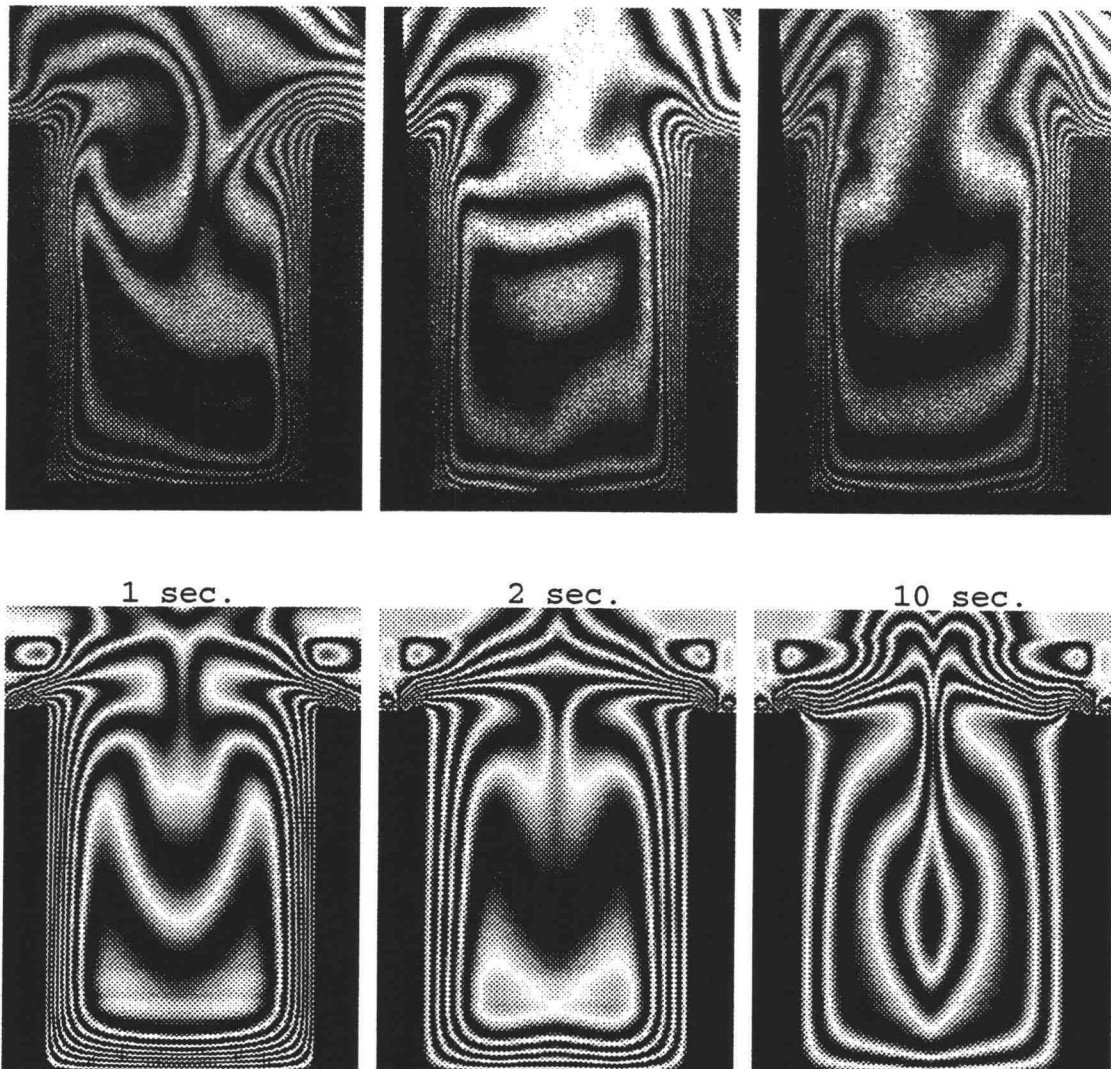


Figure 5.17 Experimental and numerically-generated fringe patterns for the case of an open cavity with $L = 5.08$ cm and $W = 3.81$ cm. Experimental results are in the top row.

and $W = 3.81$ cm. The boundary condition at the bottom of the cavity was at a constant temperature. A much larger core region at the center of the cavity is evident in the experimental results. As with the case shown in figure 5.16, numerical results after long times are not similar to experimental results due to air flow in the z -direction. Also, experimental results depict less stable behavior at the cavity center for the case in figure 5.17. Fringes near the wall show relatively stable patterns. These fringe pattern differences at the center and at the cavity wall are related to an error in the setup of the interferometer; this was discussed in section 5.3.

Fringe Comparison of 16 cases of open cavities

Sixteen open cavity cases were considered, values of cavity widths were $W = 1/4"$, $5/8"$, $1"$, and $1.5"$, and heights were $L = 1/2"$, $1"$, $1.5"$, and $2"$. Fringe patterns, both experimental and numerically-generated, are shown in figure 5.18 in the following 6 pages. Four fringe patterns are shown for each case. These are: image(a) - experimental fringe pattern at steady state using the apparatus shown in figure 5.2; image(b) - experimental fringe pattern at steady state using the apparatus shown in figure 5.3; image(c) - numerically-generated fringe patterns at 1 second; and image (d) - numerically-generated fringe patterns at steady state. In this figure, fringes

(1) Open cavity with $L = 5.08$ cm and $W = 3.81$ cm

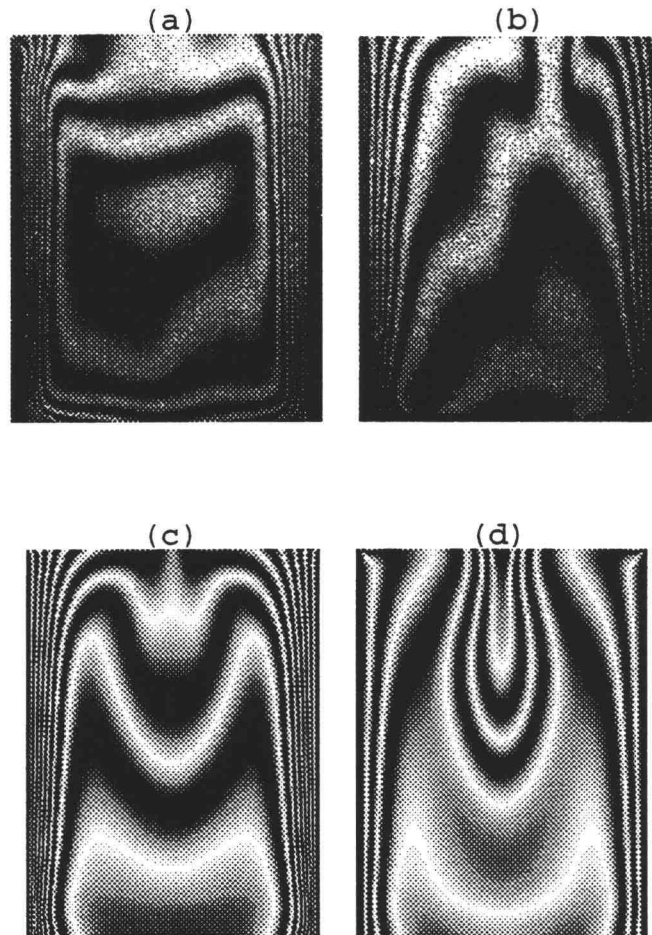
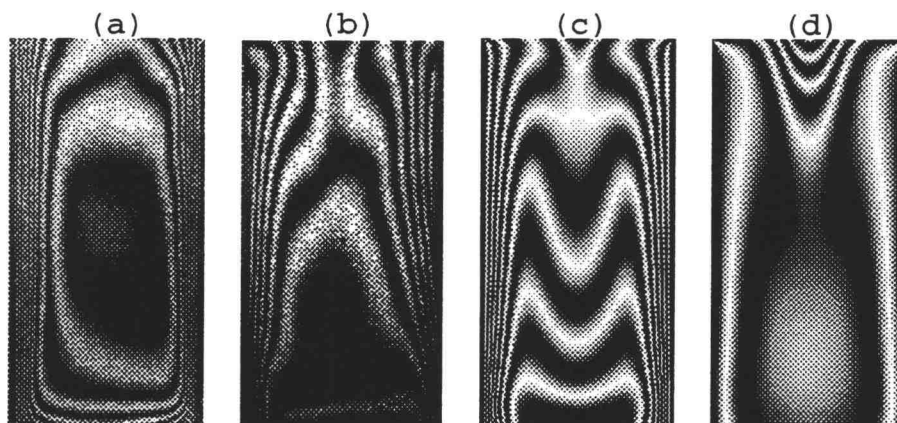
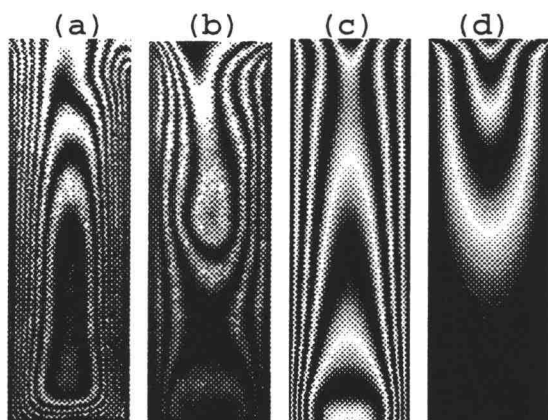


Figure 5.18 Experimental and numerically-generated fringe patterns for the 16 selected cases of open cavities; (a) Experimental fringe patterns for the open cavity without windows on both ends of the test section (b) Experimental fringe patterns for the open cavity with windows on both ends (c) Numerically-generated fringe patterns at 1 second (d) Numerically-generated fringe patterns at steady state

(2) Open cavity with $L = 5.08$ cm and $W = 2.54$ cm



(3) Open cavity with $L = 5.08$ cm
and $W = 1.59$ cm



(4) Open cavity with $L = 5.08$ cm
and $W = 0.635$ cm

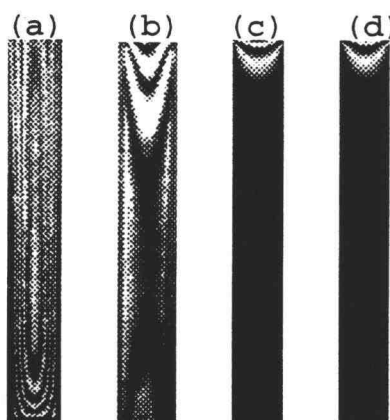
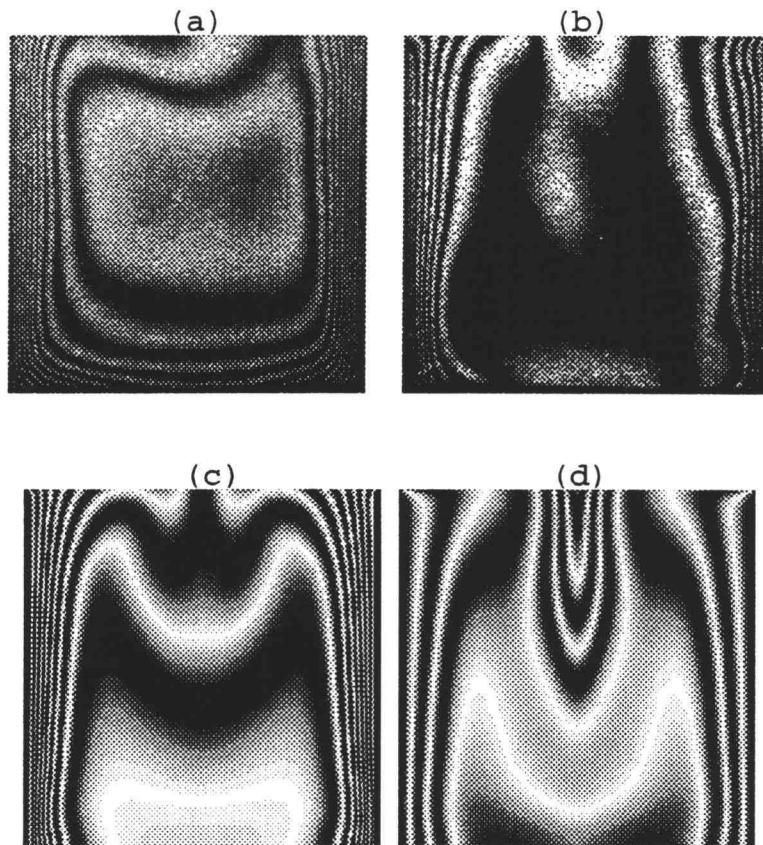


Figure 5.18 Continued

(5) Open cavity with $L = 3.81$ cm and $W = 3.81$ cm



(6) Open cavity with $L = 3.81$ cm and $W = 2.54$ cm

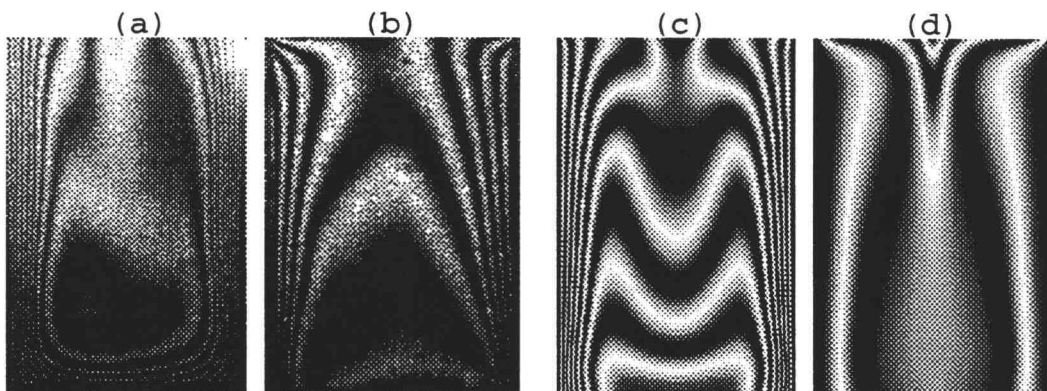
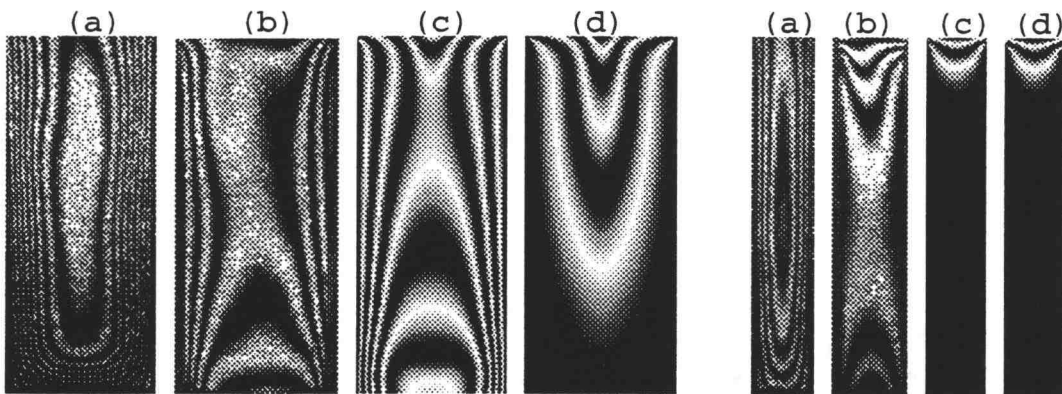


Figure 5.18 Continued

(7) Open cavity with $L = 3.81$ cm
and $W = 1.59$ cm

(8) Open cavity with $L = 3.81$
cm and $W = 0.635$ cm



(9) Open cavity with $L = 2.54$ cm and $W = 3.81$ cm

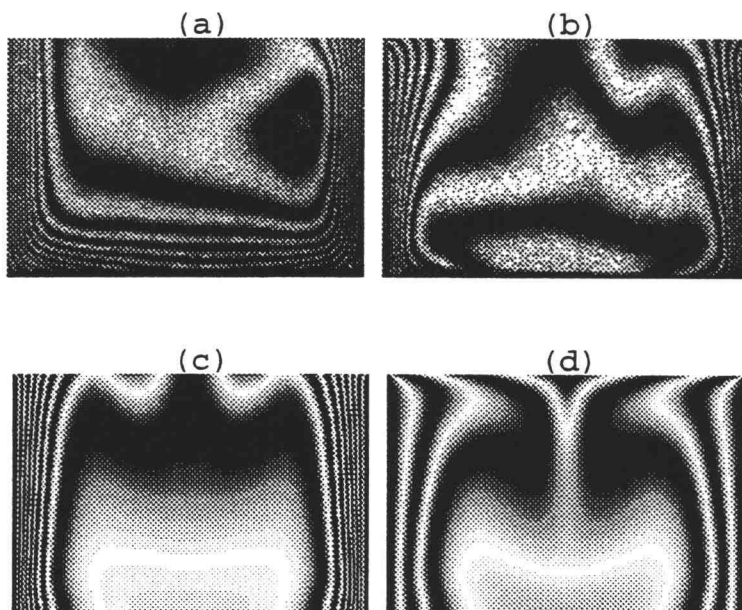
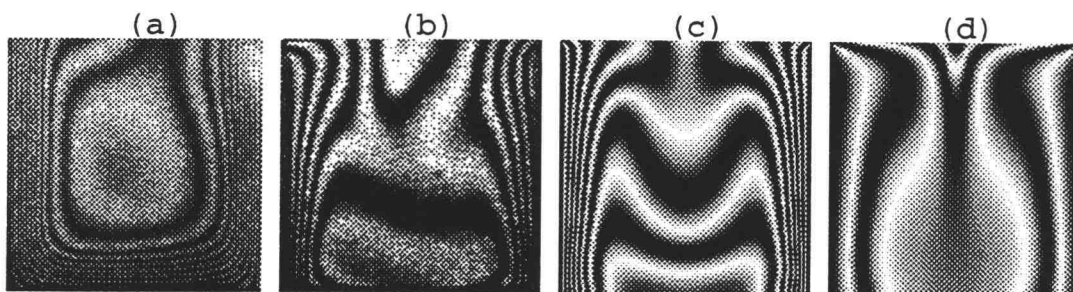
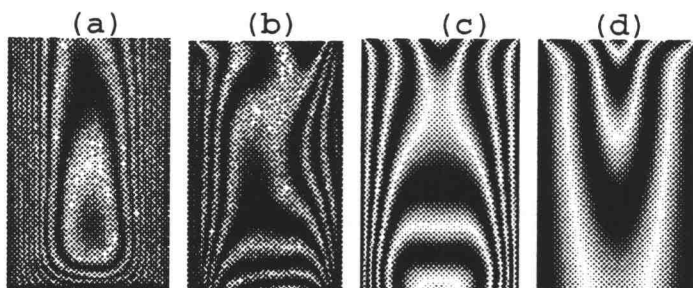


Figure 5.18 Continued

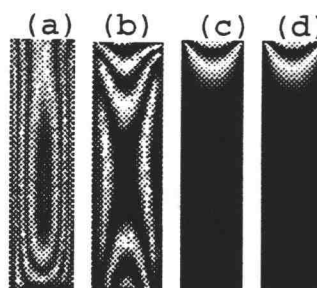
(10) Open cavity with $L = 2.54$ cm and $W = 2.54$ cm



(11) Open cavity with $L = 2.54$ cm
and $W = 1.59$ cm



(12) Open cavity with $L = 2.54$ cm
and $W = 0.635$ cm



(13) Open cavity with $L = 1.27$ cm and $W = 3.81$ cm

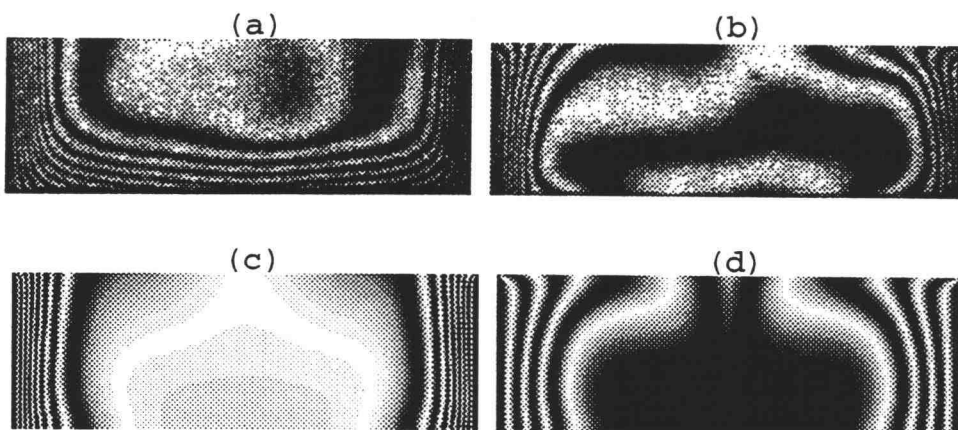
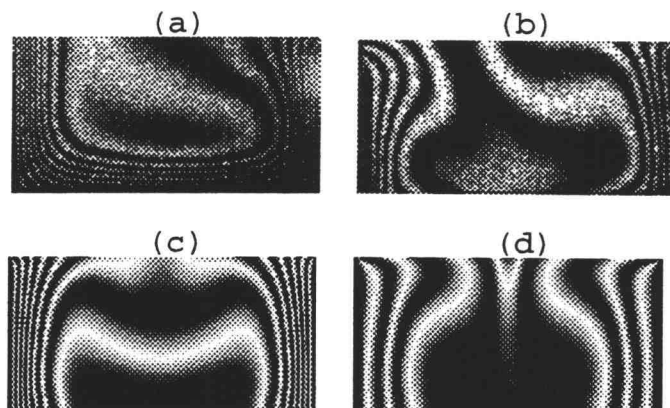
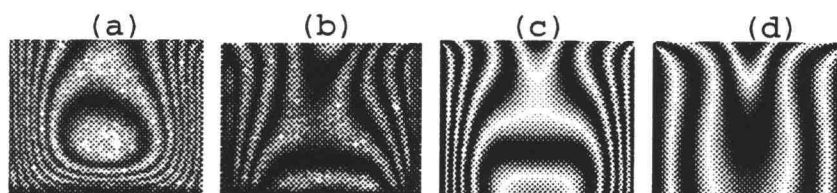


Figure 5.18 Continued

(14) Open cavity with $L = 1.27$ cm and $W = 2.54$ cm



(15) Open cavity with $L = 1.27$ cm and $W = 1.59$ cm



(16) Open cavity with $L = 1.27$ cm and $W = 0.635$ cm

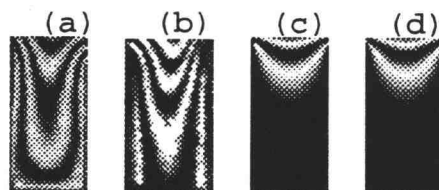


Figure 5.18 Continued

in the open cavity are shown, those in the reservoir are excluded. Quantitative analysis of the heat transfer rates discussed in the next section were based on interpretation the fringes in these images.

From these fringe patterns, several conclusions can be made. For the two-dimensional open cavity, the model used in figure 5.3 give a better approximation than in figure 5.2. Thus, as expected, the addition of two windows on both ends of the cavity did reduce the third dimensional effect. Fringe patterns for shorter cavities were more similar than for longer cavities. This is again related to two-dimensional modeling approximation. Even with windows on both ends, the apparatus is, nevertheless, still a three-dimension cavity. The approximation is better when the depth-to-height ratio of the cavity is increased, i.e. with a fixed depth test section, shorter cavities are much more alike. A better two-dimensional approximation is to increase the depth of the test section. There is a practical trade-off, however, because of the increased difficulty in counting the fringes.

Another observation, relating to the fringe patterns in figure 5.18, is the similarity between experimental and numerical results for narrower and taller cavities. For a cavity with $W = 0.635$ cm and $L = 5.08$ cm, the fluid in the bottom of the cavity is seen to be stratified at the same temperature of the cavity walls, in both experimental and numerical cases. Numerical results for this case show a

slight oscillation in the fringe pattern. Experimental results for this case show a much larger amplitude fluctuations. As with the patterns of figure 5.16, those in this case remained stable until the moment when the fluid burst out from the bottom of the cavity. Figure 5.19 shows a series of fringe patterns for this case.

Figure 5.19(a) shows fringe pattern for the open cavity where only the left wall was heated and the other wall maintain at the room temperature. Figure 5.19(b)-(e) show oscillating behavior at different times, and figure 5.19(f) shows the numerically-generated fringe pattern for the same case. Both the experimental and numerical results show that the temperature changes rapidly at the open end

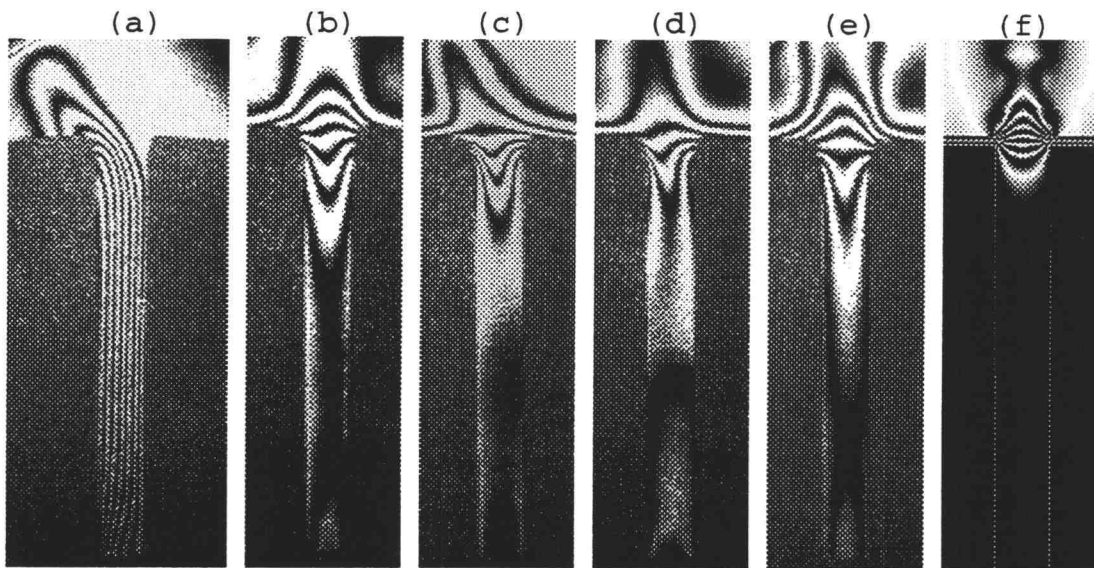


Figure 5.19 Fringe patterns at different times for the case of an open cavity with $W = 0.635$ cm and $L = 5.08$ cm; (a) Fringe pattern with only the left wall of the cavity heated (b)-(e) Fringe patterns at different times with both walls heated (f) Numerically-generated fringe pattern at steady-state for the same case

of the cavity. Also, experimental results show that, at the open end of the cavity, the fringe patterns were unstable.

5.6 COMPARISON OF HEAT TRANSFER RATES BETWEEN EXPERIMENTAL AND NUMERICAL RESULTS

A quantitative comparison of the heat transfer rates for the 16 selected cases depicted in figure 5.18 is discussed in this section. The parameter used for this comparison is the average Nusselt number defined in Eq.(5.3). Note that the characteristic length for these Nusselt numbers is the width, and the characteristic length for the Nusselt numbers in section 5.4 is the height of the vertical channel.

Table 5.1 lists the Nusselt number values corresponding to the fringe patterns in figure 5.18. The first column of experimental Nusselt number values, (a) w/o, lists Nusselt number values without the two windows on both ends of the test section. The second column, (b) w/, lists values with the two windows on the ends of the test section. Numerical results are listed at times of 1, 2, and 5 seconds after the heat transfer process began, and at steady state. Note that steady state values are average values from 11 seconds to 20 seconds. Fringe patterns, however, were shown only at 1 second and 20 seconds in

Table 5.1 Experimental and numerical results of Nusselt number for the selected cases of open cavities

Dimensions of selected cases				Nuselt number, Nu					
				Experimental		Numerical			
No.	W(cm)	L (cm)	L / W	(a) w/o	(b) w/	(c) 1 sec.	2 sec.	5 sec.	(d) steady
1	3.81	5.08	1.33	6.334	4.506	5.229	3.476	1.832	2.214
2	2.54	5.08	2.00	4.568	2.721	2.768	1.400	0.807	0.830
3	1.588	5.08	3.20	2.469	1.641	0.971	0.412	0.239	0.234
4	0.635	5.08	8.00	1.070	0.405	0.054	0.051	0.051	0.051
5	3.81	3.81	1.00	7.174	5.236	5.494	3.764	1.978	2.504
6	2.54	3.81	1.50	4.719	2.354	2.873	1.536	1.040	1.054
7	1.588	3.81	2.40	2.735	1.238	1.033	0.472	0.319	0.316
8	0.635	3.81	6.00	0.944	0.273	0.073	0.070	0.070	0.070
9	3.81	2.54	0.67	9.200	5.960	6.042	4.348	2.489	2.963
10	2.54	2.54	1.00	5.220	2.867	3.182	1.836	1.397	1.407
11	1.588	2.54	1.60	2.920	1.478	1.142	0.603	0.475	0.474
12	0.635	2.54	4.00	0.854	0.492	0.108	0.105	0.105	0.105
13	3.81	1.27	0.33	9.795	6.121	6.885	5.625	3.941	3.707
14	2.54	1.27	0.50	6.140	3.432	3.977	2.698	1.977	1.959
15	1.588	1.27	0.80	3.045	1.381	1.494	1.016	0.930	0.930
16	0.635	1.27	2.00	0.681	0.610	0.216	0.213	0.213	0.213

figure 5.18. For all 16 selected cases, a steady state solution was reached after 10 seconds. Some cases show an oscillating behavior at steady state.

Figure 5.20 shows a comparison of the Nusselt numbers between the experimental results, both with and without windows on the ends of the test section, along with numerical results. These plots correspond to the cases listed in Table 5.1. In figure 5.20, (a) shows the 4 cases with $L = 5.08$ cm; (b) shows the 4 cases with $L = 3.81$ cm; (c) shows the 4 cases with $L = 2.54$ cm; and (d) shows the 4 cases with $L = 1.27$ cm in the Table 5.1.

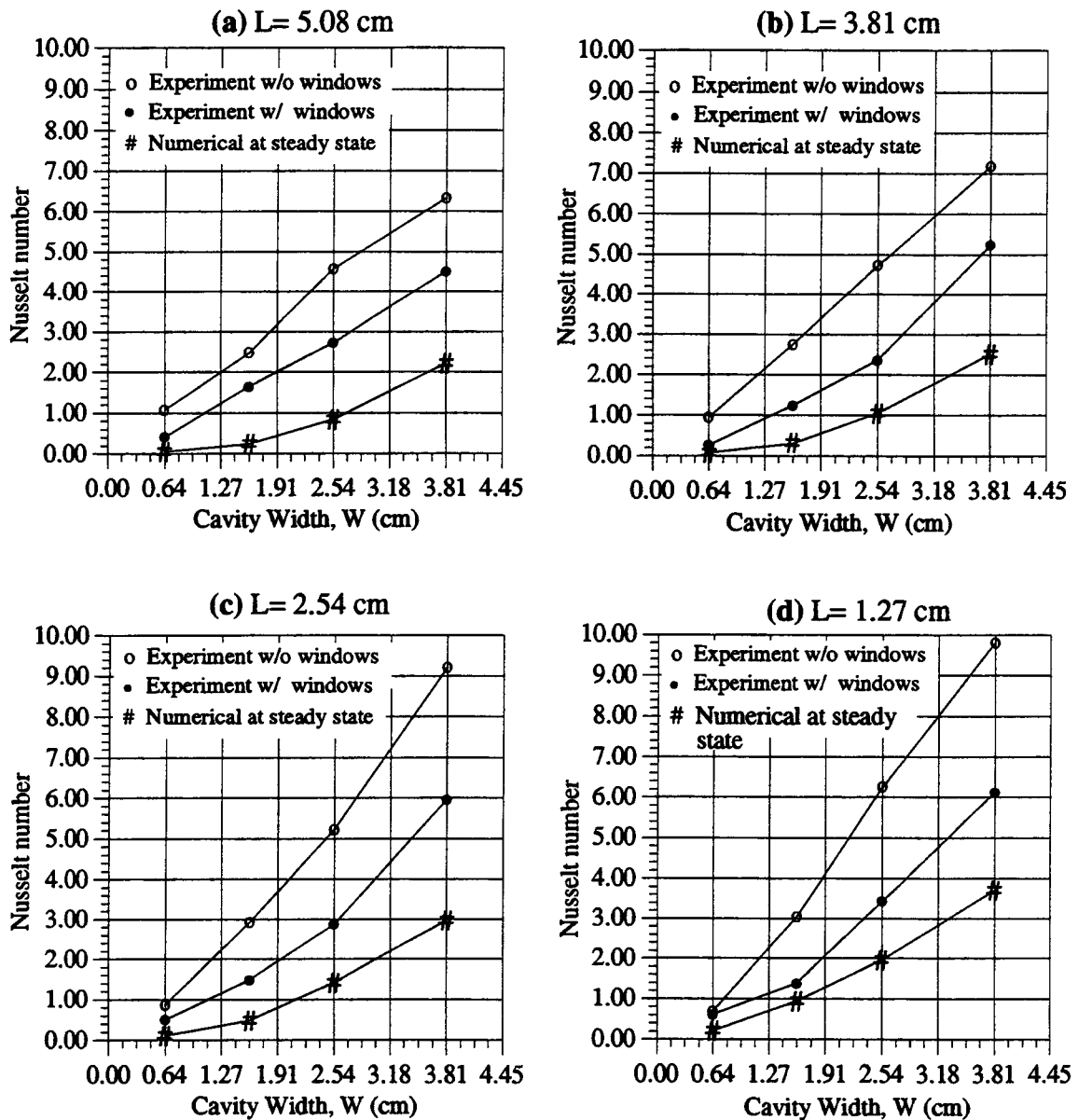


Figure 5.20 Comparison between the numerical and experimental results of Nusselt number for selected cases of open cavities; (a) $L = 5.08$ cm (b) $L = 3.81$ cm (c) $L = 2.54$ cm (d) $L = 1.27$ cm

It is apparent that with windows on both ends of the test section, better results were obtained. Without the windows, much higher values of Nusselt number were observed due to air flow in the z -direction, i.e. air flow from both

ends of the test section. Nusselt number values obtained both experimentally and numerically compare better for shorter cavities.

Figure 5.21 shows the same sort of plots for the 16 selected cases. Rather than plotting Nu versus the width of the cavity, this figure shows four plots of Nusselt number values versus the cavity height with a fixed cavity width. Cases for very narrow open cavities have lower Nusselt numbers values due to the definition of the Nusselt number, which use the width as the characteristic length. Numerical prediction shows that the taller the cavity the less the heat transfer rates for open cavities with the width fixed. Experimental results without windows on both ends agree with this trend except for the very narrow cases. The other experimental result, with windows on the test section, did not show this general trend. Fringe patterns from this setup exhibit a much more unsteady behavior.

From the comparisons in Table 5.1 and figures 5.20 and 5.21, experimental results without the two windows yielded a much higher values of Nusselt number. The effect of air flow in the z -direction was the cause of these higher values. As indicated in figure 5.2, the ends of the test section were open to the atmosphere allowing cold fluid to enter on both ends of the cavity. Entrainment of the hot fluid results in higher fluid temperatures for both the

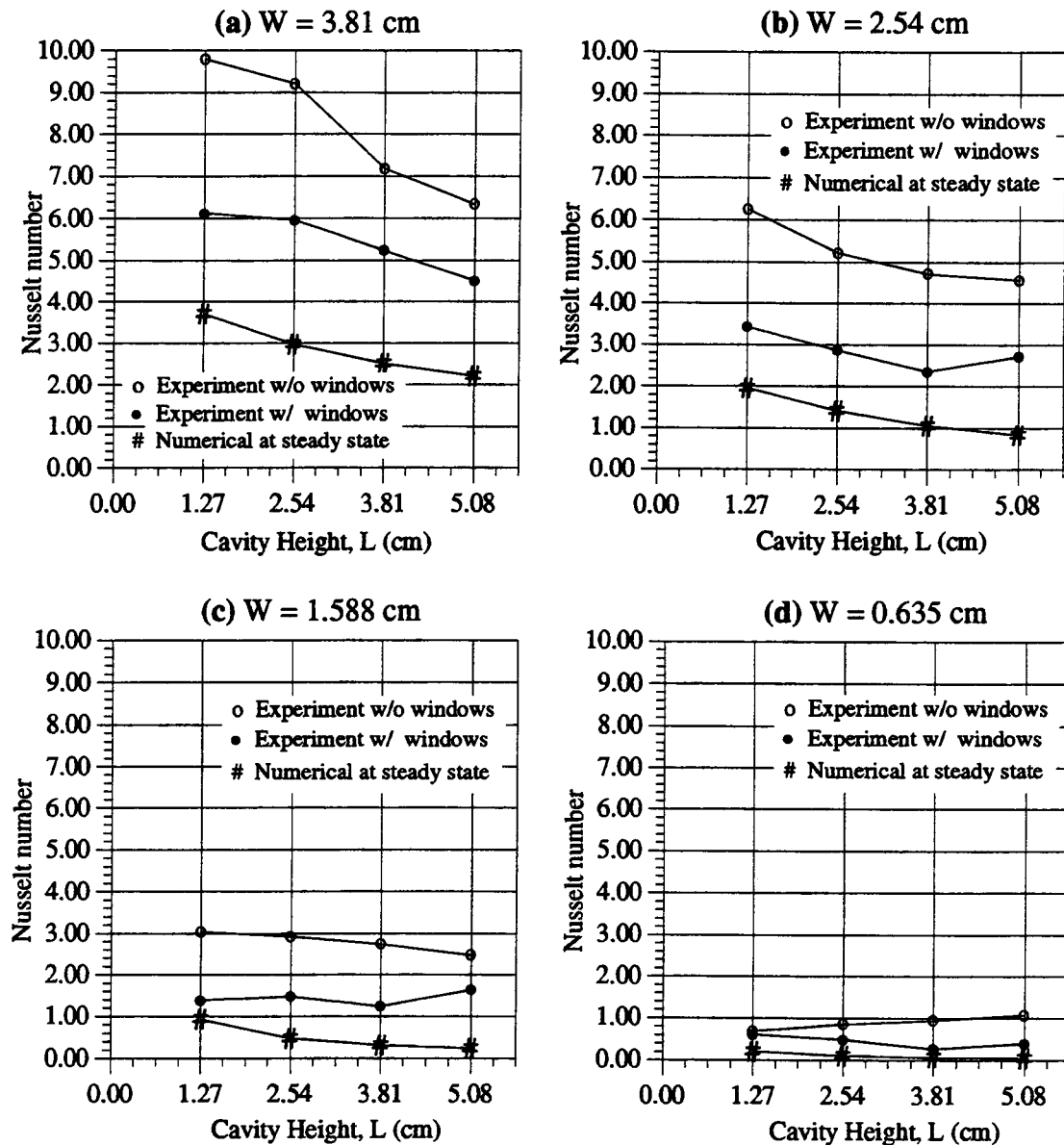


Figure 5.21 Comparison between the numerical and experimental results of Nusselt number for selected cases of open cavities; (a) $W = 3.81$ cm (b) $W = 2.54$ cm (c) $W = 1.588$ cm (d) $W = 0.635$ cm

numerical model and for the experimental situation with windows on both ends.

Heat transfer rates due to z -directional flow also depend on the dimensions of the cavity. For the cases of

open cavities without the two windows in Table 5.1 and figure 5.21, the shorter the cavity height the higher the heat transfer rate for all cases except for those which are very narrow, i.e. open cavities with $W = 0.635$ cm. In general, the smaller the cross-sectional area of the cavity, the less effect of z -directional air flow. For very narrow cavities, however, changes in the balance between the momentum and viscous forces will affect the heat transfer rates. For cases with wider openings, viscous force effects were relatively small.

Nusselt numbers evaluated at the mid-section

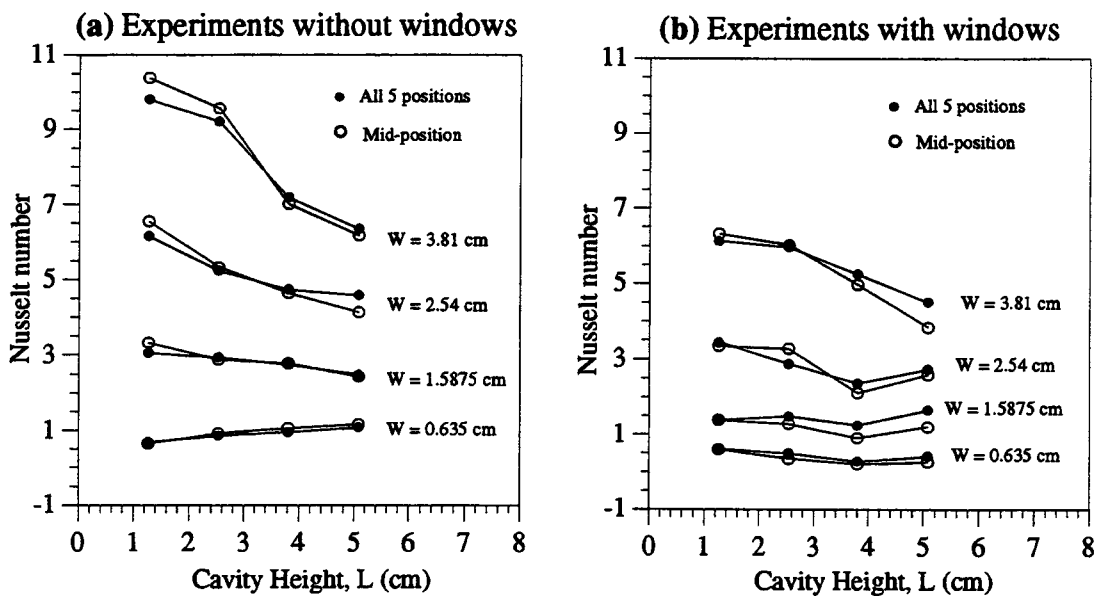


Figure 5.22 Nusselt number from experimental results evaluated using all 5 data points and using only the mid-point in figure 5.3; (a) Cases of open cavities without windows (b) Cases of open cavity with windows

Another observation from the experimental fringe patterns in figure 5.18 is that heat transfer rates along the entire cavity wall can be approximated by the calculation of the heat transfer rates at the mid-section at the wall. The reason for this result is that the thermal boundary-layer thickness at the mid-section is approximately the average thickness of the overall thermal boundary-layer. Figure 5.22 shows comparisons between these cases.

Comparisons of temperature profiles

Since the evaluation from the mid-section of the open cavity describe the heat transfer rates quite well, further comparisons between temperature profiles obtained experimentally and numerically will relate to the mid-section of the cavity.

Temperature profiles at the mid-section from experimental and numerical result are depicted in figure 5.23 for the case, $W = 3.81$ cm. Numerical temperature predictions are higher than the experimental results. The experimental setup with windows is, clearly, a better approximation for the temperature field and, consequently, the heat transfer rates would be true than without the windows.

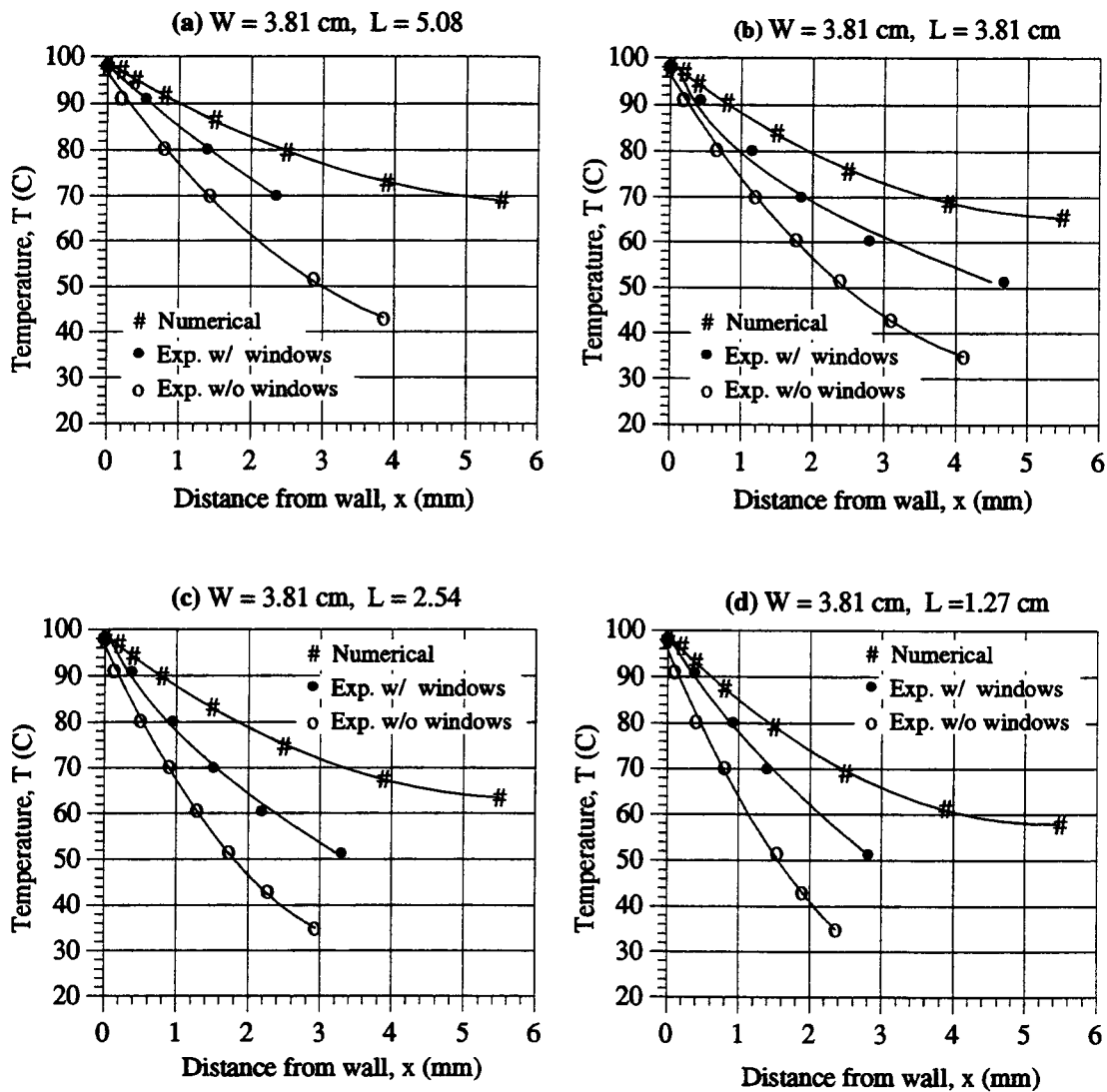


Figure 5.23 Temperature profiles at the mid-section of the open cavities with a fixed width at $W = 3.81$ cm

Figure 5.24 shows temperature profiles at the mid-section for all four cases of open cavities at $W = 0.635$ cm. Temperature profiles at the cavity opening from the numerical calculation are also plotted at different locations. At the mid-section of the open cavity, numerical results indicate that there to be no heat transfer occurring. Numerical temperature predictions at

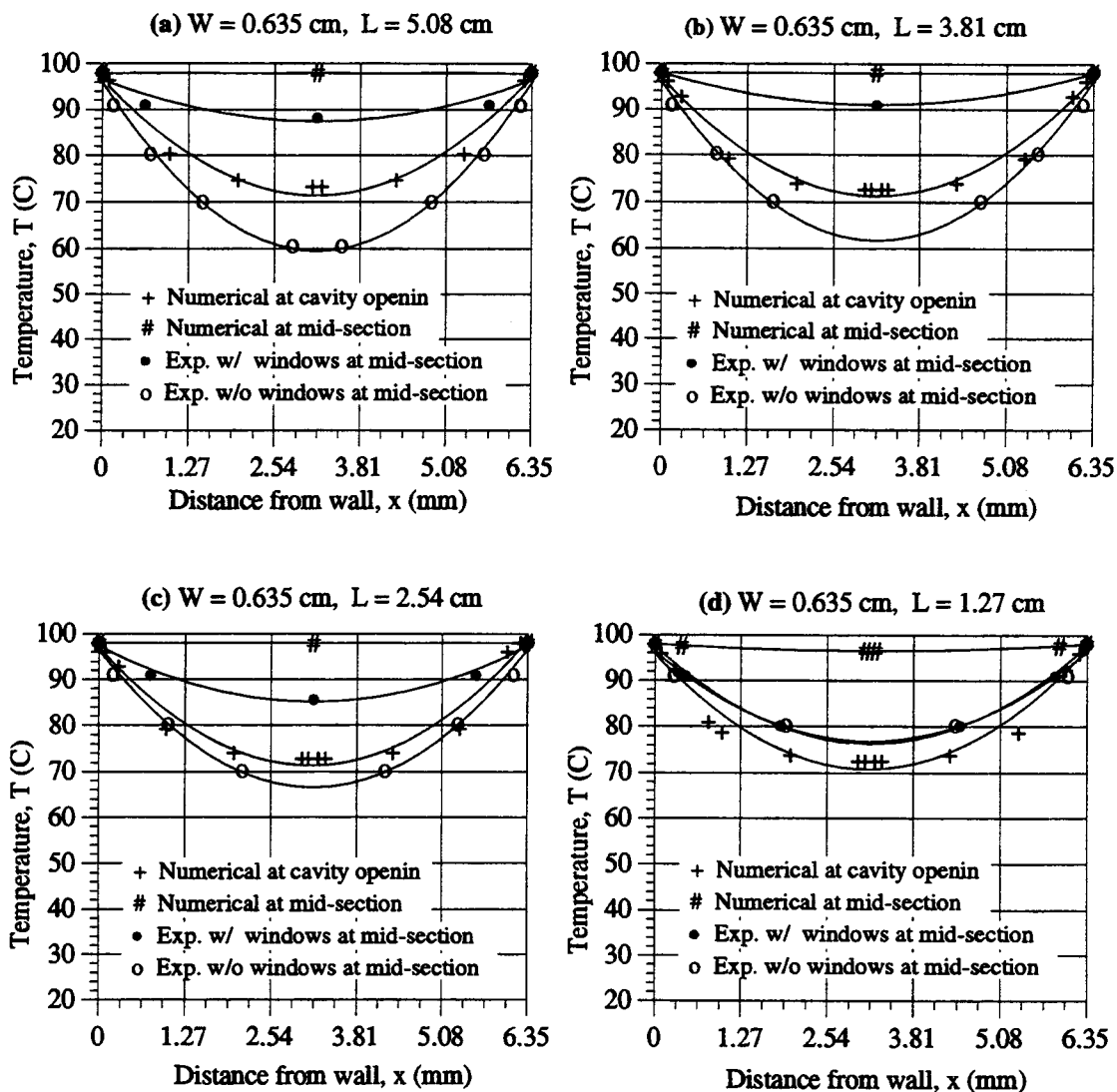


Figure 5.24 Temperature profiles at the mid-section of the open cavities with a fixed width at $W = 0.635$ cm

the mid-section are much higher than are those from experimentals.

Another difference between experimental and numerical fringe patterns is the magnitude of the oscillation. Both show oscillating behavior, however the magnitude for experimental results is much larger than that from numerical calculations.

For these very narrow open cavities, fluid at the bottom will be at a much higher temperature than that at the top. Due to the very narrow width of the cavity, it is unlikely that this fluid will be able to flow to the reservoir. This produces an unstable situation with lighter fluid being placed under a heavier fluid. Due to this unstable situation, oscillatory fluid motion occurred.

There are several reasons for the disagreement between the numerical model and the experiments. First, the numerical model assumed laminar flow behavior, but the actual flow is somewhat unsteady or semi-turbulent. Second, the numerical model is an ideal two-dimensional prediction, but the experimental setup is, at best, an approximation for two-dimensional behavior. Third, the numerical model included ideal adiabatic and constant-temperature boundary conditions, but this was not possible in the experimental setup. Fourth, the numerical model used constant properties for the fluid. The use of variable properties at different temperatures would improve the agreement between the two models. Also note that numerical model assumed a symmetric computational domain as shown in figure 2.1. Numerical results of flow behavior, thus, were forced to be symmetrical.

5.7 HEAT TRANSFER CORRELATIONS

To correlate heat transfer rates as functions of the important variables, values of Nusselt number were determined over a range in Rayleigh number and the results were related functionally.

Figure 5.25 shows Nusselt numbers as functions of Rayleigh number based on values listed in table 5.1. The Rayleigh numbers, Ra_w , used in this figure were based on the cavity width. Only the experimental results with windows are shown. Equations for the various cases are also shown in this figure.

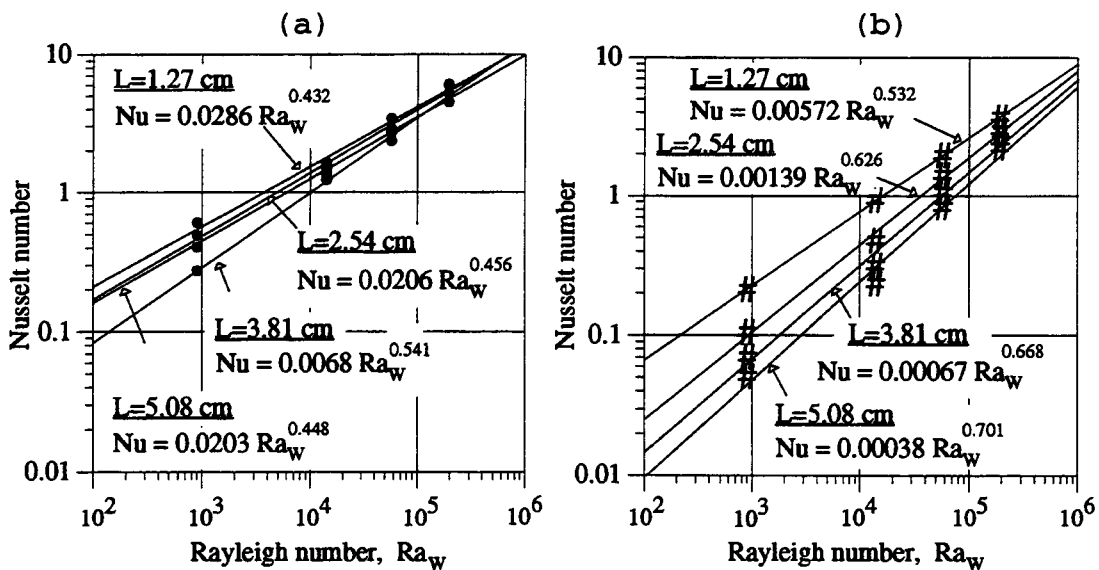


Figure 5.25 Correlation between Nusselt number and Rayleigh number;
 (a) Experimental result with windows on the ends (b) Numerical result

From figure 5.25(b), numerical results imply that the rate of heat transfer is also a function of the cavity

length, L . In a dimensionless representation, a more general relationship is the Nusselt number as a function of the Rayleigh number, Ra_w , and the aspect ratio of the cavity, L/D ; i.e. $Nu = f(Ra_w, L/D)$. To find such a correlation, the dependent variable, Nu , and the independent variables, Ra_w and L/D , were first transformed into the logarithmic domain as $y = \ln(Nu)$, $x_1 = \ln(Ra_w)$, and $x_2 = \ln(L/D)$. A multiple linear regression model was used to fit these logarithmic variables to achieve an equation in the form; $y = a_0 + a_1x_1 + a_2x_2$. The coefficients, a_0 , a_1 , and a_2 were evaluated according to

$$\begin{bmatrix} n & \sum_i x_{1i} & \sum_i x_{2i} \\ \sum_i x_{1i} & \sum_i (x_{1i})^2 & \sum_i x_{1i}x_{2i} \\ \sum_i x_{2i} & \sum_i x_{1i}x_{2i} & \sum_i (x_{2i})^2 \end{bmatrix} \begin{Bmatrix} a_0 \\ a_1 \\ a_2 \end{Bmatrix} = \begin{Bmatrix} \sum_i y_i \\ \sum_i x_{1i}y_i \\ \sum_i x_{2i}y_i \end{Bmatrix} \quad (5.5)$$

MathCad was used to evaluate the coefficients.

The form of the correlation between the dependent variable, Nu , and the independent variables, Ra_w and L/W , was

$$Nu = \exp(a_0) \cdot (Ra_w)^{a_1} \cdot \left(\frac{L}{W}\right)^{a_2} \quad (5.6)$$

The complete correlation using the numerical values at steady state in table 5.1 is

$$Nu = 0.020 \cdot (Ra_w)^{0.382} \cdot \left(\frac{L}{W}\right)^{-0.75} \quad (5.7)$$

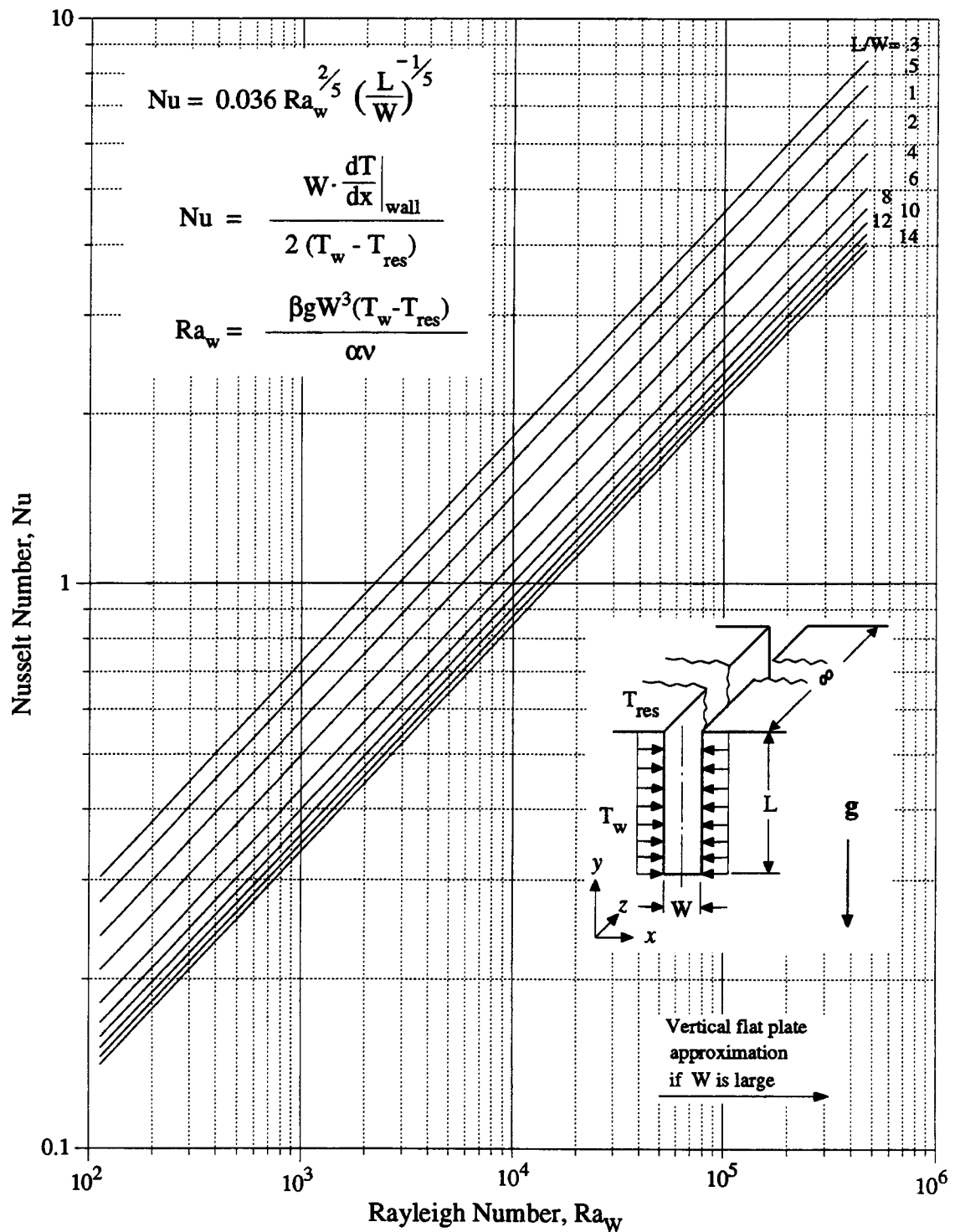


Figure 5.26 Relationship between Nu and Ra_w for different aspect ratio open cavities based on experimental results with windows on both ends of the test section

The correlation using the experimental values with windows on both ends is

$$\text{Nu} = 0.036 \cdot \text{Ra}_w^{2/5} \cdot \left(\frac{L}{W} \right)^{-1/5} \quad (5.8)$$

Experimental results are considered more accurate than numerical results as was discussed in section 5.6.

Numerical results, however, provide information on general trends. To evaluate heat transfer rates for two-dimensional open cavities with constant wall temperature, Eq.(5.8) is recommended.

Figure 5.26 shows Nu versus Ra_w for different values of aspect ratio, L/W , cavities on a logarithmic scale. Small values of Rayleigh numbers are shown. Large values of Rayleigh number, Ra_w , are associated with larger values of the dimension, W . For a very wide cavity, a vertical flat plate correlation is recommended.

5.8 FRINGE COMPARISONS BETWEEN EXPERIMENTAL AND NUMERICAL RESULTS AT THE TUBE OPENING

A comparison between experimental and numerical results for open thermosyphons in cylindrical coordinates is described in this section. The location at which this comparison was made is the opening of the vertical tube. Experimental results showed the air flow to be extremely

unstable and oscillatory at the tube opening. Experimental and numerical-generated fringe patterns were compared qualitatively.

Figure 5.27 shows the schematic of the apparatus used for the experimental detection of fringes at the tube opening. To control the vertical tube at a near constant wall temperature, an aluminum rod was used as the vertical tube because of its high thermal conductivity and high heat capacity. Two cartridge heaters, rated at 300 watts, were used to heat the aluminum rod to the desired temperature.

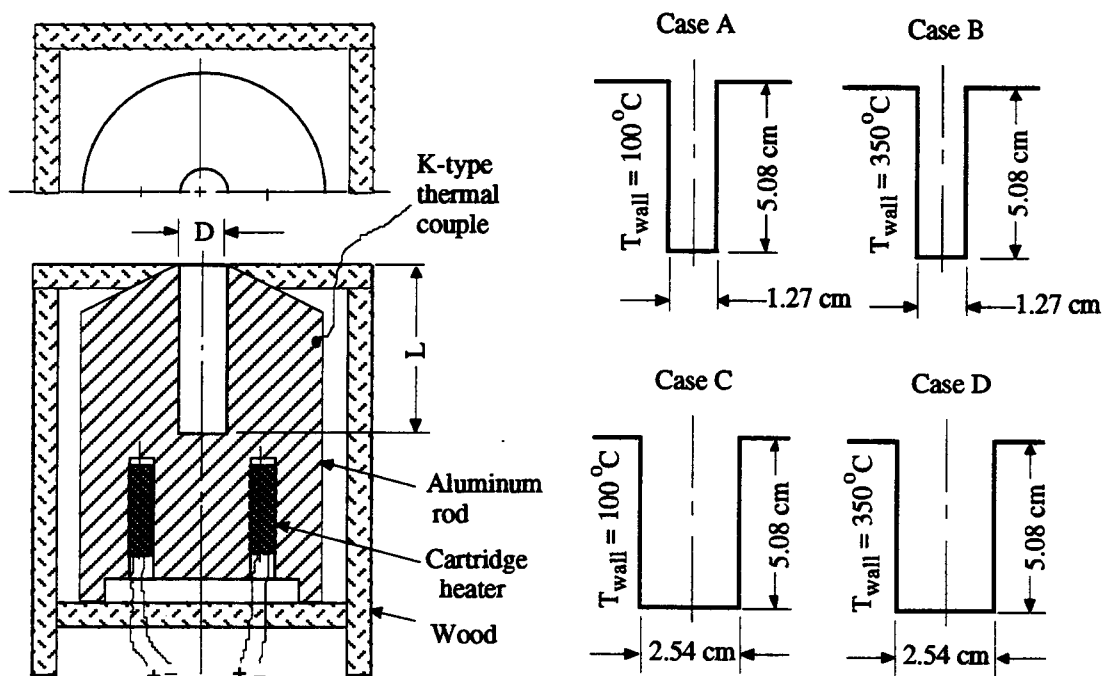


Figure 5.27 Schematic of the apparatus for observing fringes at the tube opening; dimensions and thermal boundary conditions for four selected cases.

A K-type thermocouple was used to measure the temperature. Temperature control was relatively easy due to the large heat capacity of the material. When controlling the temperature to 100 °C, the thermocouple reading ranged from 95 °C to 105 °C. For a wall temperature of 350 °C, the range was between 330 °C and 360 °C.

Four cases of open thermosyphons were used for comparison. They are shown in figure 5.27 also. Case A consisted of a 0.5-in-diameter, 2-in-long length vertical tube with a constant wall temperature of 100 °C. Case B consisted of the same size tube with a wall temperature of 350 °C. Case C involved a 1-in-diameter and 2-in-long vertical tube with a constant wall temperature of 100 °C. The last case, case D, consisted of the same-size vertical tube at a temperature of 350 °C.

Figures 5.28-5.31 show the experimental and numerically-generated fringe patterns for these four selected cases. The experimental fringe patterns were taken at different times using the CCD camera. The fringe patterns for the numerical result were generated using the technique described in section 4.7 in the cylindrical coordinates. Three numerically-generated fringe patterns are shown for each case in figures 5.28-5.31. These fringe patterns provide a qualitative comparisons between the experimental and numerical results of the temperature in the cylindrical coordinates.

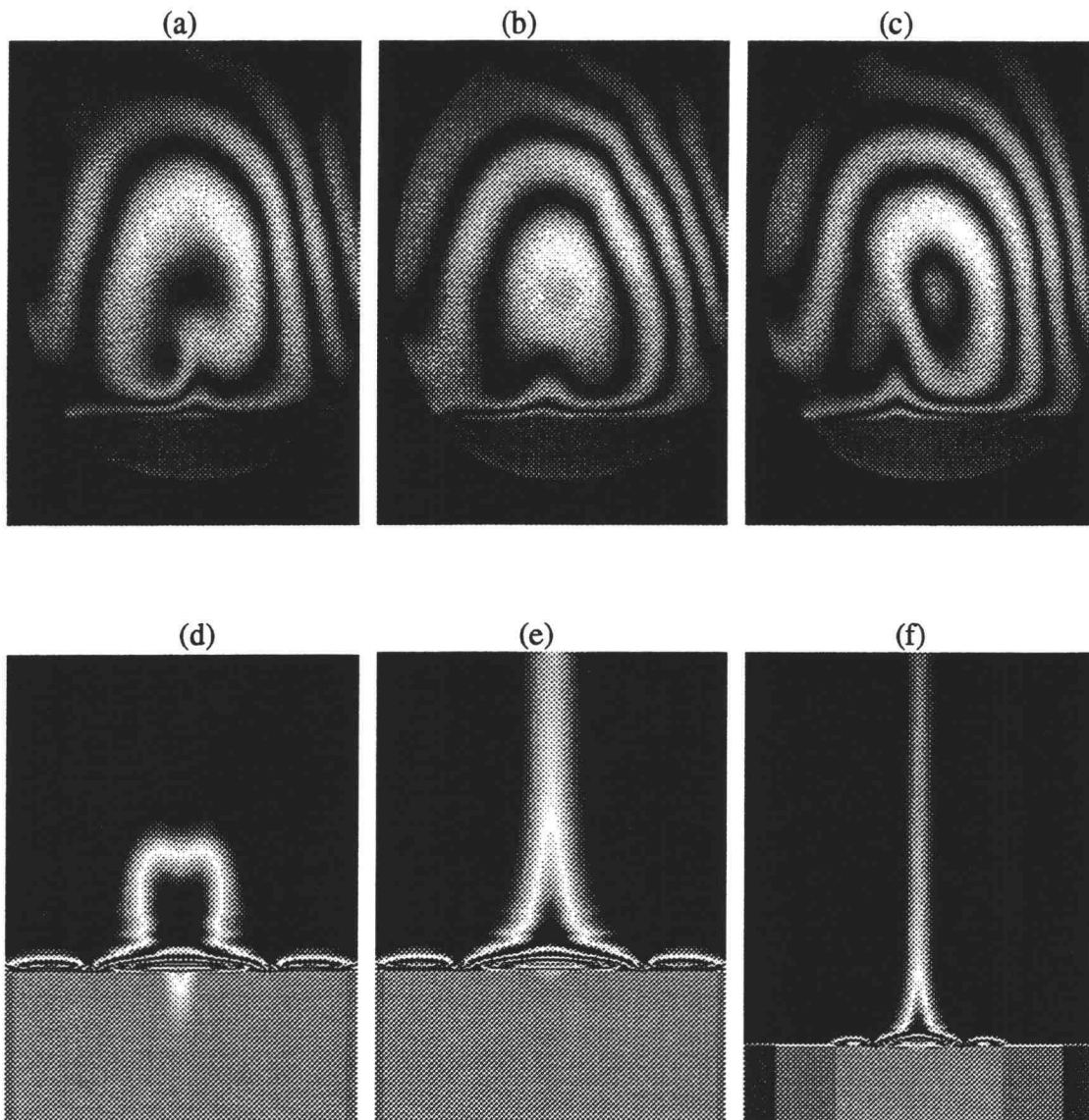


Figure 5.28 Comparison of experimental and numerical fringes at the tube opening for case A. Images (a)-(c) are experimental fringes. Flow behavior was unstable and oscillating at the tube opening. Images (d)-(f) are numerically-generated fringes. Image (d) is at 1 second; Image (e) is at steady state (10 seconds); Image (f) is also at steady state.

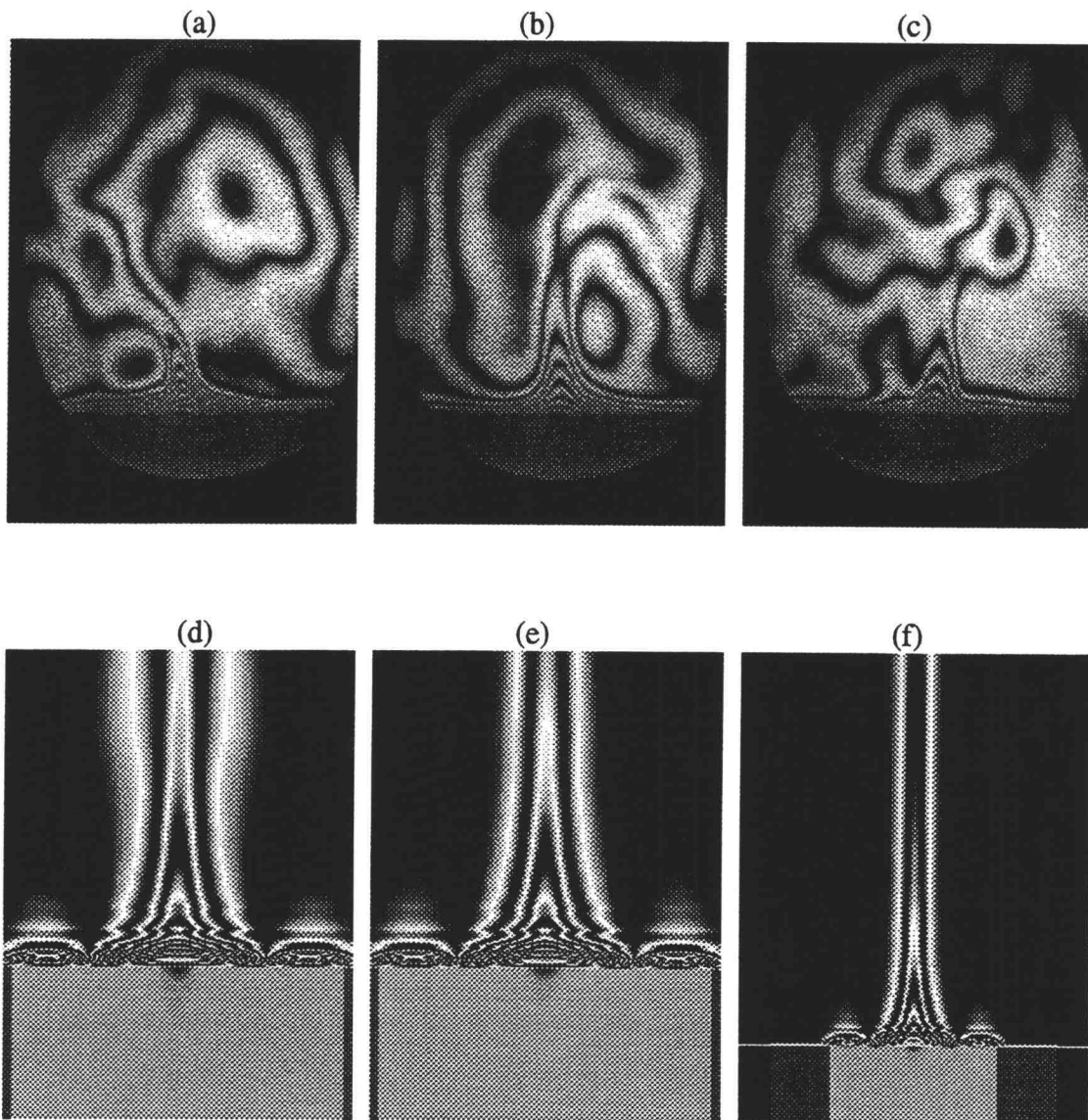


Figure 5.29 Comparison of experimental and numerical fringes at the tube opening for case B. Images (a)-(c) are experimental fringes. Flow behavior was unstable and oscillating at the tube opening. Images (d)-(f) are numerically-generated fringes. Image (d) is at 1 second; Image (e) is at steady state (10 seconds); Image (f) is also at steady state.

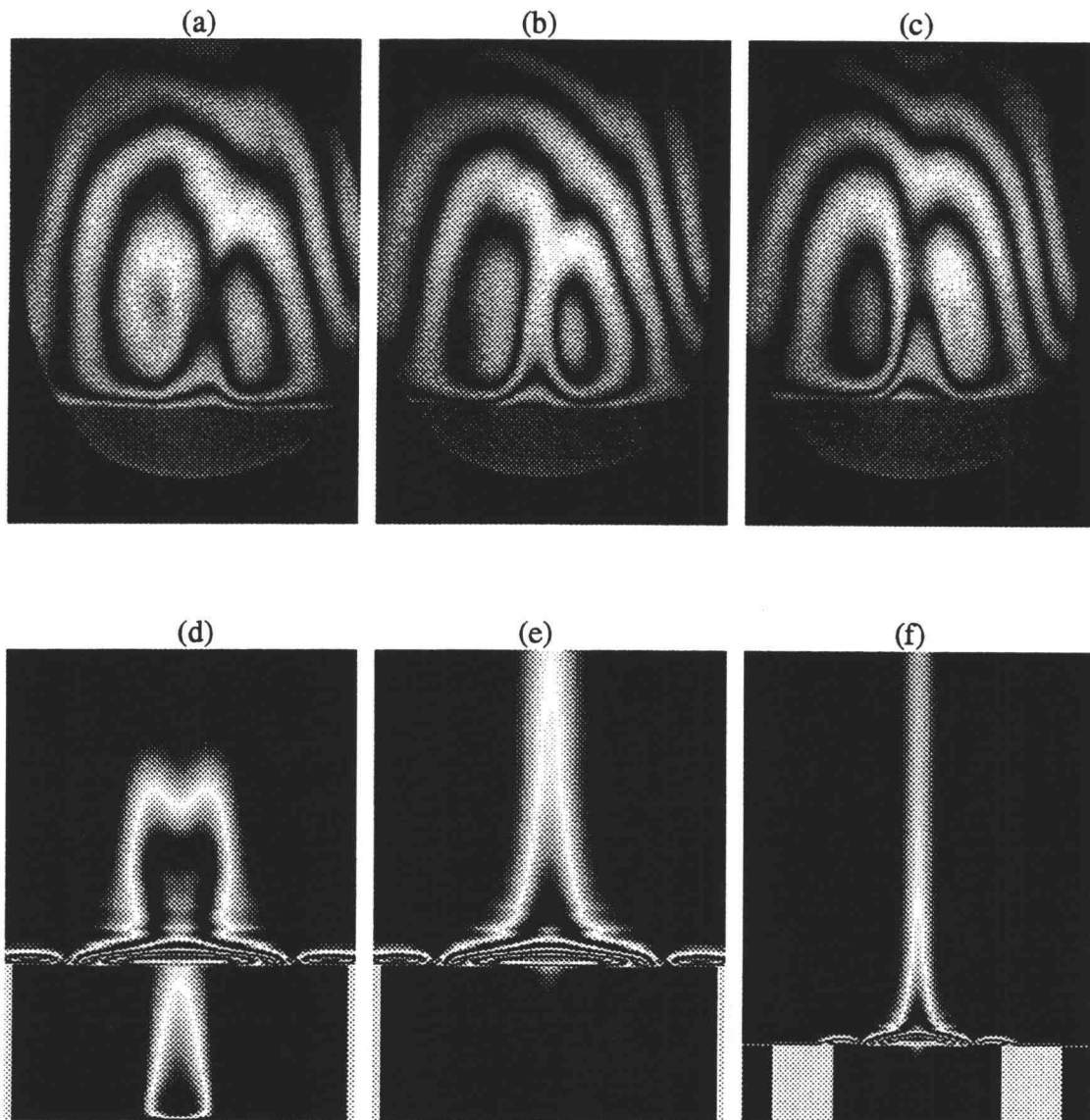


Figure 5.30 Comparison of experimental and numerical fringes at the tube opening for case C. Images (a)-(c) are experimental fringes. Flow behavior was unstable and oscillating at the tube opening. Images (d)-(f) are numerically-generated fringes. Image (d) is at 1 second; Image (e) is at steady state (10 seconds); Image (f) is also at steady state.

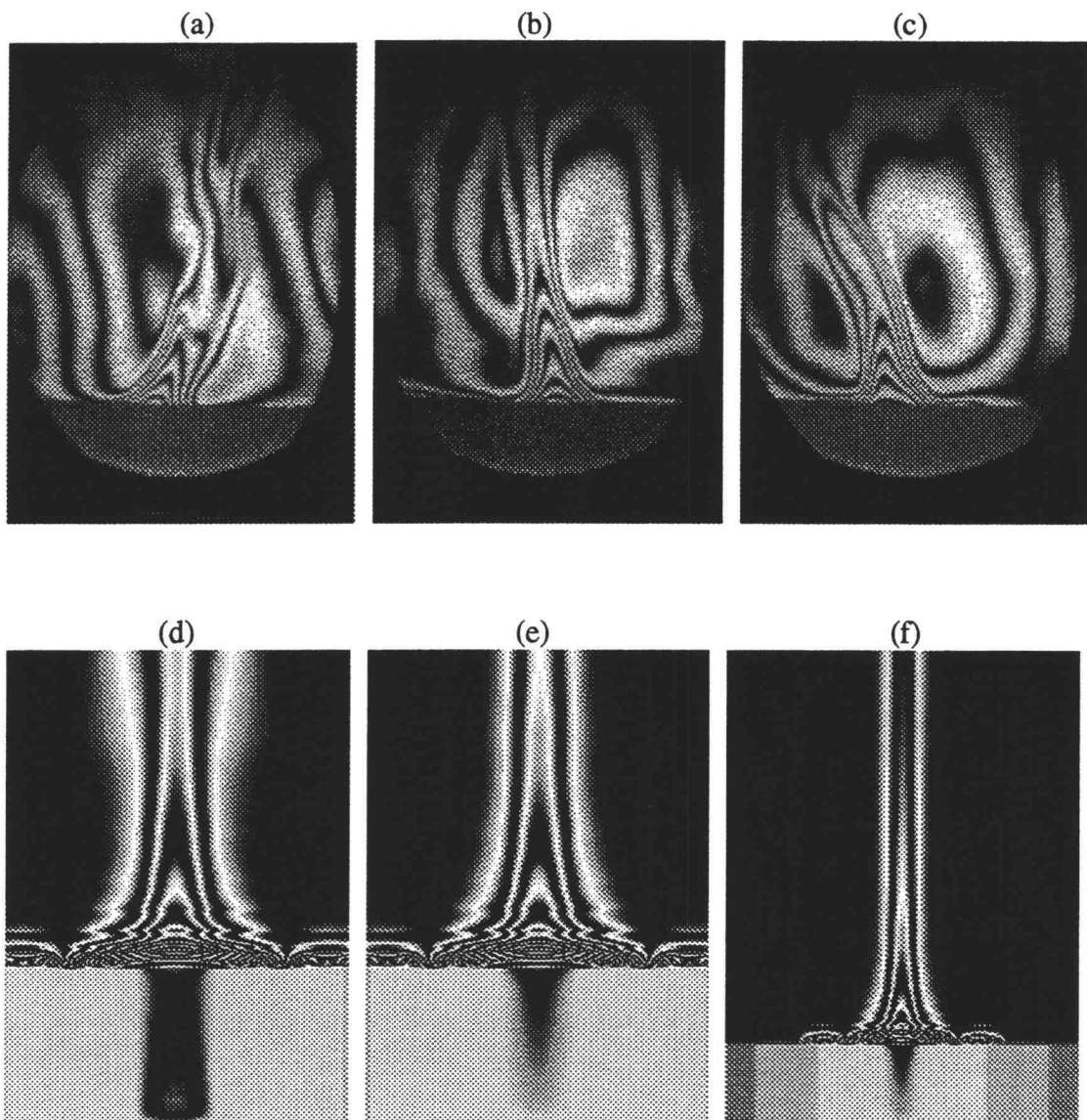


Figure 5.31 Comparison of experimental and numerical fringes at the tube opening for case D. Images (a)-(c) are experimental fringes. Flow behavior was unstable and oscillating at the tube opening. Images (d)-(f) are numerically-generated fringes. Image (d) is at 1 second; Image (e) is at steady state (10 seconds); Image (f) is also at steady state.

VI. CONCLUSIONS AND RECOMMENDATIONS

This study investigated the nature of fluid motion and the heat transfer rate through the tube wall for the devices of open thermosyphons. A FORTRAN computer program based on the three fundamental laws of conservation - mass, momentum, and energy - was developed to calculate the flow and temperature fields for this configuration. The numerical solution was based on the TEMPEST [16] solution procedure which is a semi-implicit, time-marching, finite-volume procedure. Eighty cases of open thermosyphons with either constant wall temperatures or linearly-varying wall temperatures were examined.

Open cavities were also studied using a Mach-Zehnder interferometer. By counting interference fringes near the open cavity walls, heat transfer rates through the vertical wall were evaluated. Nusselt numbers were used as measuring parameters for the heat-transfer rates. Experimental and numerical results were compared.

Several conclusions and recommendations from this study are stated in the following sections.

6.1 CONCLUSIONS

Numerical results yielded the following information. The rate of heat transfer through the vertical wall was a strong function of the tube radius. For narrow tubes with

smaller radius, with an increase in the tube radius, the rate of heat transfer increased rapidly and then approached an asymptotic limit. Figure 3.2 shows such an asymptotic relation. The Nusselt number variation with tube radius was linear. The types of thermal boundary conditions had little effect on these relations.

Fluid motion and the rate of heat transfer through the tube showed oscillatory behavior, even at steady state. Smaller-diameter tubes were observed to experience larger-amplitude oscillations except for very small tube radii where viscous effects predominated. Fluid at the end of the tube was stagnant for very large length-to-radius (aspect ratio) cases.

Experimental results for the temperature fields, detected by a Mach-Zehnder interferometer, showed a general agreement with the numerical results. This was shown through the comparisons between experimental and numerically-generated fringe pattern in figure 5.18. Experimental apparatus with two optical windows on both sides of the test section to block out the third directional air flow gave a better approximation with the two-dimensional numerical results. Based on these experimental results, a correlation between Nusselt number, Nu , and Rayleigh number, Ra_w , for different aspect ratios, L/W , was determined to be $Nu = 0.036 \cdot Ra_w^{2/5} \cdot (L/W)^{-1/5}$. Oscillatory behavior of the fringe patterns was also observed for the configurations of vertical channels and

open cavities. The narrower the width the faster the oscillating frequency due heavier fluid at the top of these configurations.

Quantitative comparison between experimental and numerical results for the configuration of 16 open cavities showed that numerical calculations predicted a higher heat transfer rates. This is due to many differences between the numerical and experimental modeling. One of the major factor for this difference is the use of a laminar-flow numerical model to predict a possible turbulent flow field. Considering the heat transfer rate, however, both numerical and experimental predicted a higher Nusselt number values for shorter cavities. For very narrow cavities, both numerical and experimental result show that the fluid at the bottom of the cavities was stratified. Temperature changes rapidly at the cavity opening.

Errors resulting from imperfect alignment of the interferometer are directly related to the spacing between fringes. The smaller the fringe spacing, the less the error due to imperfect alignment of the MZ interferometer. This error, for the fringes near the open-cavity wall, was less than 3% for this study.

6.2 RECOMMENDATIONS

1. Interference patterns from two plane waves and two spherical waves may have other uses for measuring small change of lengths and angles precisely. As described in

section 4.5 in this study, small change of the relative positions and angles of the two waves produced an distinguishable interference pattern on the observation screen. Results of these patterns agree with those using interference patterns for two spherical waves (figure 4.6 and figure 4.13). Further study and application of this effect are therefore recommended.

2. A plane-wave source is essential to obtain a true infinite fringe field with the Mach-Zehnder interferometer. To obtain a larger area of maximum (or minimum) on the screen , for use in detecting large cross sections of the temperature field, larger diameter and smoother optics are required. The cause of the slightly-spherical plane wave following the collimating lens, L_2 , in figure 4.1 of this study, was undetermined. Replacement of this collimating lens with a very smooth surface and at a designed wavelength may improve the interferometer. The size of the pinhole in the spatial filter, as well as the laser cavity configuration, may also affect the collimation of the light wave.
3. An interpolating technique, described in section 4.7, was used to enhance the quality of the images plotted in this study. This technique may be useful in combination with numerical results to yield improved accuracy. The accuracy of the results of interpolation depends on the type of curve fitting done and the location of the data

points selected for the interpolation. The 9 data points used in this study were located at the lower-right corner as shown figure 4.17. Different locations could be used, such as the upper-left 9 data points, the lower-left and the upper-right, or the averages of these four. Numerical experiments for determining the accuracy of curve fitting and the data points used in such a scheme are recommended.

4. Counting of fringe patterns involved numerous of times for the calculation of the heat transfer rates, even with the effect of magnification. In this study, only 5 positions were selected for the calculation of the heat transfer rates. More positions are desired for better accuracy. A computer program to count the distance between fringes and calculate the heat transfer rates from the fringe patterns are recommended to be developed. With this program, heat transfer rates from many images of fringe patterns can be evaluated more effectively. Better statistical values of the heat transfer rates can be evaluated for these oscillatory fringe patterns.
5. Many aspects of the numerical modeling can be improved to give a better approximation with the experimental results. A turbulence model is recommended for the numerical calculation.

REFERENCES

1. Schmidt, E. H. W., Heat Transmission by Natural Convection at High Centrifugal Acceleration in Water-Cooled Gas-Turbine Blades, *Proc. of the General Discussion in Heat Transfer*, The Institution of Mechanical Engineers and ASME, London, England, pp. 361-363, September 1951.
2. Long, E. L., The Long Thermopile, *Proc. Int. Conf. on Permafrost*, National Academy of Sciences, Washington, pp. 487-491, 1963.
3. Long, E. L., Designing friction piles for increased stability at lower installed cost in permafrost, *Proc. 2nd. Int. Conf. on Permafrost*, National Academy of Sciences, Yakutsk, pp. 693-699, 1973.
4. Kestin, J., Sourcebook on the Production of Electricity from Geothermal Energy, Doc.# DOE/RA/4051-1, U.S. Department of Energy, Assistant Secretary for Resource Applications, Division of Geothermal Energy, Washington, D.C. 20585, March 1980.
5. DiPippo, R., Geothermal Energy as a Source of Electricity - A Worldwide Survey of the Design and Operation of Geothermal Power Plants, Doc.# DOE/RA/28320-1, U.S. Department of Energy, Assistant Secretary for Resource Applications, Division of Geothermal Energy, Washington, D.C. 20585, January 1980.

6. Lock, G. S. H., *The Tubular Thermosyphon - Variations on a Theme*, Oxford University Press, pp. 17-19, 1992.
7. Japikse, D. and E. R. F. Winter, Single-Phase Transport Processes in the Open Thermosyphon, *Int. J. Heat Transfer*, Pergamon Press, Vol. 14, pp. 427-441, 1971.
8. Dunn, P. D. and D. A. Reay, *Heat Pipes*, 3rd Edition, Pergamon Press, Oxford, 1982.
9. Eckert, E. R. G. and T. Jackson, Analytical Investigation of Flow and Heat Transfer in Coolant Passages of Free Convection Liquid-Cooled Turbines, NACA RME50d25, July 18, 1950.
10. Ostrach, S. and P. R. Thornton, On the Stagnation of Natural-Convection Flows in Closed-End Tubes, *Trans. ASME*, Vol. 80, pp. 363-366, 1958.
11. Lighthill, M. J., Theoretical Considerations of Free Convection in Tubes, *Quarterly J. of Mech. and App. Math.*, Vol. 6, pp. 398-439, 1953.
12. Martin, S., Free Convection in an Open Thermosyphon with Special Reference to Turbulent Flow, *Proc. of Roy Society, Series A*, Vol. 230, p. 502, 1955.
13. Hasegawa, S., K. Nishikawa and K. Yamagata, Heat Transfer in an Open Thermosyphon, *Bulletin of JSME*, Vol. 6, No. 22, 1963.
14. Japikse, D., Heat Transfer in Open and Closed Thermosyphons, Ph.D. thesis, Mechanical Engineering, Purdue University, Chap. 4, 1969.

15. Fukuda, M., Laminar Natural Convection in Vertical Tubes with One End Closed, Ph.D. thesis, Mechanical Engineering, Oregon State University, Chap. 3, 1981.
16. Trent, D. S. and L. L. Eyler, TEMPEST, A Three-Dimensional Time-Dependent Computer Program for Hydrothermal Analysis, Volume 1: Numerical Methods and Input Instructions., Doc. #PNL-4348 Vol. Rev. 2, Pacific Northwest Laboratory, Battelle Memorial Institute, Richland, Washington, 1989.
17. Goldstein, R. J., *Fluid Mechanics Measurements*, Hemisphere Publishing Co., Washington, p. 378, 1983.
18. Welty, J. R., C. E. Wicks and R. E. Wilson, *Fundamentals of Momentum, Heat, and Mass Transfer*, 3rd ed., Wiley, New York, p. 229, 1984.
19. Gerald, C. F. and O. P. Wheatley, *Applied Numerical Analysis*, Addison-Wesley, Reading, Mass., p. 128, 1984.
20. Roache, P. J., *Computational Fluid Dynamics*, Hermosa, Albuquerque, New Mexico, p. 65, 1972.
21. Davis, G. de Vahl and I. P. Jones, Natural Convection in a Square Cavity: A Comparison Exercise, *Int. J. for Numerical Methods in Fluids*, Vol. 3, pp. 227-248, 1983.
22. Paolucci, S. and D. R. Chenoweth, Transition to Chaos in a Differentially Heated Vertical Cavity, *J. Fluid Mech.*, Vol. 201, pp. 379-410, 1989.
23. Ivey, G. N., Experiment on Transient Natural Convection in a Cavity, *J. Fluid Mech.*, Vol. 144, pp. 389-401, 1984.

24. Hecht, E., *Optics*, 2nd Edition, Addison-Wesley Publishing Company, Inc., Reading, Massachusetts, 1987.
25. Meyer-Arendt, J. R., *Introduction to Classical and Modern Optics*, 2nd ed., Prentice-Hall, Englewood Cliffs, New Jersey, p. 188, 1984.
26. Hauf, W. and U. Grigull, *Optical Methods in Heat Transfer*, *Advances in Heat transfer*, Academic Press, New York, NY, Vol. 6, pp. 131-366, 1970.
27. Vest, C. M., *Holographic Interferometry*, John Wiley & Sons, New York, NY, pp. 363-365, 1979.
28. Tilton, L. W. and J. K. Taylor, *Refractive Index of Distilled Water for Visible Radiation, at Temperature 0 to 60°C*, *J. Res. Natl. Bur. Stands.*, Vol. 20, 1938.
29. Dobbins, H. M. and E. R. Peck, *Change of Refractive Index of Water as a Function of Temperature*, *J. of The Optical Society of America*, Vol. 63, no. 3, pp. 318-320, March 1973.
30. Radulovic, P. T., *Holographic Interferometry of Asymmetric Temperature or Density Fields*, Doctoral dissertation, University of Michigan, 1977.
31. Howard, B. and T. O. Connor, *Kodak DCS 420 Camera: Say Cheese and Forget about Film*, *PC Magazine*, Ziff-Davis Publishing Company, New York, NY, Vol. 13, No. 21., p. 40, December 6, 1994.
32. Heid, J., *Photography without Film*, *Macworld*, International Data Group, Vol. 11, No. 9, pp. 141-147, September 1994.

33. Lexel Corporation, Model 85 Ion Laser manual, Ion Laser Theory, page 7, Lexel Corporation, Fremont, CA.
34. Melles Griot Corporation, Optics Guide 5 - Manufacturer Catalog, Irvine, California, p. 2-2, 1990.
35. Das, P., *Lasers and Optical Engineering*, Springer-Verlag New York Inc., New York, p. 68, 1991.
36. Showole, R. A. and J. D. Tarasuk, Experimental and Numerical Studies of Natural Convection with Flow Separation in Upward-Facing Inclined Open Cavities, *J. Heat Transfer*, Vol. 115, pp. 592-605, August 1993.
37. Holman, J. P. and W. J. Gajda, Jr., *Experimental Methods for Engineers*, 5th ed., McGraw-Hill, New York, p. 266, 1989.
38. Ostrach, S., An Analysis of Laminar Free-Convection Flow and Heat-transfer about a Flat Plate Parallel to the Direction of Generating Body Force, NACA Technical Note 2635, 1952 (NACA Report 1111, 1953).
39. Churchill, S. W. and H. H. S. Chu, Correlating Equations for Laminar and Turbulent Free Convection from a Vertical Plate, *Int. J. Heat Mass Transfer*, Vol. 18, pp. 1323-1329, 1975.
40. Welty, J. R., *Engineering Heat Transfer*, SI Version, Wiley, New York, p. 246, 1978.
41. Bejan, A., *Convection Heat Transfer*, Wiley, New York, p. 140, 1984.
42. Newport Corporation, Newport 1990 Catalog, Fountain Valley, California, p. N-82, 1990.

APPENDICES

APPENDIX A

NUMERICAL DISCRETIZATION OF THE GOVERNING EQUATIONS

Discretization of the three governing equations is described in this section. Each was retained in its conservative form. A first-order finite-difference approach was applied to each term. An explicit upwind method was used for discretization of the advective terms.

If we consider the three governing equations, Eqs. (2.1)-(2.4), the left-hand sides can be expressed in the following general form

$$\text{LHS} = \frac{\partial \rho \chi}{\partial t} + \frac{1}{r} (\rho u \chi) + \frac{\partial}{\partial r} (\rho u \chi) + \frac{\partial}{\partial z} (\rho v \chi) \quad (\text{A.1})$$

where, χ is unity for the continuity equation; velocity components, u and v , in the momentum equations; and temperature, T , in the energy equation. Note that the density is on the right-hand sides of the momentum and energy equations. The variables, $\rho \chi$, together with the normal velocity are the fluxes across the computational cell surfaces as shown in figure A.1. For simplicity, χ is called the flux variable and u_n is called the flux velocity.

APPENDIX A Continued.

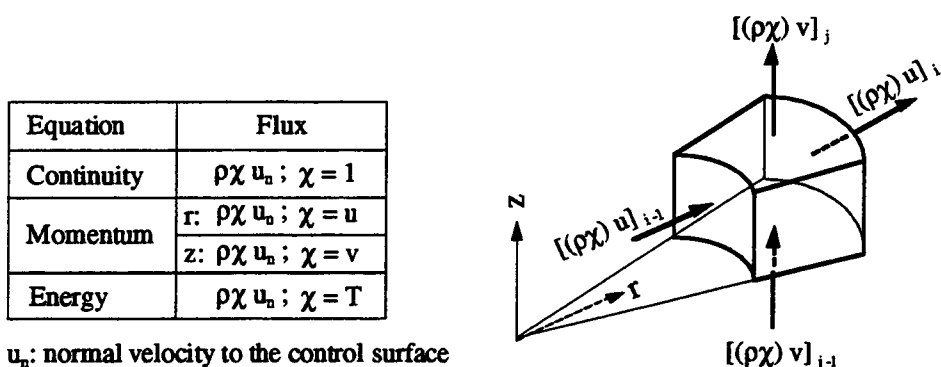


Figure A.1 Advective fluxes across the computational cell surfaces for the three governing equations

The temporal and advective terms on the left-hand sides of the three governing equations were developed from considering the flux across a control surface. Explicitly expressing these terms in words [17],

$$\text{LHS} = \frac{\left\{ \left[\begin{array}{l} \text{rate of accumulation} \\ \text{of flux variable, } \rho\chi, \\ \text{within control volume} \end{array} \right] + \left[\begin{array}{l} \text{rate of flux} \\ \text{variable, } \rho\chi, \text{ out} \\ \text{of control volume} \end{array} \right] - \left[\begin{array}{l} \text{rate of flux} \\ \text{variable, } \rho\chi, \text{ into} \\ \text{control volume} \end{array} \right] \right\}}{\left[\text{control volume} \right]} \quad (\text{A.2})$$

For a control volume shown in figure A.1 with dimensions shown in figure 2.4, Eq. (A.2) is mathematically described as

$$\text{LHS} = \left(\frac{1}{\text{CV}_{i,j}} \right) \cdot \left\{ \begin{array}{l} \frac{\rho\chi \cdot \text{CV}_{i,j}}{\Delta t} + \left([(\rho\chi)u]_i A_{1,i,j} - [(\rho\chi)u]_{i-1} A_{1,i-1,j} \right) \\ + \left([(\rho\chi)v]_j A_{2,i,j} - [(\rho\chi)v]_{j-1} A_{2,i,j-1} \right) \end{array} \right\} \quad (\text{A.3})$$

APPENDIX A Continued.

After taking the limits for an infinitesimal control volume, the computation cell volume $CV_{i,j}$, Eq.(A.3) becomes the differential form of Eq.(A.1) in two-dimensional cylindrical coordinates.

One assumption for predicting the laminar flow behavior for an open thermosyphon is the Boussinesq approximation. This approximation considers the density is a constant, ρ_0 , at the reference temperature except for the gravity term. This constant density, ρ_0 , was moved to the right-hand sides of Eqs.(2.2)-(2.4). After moving the density to the right-hand-side and rearranging, Eq.(A.3) becomes

$$\frac{\text{LHS}}{\rho_0} = \frac{\chi}{\Delta t} + \frac{1}{CV_{i,j}} \left\{ \begin{array}{l} ([\chi u]_i A1_{i,j} - [\chi u]_{i-1} A1_{i-1,j}) \\ + ([\chi v]_j A2_{i,j} - [\chi v]_{j-1} A2_{i,j-1}) \end{array} \right\} \quad (\text{A.4})$$

The first term on the right-hand side of Eq.(A.4) is the temporal term. Terms inside the braces are the advective terms. The discretization scheme for the advective terms in the momentum and energy equations was based on the approach given by Eq.(A.4). This is the finite-volume method for numerical discretization. In the continuity equation, the divergence was calculated from Eq.(A.4).

APPENDIX A Continued.

Continuity equation:

As stated earlier, in the continuity equation the flux variable, χ , is 1. Since the time rate change of a constant is zero, the finite-volume discretization scheme for the continuity equation becomes

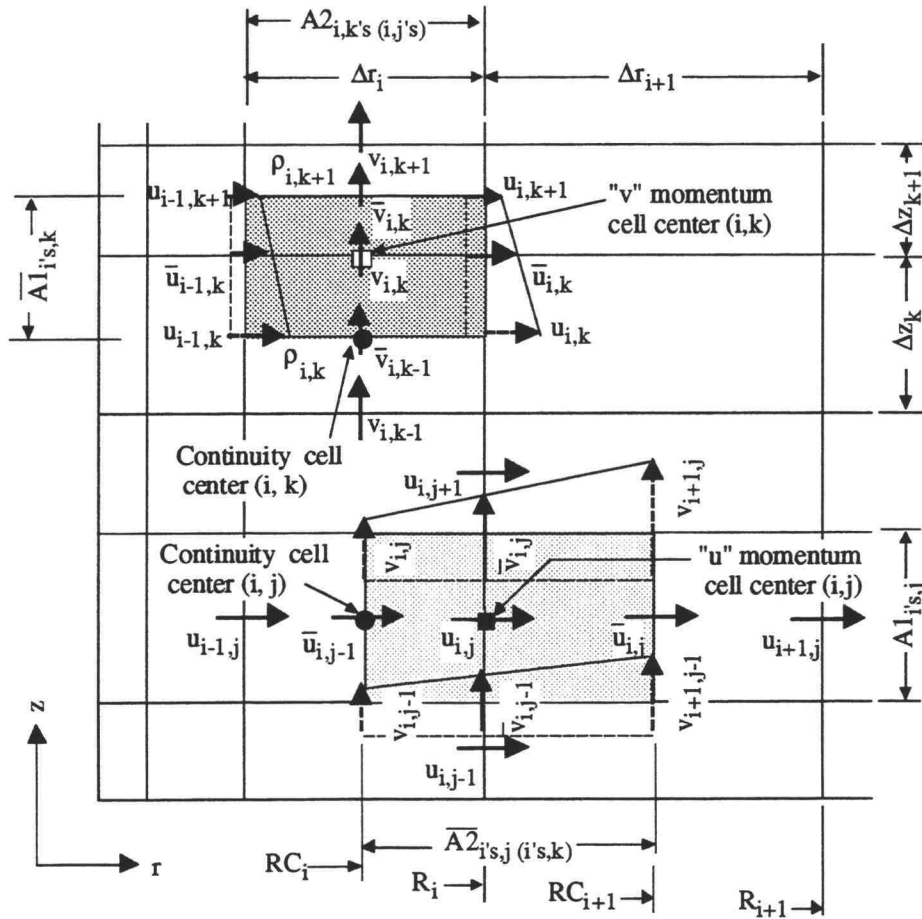
$$\frac{(u_i A_{1,i,j} - u_{i-1} A_{1,i-1,j})}{CV_{i,j}} + \frac{(v_j A_{2,i,j} - v_{j-1} A_{2,i,j-1})}{CV_{i,j}} = D_{i,j} \quad (A.5)$$

where the divergence, $D_{i,j}$, for cell (i,j) is zero if the velocity field satisfies continuity.

Advective terms of momentum equation

The flux variables for the momentum equations are u , and v , as shown in figure A.1. An upwind scheme was used for discretizing the advective terms.

For momentum flux in the r -direction for the lower cell in figure A.2, the flux variables, $u_{i-1,j}$, $u_{i+1,j}$, $u_{i,j}$, $u_{i,j-1}$, $u_{i,j+1}$, are located at the centers of the "u" momentum cells. The flux velocities, $\bar{u}_{i-1,j}$, $\bar{u}_{i,j}$, $\bar{v}_{i,j-1}$, and $\bar{v}_{i,j}$, crossing the cell surfaces, $A_{1,i-1,j}$, $A_{1,i,j}$, $\bar{A}_{2,i,j-1}$, and $\bar{A}_{2,i,j}$, were obtained from linear interpolation of the corresponding velocities located



Note: the index k indicates the alphabetical order of the cell number in the z direction in this figure, where $k = j + 2$.

Figure A.2 Non-uniform "u" and "v" momentum cells for advective term discretization in the momentum equation

at the continuity cell surfaces. The discretization form for the advective terms from Eq.(A.4) is

$$\begin{aligned}
 u \Big|_{\text{adve. terms}} = & \left(u_{\text{upwind}} \bar{u}_i A1_{i,j} - u_{\text{upwind}} \bar{u}_{i-1} A1_{i-1,j} \right) \\
 & + \left(u_{\text{upwind}} \bar{v}_j \overline{A2}_{i,j} - u_{\text{upwind}} \bar{v}_{j-1} \overline{A2}_{i,j-1} \right)
 \end{aligned}
 \tag{A.6}$$

APPENDIX A Continued.

The upwind scheme for Eq. (A.6) is therefore

$$\begin{aligned}
 u|_{\text{upwind}} = & \left(\begin{aligned} & \frac{1}{2}u_{i,j}(|\bar{u}_i| + \bar{u}_i)A1_{i,j} - \frac{1}{2}u_{i+1,j}(|\bar{u}_i| - \bar{u}_i)A1_{i,j} \\ & -\frac{1}{2}u_{i-1,j}(|\bar{u}_{i-1}| + \bar{u}_{i-1})A1_{i-1,j} + \frac{1}{2}u_{i,j}(|\bar{u}_{i-1}| - \bar{u}_{i-1})A1_{i-1,j} \end{aligned} \right) \\
 & + \left(\begin{aligned} & \frac{1}{2}u_{i,j}(|\bar{v}_j| + \bar{v}_j)\bar{A}2_{i,j} - \frac{1}{2}u_{i,j+1}(|\bar{v}_j| - \bar{v}_j)\bar{A}2_{i,j} \\ & -\frac{1}{2}u_{i,j-1}(|\bar{v}_{j-1}| + \bar{v}_{j-1})\bar{A}2_{i,j-1} + \frac{1}{2}u_{i,j}(|\bar{v}_{j-1}| - \bar{v}_{j-1})\bar{A}2_{i,j-1} \end{aligned} \right) \quad (\text{A.7})
 \end{aligned}$$

where, the flux velocities were linearly interpolated according to the following relations:

$$\bar{u}_{i-1,j} = \frac{1}{2}(u_{i,j} + u_{i-1,j}) \quad (\text{A.8})$$

$$\bar{u}_{i,j} = \frac{1}{2}(u_{i+1,j} + u_{i,j}) \quad (\text{A.9})$$

$$\bar{v}_{i,j-1} = v_{i,j-1} + (v_{i+1,j-1} - v_{i,j-1}) \left[\frac{\Delta r_i}{\Delta r_i + \Delta r_{i+1}} \right] \quad (\text{A.10})$$

$$\bar{v}_{i,j} = v_{i,j} + (v_{i+1,j} - v_{i,j}) \left[\frac{\Delta r_i}{\Delta r_i + \Delta r_{i+1}} \right] \quad (\text{A.11})$$

Similarly, for the "v" momentum cell (i,k) in figure A.2, the discretization form is

$$\begin{aligned}
 v|_{\text{adve. terms}} = & \left(v_{\text{upwind}} \bar{u}_i \bar{A}1_{i,k} - v_{\text{upwind}} \bar{u}_{i-1} \bar{A}1_{i-1,k} \right) \\
 & + \left(v_{\text{upwind}} \bar{v}_k A2_{i,k} - v_{\text{upwind}} \bar{v}_{k-1} A2_{i,k-1} \right) \quad (\text{A.12})
 \end{aligned}$$

APPENDIX A Continued.

Note that the missing index in the z-direction is k for this "v" momentum finite-volume discretization. The upwind scheme for Eq. (A.12) is

$$v|_{\text{upwind}} = \left(\begin{array}{l} \frac{1}{2}v_{i,k}(|\bar{u}_i| + \bar{u}_i)\bar{A}1_{i,k} - \frac{1}{2}v_{i+1,k}(|\bar{u}_i| - \bar{u}_i)\bar{A}1_{i,k} \\ -\frac{1}{2}v_{i-1,k}(|\bar{u}_{i-1}| + \bar{u}_{i-1})\bar{A}1_{i-1,k} + \frac{1}{2}u_{i,k}(|\bar{u}_{i-1}| - \bar{u}_{i-1})\bar{A}1_{i-1,k} \end{array} \right) + \left(\begin{array}{l} \frac{1}{2}v_{i,k}(|\bar{v}_k| + \bar{v}_k)A2_{i,k} - \frac{1}{2}v_{i,k+1}(|\bar{v}_k| - \bar{v}_k)A2_{i,k} \\ -\frac{1}{2}v_{i,k-1}(|\bar{v}_{k-1}| + \bar{v}_{k-1})A2_{i,k-1} + \frac{1}{2}u_{i,k}(|\bar{v}_{k-1}| - \bar{v}_{k-1})A2_{i,k-1} \end{array} \right) \quad (\text{A.13})$$

where, the flux velocities are

$$\bar{u}_{i-1,k} = u_{i-1,k} + (u_{i-1,k+1} - u_{i-1,k}) \left[\frac{\Delta z_k}{\Delta z_k + \Delta z_{k+1}} \right] \quad (\text{A.14})$$

$$\bar{u}_{i,k} = u_{i,k} + (u_{i,k+1} - u_{i,k}) \left[\frac{\Delta z_k}{\Delta z_k + \Delta z_{k+1}} \right] \quad (\text{A.15})$$

$$\bar{v}_{i,k-1} = \frac{1}{2}(v_{i,k} + v_{i,k-1}) \quad (\text{A.16})$$

$$\bar{v}_{i,k} = \frac{1}{2}(v_{i,k+1} + v_{i,k}) \quad (\text{A.17})$$

Advective terms of energy equation

The flux variable for the energy equation is T as shown in figure A.1. Consider the continuity cell (i,j) in

APPENDIX A Continued.

The upwind scheme for Eq. (A.18) is

$$\begin{aligned}
 T|_{\text{upwind}} = & \left(\begin{array}{l} \frac{1}{2} T_{i,j} (|u_i| + u_i) A1_{i,j} - \frac{1}{2} T_{i+1,j} (|u_i| - u_i) A1_{i,j} \\ -\frac{1}{2} T_{i-1,j} (|u_{i-1}| + u_{i-1}) A1_{i-1,j} + \frac{1}{2} T_{i,j} (|u_{i-1}| - u_{i-1}) A1_{i-1,j} \end{array} \right) \\
 & + \left(\begin{array}{l} \frac{1}{2} T_{i,j} (|v_j| + v_j) A2_{i,j} - \frac{1}{2} T_{i,j+1} (|v_j| - v_j) A2_{i,j} \\ -\frac{1}{2} T_{i,j-1} (|v_{j-1}| + v_{j-1}) A2_{i,j-1} + \frac{1}{2} T_{i,j} (|v_{j-1}| - v_{j-1}) A2_{i,j-1} \end{array} \right) \quad (\text{A.19})
 \end{aligned}$$

Other terms in the momentum and energy equations

First order finite-difference discretization was used for the rest of the terms in the momentum and energy equations in two-dimensional cylindrical coordinates. A listing of the discretization forms for these terms follows.

A. Pressure term:

Referring to figure A.3, the first-order finite-difference discretization forms of the pressure terms are

$$\text{r-direction: } -\frac{1}{\rho_o} \frac{\partial p}{\partial r} = -\frac{1}{\rho_o} \left[\frac{P_{i+1,j} - P_{i,j}}{(\Delta r_{i+1} + \Delta r_i) / 2} \right] \quad (\text{A.20})$$

$$\text{z-direction: } -\frac{1}{\rho_o} \frac{\partial p}{\partial z} = -\frac{1}{\rho_o} \left[\frac{P_{i,j+1} - P_{i,j}}{(\Delta z_{j+1} + \Delta z_j) / 2} \right] \quad (\text{A.21})$$

APPENDIX A Continued.

B. Viscous and diffusion terms:

The discretization forms of the three terms inside the square brackets of Eq.(2.2) are

$$\begin{aligned} \frac{1}{r} \frac{\partial}{\partial r} \left(r \frac{\partial u}{\partial r} \right) &= \frac{1}{R_i} \frac{1}{(\Delta r_{i+1} + \Delta r_i)/2} \left[\left(RC_{i+1} \frac{u_{i+1} - u_i}{\Delta r_{i+1}} \right) - \left(RC_i \frac{u_i - u_{i-1}}{\Delta r_i} \right) \right] \\ &= \frac{2 RC_{i+1} (u_{i+1} - u_i)}{R_i \Delta r_{i+1} (\Delta r_{i+1} + \Delta r_i)} - \frac{2 RC_i (u_i - u_{i-1})}{R_i \Delta r_i (\Delta r_{i+1} + \Delta r_i)} \end{aligned} \quad (\text{A.22})$$

$$\frac{u}{r^2} = \frac{u_i}{R_i^2} \quad (\text{A.23})$$

and

$$\begin{aligned} \frac{\partial}{\partial z} \left(\frac{\partial u}{\partial z} \right) &= \frac{1}{\Delta z_i} \left[\left(\frac{u_{j+1} - u_j}{(\Delta z_{j+1} + \Delta z_j)/2} \right) - \left(\frac{u_j - u_{j-1}}{(\Delta z_j + \Delta z_{j-1})/2} \right) \right] \\ &= \frac{2 (u_{j+1} - u_j)}{\Delta z_j (\Delta z_{j+1} + \Delta z_j)} - \frac{2 (u_j - u_{j-1})}{\Delta z_j (\Delta z_j + \Delta z_{j-1})} \end{aligned} \quad (\text{A.24})$$

Discretization forms of the two terms inside the square brackets of Eq.(2.3) are

$$\begin{aligned} \frac{1}{r} \frac{\partial}{\partial r} \left(r \frac{\partial v}{\partial r} \right) &= \frac{1}{RC_i} \frac{1}{\Delta r_i} \left[R_i \frac{(v_{i+1} - v_i)}{(\Delta r_{i+1} + \Delta r_i)/2} - R_{i-1} \frac{(v_i - v_{i-1})}{(\Delta r_i + \Delta r_{i-1})/2} \right] \\ &= \frac{2 R_i (v_{i+1} - v_i)}{RC_i \Delta r_i (\Delta r_{i+1} + \Delta r_i)} - \frac{2 R_{i-1} (v_i - v_{i-1})}{RC_i \Delta r_i (\Delta r_i + \Delta r_{i-1})} \end{aligned} \quad (\text{A.25})$$

APPENDIX A Continued.

and

$$\begin{aligned} \frac{\partial}{\partial z} \left(\frac{\partial v}{\partial z} \right) &= \frac{1}{\Delta z_i} \left[\left(\frac{v_{j+1} - v_j}{(\Delta z_{j+1} + \Delta z_j)/2} \right) - \left(\frac{v_j - v_{j-1}}{(\Delta z_j + \Delta z_{j-1})/2} \right) \right] \\ &= \frac{2(v_{j+1} - v_j)}{\Delta z_j(\Delta z_{j+1} + \Delta z_j)} - \frac{2(v_j - v_{j-1})}{\Delta z_j(\Delta z_j + \Delta z_{j-1})} \end{aligned} \quad (\text{A.26})$$

Finally, discretization forms of the two terms inside the square brackets of in the energy equation, Eq.(2.3), are

$$\begin{aligned} \frac{1}{r} \frac{\partial}{\partial r} \left(r \frac{\partial T}{\partial r} \right) &= \frac{1}{RC_i} \frac{1}{\Delta r_i} \left[R_i \frac{(T_{i+1} - T_i)}{(\Delta r_{i+1} + \Delta r_i)/2} - R_{i-1} \frac{(T_i - T_{i-1})}{(\Delta r_i + \Delta r_{i-1})/2} \right] \\ &= \frac{2 R_i (T_{i+1} - T_i)}{RC_i \Delta r_i (\Delta r_{i+1} + \Delta r_i)} - \frac{2 R_{i-1} (T_i - T_{i-1})}{RC_i \Delta r_i (\Delta r_i + \Delta r_{i-1})} \end{aligned} \quad (\text{A.27})$$

and

$$\begin{aligned} \frac{\partial}{\partial z} \left(\frac{\partial T}{\partial z} \right) &= \frac{1}{\Delta z_i} \left[\left(\frac{T_{j+1} - T_j}{(\Delta z_{j+1} + \Delta z_j)/2} \right) - \left(\frac{T_j - T_{j-1}}{(\Delta z_j + \Delta z_{j-1})/2} \right) \right] \\ &= \frac{2(T_{j+1} - T_j)}{\Delta z_j(\Delta z_{j+1} + \Delta z_j)} - \frac{2(T_j - T_{j-1})}{\Delta z_j(\Delta z_j + \Delta z_{j-1})} \end{aligned} \quad (\text{A.28})$$

APPENDIX A *Continued.*

C. Gravity term:

The gravity term in Eq.(2.3) is calculated according to the cell position in the z-direction. Referring to the "v" momentum cell in figure A.2, the gravity force is linearly interpolated as

$$\frac{g}{\rho_0} \rho = \frac{g}{\rho_0} \left[\rho_{i,k} + (\rho_{i,k+1} - \rho_{i,k}) \frac{\Delta z_{i,k}}{\Delta z_{i,k+1} + \Delta z_{i,k}} \right] \quad (\text{A.29})$$

All terms except the temporal term were calculated from the momentum equation for each cell to evaluate provisional velocities for the explicit momentum equation solver shown in figure 2.8. The energy advective and diffusion terms were calculated to find the temperature field in the energy equation as shown in figure 2.8. After the velocity and temperature fields were obtained at the new time level, the solution procedure advanced to the next time step with a time step, Δt . This time step was limited to satisfy the stability criterion.

Stability criterion

The stability criteria for the time step can be found in [16]. The stability criterion in this study was based on two criteria for the momentum and the energy equations.

These criteria are

APPENDIX A Continued.

$$\text{Momentum: } \Delta t \leq \text{Min.} \left\{ \left(\frac{|u_{i,j}|}{\Delta r_i} + \frac{|v_{i,j}|}{\Delta z_j} + 2\nu \left[\frac{1}{(\Delta r_i)^2} + \frac{1}{(\Delta z_j)^2} \right] \right)^{-1} \right\} \quad (\text{A.30})$$

$$\text{Energy: } \Delta t \leq \text{Min.} \left\{ \left(\frac{|u_{i,j}|}{\Delta r_i} + \frac{|v_{i,j}|}{\Delta z_j} + 2\alpha \left[\frac{1}{(\Delta r_i)^2} + \frac{1}{(\Delta z_j)^2} \right] \right)^{-1} \right\} \quad (\text{A.31})$$

where, ν is kinematic viscosity, and α is the thermal diffusivity of the fluid. The computer program automatically choose the smaller Δt . For water, Eq.(A.30) applied; for air, Eq.(A.31) applied. The discretization form of a non-uniform grid for the stability criteria of Eq.(A.30) and Eq.(A.31) is

$$\Delta t \leq \text{Min.} \left\{ \left(\frac{|u_{i,j}|}{\frac{1}{2}(\Delta r_i + \Delta r_{i+1})} + \frac{|v_{i,j}|}{\frac{1}{2}(\Delta z_j + \Delta z_{j+1})} + 2 \text{Min.} \left\{ \begin{array}{l} \alpha \\ \nu \end{array} \right\}_{i,j} \left[\frac{1}{\Delta r_{i+1}(\Delta r_i + \Delta r_{i-1})} + \frac{1}{\Delta r_i(\Delta r_i + \Delta r_{i+1})} \right] + 2 \text{Min.} \left\{ \begin{array}{l} \alpha \\ \nu \end{array} \right\}_{i,j} \left[\frac{1}{\Delta z_{j+1}(\Delta z_j + \Delta z_{j-1})} + \frac{1}{\Delta z_j(\Delta z_j + \Delta z_{j+1})} \right] \right)^{-1} \right\} \quad (\text{A.32})$$

In addition, a conservative factor, 0.9, was applied to multiply the minimum Δt to ensure numerical stability.

APPENDIX A Continued.

Plot of the streamfunction

Plots of isotherms and streamlines were used to depict graphically the temperature distribution and flow behavior of the computational region. Temperature fields were obtained at the third phase of the solution procedure as shown in figure 2.8, however no streamfunction fields were solved in this solution procedure.

Streamfunctions are related to the velocity field according to

$$u = -\frac{1}{r} \frac{\partial \Psi}{\partial z} \quad (\text{A.33})$$

$$v = -\frac{1}{r} \frac{\partial \Psi}{\partial r} \quad (\text{A.34})$$

With reference to figure A.3, where Ψ 's are located at the four corners of the continuity cell (i,j) , the discretization form of Eq.(A.34) relating Ψ and $v_{i,j}$ is

$$v_{i,j} = -\frac{1}{RC_i} \frac{\Psi_{i,j} - \Psi_{i-1,j}}{\Delta r_i} \quad (\text{A.35})$$

By Rearranging Eq.(A.35), the streamfunction, $\Psi_{i,j}$, can be found in reference to a known value of Ψ starting at the boundary as

$$\Psi_{i,j} = \Psi_{i-1,j} - RC_i \Delta r_i v_{i,j} \quad (\text{A.36})$$

APPENDIX B

SETUP OF THE MACH-ZEHNDER INTERFEROMETER

The basic optics required for a Mach-Zehnder interferometer are two mirrors and two beamsplitters. The two mirrors used in this study were first-surface mirrors. Rays of light will not enter the substrate of such a mirror. Thus, it is easier to keep track of a ray. The two beamsplitters, on the other hand, are geometrically more complex than mirrors. Figure B.1 shows the dimensions of a beamsplitter, specified by the manufacture [42], used in this experiment.

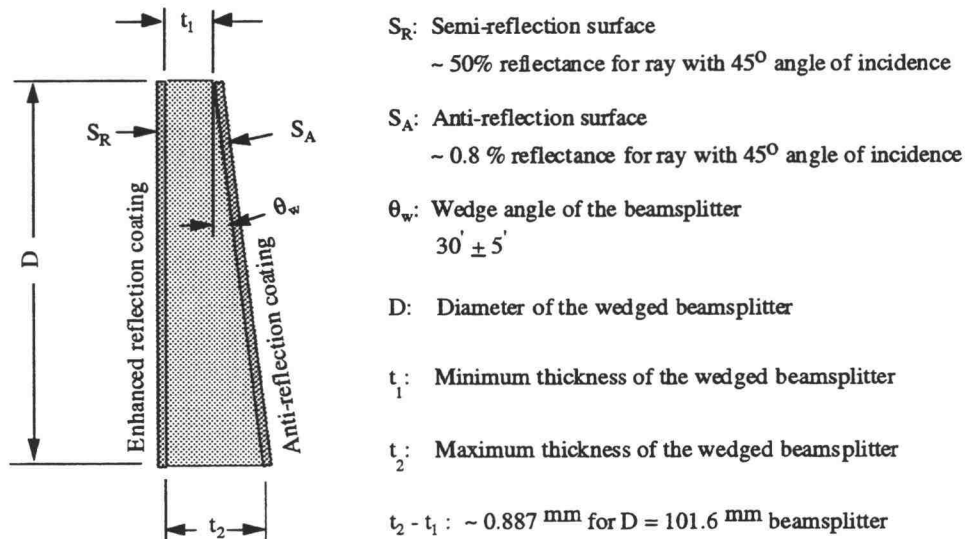


Figure B.1 Schematic of a beamsplitter

APPENDIX B Continued.

As shown in figure B.1, one surface of the beamsplitter was coated with an enhanced reflective thin film - a reflection coating. For a light ray with an angle of incidence approximating 45° , this coating allows 50% of the intensity to be reflected and 50% to be transmitted. The other surface of the beamsplitter was coated with an anti-reflection coating that allowed only 0.8% of the intensity to be reflected and the other 99.2% to be transmitted. The purpose of this anti-reflection coating is to eliminate ghost images of the reflected rays.

In addition to the anti-reflection coating, the anti-reflection surface, S_A , was oriented with a slightly wedged angle, θ_w , as shown in figure B.1. This wedge angle on the anti-reflection surface, S_A , reflects a transmitted ray at a larger angle than does the semi-reflection surface, S_R . The two reflected rays from S_A and S_R are then far apart due to θ_w , thus the ghost images are completely eliminated.

A beamsplitter used in this study will reflect and transmit a light beam depending on the surface coating, the angle of incidence, and the wavelength of the light beam. To describe rays traveling in a wedged beam splitter in the following discussion, we will assume 50% reflection and 50% transmission on S_R , and 0.8% reflection and 99.2% transmission on S_A while disregarding the angle of

APPENDIX B Continued.

incidence, wavelength of the incident light, and the coating materials.

In figure B.2, a collimated beam with a beam diameter D_i enters the beamsplitter from the semi-reflection surface with an angle of incidence θ_i . Rays A and B, separated by the beam diameter, are the uppermost and lowermost rays of the collimated beam paralleling the direction of propagation. These two rays are refracted with an angle θ_t in the beamsplitter and refracted into the air with an output angle θ_o according to Snell's law. The output angle and the incident angle would be the same if the two

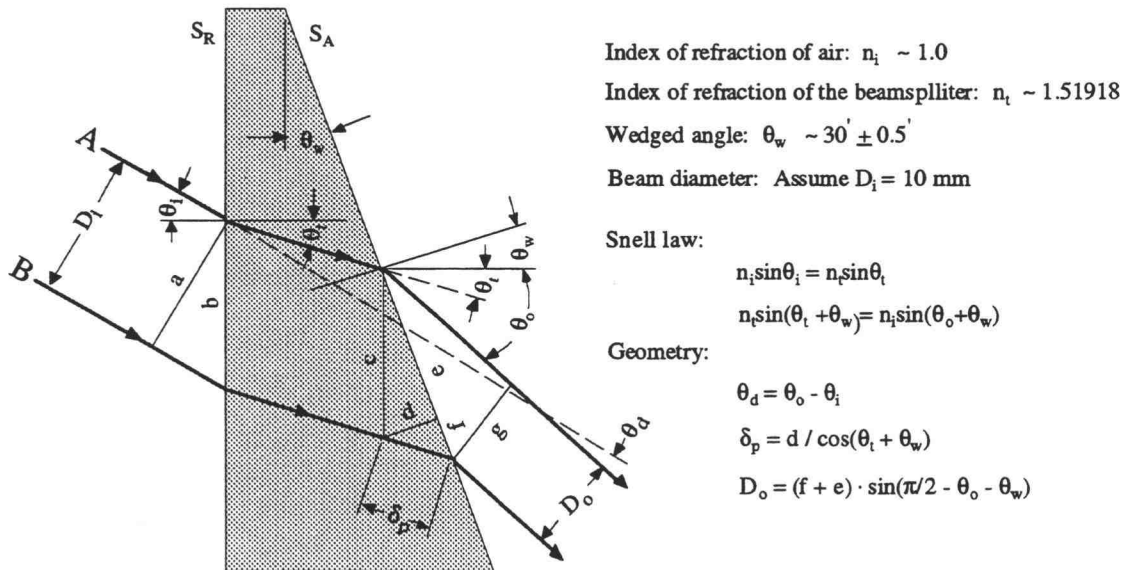


Figure B.2 Geometrical depict of rays traveling through a wedged beamsplitter

APPENDIX B Continued.

surfaces, S_R and S_A , of the beamsplitter were parallel to each other. Three geometrical changes can be observed due to the presence of θ_w . They are the difference of the angle, θ_d , between the incident beam and the output beam; the path difference, δ_p , between ray A and ray B; and the beam diameter difference, $D_i - D_o$, between the incident beam and the outgoing beam. These three differences depend on the angle of incidence of the incoming beam. A plot of these quantities as functions of θ_i is shown in figure B.3. Note that values of all three functions increase as θ_i increases.

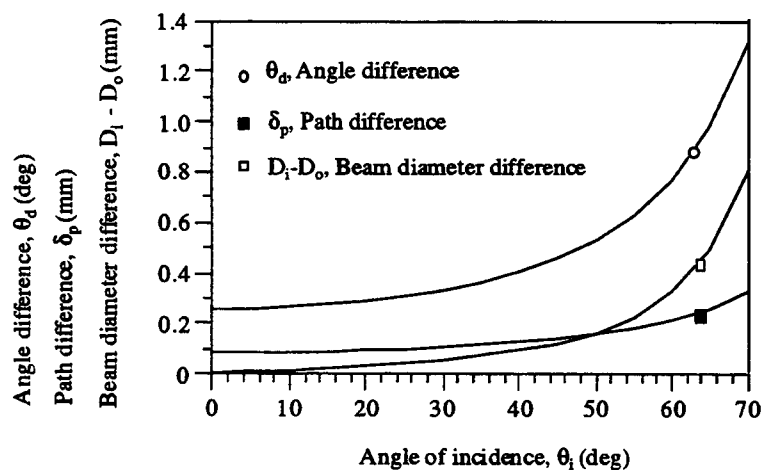


Figure B.3. Plot of θ_d , δ_p , $D_i - D_o$ as functions of θ_i for a beamsplitter

APPENDIX B Continued.

One goal of arranging a Mach-Zehnder interferometer is to achieve same characteristics, θ_d , δ_p , $D_i - D_o$, at the output of the two beamsplitters. To do this, it is necessary to have the same angle of incidence for the two beams impinging on the beamsplitters. For the case of the same angle of incidence, the difference between the light ray reflecting from the semi-reflection surface, S_R , and the anti-reflection surface, S_A , will be discussed first. Figure B.4 shows a light ray striking the beamsplitter on the semi-reflecting surface, S_R . Due to the enhanced reflection coating on S_R , 50% of its intensity is reflected onto the observation screen and the other 50% is transmitted into the beamsplitter. The transmitted ray will then strike on the anti-reflection surface, S_A .

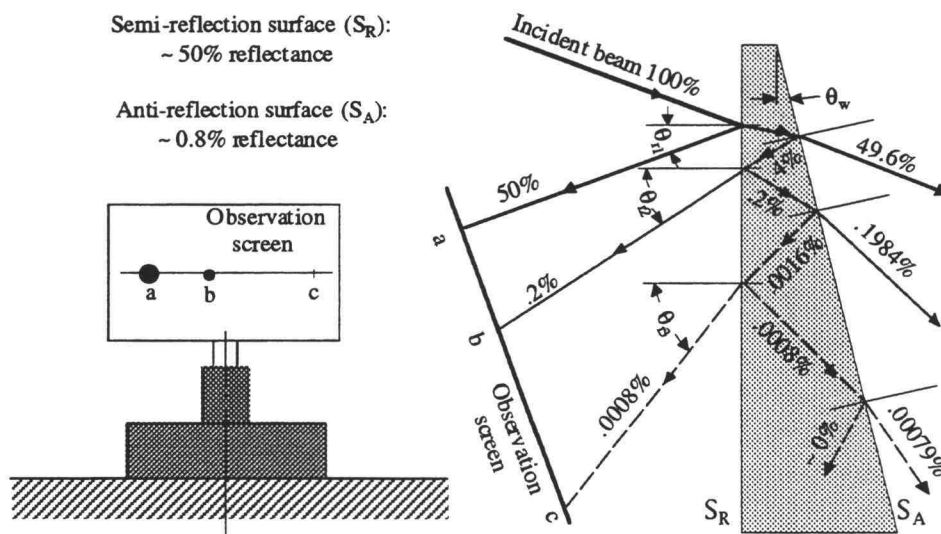


Figure B.4 Light spots reflected from the semi-reflection surface of a beamsplitter

APPENDIX B Continued.

Because of the anti-reflection coating on S_A , most of the intensity of this beam, 99.2% of 50%, i.e. 49.6% of its original intensity, is transmitted into the air, and only a small portion, 0.4% of its original intensity reflects back on S_R . Then, 0.2% transmits onto the observation screen and 0.2% reflects back S_A , etc. Two spots, a and b, of light can be observed on the screen. By carefully examining the screen, a third spot, c, of light can be found. The intensity of spot c is very weak. The reflecting angle, θ_{r2} , is larger than θ_{r1} , and θ_{r3} is larger than θ_{r2} due to the wedge angle, θ_w , of the beamsplitter. Thus, no ghost images will be formed.

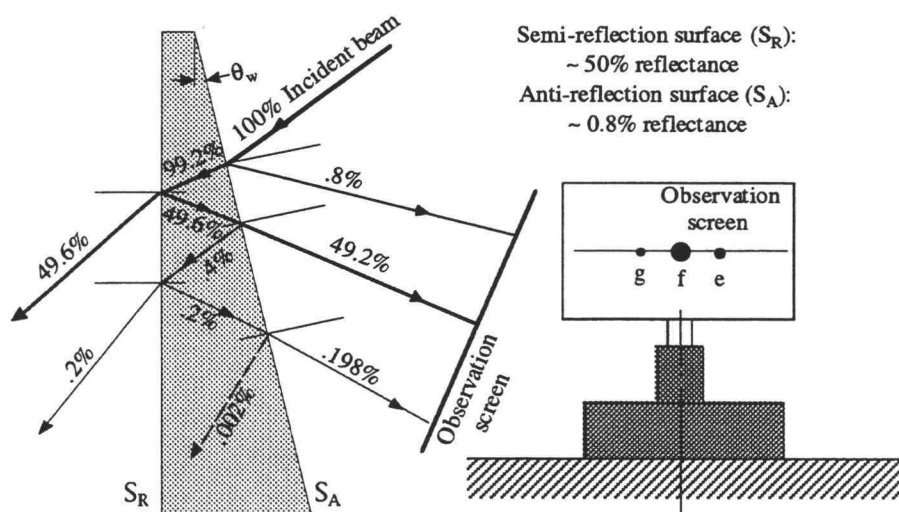


Figure B.5 Light spots reflected from the anti-reflection surface of a beamsplitter

In contrast to a ray striking S_R , figure B.5 shows a ray striking the anti-reflection surface, S_A . Just as with

APPENDIX B Continued.

a ray striking S_R , three spots, e, f, and g, of light can be observed on the observation screen. The lowest intensity light spot, g, is as bright as light spot b, shown in figure B.4. To align both beamsplitters with identical angles of incidence, these reflecting spots can be used as reference points.

Figure B.6 shows the final setup of the Mach-Zehnder interferometer in a 60° parallelogram configuration. Larger beam cross sections can be obtained for this type of configuration [26]. A collimated beam with a diameter D_i is separated by beamsplitter, B_1 , into two beams. One beam passes one arm of the interferometer

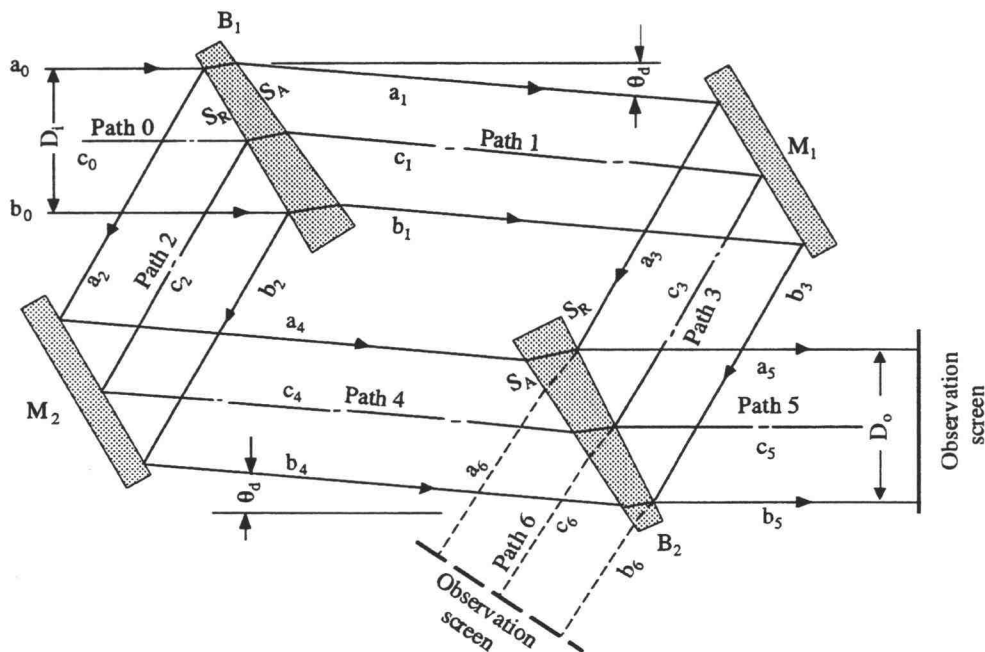


Figure B.6 Arrangement of the Mach-Zehnder interferometer

APPENDIX B Continued.

through path 0, 2 and 4, and the other beam passes the other arm of the interferometer through path 0, 1 and 3.

These two beams are then recombined either on the screen on path 5 or on path 6. The semi-reflection surface of B_1 , and the semi-reflection surface of B_2 are arranged in opposite fashion so that each beam transmits either only once through the beamsplitter on the screen on path 5, or twice on path 6. A beam diameter will not be altered if it is merely reflected by first-surface mirrors. Thus, beam diameters on path 0, 2, and 4 are the same as are beam diameters on path 1, 3, and 5. To insure that the resulting beam diameters are the same on path 5 from both path 0, 2 and on 4 from path 0, 1, and 3, the incident angle on S_R of B_1 must equal the incident angle on S_A of B_2 . To do this, S_R of B_1 must be arranged parallel to S_R of B_2 .

For a coarse alignment, it is better to use a smaller diameter beam in the interferometer. The center lines, c_0 to c_6 , in figure B.6 are the paths of the smaller beam before it is collimated. Figure B.7 shows the procedures for coarse alignment of the interferometer.

Procedure 1 in figure B.7 is to orient the wedged surface, the anti-reflection surface, S_A , of B_1 normal to the surface of the optical table. This can be done by examining the transmitted light spot on the observation screen S_2 and the reflected spots, a and b on S_1 . These

APPENDIX B Continued.

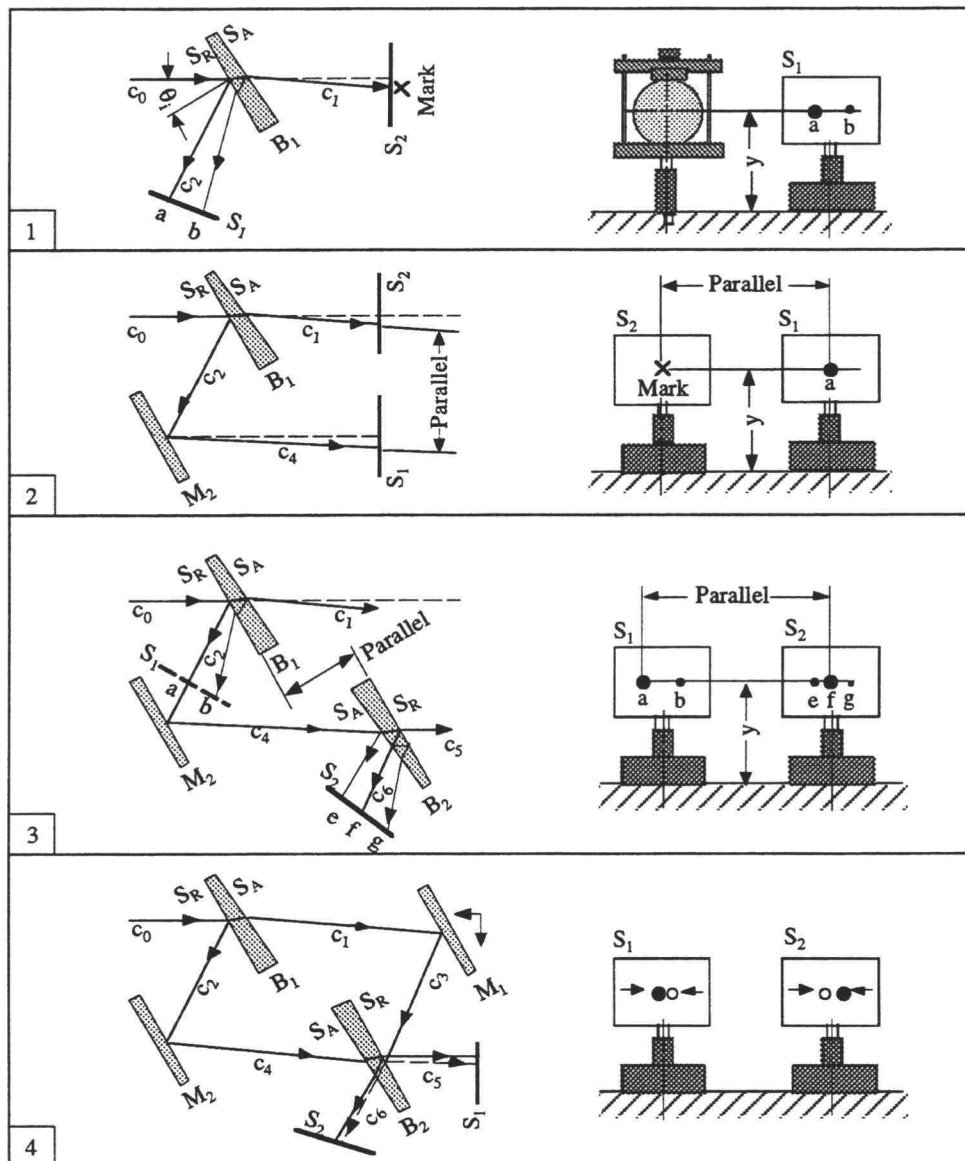


Figure B.7 Alignment procedures of the Mach-Zehnder interferometer

three spots must be at the same height above the surface of the optical table. The position of these spots is the source as the height of the incident beam striking B_1 , and

APPENDIX B Continued.

the centers of all optics in the interferometer should be at this same height also.

Procedure 2 is to arrange the light beam c_1 on path 1 parallel to c_4 on path 4. This can be accomplished referring to the marked spot on S_2 and the light spot reflecting from the mirror, M_2 , as shown.

Procedure 3 is to arrange an identical angle of incidence of c_0 and c_4 striking the two beamsplitters. This can be done by examining the reflecting spots of a and f on S_1 and S_2 as shown.

The last coarse alignment procedure is to recombine the two separated beams. This can be done by moving the mirror, M_1 , back and forth to recombine the two spots on each screen into one. If this alignment is sufficiently accurate, interference fringes can be seen using a lens to cause a divergence in either of the recombined beams.

After the input beam is collimated, fringes will appear on the observation screen. To use a wedged fringe field, no additional precise adjustment is needed in the alignment. Such fringe fields can be obtained by tilting one of the four optics. To use an infinite fringe field, precise alignment is needed. To obtain such a fringe field, one must align the two arms to be equal in length as stated in chapter 4 since no perfect "plane" wave can be obtained. Fringe patterns from the numerical results of

APPENDIX B Continued.

two-point-source interference are useful as references for precise alignment of the infinite fringe field.